CFD Modeling and Simulation in Materials Processing 2016

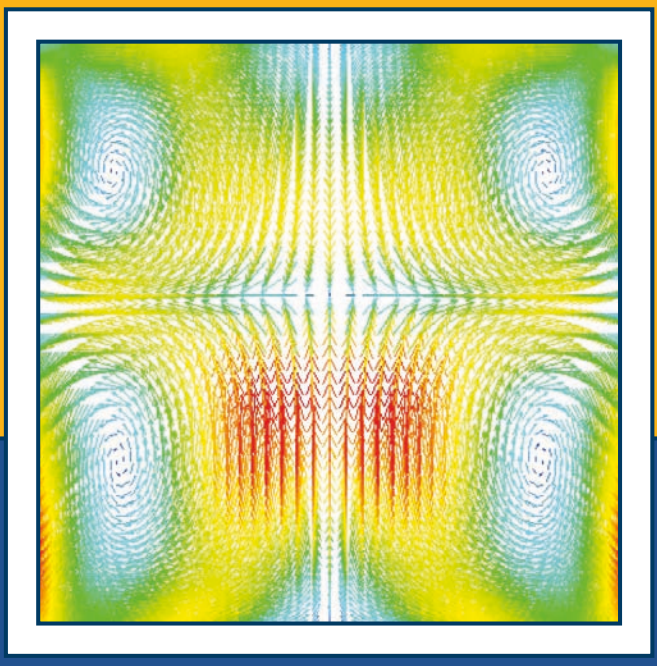

Edited by
Laurentiu Nastac, Lifeng Zhang, Brian G. Thomas, Miaoyong Zhu, Andreas Ludwig, Adrian S. Sabau, Koulis Pericleous, and Hervé Combeau

TMS

Springer

CFD Modeling and Simulation in Materials Processing 2016

TMS2016

145th Annual Meeting & Exhibition

FEBRUARY 14-18 DOWNTOWN NASHVILLE, TENNESSEE MUSIC CITY CENTER

New proceedings volumes from the TMS2016 Annual Meeting:

- 7th International Symposium on High-Temperature Metallurgical Processing
- CFD Modeling and Simulation in Materials Processing 2016
- Characterization of Minerals, Metals, and Materials 2016
- Energy Technology 2016: Carbon Dioxide Management and Other Technologies
- EPD Congress 2016
- Light Metals 2016
- Magnesium Technology 2016
- Rare Metal Technology 2016
- REWAS 2016
- Shape Casting: 6th International Symposium
- TMS 2016 Supplemental Proceedings

CFD Modeling and Simulation in Materials Processing 2016

Proceedings of a symposium sponsored by
the Process Technology and Modeling Committee
of the Extraction and Processing Division
and the Solidification Committee of
the Materials Processing and Manufacturing Division
of The Minerals, Metals & Materials Society (TMS)

held during

TMS2016
145th Annual Meeting & Exhibition

FEBRUARY 14-18 DOWNTOWN NASHVILLE, TENNESSEE MUSIC CITY CENTER

Edited by:

Laurentiu Nastac, Lifeng Zhang, Brian G. Thomas, Miaoyong Zhu, Andreas Ludwig, Adrian S. Sabau, Koulis Pericleous, and Hervé Combeau

Editors
Laurentiu Nastac
Lifeng Zhang
Brian G. Thomas
Miaoyong Zhu
Andreas Ludwig
Adrian S. Sabau
Koulis Pericleous
Hervé Combeau

ISBN 978-3-319-65132-3 ISBN 978-3-319-65133-0 (eBook)
DOI 10.1007/978-3-319-65133-0

Chemistry and Materials Science: Professional

Published by Springer International Publishers, Switzerland, 2016
Reprint of the original edition published by John Wiley & Sons, Inc., 2016, 978-1-119-22576-8

Printed on acid-free paper

This Springer imprint is published by Springer Nature
The registered company is Springer International Publishing AG
The registered company address is: Gewerbestrasse 11, 6330 Cham, Switzerland

TABLE OF CONTENTS

CFD Modeling and Simulation in Materials Processing 2016

Iron and Steelmaking (Tundish, Casting, Converter, Blast Furnace)

Microstructure Evolution

Casting with External Field Interaction

Smelting, Degassing, Ladle Processing, Mechanical Mixing, and Ingot Casting

Poster Session

PREFACE

This book contains the proceedings of the symposium, "CFD Modeling and Simulation in Materials Processing," held at the TMS 2016 Annual Meeting & Exhibition in Nashville, Tennessee, February 14–18, 2016.

This symposium dealt with computational fluid dynamics (CFD) modeling and simulation of engineering processes. The papers published in this book were requested from researchers and engineers involved in the modeling of multiscale and multiphase phenomena in material processing systems.

The symposium focused on the CFD modeling and simulation of the following processing areas: Iron and Steelmaking (Tundish, Casting, Converter, Blast Furnace), Smelting, Degassing, Ladle Processing, Mechanical Mixing, and Ingot Casting, Casting with External Field Interaction and Microstructure Evolution.

The symposium also covered applications of CFD to engineering processes and demonstrated how CFD can help scientists and engineers to better understand the fundamentals of engineering processes.

On behalf of all symposium organizers and participants,

Prof. Laurentiu Nastac
The University of Alabama
Dept. of Metallurgical & Materials Engineering

EDITORS

Laurentiu Nastac is currently an Associate Professor of Metallurgical and Materials Engineering at The University of Alabama, Metallurgical and Materials Engineering Department, Tuscaloosa, Alabama, a Key FEF Professor and the Director of the Solidification Laboratory and the UA-COE foundry. For his teaching and research interests please visit his website: http://lnastac.people.ua.edu/. Dr. Nastac received the Diploma Engineering degree in Metallurgy and Materials Science from the University "Politehnica" of Bucharest, Romania in 1985 and the M.S. and Ph.D. degrees in Metallurgical and Materials Engineering from The University of Alabama, Tuscaloosa in 1993 and 1995, respectively. He has held various engineering, research, and academic positions in Romania and the United States. At Caterpillar he conducted research in the area of macro transport and solidification-kinetics modeling and developed specialized casting simulation software. At Concurrent Technologies Corporation (CTC) he conducted research primarily in the area of advanced metalcasting and solidification processes with emphasis on the modeling and simulation of casting phenomena. In 1999, in recognition of his work on solidification of titanium-based alloys and superalloy remelt ingots, he received the prestigious Bunshah Best Paper Award from the American Vacuum Society, Vacuum Metallurgy Division. More recently, he received the NMC (Navy Metalworking Center) achievement award and 2 CTC awards. Dr. Nastac developed eight software tools; made more than 160 presentations; co-authored three patents, over 150 conference and journal articles and more than 70 scientific reports in the materials science and manufacturing fields; and co-authored 10 books—one is a monograph titled *Modeling and Simulation of Microstructure Evolution in Solidifying Alloys* published by Springer in 2004. He is a key reader for *Metallurgical and Materials Transactions*, a member of the Editorial Board of the *International Journal of Cast Metals Research*, and a member of the TMS Solidification Committee; he has served on scientific committees and as an organizer for international conferences dedicated to CFD modeling and simulation in materials processing area and for casting and solidification processes.

Lifeng Zhang currently is a Professor and the Dean of the School of Metallurgical and Ecological Engineering at University of Science and Technology Beijing, and a Distinguished Professor of Yangtze River Scholars of China. Lifeng received his Ph.D. degree from University of Science and Technology Beijing in 1998 and has extensive teaching and research work at different universities – University of Science and Technology Beijing, Missouri University of Science and Technology, Norwegian University of Science and Technology, University of Illinois at Urbana-Champaign, Technical University of Clausthal, and Tohoku University. Lifeng has compound backgrounds in primary production, refining, casting, and recycling of metals, recycling of electronic wastes and solar grade silicon, and process modeling for metallurgical processes. Lifeng has published over 300 papers and gave over 180 presentations at meetings and conferences. He is a key reader of *Metallurgical and Materials Transactions A* and *Metallurgical and Materials Transactions B*, advisory board member of *ISIJ International*, member of the editorial board of *Ironmaking and Steelmaking*, *Revue de Métallurgie*, *Journal of Metals and Metallurgy*, and *Advances in Manufacturing*, and a member of the board of review of *Iron and Steel Technology* (AIST Transactions). Lifeng is a member of TMS, AIST, and ISIJ. He has received several best paper awards from TMS and AIST, and has been a reviewer for over 60 journals.

Brian G. Thomas is the Gauthier Professor of Mechanical Engineering at the University of Illinois and Director of the Continuous Casting Consortium. His research efforts focus on computational modeling of continuous casting of steel and related processes. He received his Bachelors of Metallurgical Engineering from McGill University, (Montreal, Canada) in 1979 and Ph.D. in Metallurgical Engineering in 1985 from the University of British Columbia, Canada. He has worked in the research departments of Algoma Steel, Sault Ste. Marie, Canada and BHP in Melbourne, Australia. Dr. Thomas has coauthored over 350 papers, and been recognized with several awards: Presidential Young Investigator Award from NSF, Outstanding Young Manufacturing Engineer Award from SME, Xerox Award from UIUC, Distinguished Scientist and Application to Practice Awards from TMS, Baosteel Honorary Professor, HPC Innovation Award, Fellow of ASM International, and 14 best paper awards (from AFS, AIME, ISS, AIST, TMS, CIM, and ASM International). He has given over 200 presentations worldwide and co-instructed many short courses to industry, including the annual Brimacombe Continuous Casting Course.

Miaoyong Zhu is currently Professor and Dean of Metallurgy School (MS), Northeastern University (NEU), Shenyang, China. He was awarded the Changjiang Scholars Distinguished Professor by The Ministry Education of China in 2012. Dr. Zhu received the B.S., M.S., and Ph.D. degrees in Ferrous Metallurgy from Northeastern University, China in 1988, 1991, and 1994, respectively, and after earning his Ph.D., he continued his postdoctoral study in NEU for two years. Dr. Zhu was promoted to an Associated Professor in 1995 and Full Professor in MS in 1999.

He has experience as a Ph.D. student, postdoctoral fellow, and visiting researcher in Advanced Research Laboratories of Nippon Steel Corporation, Japan, in 1993, 1995 and 1997, respectively, and a guest researcher in the Metallurgy Department, Royal Institute of Technology (KTH), Sweden, in 1998. He has conducted research primarily in the areas of clean steel making and continuous casting processes with emphasis on the simulation and control of non-metallic inclusion behavior during steel refining and solidification phenomena of continuous casting.

Dr. Zhu has co-authored 52 patents and more than 240 publications in the steelmaking field, and has edited five books. Dr. Zhu is the winner of National Outstanding Young Scientists Foundation, China, and he also was awarded the "Wei Shoukun Science Technology and Education Prize" (for Young Metallurgist) in 2012.

Andreas Ludwig is Full Professor at the Metallurgy Department of the Montanuniversitaet Leoben in Austria, Europe. For his teaching and research interests please visit his website: http://smmp.unileoben.ac.at/. Dr. Ludwig received a Diploma in Physics from the University Düsseldorf, Germany in 1987, a Ph.D. degree in Engineering from the Rheinisch-Westfälischen Technischen Hochschule RWTH, Aachen, Germany in 1992, and a habilitation degree in Materialphysics also from the RWTH Aachen in 1999. His research career started in 1988 at the Max-Planck-Institute for Iron-research in Düsseldorf, Germany. In 1993/4 he did his post-doctoral research at the Ecole Polytechnique Federal de Lausanne, EPFL, Switzerland with Prof. W. Kurz as a fellow from the German Science Foundation. In 1992/3 and then 1994/2002 he led the simulation group at the Foundry Institute of the RWTH, Aachen. In 2003 he was appointed as full professor at the Montanuniversitaet Leoben. In addition, he acted 2004/11 as head of the Christian-Doppler Laboratory of Multiphase Modeling of Metallurgical Processes. Since 2008 he has been scientific area leader of the K2-Center for Materials

Engineering, Process Engineering and Product Development (MPPE), since 2009 member of the Austrian Committee of the International Institute for Applied System Analysis (IIASA)," and since 2014 board member of the Austrian Science Fund (FWF) as deputy reporter for Engineering Technology. He has chaired four international conferences, written more than 320 scientific papers, and currently holds an H-factor of 18. Since spring 2013, the database SCOPUS reveals Prof. Ludwig to be the world-leading scientist with regards of publications on macrosegregation.

Adrian S. Sabau received his Diploma of Inginer in Mechanical Engineering/Materials Processing from the University of Craiova, Romania in 1992 and a Ph.D. degree in Mechanical Engineering from Southern Methodist University in 1996. In 1999, Dr. Sabau joined Oak Ridge National Laboratory as a Research Staff Member of the Materials Science and Technology Division, where he currently is a Senior Research Staff Member since 2008. Dr. Sabau is the recipient of two R&D 100 awards in process sciences. Dr. Sabau seeks to advance the materials processing, metal casting, photonic processing, and materials for energy applications through the development of solution algorithms, computational and experimental methodologies for the property measurement, process analysis, and materials behavior in response to conditions experienced in service, such as oxide exfoliation in steam boiler tubes and high-heat flux of tungsten-based materials for fusion applications. Dr. Sabau has published more than 50 journal papers, 73 conference papers, and has three patent applications.

Koulis Pericleous holds the Chair of Computational Fluid Dynamics at the University of Greenwich, London and he is a Director of the Centre for Numerical Modelling and Process Analysis. Details of his current research interests and other academic activities please visit his website: http://staffweb.cms.gre.ac.uk/~k.pericleous/. Dr. Pericleous received his Bachelor's degree in Aeronautics at Queen Mary College, University of London, in 1974 and subsequently a Ph.D. in Unsteady Aerodynamics at the same institution. On leaving University, he joined the scientific software company CHAM, where he worked under Professor Spalding in the development of the first commercial CFD code PHOENICS. For the next ten years, he held various positions in CHAM, rising to Head of Consultancy Services in 1987. Under his direction, his team worked on a wide range of industrial problems, many in the metals processing sector. A notable

example was the development through CFD of the novel HiSmelt process in Australia, for the production of iron directly from ore. He rejoined the Academia at the University of Greenwich in 1989, becoming a full Professor in 1994. In his 26 plus years at Greenwich, he gained several U.K. government and European grants on important research projects. These were mostly collaborative with industrial partners in the area of advanced materials. Examples include the cold crucible melting and casting of TiAl turbine blades, the gas atomization of NiAl powders, the production of lightweight metal-matrix nanocomposites using electromagnetic interaction, the ultrasonic processing of flowing volumes of aluminum, modeling levitated melts in the ISS MSL facility etc. Prof. Pericleous and his team developed a number of CFD tools for industry, including the multi-physics code PHYSICA and the aluminum electrolysis code MHD-Valdis. He is the author of almost 300 publications and he supervised 33 Ph.D. students. He is a grant reviewer for several U.K. and European national bodies and is on the editorial board of three archival journals.

Hervé Combeau holds an M.Sc. from the Institut National Polytechnique de Lorainne (INPL, 1981) and earned his doctorate degree in mechanical engineering from the same university in 1986. Dr. Combeau started his career at university in 1986 as assistant professor at the Nancy I university (IUT Longwy) where he taught heat transfer, air treatment, and thermodynamics. In 1988 he moved to the Ecole des Mines de Nancy (Lorraine University) where he is presently a professor. He teaches fluid mechanics, heat and mass transfer, modeling and numerical simulation, and combustion. Moreover, he is the head of the department Process, Energy and Environment. His main field of research is the mathematical modeling of transport phenomena occurring during solidification. He developed software used by industry for microstructures, macrosegregations and microsegregations predictions. He is the head of the 'Solidification' research group at Institut Jean Lamour. He is the author or co-author of 66 technical publications in refereed journals. From 2011 to 2014 he was the coordinator of the research network 'Solidification of metallic alloys' involving 24 research groups in France.

CFD Modeling and Simulation in Materials Processing 2016

Iron And Steelmaking (Tundish, Casting, Converter, Blast Furnace)

Session Chair:
Lifeng Zhang

CFD Modeling and Simulation in Materials Processing 2016
Edited by: Laurentiu Nastac, Lifeng Zhang, Brian G. Thomas, Miaoyong Zhu, Andreas Ludwig, Adrian S. Sabau, Koulis Pericleous, and Hervé Combeau
TMS (The Minerals, Metals & Materials Society), 2016

ON THE IMPORTANCE OF MODELING 3D SHRINKAGE CAVITIES FOR THE PREDICTION OF MACROSEGREGATION IN STEEL INGOTS

A. Ludwig[1], M. Wu[1,2], A. Kharicha[1,2]

[1]Chair of Simulation and Modelling of Metallurgical Processes, Montanuniversitaet Leoben, Austria
[2]Christian Doppler Laboratory for Advanced Process Simulation of Solidification and Melting, Montanuniversitaet Leoben, Austria

Keywords: Solidification, Macrosegregation, Steel, Ingot, Modeling

Abstract

With this work an existing 3-phase mixed columnar-equiaxed solidification model is extend to treat the formation of shrinkage cavity by including an additional phase. In the previous model a mixed columnar and equiaxed solidification approach that considers the multiphase transport phenomena (mass, momentum, species and enthalpy) is proposed to calculate the as-cast structure including columnar-to-equiaxed transition (CET) and formation of macrosegregation. In order to incorporate the formation of shrinkage cavity, a supplementary phase, i.e. gas phase or covering liquid slag phase, is considered in addition to the previously introduced 3 phases (parent melt, solidifying columnar dendrite trunks and equiaxed grains). No mass and species transfer between the new phase and the other 3 phases is necessary, but momentum and energy transfer is of critical importance for the formation of the shrinkage cavity and with that the flow and formation of macrosegregation would be influenced. Some modelling approaches for the momentum and energy transfer are suggested and tested.

Introduction

Typical steel ingots solidify with a shrinkage cavity at the hot top, and with microscopic shrinkage porosity and macrosegregation located somewhere in the cross section [1]. Those undesired casting defects result from the volume change during solidification (and the resulting feeding flow), thermal-solutal convection and crystal sedimentation. The formation mechanisms of these phenomena are rather complex as they interact with each other. Scientists have tried different approaches to model and predict their occurrence [2-9], but no model is available to calculate shrinkage cavity/porosity together with macrosegregation in a coupled manner. The formation process of the above defects is multiphasic in nature.

This work is to extend an existing 3-phase mixed columnar-equiaxed solidification model [10] to treat the formation of shrinkage cavity by including an additional gas (or covering slag) phase [11]. Four phases are necessarily considered: primary liquid melt, equiaxed crystals, columnar dendrite trunks, and gas/liquid slag. The final goal is to develop an Eulerian multiphase solidification model at the process scale to calculate the as-cast columnar-equiaxed structure including CET (columnar-to-equiaxed transition), shrinkage cavity/porosity, and macrosegregation for industrial castings.

The Numerical Model

Brief model description

- Phase definition: primary liquid (ℓ), solidifying equiaxed phase (e), columnar phase (c), and gas phase (g). Their volume fractions (f_ℓ, f_e, f_c, f_g) sum up to one. The volume averaged mass transport equations considering the mass transfer due to solidification are solved.
- There is no mass transfer between the gas and the other phases, and the gas phase is supposed to be immiscible with the other metal phases. In fact, the gas phase is sucked into the casting domain to feed the shrinkage cavity. The interface between the gas and the other phases is explicitly solved. The microscopic porosity that forms deep in the inter-dendritic region is treated differently (see below).
- The liquid, equiaxed and gas phases are moving phases, for which the corresponding volume averaged Navier-Stokes equations are solved to get $\vec{u}_\ell$, $\vec{u}_e$ and $\vec{u}_g$. For the columnar phase we assume $\vec{u}_c \equiv 0$.
- Enthalpy equations for all 4 phases are solved. Due to the fact of relatively large thermal diffusivity, we assume that only one temperature (T) represents each volume element. Therefore, a large inter-phasic volume heat exchange coefficient is applied to balance the temperatures among the phases.
- Three volume-averaged concentration fields (c_ℓ, c_e, c_c) are solved for the three metal phases. Thermodynamic equilibrium condition is assumed to apply at the liquid-solid interface, and corresponding solute partitioning at the interface occurs during solidification.
- A diffusion-governed growth kinetic is considered to calculate the growth of crystals.
- Ideal morphologies for both solid phases are assumed: spheres for equiaxed (globular) grains and cylinders for columnar (cellular) dendrite trunks.
- The columnar dendrite trunks are assumed to be originated from the mould wall. Neither nucleation of columnar trunks nor equiaxed-to-columnar transition (ECT) is taken into account.
- Heterogeneous nucleation and transport of the equiaxed crystals are considered. Grain fragments brought into the mould during filling, further fragmentation of dendrites during solidification and the attachment of equiaxed grains into columnar area (as a part of the columnar phase) are ignored.
- The diameter, d_e, and number density, n_e, of equiaxed grains and the diameter, d_c, of the columnar trunks are explicitly calculated, while a constant value for the primary arm spacing of columnar dendrites, λ_1, is assumed.

Details of the three-phase mixed columnar-equiaxed solidification model were described elsewhere [10]. Treatment of the gas phase, the formation of the shrinkage cavity and of porosity is described below.

Treatment of interactions between gas and other phases

As no mass/species transfer between the gas and the other metal phases is considered, only enthalpy and momentum conservation equations for the gas phase are necessarily solved:

$$\frac{\partial}{\partial t}\left(f_g \rho_g h_g\right) + \nabla \cdot \left(f_g \rho_g \vec{u}_g h_g\right) = \nabla \cdot \left(f_g k_g \nabla \cdot T_g\right) + Q_{\ell g}^{ex} + Q_{eg}^{ex} + Q_{cg}^{ex} \qquad (1)$$

$$\frac{\partial}{\partial t}\left(f_{\mathrm{g}}\rho_{\mathrm{g}}\vec{u}_{\mathrm{g}}\right)+\nabla\cdot\left(f_{\mathrm{g}}\rho_{\mathrm{g}}\vec{u}_{\mathrm{g}}\otimes\vec{u}_{\mathrm{g}}\right)=-f_{\mathrm{g}}\nabla p+\nabla\cdot\bar{\bar{\tau}}_{\mathrm{g}}+f_{\mathrm{g}}\rho_{\mathrm{g}}\vec{g}+\vec{U}^{\mathrm{ex}}_{\ell\mathrm{g}}+\vec{U}^{\mathrm{ex}}_{\mathrm{eg}}+\vec{U}^{\mathrm{ex}}_{\mathrm{cg}} \quad (2)$$

Key feature by introducing a new gas phase in the mixed columnar-equiaxed solidification is to treat the exchange terms, which are superscripted with 'ex' in Eq. (1) and (2). They are summarized in Table 1.

Table 1. Momentum and energy exchange terms between gas and other metal phases

$Q^{\mathrm{ex}}_{\ell\mathrm{g}}=H^{*}_{\ell\mathrm{g}}f_{\ell}f_{\mathrm{g}}\left(T_{\ell}-T_{\mathrm{g}}\right)$ $Q^{\mathrm{ex}}_{\mathrm{eg}}=H^{*}_{\mathrm{eg}}f_{\mathrm{e}}f_{\mathrm{g}}\left(T_{\mathrm{e}}-T_{\mathrm{g}}\right)$ $Q^{\mathrm{ex}}_{\mathrm{cg}}=H^{*}_{\mathrm{cg}}f_{\mathrm{c}}f_{\mathrm{g}}\left(T_{\mathrm{c}}-T_{\mathrm{g}}\right)$	$H^{*}_{\ell\mathrm{g}}$ [W/m^3/K]: the volume heat exchange coefficient is modelled according to Ranz-Marshall [11,12]. H^{*}_{eg} and H^{*}_{cg} : a constant volume heat exchange coefficient of 500 W/m^3/K is assumed.	
$\vec{U}^{\mathrm{ex}}_{\ell\mathrm{g}}=K_{\ell\mathrm{g}}\cdot\left(\vec{u}_{\ell}-\vec{u}_{\mathrm{g}}\right)$ $\vec{U}^{\mathrm{ex}}_{\mathrm{eg}}=K_{\mathrm{eg}}\cdot\left(\vec{u}_{\mathrm{e}}-\vec{u}_{\mathrm{g}}\right)$ $\vec{U}^{\mathrm{ex}}_{\mathrm{cg}}=K_{\mathrm{cg}}\cdot\left(\vec{u}_{\mathrm{c}}-\vec{u}_{\mathrm{g}}\right)$	$K_{\mathrm{pg}}=\dfrac{\rho_{\mathrm{pg}}\,\mathrm{Re}\,C_D}{144\tau_{\mathrm{pg}}}d_{\mathrm{pg}}A_{\mathrm{pg}}$ The symmetric model taken from [13] with minor modifications is applied. Subscript 'p' indicates different metal phases: 'ℓ', 'e' or 'c'.	$\mathrm{Re}=\rho_{\mathrm{pg}}\left\|\vec{u}_{\mathrm{p}}-\vec{u}_{\mathrm{g}}\right\|d_{\mathrm{pg}}/\mu_{\mathrm{pg}}$ $C_{\mathrm{D}}=\begin{cases}27.6 & \mathrm{Re}\le 1\\ 24\cdot\frac{1+0.15\mathrm{Re}^{0.687}}{\mathrm{Re}} & 1<\mathrm{Re}\le 10^3\\ 0.44 & \mathrm{Re}>10^3\end{cases}$ $\tau_{\mathrm{pg}}=\rho_{\mathrm{pg}}d^2_{\mathrm{pg}}/18\mu_{\mathrm{pg}}$ $A_{\mathrm{pg}}=6f_{\mathrm{p}}f_{\mathrm{g}}/d_{\mathrm{pg}}$ $\mu_{\mathrm{pg}}=\min(\mu_{\mathrm{p}},\mu_{\mathrm{g}})$; $\rho_{\mathrm{pg}}=\min(\rho_{\mathrm{p}},\rho_{\mathrm{g}})$ d_{pg}: modelling parameter (diameters) as function of volume fractions of involving phases.

Simplified microscopic shrinkage porosity model

The Niyama criterion modified by Carlson and Beckermann [2, 3] is implemented. We name it as CBN (Carlson-Beckermann-Niyama) criterion, Eq. (3).

$$\mathrm{CBN}=C_{\lambda}\frac{G}{\dot{T}^{5/6}}\sqrt{\frac{\Delta P_{\mathrm{cr}}}{\mu_{\ell}\beta(T_{\mathrm{Liq}}-T_{\mathrm{Eut}})}} \quad (3)$$

where $C_{\lambda}=1.44\mathrm{x}10^{-4}\ \mathrm{m}\cdot(\mathrm{K/s})^{1/3}$ is a material constant being used for determining the secondary dendrite arm spacing. G and $\dot{T}$ are the temperature gradient and cooling rate, which are evaluated at a critical temperature of T_{cr} ($=0.1\,T_{\mathrm{Liq}}+0.9T_{\mathrm{Eut}}$), assuming that T_{Eut} corresponds to the end solidification. $\beta=(\rho_{\mathrm{s}}-\rho_{\ell})/\rho_{\ell}$ is the solidification shrinkage. ΔP_{cr} is the critical pressure drop when a pore-nucleus with critical radius of r_c deep in the mushy zone can overcome capillary force ($2\sigma/r_c$) and metastatic pressure (P_{static}) to grow. ΔP_{cr} is taken as $1.01\mathrm{x}10^5$ Pa for steel [3]. The possible occurrence of shrinkage porosity and the amount of pores (volume fraction of voids) decrease with the local CBN value. The smaller the CBN value, the more probable shrinkage porosity would occur, and the larger amount of pores might form. As no threshold of CBN for the

occurrence of pores can be determined in advance, this criterion is used only for qualitative evaluation of the possible occurrence of microscopic shrinkage porosity. Although the current model offers the possibility to calculate the interdendritic flow, it is time consuming to solve the feeding deep in the mushy zone near the end of solidification, therefore a so-called 'simplified porosity model' is introduced [14, 15]. When the temperature drops below the critical temperature of T_{cr}, volume shrinkage by solidification is ignored, i.e. the solidification is assumed to occur without volume change. This treatment is made by assuming that the rest melt deep in the mushy zone solidifies as a solid-pore mixture with the mixture density equal to the liquid density.

Simulation Settings

A 2.45 ton ingot was preliminarily simulated in full 3D (average mesh size of 10 mm) and 2D (average mesh size of 5 mm). The ingot had a square cross-section. However, for the 2D calculation an axis-symmetry is assumed. Casting conditions, process parameters, experimentally measured macrosegregation and shrinkage cavity information were reported previously [16,17]. The alloy is multi-componential but currently we consider a simplified binary alloy (Fe-0.45wt.%C). The material properties and some important boundary conditions are summarized in Table 2 and Fig. 1.

Table 2. Thermodynamic & physical properties

Steel		
melting point of pure iron, T_f	K	1805.15
liquidus slope, m	K (wt.%)$^{-1}$	-80.45
equilibrium partition coefficient, k	-	0.36
melt density, ρ_ℓ	kg/m^3	6990
solid density, ρ_e , ρ_c	kg/m^3	7140
specific heat, c_p^ℓ , c_p^c , c_p^e	J/kg/K	500
thermal conductivity, k_ℓ , k_e , k_c	W/m/K	34.0
latent heat, L	J/kg	2.71×10^5
viscosity, μ_ℓ	kg/m/s	4.2×10^{-3}
thermal expansion coefficient, β_T	K^{-1}	1.07×10^{-4}
solutal expansion coefficient, β_c	wt.%$^{-1}$	1.4×10^{-2}
dendritic arm spacing, λ_1	M	5×10^{-4}
diffusion coefficient (liquid), D_ℓ	m^2/s	2.0×10^{-8}
diffusion coefficient (solid), D_e , D_c	m^2/s	1.0×10^{-9}
Covering slag		
viscosity, μ_{slag}	kg/m/s	0.01
density, ρ_{slag}	kg/m^3	2500
specific heat, c_{slag}^g	J/kg/K	1815
thermal conductivity, k_{slag}	W/m/K	4.0

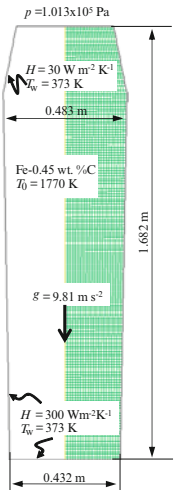

Figure 1. Configuration of the 2.45-ton industrial steel ingot.

No mould filling is calculated, and the mould is assumed to be initially filled with liquid melt of 1770 K (above liquidus of 1768.95 K). As solidification starts, the casting shrinks and it sucks the fourth slag phase from the top 'pressure inlet'. A zero-gradient boundary condition is applied at

the 'pressure inlet' for the other quantities: temperature, concentrations, equiaxed number density. No radiation heat transfer from the top to the ambience is accounted for. Nucleation parameters of equiaxed crystals are: $n_{max} = 5.0 \times 10^{-3}$ m^{-3}, $\Delta T_N = 5.0$ K, $\Delta T_\sigma = 2.0$ K. Calculation with the 4-phase model including air as gas phase is extremely time consuming (demanding tiny small time step), especially when a 3D calculation is performed. The situation can be significantly improved by considering a covering liquid slag instead of gas phase.

Results and Discussion

Example of the solidification sequence at 600 s is shown in Fig. 2. The overall solidification process is mainly governed by heat transfer. The cooling and solidification starts from the mould wall. The columnar phase develops from the mould walls and grows towards the casting centre. In the meantime equiaxed grains nucleate and grow in front of the columnar tips, and those equiaxed grains start to sink and try to settle in the bottom region. The melt is dragged downwards along the columnar tip front by the sinking grains, which in turn induces a rising melt flow in the middle of the ingot. Thermal-solutal convection contributes as well to the interdendritic flow and global melt flow in the bulk. Both $\vec{u}_\ell$ and $\vec{u}_e$ fields are naturally instable. As the flow field of the melt and the motion of the equiaxed grains are fully coupled with other transport phenomena (energy, species and mass), the instability of the flow patterns will directly influence the solidification sequence. Sedimentation of crystals at the bottom region causes the volume fraction of the equiaxed phase to reach a quite high level. When f_e in the lower part of the ingot is high enough (larger than the so-called mechanical blocking limit of 0.49, Fig. 2(b)), the columnar-to-equiaxed transition (CET) occurs. In the upper part of the ingot, the columnar tips can continue to grow, as the amount of equiaxed crystals is too low to cause blocking. Flow and crystal sedimentation are key mechanisms for the formation of macrosegregation in ingot casting, and they were discussed previously [9, 10, 17].

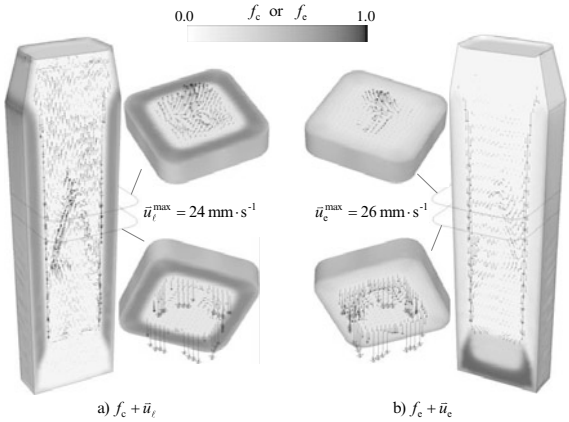

Figure 2. Solidification sequence at 600 s. Both f_c and f_e in the centre vertical section are shown in grey scale with light for lower and dark for high volume fraction. a) The velocity of the melt, $\vec{u}_\ell$ is shown together with f_c, b) while the velocity of the equiaxed crystals, $\vec{u}_e$ is with f_e. Additionally, the phase distributions and velocity fields in 2 horizontal sections are also shown.

The final segregation result is shown in Fig. 3. A conically shaped negative segregation zone is found at the bottom region, which coincides with the equiaxed sedimentation zone. A large positive segregated area just below the top shrinkage cavity is predicted. Interestingly, segregation pattern in the lower part of the ingot is quite non-symmetry and non-uniform. Some local positive segregation spots on the casting surface and even inside the cross section are found. Most possible reason for this might be the unstable flow and motion of crystals during the early stage of solidification. Note that the long calculation time (2 weeks in cluster with 12 cores of 3.5 GHz) does not allow performing parameter study in 3D. Another reason for the segregation spots can be possible numerical inaccuracies, which demands further investigation. The segregation pattern in the upper part is much more uniformly distributed on the surface and in the cross section

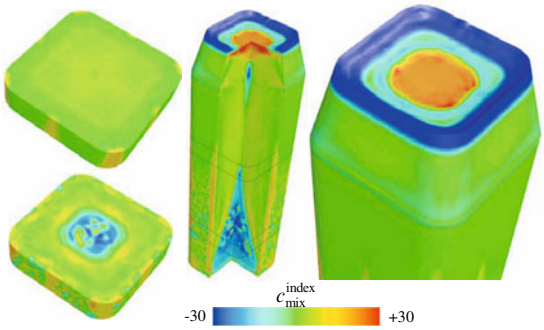

Figure 3. Final segregation distribution. The segregation index, $c_{mix}^{index}=100\times\left(c_{mix}-c_0\right)/c_0$, is used to evaluate the macrosegregation, where c_{mix} is the local mixture concentration of the metal phases (equiaxed, columnar and rest eutectic).

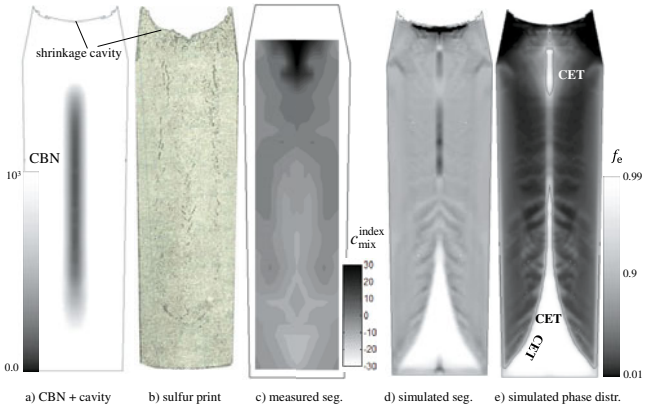

Figure 4. Comparison of the numerical simulation (2D axis symmetry with grid size of 5 mm) with experiments as reported in [16]. a) numerical prediction of the shrinkage cavity and position of the microscopic shrinkage porosity by the CBN criterion; b) sulphur print; c) reconstructed segregation map in grey scale (chemical analysis of 54 drilling samples); d) predicted segregation map in grey scale; e) phase distribution of f_e and marked CET line.

The free surface, i.e. the interface between the liquid slag and metal phase, is represented by the iso-surface of $f_g = 0.5$ with 'g' standing for the slag phase. The numerical thickness of the interface is confined in 2~3 neighbouring elements. With progressing solidification, the forming cavity is continuously filled by the slag from the inlet. The final volume of the cavity is predicted to be 0.00725 m^3, i.e. 2.15% of the volume of the entire ingot, which agrees with the solidification shrinkage of the alloy, $\beta = 2.1\%$. The formation of the microscopic shrinkage porosity is calculated indirectly by the CBN criterion, based on the thermal field as post-processing.

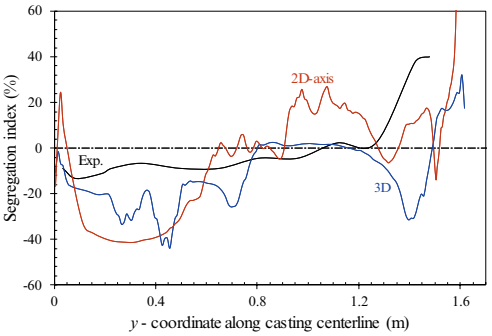

Figure 5. Comparison of centreline segregation (c_{mix}^{index}) between simulations (2D and 3D) and experimental results.

The same casting was also calculated in 2D axis symmetry (but with an average mesh size of half of that used for 3D). The solidification sequence, the shrinkage cavity and CBN criterion of the 2D result are quite similar to those of 3D. And the global macrosegregation pattern is also predicted similar: the conic-negative segregation in the equiaxed sedimentation zone and the large positive segregation below the top shrinkage cavity (Fig. 4). The major difference is that quasi-A-segregations [8, 9] in the middle radius region of the ingot are predicted by the 2D calculation, which are not clearly visible for the 3D calculation. One reason is the grid resolution, as being studied previously [17]. Another reason might be due to the dimensions of the geometry. Although the 3D calculation predicts the instable flow (fluctuation) pattern in the bulk region during solidification, the 2D calculation ignoring the swirl flow in the third dimension would exaggerate instability of the flow in the considered 2 dimensions, and exaggerate the initiation and growth of channels. The quasi-A-segregations are an indicator (although not finally proved yet) of the formation of channel segregations.

The final macrosegregation pattern, and phase distribution, and the predicted shrinkage cavity and CBN criterion are shown in Fig. 4. They show some similarity to experimental results. A similar profile of shrinkage cavity is predicted, but the volume of the cavity is smaller than that of the experiment. The simulation overestimates the negative segregation in the sedimentation zone. The middle-radius segregation is also partially evidenced by the sulphur print, but it seems not as strong as the simulation shows. The macrosegregation along the casting centreline is also plotted and compared with experimental results (Fig. 5). Both 2D and 3D calculations have predicted some similar variation features of macrosegregation along the centreline, but the quantitative deviation from the experimental result is still quite large.

Conclusion

The calculation of a 2.45 ton ingot has demonstrated the functionalities of the newly proposed 4-phase model. The current model is an extension of the previous mixed columnar-equiaxed solidification model [10] by considering an additional gas (or covering liquid slag) phase. The new phase is supposed to be immiscible with other phases. It has no mass and species transfer with other phases, but the treatment of momentum and enthalpy exchanges with other phases becomes crucially important to get a sharp interface between the liquid slag and other metal phases. Both 3D and 2D calculations show that the thickness of the interface between the slag and metal phases is confined in the 2~3 neighbouring elements. The volume of the formed cavity in the hot top coincides well with the total volume shrinkage by solidification of the ingot.

Acknowledgement

This work was financially supported by the FWF Austrian Science Fund (P23155-N24), FFG Bridge Early Stage (No. 842441), and the Austrian Federal Ministry of Economy, Family and Youth and the National Foundation for Research, Technology and Development within the framework of the Christian Doppler Laboratory for Advanced Process Simulation of Solidification and Melting.

References

[1] Moore J. and Shah N.: Int. Metals Rev., 28 (1983), p. 338-356.
[2] Niyama E., Uchida T., Morikawa M. and Saito S.: AFS Cast Met. Res. J., 7 (1982), p. 52-63.
[3] Carlson K. D., and Beckermann C.: Metall. Mater. Trans., 40A (2009), p. 163-175.
[4] Nastac L. and Marsden K.: Int. J. Cast Metal Res., 26 (2013), p. 374-382.
[5] Wu M., Schädlich-Stubenrauch J., Augthun M., Sahm P. and Spiekermann H.: Dent. Mater., 14 (1998), p. 321-328.
[6] Ludwig A., Gruber-Pretzler M., Mayer F., Ishmurzin A. and Wu M.: Mater. Sci. Eng. A, 413-414 (2005), p. 485-489.
[7] Wu M., Könözsy L., Ludwig A., Schützenhöfer W. and Tanzer R.: Steel Res. Int., 79 (2008), p. 637-644.
[8] Wu M., Li J., Ludwig A. and Kharicha A.: Comp. Mater. Sci., 79 (2013), p. 830-840.
[9] Wu M., Li J., Ludwig A. and Kharicha A.: Comp. Mater. Sci., 92 (2014), p. 267-285.
[10] Wu M. and Ludwig A.: Metall. Mater. Trans., 37A (2006), p.1613-1624.
[11] Wang T., Yao S., Zhang X., Jin J., Wu M., Ludwig A., Pustal B. and Bührig-Polaczek A.: Jinshu Xuebao/Acta Metall. Sinica, 42 (2006), p.584-590.
[12] Ranz W. and Marshall W.: Chem. Eng. Prog., 48 (1952), p.141-146.
[13] ANSYS FLUENT 12.0 User's Guide, Copyright © 2009 by ANSYS, Inc, April 2009.
[14] Mayer F., Wu M. and Ludwig A.: Steel Res. Int., 81 (2010), p. 660-667.
[15] Wu M., Domitner J. and Ludwig A.: Metall. Mater. Trans. A, 43 (2012), p. 945-963.
[16] Iron Steel Inst.: Report on the heterogeneity of steel ingots, J. Iron Steel Inst., 103 (1926), p.39-151.
[17] Li J., Wu M., Kharicha A. and Ludwig A.: Int. J. Heat and Mass Transfer, 72 (2014), p. 668-679.

CFD Modeling and Simulation in Materials Processing 2016
Edited by: Laurentiu Nastac, Lifeng Zhang, Brian G. Thomas, Miaoyong Zhu, Andreas Ludwig, Adrian S. Sabau, Koulis Pericleous, and Hervé Combeau
TMS (The Minerals, Metals & Materials Society), 2016

COMPUTATIONAL FLUID DYNAMICS SIMULATIONS OF A LABORATORY FLASH REACTOR RELEVANT TO A NOVEL IRONMAKING PROCESS

Deqiu Fan, Yousef Mohassab, H. Y. Sohn

Department of Metallurgical Engineering, University of Utah, Salt Lake City, UT 84112, USA

Keywords: CFD, Ironmaking, Gas solid reaction, Iron oxide powder, Reduction

Abstract

A computational fluid dynamic approach was used to simulate a flash reactor for a novel flash ironmaking process. In this simulation, H_2 is injected with O_2 through a non-premixed burner in the top part of the reactor to form a flame. The Euler-Lagrange approach was used in the CFD model to solve a set of gas-phase momentum, energy and turbulent closure equations. The stochastic trajectory model was used to describe particle dispersion due to turbulence. As the volume fraction of particle was in the order of 10^{-5} the system was treated as a dilute flow, namely the interparticle collisions were neglected. The partial combustion mechanism used in this model consisted of 7 chemical reactions involving 6 species. The temperature profile obtained from the simulation satisfactorily agreed with the experimental measurements, and the reduction degree obtained from the model also agreed with experimental results.

Introduction

The worldwide iron production today is predominantly by the traditional blast furnace process. Although the blast furnace has high production rates and other advantages, it suffers from the problems of high energy consumption and CO_2 emissions. A novel ironmaking technology, which utilizes hydrogen, natural gas, or coal gas to produce iron directly from iron oxide concentrate through a flash process, is under development at the University of Utah [1-8]. This process is expected to drastically reduce energy consumption compared with the blast furnace and lower environmental pollution, especially CO_2 emissions, from the steel industry.

In this study, a laboratory-scale flash reactor was used to test the reduction of magnetite concentrate with H_2 as the reductant. A non-premixed burner was designed and installed at the top of the reactor for partial combustion of H_2. In all the experiments, H_2 was fed in excess relative to the minimum required amount. During the experiment, fine particles of dry magnetite concentrate were injected from the top part of the reactor. The particles were then dispersed due to the turbulence in the fluid phase [9]. The particles were heated by radiation from the reactor wall as well as by the hot gas in the furnace. The trajectory of particle and the residence time were important factors in determining the reduction degree. This process involves particle-laden turbulent fluid flow, convective heat transfer, conduction, and thermal radiation within the gas phase and between the particles and the surroundings. Therefore, a computational fluid dynamics (CFD) model that combines the turbulent particle-laden fluid flow, heat transfer and chemical reaction was built to predict various major phenomena occurring inside the reactor. Temperature profiles inside the reactor measured during the experiments were compared with the computed results. The reduction degrees of magnetite concentrate obtained under two typical experimental conditions were also compared with those obtained by CFD.

Mathematical Model

The laboratory flash reactor is schematically represented in Figure 1 (a). Hydrogen and oxygen were injected through a non-premixed burner. The configuration of the burner is shown in Figure 1 (b). Two particle injection ports with an angle of 22.5˚ from the vertical axis of the reactor tube were installed on two sides of the burner, as Figure 1 shows. Magnetite concentrate particles were delivered into the reactor with N_2 as the carrier gas at a constant rate through a pneumatic powder feeding system.

The Euler-Lagrange approach was used in this study for simulating the turbulent, particle-laden fluid flow. The stochastic tracking model [10] was used to describe particle dispersion due to turbulence. As the volume fraction of particles was in the order of 10^{-5} the system was treated as a dilute flow and the interparticle collisions were neglected.

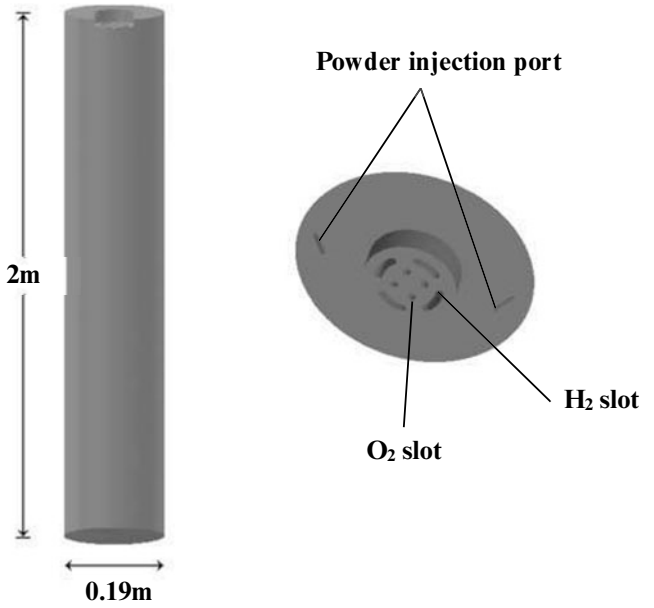

Figure 1. Schematic representation of the geometry of the laboratory-flash reactor and burner. (a) Reactor interior and (b) Burner.

Gas-Phase Governing Equations

The gas phase was treated as a continuum from the Eulerian frame of reference. With chemical reaction taken into consideration, there is an additional term appearing in the continuity, momentum and species transport equations. It represents the net rate of mass addition to the gas phase from the solid phase due to chemical reaction in continuity equation and species transport

equation. In momentum equation, the additional term arises from the force that solid particles exert on the gas. The turbulence model chosen for simulating the spread of gas jet was the realizable k-ε model [11]. Radiation was taken into account using the discrete ordinate (DO) model [12]. The governing equations for the gas-phase are summarized in Table 1.

Table 1. Governing Equations for Gas-Phase

Continuity:	$\frac{\partial}{\partial x_i}(\rho u_i) = S_p^m$	(1)
Momentum:	$\frac{\partial}{\partial x_j}(\rho u_i u_j) = -\frac{\partial p}{\partial x_i} + \frac{\partial}{\partial x_j}\left[\mu\left(\frac{\partial u_i}{\partial x_j} + \frac{\partial u_j}{\partial x_i} - \frac{2}{3}\delta_{ij}\frac{\partial u_l}{\partial x_l}\right)\right] + \frac{\partial}{\partial x_j}\left(-\rho\overline{u_i' u_j'}\right) + \rho g_i + F_{p,i}$	(2)
Energy:	$\frac{\partial}{\partial x_i}\left[u_i(\rho e + p)\right] = \frac{\partial}{\partial x_i}\left[k_{eff}\frac{\partial T}{\partial x_i}\right] + Q_r + S_p^h$	(3)
Species:	$\frac{\partial}{\partial x_j}(\rho Y_i u_j) = -\frac{\partial J_j}{\partial x_j} + R_i + S_{p,i}^m$	(4)

Gas-Phase Reactions

The H_2 partial combustion mechanism adopted in this work consisted of 7 chemical reactions involving 6 species [13]. The gas-phase model with this combustion mechanism was validated elsewhere [14]. The general rate expression of the chemical reactions can be expressed as:

$$k_f = AT^{\beta}\exp\left(-\frac{E_a}{RT}\right) \tag{5}$$

Table 2. Gas-Phase Reaction Mechanism for H_2-O_2 Combustion

Reaction		A (cm^3 mol^{-1} s^{-1})	β	E_a (cal mol^{-1})
1	$H_2+O_2=OH+OH$	0.170×10^{14}	0.0	48151
2	$H+O_2=OH+O$	0.142×10^{15}	0.0	16401
3	$OH+H_2=H_2O+H$	0.316×10^{8}	1.8	3030
4	$O+H_2=OH+H$	0.207×10^{15}	0.0	13750
5	$OH+OH=H_2O+O$	0.550×10^{14}	0.0	7000
6	$H+OH=H_2O+M$	0.221×10^{23}	-2.0	0
7	$H+H=H_2+M$	0.653×10^{18}	-1.0	0

Particle-Phase Governing Equations

The particle phase was treated as a discrete phase. The force balance that equates the particle inertia with the forces (mainly gravitational force and drag force) acting on the particle is expressed in the Lagrangian frame of reference as:

$$\frac{d\vec{u}_p}{\mathrm{d}t} = F_D\left(\vec{u} - \vec{u}_p\right) + \frac{\vec{g}\left(\rho_p - \rho\right)}{\rho_p} \tag{6}$$

The particle thermal energy equation is expressed as:

$$m_p c_{p,d} \frac{dT_p}{\mathrm{d}t} = hA_p\left(T - T_p\right) - f_h \frac{dm_o}{dt}\Delta_r H_{reac} + \varepsilon_p A_p \sigma\left(T_S^4 - T_p^4\right) \quad (7)$$

in which, the term dm_o / dt is related to particle chemical reaction rate. And the rate expression used in this study is a global nucleation and growth rate expression for magnetite reduction by H_2 [$Fe_3O_4 + 4H_2 = 3Fe + 4H_2O$]. Thus, the mass balance of the particle is described by Eq. (8) [15]:

$$\frac{dm_o}{dt} = -m_O^{\circ} \cdot 1.23\times10^7 \cdot \exp\left(-\frac{196{,}000}{RT}\right)\left[p_{H_2} - \left(\frac{p_{H_2O}}{K}\right)\right]\cdot\left(1 - X\right) \quad (8)$$

where m_o is the mass of iron-bonded oxygen in the particle at time t, m_O° is the initial mass of oxygen in the particle. As for the definition of reduction degree, X can be found in previous work [2, 3].

The gas-particle heat transfer coefficient h was evaluated using the correlation of Ranz and Marshall [16]. A value of 0.8 was chosen as the particle emissivity ε_p, as recommended by Hahn and Sohn [17].

Numerical Details

The gas-phase governing equations (1) ~ (4) were discretized and solved using the commercial CFD software package ANSYS FLUENT 15.0. A three-dimensional mesh was generated using ICEM-CFD ANSYS with a total number of 442,364 hexahedral dominating hybrid cells. Tetrahedral mesh was only used in the top part of the reactor for capturing the complex geometric configuration of the burner and powder feeding ports. Mesh independency was confirmed by halving and doubling the number of cells without changing the computational results. A total particle streams of 10,000 were released from the injection ports to establish a statistical representation of the spread of the particles due to turbulence. The particle trajectories and velocities were determined by numerically integrating the equation of particle motion, Eq. (6). As the particle trajectory was computed, Eqs. (7) and (8) were integrated to obtain the particle temperature and mass at the subsequent time step under the assumption that particle temperature and mass change slowly within one time step. The calculation was carried out by a steady state pressure-based solver and the SIMPLE scheme was chosen for the pressure-velocity coupling. A second-order upwind scheme was chosen for momentum, species transport and energy equation discretization. Coupled calculation of the gas phase and particle phase were performed at a frequency of tracking the particle trajectories and updating the particle phase source every 10 continuous phase iterations. Two typical operating conditions of the laboratory flash reactor listed in Table 3 were simulated.

Table 3. Operating Conditions for the Laboratory Flash Reactor

Parameters	Values	
	Lower	Higher
Concentrate feeding rate, kg h^{-1}	0.12	0.13
Mass-average particle size, μm	32	32
H_2 flow rate*, L h^{-1}	3600	1200
H_2 input temperature, K	298	298
O_2 flow rate, L h^{-1}	579	178
O_2 input temperature, K	298	298

*Flow rates are calculated at 298 K and 0.85 atm, the barometric pressure at Salt Lake City.

Results and discussions

Operating under the conditions listed in Table 3, the furnace wall temperature profile measured during experiments is shown in Figure 2. And this temperature profile is used as a boundary condition for the simulation.

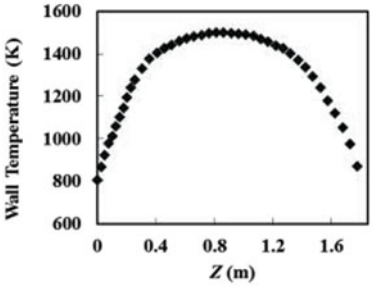

Figure 2. Measured wall temperature profile of the laboratory flash reactor

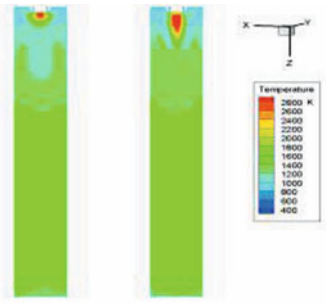

(a) (b)

Figure 3. Temperature distribution in the laboratory flash reactor. H_2 flow rate: (a) 1200 and (b) 3600 L h^{-1} at 298 K and 0.85 atm (1 atm = 101.32 kPa)

A comparison of the temperature distribution within the laboratory flash reactor under the lower (1200 L h^{-1}) and higher (3600 L h^{-1}) H_2 flow rates is shown in Figure 3. The maximum flame temperatures obtained were 2855 and 3027 K, respectively. It can be seen that a longer flame

was formed under the higher H_2 flow rate (refer to Table 3 for the detailed conditions of the two runs).

The calculated and measured gas phase temperature along the centerline of the reactor for the higher and lower H_2 flow rate are depicted in Figure 4. The gas temperature first spikes to the flame temperature and then drops to the isothermal temperature and stays until the gas travels out of the isothermal zone. It is noted that good agreements between the calculated and measured gas temperature were obtained, as shown in Figure 4, except there were some slight deviations at the end of the reactor. A comparison of the calculated and experimental reduction degrees are listed in Table 4. The model provided satisfactory agreement for the reduction degree. The particle residence time in the isothermal temperature region under the lower and higher H_2 flow rate were 4.1 s and 3.0 s, respectively.

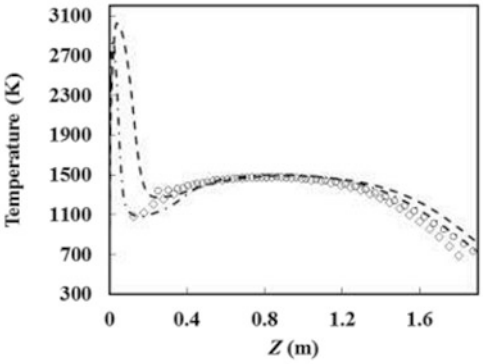

Figure 4. Gas phase temperature along the centerline of the reactor. − −, □,: experimental and calculated temperature profiles for H_2 flow rate 1200 L h^{-1}; ○,− − −: experimental and calculated temperature profiles for H_2 flow rate 3600 L h^{-1}

Table 4. Experimental and calculated reduction degree (%)

H_2 flow rate (L h^{-1})	Experimental (pct)	Calculated (pct)	Residence time (s)	EDF*
1200	83	80	4.1	0.51
3600	75	73	3.0	0.51

* EDF = $((pH_2/pH_2O)_{off\ gas} - (1/K_e))/(1/K_e)$[2,3]

Conclusions

A laboratory-scale flash reactor that represents a novel ironmaking process has been simulated using CFD. The gas phase temperature profile obtained by incorporating the 7-step H_2 partial combustion mechanism agrees well with the temperatures measured during the experiment. Predicted reduction degree agrees well with experimental ones. The model proposed in this work well describes the fluid flow, heat transfer and mass transfer within the laboratory flash reactor and will be used in the design and optimization of larger flash reactors.

Acknowledgments

The authors acknowledge the financial support from the U.S. Department of Energy under Award Number DEEE0005751 with cost share by the American Iron and Steel Institute (AISI) and the University of Utah. The support and resources from the Center for High Performance Computing at the University of Utah are gratefully acknowledged.

References

1. M.Y. Mohassab Ahmed, "*Phase Equilibria between Iron and Slag in CO/CO2/H2/H2O Atmospheres Relevant to a Novel Flash Ironmaking Technology*" (PhD Dissertation, The University of Utah, 2013).
2. F. Chen, Y. Mohassab, T. Jiang, and H.Y. Sohn, "Hydrogen Reduction Kinetics of Hematite Concentrate Particles Relevant to a Novel Flash Ironmaking Process." *Metall. Mater. Trans. B*, 46 (2015), 1133-1145.
3. F. Chen, Y. Mohassab, S. Zhang, and H.Y. Sohn, "Kinetics of the Reduction of Hematite Concentrate Particles by Carbon Monoxide Relevant to a Novel Flash Ironmaking Process." *Metall. Mater. Trans. B*, 46 (2015), 1716-1728.
4. M.Y. Mohassab-Ahmed, H. Y. Sohn, "Effect of Water Vapor Content in H_2–H_2O–CO–CO_2 Mixtures on the Equilibrium Distribution of Manganese between CaO–MgO_{sat}–SiO_2–Al_2O_3–FeO–P_2O_5 Slag and Molten Iron." *Steel Res. Int.*, 85 (2014), 875-884.
5. M.Y. Mohassab-Ahmed, H. Y. Sohn, "Effect of Water Vapor Content in H_2-H_2O-CO-CO_2 Mixtures on the Activity of Iron Oxide in Slags Relevant to a Novel Flash Ironmaking Technology." *Ironmaking Steelmaking*, 41(2014), 665 - 675.
6. Y. Mohassab and H. Sohn, "Effect of Water Vapour on Distribution of Phosphorus between Liquid Iron and MgO Saturated Slag Relevant to Flash Ironmaking Technology." *Ironmaking Steelmaking*, 41 (2014), 575-582.
7. Y. Mohassab and H.Y. Sohn, "Effect of Water Vapor on Sulfur Distribution between Liquid Fe and MgO Saturated Slag Relevant to a Flash Ironmaking Technology." *Steel Res. Int.*, 86 (2014), 753–759.
8. Y. Mohassab and H.Y. Sohn, "Analysis of Slag Chemistry by FTIR-RAS and Raman Spectroscopy: Effect of Water Vapor Content in H_2-H_2O-CO-CO_2 Mixtures Relevant to a Novel Green Ironmaking Technology." *Steel Res. Int.*, 86 (2014), 740-752.
9. Y.B. Hahn and H.Y. Sohn, "Mathematical Modeling of Sulfide Flash Smelting Process: Part I. Model Development and Verification with Laboratory and Pilot Plant Measurements for Chalcopyrite Concentrate Smelting." *Metall. Mater. Trans. B*, 21 (1990), 945-958.
10. A.D. Gosman and E. Ioannides, "Aspects of Computer Simulation of Liquid-Fueled Combustors." *J. Energy*, 7 (1983), 482-490.

11. T.-H. Shih, W.W. Liou, A. Shabbir, Z. Yang, and J. Zhu, "A New k-ϵ Eddy Viscosity Model for High Reynolds Number Turbulent Flows." *Comput. Fluids*, 24 (1995), 227-238.
12. E.H. Chui and G.D. Raithby, "Computation of Radiant Heat Transfer on a Nonorthogonal Mesh Using the Finite-Volume Method." *Numer. Heat Tr. B-Fund.*, 23 (1993), 269-288.
13. D.R. Eklund, J.P. Drummond, and H.A. Hassan, "Calculation of Supersonic Turbulent Reacting Coaxial Jets." *AIAA*, 28 (1990), 1633-1641.
14. M. Olivas-Martinez, "*Computational Fluid Dynamic Modeling of Chemically Reacting Gas-Particle Flows*", PhD Dissertation, The University of Utah, 2013.
15. D.Q. Fan, Y. Mohassab, M. Elzohiery, H. Y. Sohn, "Analysis of the Hydrogen Reduction Rate of Magnetite Concentrate Particles in a Drop-Tube Reactor Using Cfd Modeling", *In Preparation*.
16. W. E. Ranz and W.R. Marshall, "Evaporation from Drops, Part I and Part II." *Chem. Eng. Prog.*, 48 (1952), 173–180.
17. Y.B. Hahn and H.Y. Sohn, "Mathematical Modeling of Sulfide Flash Smelting Process: Part Ii. Quantitative Analysis of Radiative Heat Transfer." *Metall. Mater. Trans. B*, 21 (1990), 959-966.

CFD Modeling and Simulation in Materials Processing 2016
Edited by: Laurentiu Nastac, Lifeng Zhang, Brian G. Thomas, Miaoyong Zhu, Andreas Ludwig, Adrian S. Sabau, Koulis Pericleous, and Hervé Combeau
TMS (The Minerals, Metals & Materials Society), 2016

FLUID FLOW AND INCLUSION MOTION IN A FIVE-STRAND CONTINUOUS CASTING TUNDISH

Abulikemu Yasen, Dongteng Pan

School of Ecological and Metallurgical Engineering
University of Science and Technology Beijing
Beijing 100083, China
Email: pandongteng@163.com

Keywords: Fluid flow; Inclusion; Temperature; Five-strand tundish

Abstract

The tundish in the current study was for a five-strand billet continuous caster. The effect of closing different outlets on the fluid flow, temperature and inclusion removal was investigated. The top surface level fluctuations at the inlet zone isolated by the tall turbulence inhibitor weir was very severe and caused slag entrainment. The simulation shows that the highest level fluctuation was 0.87 mm while the lowest one was -0.389 mm. The fraction of inclusions entering the outlet far away from the inlet was much higher than entering other outlets. Closing any strand had a certain effect on the removal of inclusions to the top and on the fraction of inclusions to different strands. The temperature difference between inlet and outlet of tundish was increased by closing outlets for the current tundish and the increase of maximal temperature difference was 1~2 K.

Introduction

Tundish is the metallurgical vessel that links the discontinuous process of the secondary metallurgy in the ladle with the continuous casting process in the mold. During the transfer of metal through the tundish, molten steel interacts with refractories, slag, and atmosphere. A tundish is designed to provide maximum opportunity for carrying out various metallurgical operations such as inclusion separation, bubble flotation, alloying, inclusion modification by calcium treatment, superheat control, thermal and composition homogenization, leading to the development of a separate area of secondary refining of steel, referred to as "Tundish Metallurgy" [1, 2]. The top surface level fluctuations, inclusions and temperature are all affected by fluid flow. There are many researchers who had investigated fluid flow of molten steel through numerical simulation and proofed it fit well with production practice[3-9]. However, most models established for multi-strand tundish are four-strand or six-strand[10-15]. The current study builds a tundish model for a five-strand billet continuous caster. Simulations of the fluid flow and non-metallic inclusions of molten steel are presented. However, the five-strand tundish didn't work very well. So the effect of closing different strands on the fluid flow, temperature and inclusion removal was investigated. Additional, there are some solutions for the problems that found in the study.

Mathematical Formulation

For a steady and incompressible Newtonian fluid flow, the continuity equation and Reynolds-averaged Navier-Stokes equations conserves mass and momentum at every point of a three dimensional fluid flow model in a computational domain[16]. The term of $\beta(T_o-T)\rho g$ was added to the momentum equations to

include the effect of natural convection on the fluid flow. The κ-ε model[17] was used to simulate the turbulence. It gives the the turbulent viscosity $_t$ as

$$\mu_t = \rho C_\mu \frac{\kappa^2}{\varepsilon} \tag{1}$$

where C = 0.09; κ is turbulent kinetic energy, ($m^2 \cdot s^{-2}$); ε is turbulent dissipation, ($m^2 \cdot s^{-3}$).
This approach requires solving two additional partial differential equations for the transport of turbulent kinetic energy and its dissipation rate.

$$\rho u_j \frac{\partial \kappa}{\partial x_j} = \frac{\partial}{\partial x_j}\left(\frac{\mu_t}{\sigma_\kappa}\frac{\partial \kappa}{\partial x_j}\right) + \mu_t \frac{\partial u_j}{\partial x_i}\left(\frac{\partial u_i}{\partial x_j} + \frac{\partial u_j}{\partial x_i}\right) - \rho\varepsilon \tag{2}$$

$$\rho u_j \frac{\partial \varepsilon}{\partial x_j} = \frac{\partial}{\partial x_j}\left(\frac{\mu_t}{\sigma_\varepsilon}\frac{\partial \varepsilon}{\partial x_j}\right) + C_1 \mu_t \frac{\varepsilon}{\kappa}\frac{\partial u_j}{\partial x_i}\left(\frac{\partial u_i}{\partial x_j} + \frac{\partial u_j}{\partial x_i}\right) - C_2 \frac{\varepsilon}{\kappa}\rho\varepsilon \tag{3}$$

where x_i is coordinate direction x, y or z, m; ρ is liquid density, ($kg \cdot m^{-3}$); u_i is velocity component in x_i direction, ($m \cdot s^{-1}$); σ_κ, σ_ε, C_1, C_2 are empirical constants, and σ_κ = 1.0, σ_ε = 1.3, C_1 = 1.44, C_2 = 1.92.
The heat-transfer model solved a 3-D energy transport equation and the energy Prandtl number was 0.85. Besides, DPM model was used to track paticles. Figure 1 shows the geometry and dimensions of the five-strand tundish which has five evenly distributing outlets. The circled part is the turbulence inhibitor. Figure 2 shows the mesh of the model. The total cells in tundish mesh system to be studied is 300 000. The first wall-adjacent grid size is estimated to be 1 mm[2].

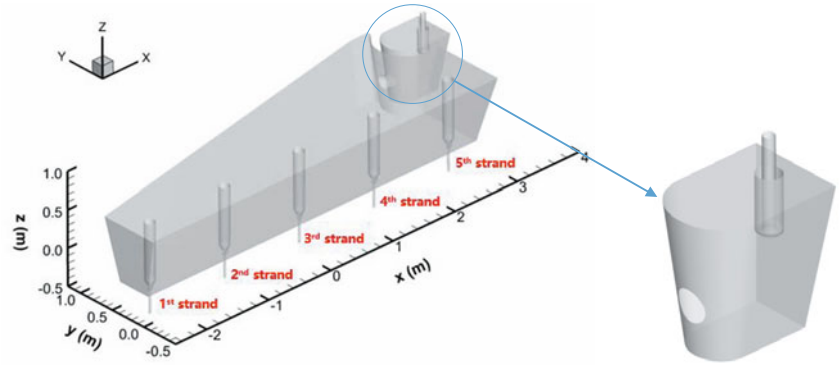

Figure 1. Geometry and dimensions of tundish

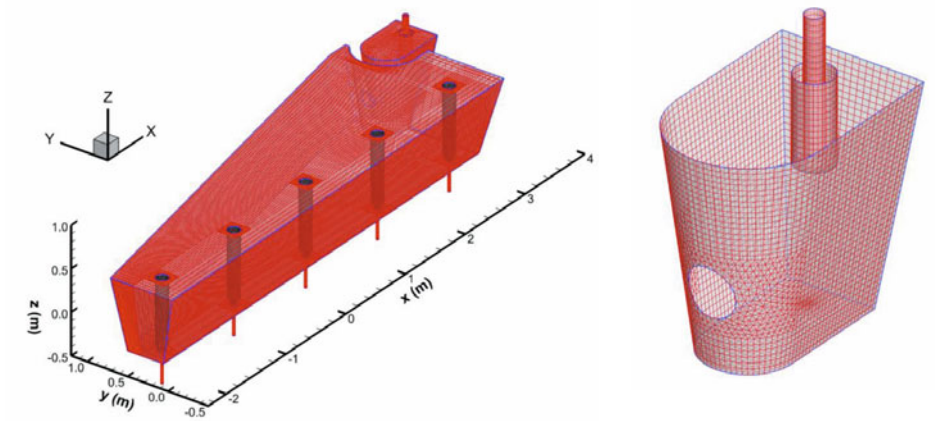

Figure 2. Mesh of the model: the whole tundish and the turbulence inhibitor

Table I shows the major parameters of the tundish that are used in the current simulation. In addition, major boundary conditions are as follows: Inlet uses inlet velocity, and outlets are pressure out; top surface is flat and its shear stress is zero; 12 800 particles of non-metallic inclusions are injected at the inlet; removal condition of inclusions is "Trap" at the top surface while is "Escape" at outlets.

Table I. Major parameters used in the simulation

Parameter	Data
Billet section	150×150 mm^2
Pulling velocity	1.80 m/min
Inlet temperature of tundish	1838 K
Liquid level under common pouring conditions	850 mm
Immersion depth of tundish upper nozzle	300 mm
Inlet velocity of tundish	0.88 m/s
Inlet turbulent kinetic energy	0.00408 m^2/s^2
Inlet turbulent kinetic energy dissipation rate	0.04265 m^2/s^3

Results and Discussion

The effect of closing different outlets on the fluid flow, temperature and inclusion removal was investigated in this study. In aspect of fluid flow, the top surface level fluctuations at the inlet zone isolated by the tall turbulence inhibitor weir are focused on, as shown in Figure 3. While closing any strand (opening four outlets), the level fluctuation comes softer. Figures 4 and 5 shows directly the comparison of the highest level fluctuations and the lowest ones among different cases. "All" refers to common pouring condition and Number 1~5 refers to close different strand. It is obvious that the level fluctuation at the inlet zone is the most severe under common pouring condition. The maximal level fluctuation is 0.87 mm and the other one is -0.389 mm. According to production practice, severe level fluctuation may cause slag entrainment and increase inclusions in molten steel. So it is necessary to

reduce level fluctuation and mitigate secondary pollution of molten steel. An efficient way is to lower the speed of fluid flow at the inlet zone.

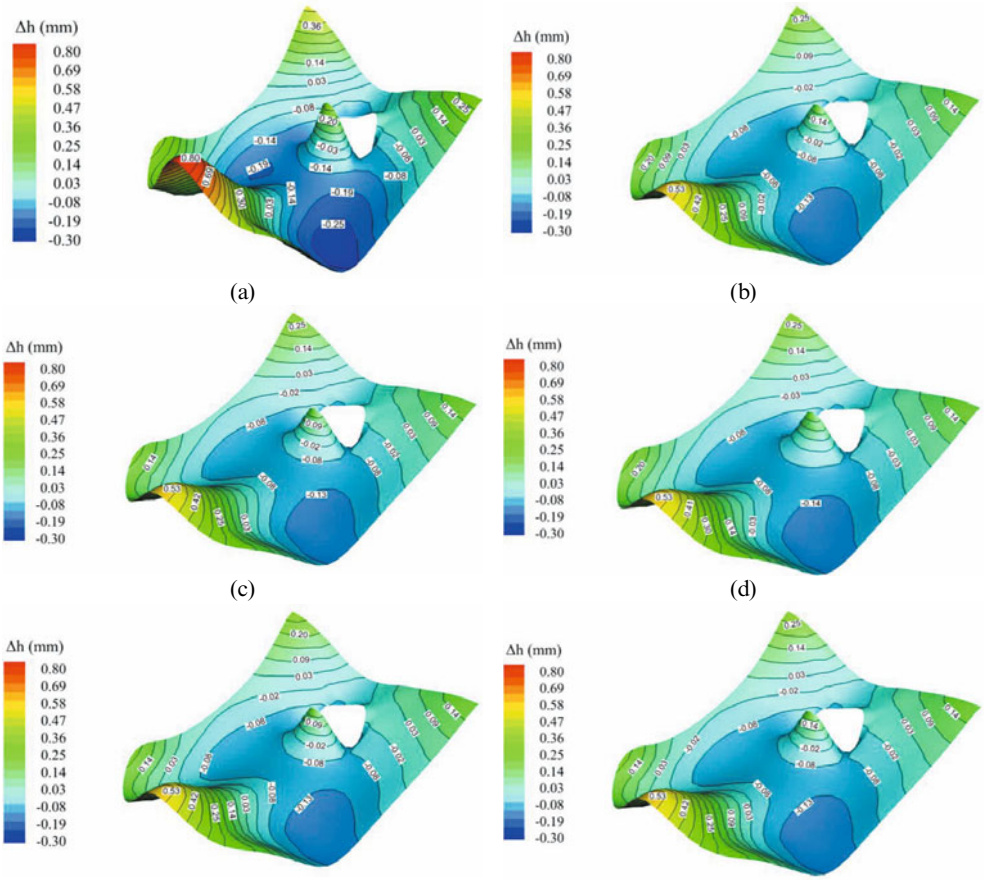

Figure 3. Top surface level at the inlet zone for pouring conditions: (a) common and (b)-(f) closing 1st to 5th strand respectively

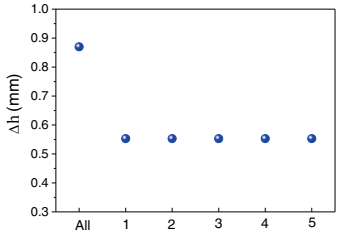

Figure 4. The highest level fluctuation

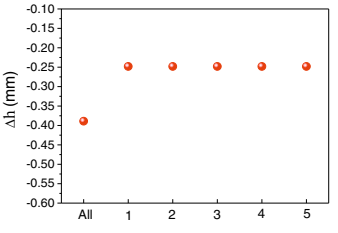

Figure 5. The lowest level fluctuation

One of the most important roles of tundish is to remove inclusions in molten steel. Figure 6 shows the relationship between removal fraction and diameter of non-metallic inclusions. Red open square line refers to common pouring condition. The removal fraction of inclusions is much higher than every other five lines, which refers to close one strand from the first one to the fifth respectively. When closing any strand, the removal fraction of inclusions are similar with each other. In another way, when inclusions' diameters are from 10 to 100 m, the increase of inclusions removal fraction is in proportion to inclusions' diameter in different cases. The inclusions removal fractions are from 60% to 90%. When closing different strand, the fractions of non-metallic inclusions at different outlets of tundish vary from each other, as shown in Figure 7. The fraction of inclusions entering the outlet far away from the inlet was much higher than entering other outlets. While diameter of inclusions comes larger, the fraction of them at the outlet deceases. Combining with discussions above and the production practice, it is reasonable to close the first strand.

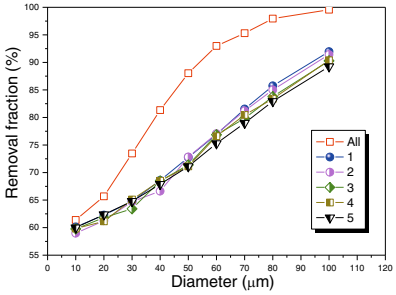

Figure 6. Removal fraction of inclusions from tundish depending on the size of inclusions

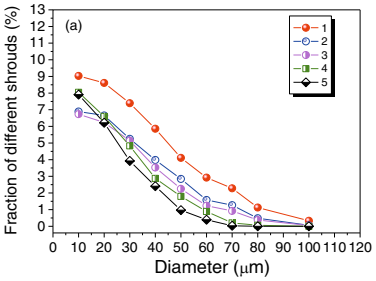

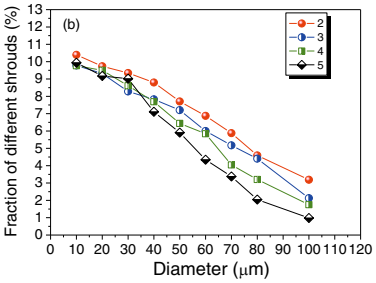

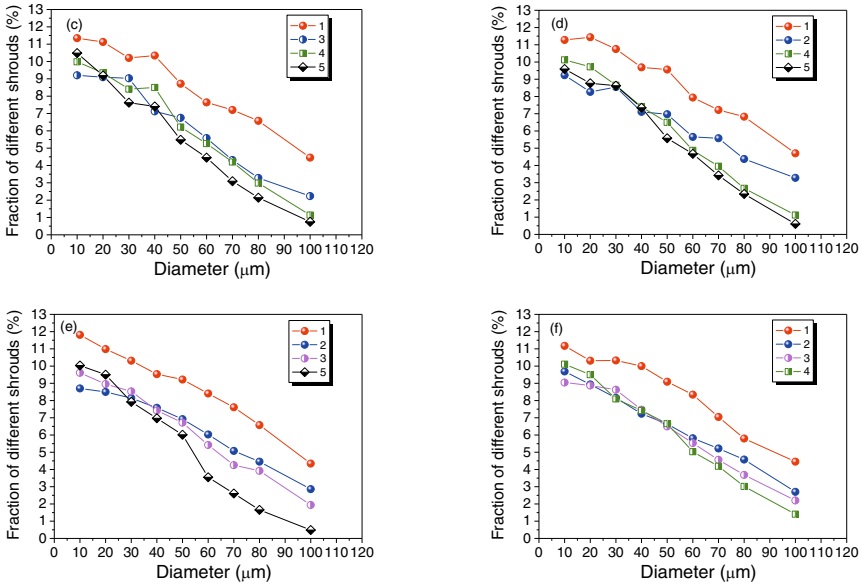

Figure 7. Fraction of non-metallic inclusions at different outlets of tundish when pouring condition is (a) common and (b) ~ (f) closing 1st to 5th strand respectively

The study also discuss the temperature field of the tundish model used. Table II shows the maximal temperature difference between inlet and outlet of tundish in different cases and figures out the outlet of the lowest temperature. It is easy to conclude that the temperature difference between inlet and outlet of tundish is increased by closing outlet for the current tundish. One probable explanation is that the pouring rate is reduced by closing outlet and the heat dissipation increases, which brings larger temperature difference between inlet and outlet. In terms of Figure 8, temperature of the top surface is much lower than the inlet zone of tundish. When pouring with five strand, the temperature of molten steel in tundish is 1826~1829 K. However, closing any strand may decrease the temperature to 1823~1827 K.

Table II. Temperature difference between inlet and outlet in tundish

Case	Maximal temperature difference between inlet and outlet	Outlet of the lowest temperature in tundish
Common pouring	9 K	5th strand
Close 1st strand	11 K	5th strand
Close 2nd strand	11 K	5th strand
Close 3rd strand	11 K	5th strand
Close 4th strand	11 K	5th strand
Close 5th strand	10 K	5th strand

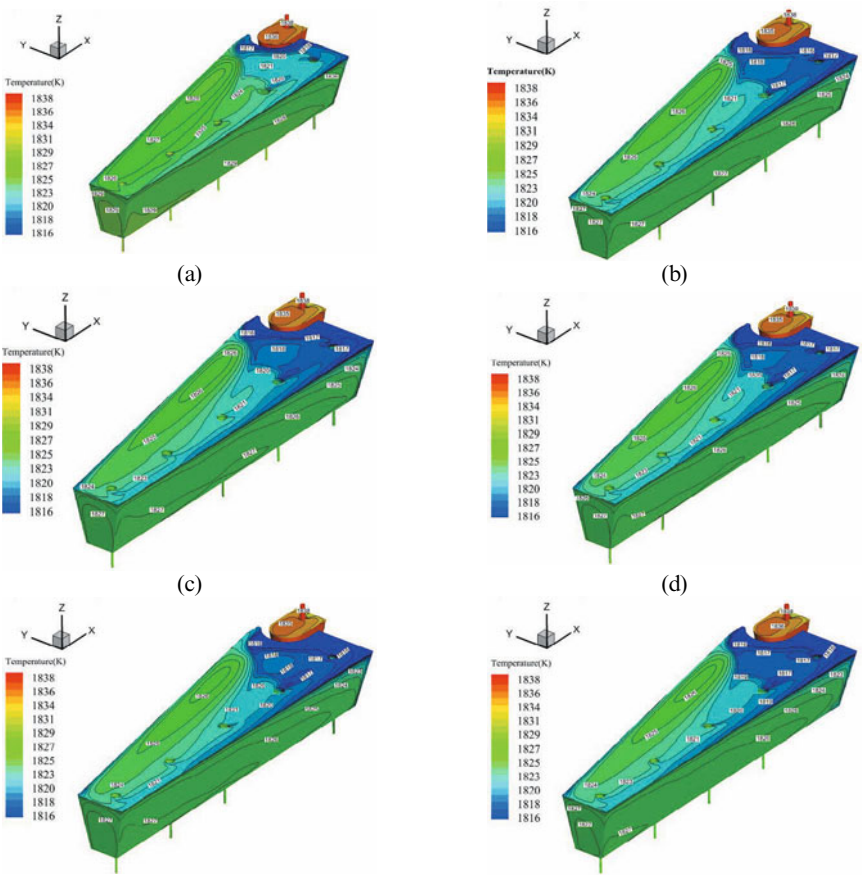

Figure 8. Temperature field of tundish in different cases when pouring condition is (a) common and (b) ~ (f) closing 1st to 5th strand respectively

Conclusions

Based on the simulation results and discussions above, here are some conclusions about the fluid flow, temperature and inclusion removal of the five-strand tundish:

(1) The top surface level fluctuations at the inlet zone isolated by the tall turbulence inhibitor weir is very severe and may cause slag entrainment The highest level fluctuation is 0.87 mm and the lowest one is -0.389 mm.

(2) The fraction of inclusions entering the outlet far away from the inlet was much higher than entering other outlets.

(3) The temperature difference between inlet and outlet of tundish was increased by closing outlets for

the current tundish. The increase of maximal temperature difference is 1~2 K.

References

1. Y. Sahai and T. Emi, *Tundish technology for clean steel production* (World Scientific, 2008).
2. L. Zhang, et al., "Effect of thermal buoyancy on fluid flow and inclusion motion in tundish without flow control devices--Part I: Fluid flow," *Journal of Iron and Steel Research (International)*, (04) 2005, 20-27.
3. H. Solhed and L. Jonsson, "An investigation of slag floatation and entrapment in a continuous-casting tundish using fluid-flow simulations, sampling and physical metallurgy," *Scandinavian Journal of Metallurgy*, 32 (1) 2003, 15-32.
4. H. Odenthal, et al., "Mechanism of fluid flow in a continuous casting tundish with different turbo-stoppers," *Steel Research*, 72 (11-12) 2001, 466-476.
5. F.M. Najjar, B.G. Thomas, and D.E. Hershey, "Numerical study of steady turbulent flow through bifurcated nozzles in continuous casting," *Metallurgical and Materials Transactions B*, 26 (4) 1995, 749-765.
6. P. Gardin, et al., "An experimental and numerical CFD study of turbulence in a tundish container," *Applied Mathematical Modelling*, 26 (2) 2002, 323-336.
7. L. Zhang, S. Taniguchi, and K. Cai, "Fluid flow and inclusion removal in continuous casting tundish," *Metallurgical and Materials Transactions B*, 31 (2) 2000, 253-266.
8. B.G. Thomas and L. Zhang, "Mathematical modeling of fluid flow in continuous casting," *ISIJ International*, 41 (10) 2001, 1181-1193.
9. D.B. Spalding, "Mathematical modeling of fluid-mechanics, heat-transfer and chemical-reaction processes: A lecture course," *NASA STI/Recon Technical Report N*, 81 1980, 30414.
10. T. Merder, A. Bogusławski, and M. Warzecha, "Modelling of flow behaviour in a six-strand continuous casting tundish," *Metalurgija*, 46 (4) 2007, 245-249.
11. L. Zhong, et al., "Fluid flow in a four-strand bloom continuous casting tundish with different flow modifiers," *ISIJ International*, 47 (1) 2007, 88-94.
12. A. Kumar, D. Mazumdar, and S.C. Koria, "Modeling of fluid flow and residence time distribution in a four-strand tundish for enhancing inclusion removal," *ISIJ International*, 48 (1) 2008, 38-47.
13. J. Madias, et al., "Design and plant experience using an advanced pouring box to receive and distribute the steel in a six strand tundish," *ISIJ International*, 39 (8) 1999, 787-794.
14. P.K. Jha, P.S. Rao, and A. Dewan, "Effect of height and position of dams on inclusion removal in a six strand tundish," *ISIJ International*, 48 (2) 2008, 154-160.
15. P.K. Jha and S.K. Dash, "Effect of outlet positions and various turbulence models on mixing in a single and multi strand tundish," *International Journal of Numerical Methods for Heat & Fluid Flow*, 12 (5) 2002, 560-584.
16. J.O. Hinze, *Turbulence* (New York, NY: McGraw-Hill, 1975).
17. B.E. Launder and D.B. Spalding, "The numerical computation of turbulent flows," *Computer Methods in Applied Mechanics and Engineering*, 3 (2) 1974, 269-289.

CFD Modeling and Simulation in Materials Processing 2016
Edited by: Laurentiu Nastac, Lifeng Zhang, Brian G. Thomas, Miaoyong Zhu, Andreas Ludwig, Adrian S. Sabau, Koulis Pericleous, and Hervé Combeau
TMS (The Minerals, Metals & Materials Society), 2016

LIQUID STEEL FLOW AND INTERACTIONS WITH NONMETALLIC PHASES IN THE CONTINUOUS CASTING TUNDISH USING CFD & PHYSICAL MODELING

Christopher Eastman Jr.[1], Peter Glaws[1], Dongbu Cao[1]

[1]TimkenSteel Corporation
1835 Dueber Ave. SW; Canton, OH 44706, USA

Keywords: CFD, tundish modeling, continuous casting, inclusions, steel cleanness

Abstract

Tundish geometry and operational practices have a significant effect on steel flow, inclusion removal, and potential flux entrainment. Innovative multi-phase computational fluid dynamics (CFD) modeling, in conjunction with advanced physical water modeling, of tundish flow during various casting conditions was performed to optimize the tundish design, create efficient operational practices, and ultimately achieve highest quality steel. Residence time distribution measurements were used to validate strong agreement between the two modeling techniques simulated in parallel. Motion tracking of various sized nonmetallic particles during simulations provided quantitative information on the expected impact on cleanness of the steel exiting the tundish. Interactions between the liquid steel, flux, and gases during various tundish operations were simulated to measure the propensity of flux entrainment during certain casting events. 3-D video results provided visuals of the steel and nonmetallic phases at all areas of interest.

Introduction

Equipment design and operational excellence are what set the highest quality steel makers apart from the rest of the industry. More specifically, tundish design and casting practices are vital components to establishing clean steel as a core competency. The external shape of the tundish dictates the relative position of the ladle with the nozzles above the strands, overall capacity and therefore mean residence time, and general flow path. While the external geometry determines the mean residence time, the internal geometries define the distribution of residence time around the mean. Flow modifiers such as baffles, weirs, dams, and turbulence suppressors guide the liquid steel flow in desired paths to maximize inclusion flotation and shape the residence time distribution curve. These refractory components can also play an important role in maintaining good cleanness levels during non-steady-state tundish events. While they can provide significant value, they also come with a cost that often deters a commodity product melt shop from incorporating into their tundish design. Any special bar quality (SBQ) steel manufacturers that supply to demanding applications understand that steel cleanness is not a compromise but a necessity. These are the steelmakers that invest in premium tundish design. Often, part of the investment involves conducting flow simulations to optimize internal geometries and casting practices.

Early studies using physical tundish modeling included injecting a tracer into a tub of water with an inlet and an outlet. Flow rates were crudely controlled, temperature effects were ignored, and

flow modifier geometries were rudimentary. Physical water modeling continued to evolve through the introductions of non-isothermal water control, more sophisticated optical spectrometers that correlate light absorbance to the concentration of dye, and automated flow rates to match certain tundish processes during sequence casting. Later advances included digital particle image velocimetry and planar laser induced fluorescence to measure the planar velocity of particles in the water [1].

Steel manufacturers have also been taking advantage of the enhanced capabilities of computational fluid dynamics (CFD) modeling to ultimately save on time, materials, labor, and money. However, the current study also confirms the significant value that a state-of-the-art physical water model provides that a CFD model cannot produce quite as well.

Product quality and the performance of a manufactured component are closely correlated with steel cleanness. As the oxide inclusion content increases, steel cleanness decreases, and the mechanical performance of the part such as fatigue resistance or fracture toughness deteriorates. Oxide inclusion content is determined during liquid steel processing before solidification. Because the tundish handles all liquid steel in a continuous casting machine, it is often identified as the area that has greatest impact on steel cleanness.

Some characteristics of an optimum liquid steel flow pattern include:

- Minimal turbulence or surface undulations that could cause flux entrainment.
- Upward flow to aid inclusions in floating out of the steel bath and being absorbed in the surface flux layer.
- No dead zones, or areas with stagnant flow.
- A sufficiently long mean residence time to maximize inclusion flotation, but short enough to avoid freezing or areas of stagnant flow.

Physical & CFD Modeling

Steel manufacturers have multiple options available for evaluating the performance of tundish designs. Many refractory suppliers that provide the material needed to prepare a tundish for continuous casting have the ability to provide tundish modeling services as part of a program. These capabilities range from a simplistic physical water modeling setup to fully automated physical water modeling and CFD modeling [2]. In general, refractory companies are less concerned about the cleanness of the steel product and more focused on providing quality material to the caster that they supply, avoiding any materials-related failures causing production downtime.

Physical modeling and CFD modeling both have advantages and limitations. Physical water modeling produces complete visualization and includes slight variations in the process that would also be seen in the liquid steel tundish. However, a water model requires fabrication, internal labor and technical resources, setup and cleanup time, and multi-media modeling can be difficult to represent and manage. Perhaps the most significant capability of physical modeling is to test non-steady-state events that occur during sequence casting in the tundish. Through the use of automated flow control and temperature control, normal or abnormal conditions can be simulated.

CFD modeling has limited setup and cleanup time, can be run unattended, quantify local flow rates, temperature gradients, and phase fractions, and simulate the flow of nonmetallic media such as ladle slag, tundish flux, and nonmetallic inclusions in the steel bath. A computational model should be repeatable and yield equivalent results if the input is the same. Repeatability can be both an advantage and disadvantage. In reality, no two sequences in a liquid steel tundish will be identical, and thus many of the nuances that occur during casting are hard to capture and evaluate with a CFD model. Though post-processing allows for images and videos to be produced at any defined angle and in any define plane, a complete depth of field through the tundish is not easy to achieve with a CFD model. Computational time, cost of license software and CPU power are all necessary to produce a successful CFD model.

The two different methods have their advantages, but ultimately coupling the methods presents a method of validation [3]. At TimkenSteel Corporation's Faircrest Steel Plant, a combinatorial approach was taken when designing the tundish for a new three-strand jumbo bloom vertical continuous caster. Physical modeling and computation fluid dynamics were performed with individual purposes to accomplish a single goal: provide answers to the challenges during commissioning, and produce a robust tundish design that will meet or exceed existing quality levels established by TimkenSteel operations. The importance of steel cleanness to TimkenSteel can be represented by the 400 physical water modeling tests (over 1,000 working hours) and more than two years of internal CFD modeling efforts to-date.

Experimental Procedure

A 0.4 linear scale tundish model was constructed of Lexan plexiglass to develop an internal design to meet the required optimum flow pattern. Twenty different internal geometries were tested before deciding on the design that provided the best flow pattern for optimized steel cleanness and consistency between strands. For a multi-strand tundish that has different distances from the ladle nozzle to the tundish nozzles, consistent residence times and temperatures at each strand can only be achieved using flow modifiers. In order for product to have consistent quality at each strand, the flow pattern should be nearly equivalent.

When designing experiments, operational experience and expertise, including technologies and practices used at the TimkenSteel Harrison continuous caster, were utilized along with new ideas to develop and fine-tune liquid steel management in the tundish during sequence casting. This includes both steady-state casting (representing the middle of a heat), as well as inter-heat activities.

The caster manufacturer utilized a CFD code for our specific tundish to evaluate initial internal designs. These initial CFD efforts were performed simultaneously with internal physical modeling. At that time, the physical water modeling efforts were moving much quicker than the external CFD modeling. As hot commissioning of the caster grew closer, the external modeling efforts had ceased and the caster manufacturer assisted TimkenSteel in setting up an internal CFD model. The goal of the internal CFD model was to have it operating effectively such that it produced results that matched those generated by the water model. Once commissioning

commenced, the focus of the CFD model shifted towards modeling abnormal conditions at the caster that would otherwise be too difficult or time-consuming to model with water.

The CFD model used a k-epsilon turbulence model [4], steel and flux (or slag) nominal densities of 7,000 and 3,500 kg/m^3 (temperature dependent densities were used for RTD simulations), heat transfer coefficients 3370 W/m^2K, and surface tensions of 1.5 and 0.5 N/m, respectively. A tundish temperature difference between the incoming steel and outflowing steel was 3 °C on average. All internal and external walls and floors were considered slip boundaries allowing shear flow, while the surface was treated as a slip boundary for RTD simulations but a moving boundary for flux flow simulations. While computing power and efficiency are always a concern in a quick results environment, the model was often cut at the line of symmetry in the tundish to dramatically reduce the required computational time for a simulation.

Results & Discussion

Three objectives were accomplished utilizing the two modeling methods: a) coupling an optimized tundish design with clean steel practices, b) evaluation of nonmetallic inclusion particle tracing during steady-state casting, and c) evaluation of the effects of casting conditions on flux-steel interaction. These results served as the foundation for initial casting practices at TimkenSteel Faircrest during commissioning.

Model Comparison

The residence time distribution (RTD) curve of liquid steel flow in a tundish describes how much liquid spends a certain amount of time in the tundish. The RTD curve contains information regarding the amounts of plug flow, mixed flow, and dead volume in the tundish. In general, plug flow is desired, resulting in longer minimum residence times and a tighter distribution. By increasing the amount of plug flow in the tundish, or lengthening the minimum residence time, nonmetallic inclusions entering the tundish have a longer time to float to the surface and be absorbed into the flux. From the water modeling efforts, a comparison between a standard tundish without any optimized flow modifiers and the optimized tundish design created at TimkenSteel Faircrest shows that the minimum residence time can be increased by a factor of ten, or a factor of three as an average across all three strands (Figure 1). Minimum residence time correlates directly with the cleanness of steel. Figure 2 illustrates what the expected impact a tundish design and operational practices could have on ultrasonic testing. Oxide content could be much greater in a poorly designed or operated tundish compared to an optimized tundish design that follows clean steel practices.

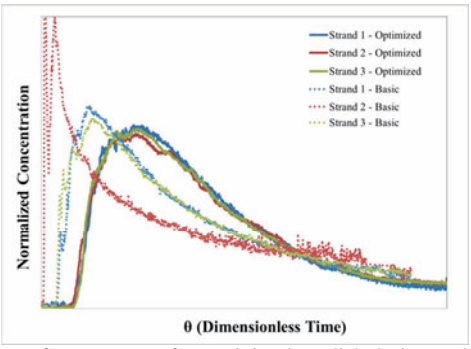

Figure 1: A comparison of RTD curves for a minimal tundish design and an optimized tundish design. The discontinuous trend lines represent the basic tundish design, while the solid lines represent the optimized tundish design.

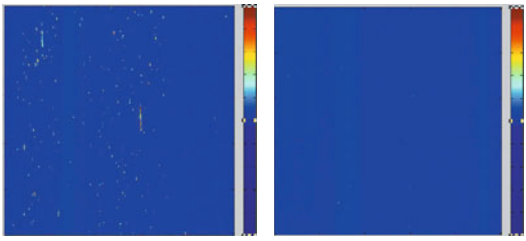

Figure 2: Ultrasonic testing results from an oxide inclusion-rich steel (left), and a steel with high steel cleanness (right).

After deciding on the optimum internal geometry arrangement, the same geometries were replicated in the computational model. The CFD-generated RTD curves were produced using a pulse tracer injection during steady-state flow conditions (to simulate the steady-state testing performed using the water model). The tracer was tracked through the tundish and measured as it exited through each tundish nozzle. Certain process parameters such as the heat extraction from the walls of the tundish can vary with tundish design and type of refractory materials. These parameters were adjusted to better fit the particular tundish design. The flow patterns (Figure 3) and their corresponding RTD curves (Figure 4) for the two modeling methods were in good agreement.

Furthermore, the physical model was used to develop operational practices that promote steel cleanness and maximize yield. Transitional tundish events that often impact steel cleanness and chemical mixing can be managed properly through the use of tundish flow modifiers and appropriate standard practices. The present work exemplifies the value in utilizing both tools to take advantage of their different capabilities. Visual results from both models also resembled each other very well.

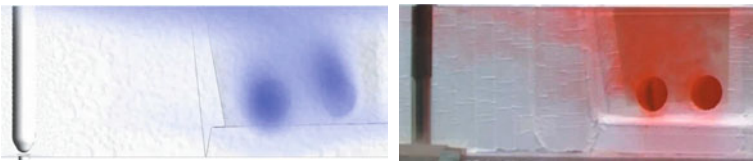

Figure 3: Visualization of dye rising out of baffle holes during the physical and CFD simulations.

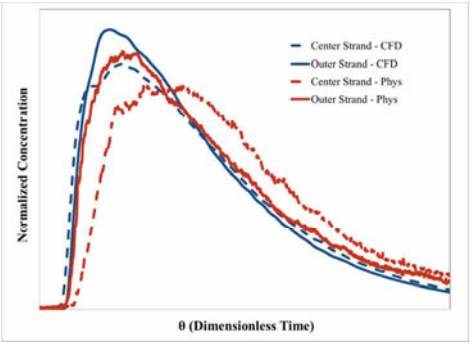

Figure 4: RTD curves showing the good agreement between the physical model and CFD model results from a pulse concentration simulation. The red and blue lines represent results from the physical and computational models, respectively. The continuous and discontinuous lines represent outer and inner strands, respectively.

Nonmetallic Particle Tracing

Nonmetallic particles of various sizes were added to the tundish during CFD simulations to gather quantitative information on the expected impact on cleanness of the steel exiting the tundish [5]. For every particle tracing simulation, a group of 300 particles were pulse injected from incoming ladle stream. Simulations were performed for particles ranging in size from 10 μm to 100 μm. Individual particles were tracked through the tundish for a period of approximately two times the mean residence time (Figure 5). Each particle was given the ability to either absorb into the surface layer if reached, stick to the refractory walls if impacted with significant velocity, recirculate inside the tundish, or exit the tundish through the tundish nozzle into the mold. For the largest inclusions, less than 5% of the inclusions introduced exit the tundish into the molds, most of which exit by absorption into the surface layer. It is evident that the flow modifiers are efficient at creating flow patterns that maximize inclusion flotation and therefore minimize inclusion content in the liquid steel exiting the tundish.

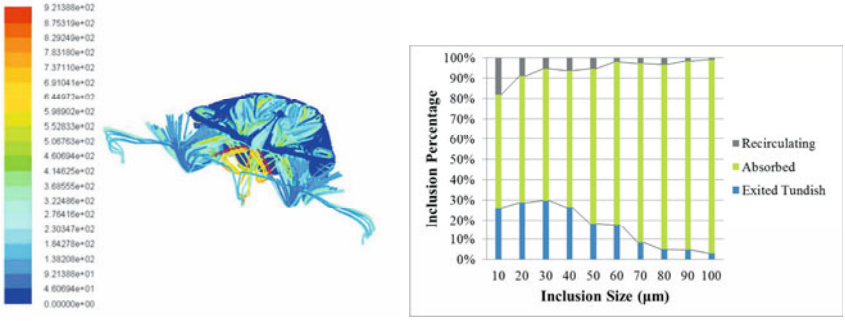

Figure 5: Left: Flow paths of nonmetallic inclusions throughout the three-strand tundish from a pulse-injected particle tracing simulation. The color scale represents the total residence time of the particle. Right: Distribution of particles by size after a period of steady-state flow.

Surface Flux Flow and Interaction

Interactions between the liquid steel, flux, and gases during various tundish operations are often the cause of inclusion formation and have a negative impact on steel cleanness. These interactions were simulated to measure the propensity of flux entrainment during certain casting events. For valid simulation of the interactions between the liquid steel and flux, correct use of physical properties (i.e. viscosity and surface tension) is critical. Flux flow rates and total mass exiting the pourbox were evaluated based on boundary conditions and process variables including the amount of surface flux existing in the tundish and the tundish weight at ladle open. Changes in these variables were shown to have a major effect on the amount of flux entrained into the liquid steel bath (Figure 6). Accompanying the flux flow rates and mass data with 3-dimensional video allows the viewer to visually see the flow pattern of flux and evaluate the cause of flux flow into the trough (Figure 6). A more comprehensive understanding of the fluid flow during certain process conditions can be achieved with the combination of visual and quantitative results.

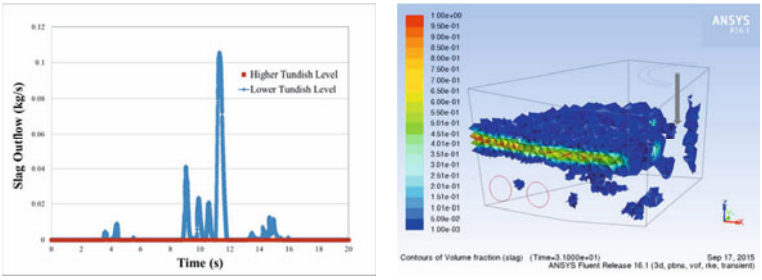

Figure 6: Left: Measured flow rates of non-metallic phases out of pourbox for a low tundish level (blue) and a high tundish level (red). Right: 3-D visualizations of the flow of flux with the steel. The gray arrow represents the liquid steel stream entering the tundish.

Conclusions

Any model needs validation. Pairing physical and computational modeling, considering the difficulty of full-scale operational validation using liquid steel, is an effective way to provide checks and balances for each modeling technique. As stated previously, both physical modeling and computational modeling have significant advantages and capabilities; it is the combination of both that creates a powerful evaluative tool to ensure optimum tundish performance and steel cleanness.

Since the beginning of hot commissioning, actual tundish performance matches the results found from the water and CFD models:

- No evidence of localized tundish freezing has been found after completing a sequence.
- Unique tundish furniture is robust enough to handle a very mixed and specialized steel grade portfolio.
- Initial cleanness metrics from preliminary testing during hot commissioning of the vertical bloom caster has met and exceeded cleanness produced at existing steelmaking operations.

By conducting industry-leading physical and computational tundish modeling as part of the internal development and design phase of the new jumbo bloom vertical caster, the project and commissioning team was ready with answers to questions that have not yet been formulated, and the caster was equipped with a tundish design that will meet or exceed TimkenSteel clean steel expectations, consistent with the company's reputation as a global leader in high performance clean air-melted steels.

Acknowledgements

The authors of this paper would like to thank SMS Concast for the initial CFD model and results, and for the assistance in creating the TimkenSteel CFD tundish model.

References

1. R. Koitzsch, et al., "Simulation of Steelgrade Change in a Water Model Tundish Using the Combined DPIV/PLIF Technique," (Paper presented at METAL Conference, 2007).

2. M. Clark, et al., "Modelling for Tundish Applications," (Report, Foseco Steel).

3. P. Vayrynen, et al., "On Validation of Mathematical Fluid Flow Models for Simulation of Tundish Water Models and Industrial Examples," (Paper presented at AISTech Conference, 2, (2008): 41-50.)

4. K.-Y. Chien, "Predictions of Channel and Boundary-Layer Flows with a Low-Reynolds-Number Turbulence Model," (Paper 80-0134 presented at the AIAA 18th Aerospace Sciences Meeting, Pasadena, California, 14-16 January 1980).

5. H. Ling, L. Zhang, "Numerical Simulation of the Growth and Removal of Inclusions in the Molten Steel of a Two-Strand Tundish," *JOM*, 65 (9) (2013), 1155-1163.

CFD Modeling and Simulation in Materials Processing 2016
Edited by: Laurentiu Nastac, Lifeng Zhang, Brian G. Thomas, Miaoyong Zhu, Andreas Ludwig, Adrian S. Sabau, Koulis Pericleous, and Hervé Combeau
TMS (The Minerals, Metals & Materials Society), 2016

SIMULATION OF FLUID FLOW AND HEAT TRANSFER IN PLASMA ARC REGION OF AC ELECTRIC ARC FURNACE

Qipeng Dong, Jiongming Zhang

State Key Laboratory of Advanced Metallurgy, University of Science and Technology Beijing
No. 30, College Road, Haidian District, Beijing 100083, China

Keywords: AC plasma arc, Mathematical model, Energy source, Metal vapor

Abstract

A mathematical model describing the characteristic of AC plasma arc in electric arc furnace has been developed basing on the model of DC plasma arc. Because of the specificity of AC power, variety of energy in plasma arc region has been considered using varied energy source. Moreover, due to the considerable effect of metal vapor from the vaporization of bath on the transport properties of AC plasma arc, the effect has been taken into account in the simulation. To calculate the velocity and temperature distributions in AC plasma arc region, the time-dependent conservation equations of mass, momentum, and energy are solved in conjunction with the Maxwell's equations of electromagnetic field. The heat transfer from plasma arc to a rigid math surface is calculated.

Introduction

Electric arcs are widely used for waste disposal, steel-making and welding process, etc. AC plasma arc as well as DC plasma arc is used.[1] In order to improve the using of electric arcs and optimize them, characteristics of them should be known well, such as temperature, velocity, etc. However, because of complex feature and high temperature of plasma arcs, the general way of observation and measurement can hardly apply to the plasma arc. So, numerical modeling has been the principal method for studying and improving electric arc process in past decades.
K.C. Hsu et al[2] presented a two-dimensional model to study the flow fluid and heat transfer in the arc region. A crucial boundary condition for current density in cathode was established, and the predicted temperature distributions showed good agreement with experimental measurement. McKelliget and Szekel[3] developed a mathematical model to predict the velocity, temperature, and current density distributions in inert gas welding arcs. The mechanisms of heat and momentum transfer to the anode were also investigated. Good agreement between the predicted results and experimental data had been obtained. F Lago and JJ Gonzalez[4] developed a two-dimensional numerical model of the interaction between an electric and a solid anode of different types. The anode material vapor in the plasma column and the latent heat of vaporization were taken into account in their work. Larsen and Bakken[5] published their work on the AC arcs in silicon metal furnace. An improved Channel Arc Model for simulation of AC arcs had been presented. Satisfactory agreement between simulated and measured current and voltage waveforms were obtained. However, characteristics of AC arc were not studied. Savarsdottir and Bakken[6] developed a Magneto-Hydrodynamic model for high current AC arcs in submerged-arc furnaces. But the model was almost the same as the model of DC plasma arc, and they didn't consider the differences between AC and DC arcs. Recently, Moghadam and Seyedein[7] et al.

presented a two-dimensional mathematical model to describe the heat transfer and fluid flow in AC arc zone of ferrosilicon submerged-arc furnace. They found that the optimal arc length in furnace is 10cm. However, they didn't notice that energy source will change according to different directions of current.

A lot of works had been done on the electric arc in welding or electric arc furnace, but most of them were concentrated on DC plasma arc. The research on AC plasma arc is very limited and the differences between AC and DC plasma arc aren't considered in previous models. So, not like the DC plasma arc, characteristics of AC plasma arcs are not known well. Because of the different power, the features of AC plasma arc must be different with the DC plasma arc's, and the previous models can't be used in the simulation of AC arc directly. Given this, a mathematical model is developed in this work to study the major characteristics of single-phase AC plasma arc.

Mathematical model

The computational domain considered for modeling the AC plasma arc is given in figure 1. When a free-burning arc is not affected by external forces such as magnetic or convective forces, it presents a natural axis of symmetry, and a two-dimensional model is enough for its description.

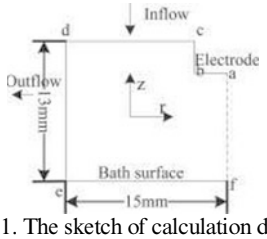

Figure 1. The sketch of calculation domain.

Assumptions

The AC plasma arc is a very complicated physical phenomenon, in order to simplify the mathematical model, the following assumptions have been made in this study:

1) The flow is assumed to be laminar. Characteristic of fluid flow can be classified by the Reynolds number, which can be calculated using the following equation ($Re=\rho \mathbf{v} l / \mu$).

The temperature of 15000K was taking into account here, so corresponding parameters were gotten: density $\rho \sim 0.032 kg/m^3$, kinetic viscosity $\mu \sim 7.1\times10^{-5} Pa\cdot s$, arc length $l \sim 0.01m$ and velocity $\mathbf{v} \sim 300m/s$. The value of Reynolds number was calculated to be 1352. In a free jet, transition from laminar to turbulent flow is found to take place at Reynolds numbers around 1.0×10^5.Therefore, a laminar flow regime is expected in the arc.

2) The arc is local thermal equilibrium (LTE), which means that the electron and heavy particle temperatures are similar. Hsu and Pfender[2] have found that this assumption is applicable over most of the arc except in the arc fringes and the regions near the cathode and anode surfaces.

3) The shielding gas of arc is assumed to be pure argon at 1 atm. Due to the considerable effect of metal vapor from vaporization of bath on transport properties of AC plasma arc, the effect has been taken into account basing on the results of previous research[8].

4) Deformation of the bath surface is neglected.

5) The plasma is supposed to be optically thin and an approximate method is used to model the radiation.

Transport equations

Under two-dimensional axisymmetric cylindrical coordinate system, time-dependent transport equations of AC arc are written as follows:

1) Conservation of mass

$$\frac{\partial \rho}{\partial t}+\frac{1}{r}\frac{\partial}{\partial r}(r\rho v)+\frac{\partial}{\partial z}(\rho u)=0 \tag{1}$$

where, ρ is the density, t is time, r is the radial distance and z is the axial distance, **v** and **u** are the velocity components in the radial and axial directions, respectively.

2) Conservation of axial momentum

$$\frac{\partial(\rho u)}{\partial t}+\frac{1}{r}\frac{\partial}{\partial r}(r\rho vu)+\frac{\partial}{\partial z}(\rho uu)=-\frac{\partial P}{\partial z}+\frac{\partial}{\partial z}\left(2\mu\frac{\partial u}{\partial z}\right)+\frac{1}{r}\frac{\partial}{\partial r}\left\{r\mu\left(\frac{\partial v}{\partial z}+\frac{\partial u}{\partial r}\right)\right\}+F_z \tag{2}$$

The source of momentum is Lorentz force which is produced by self-induced magnetic field. The Lorentz force component ($\mathbf{F_z}$) is given as: $F_z = j_r B_\theta$.

where, P is static pressure, is the viscosity, **j** is the current density and B_θ is the azimuthal magnetic field.

3) Conservation of radial momentum

$$\frac{\partial(\rho v)}{\partial t}+\frac{1}{r}\frac{\partial}{\partial r}(\mathrm{r}\rho vv)+\frac{\partial}{\partial z}(\rho uv)=-\frac{\partial P}{\partial r}+\frac{2}{r}\frac{\partial}{\partial r}\left(r\mu\frac{\partial v}{\partial r}\right)+\frac{\partial}{\partial z}\left\{\mu\left(\frac{\partial v}{\partial z}+\frac{\partial u}{\partial r}\right)\right\}-\frac{2\mu v}{r^2}+F_r \tag{3}$$

The Lorentz force component ($\mathbf{F_r}$) is given as: $F_r = -j_z B_\theta$.

4) Conservation of energy

$$\frac{\partial(\rho h)}{\partial t}+\frac{1}{r}\frac{\partial}{\partial r}(r\rho vh)+\frac{\partial}{\partial z}(\rho uh)=\frac{\partial}{\partial z}\left(\frac{k}{c_p}\frac{\partial h}{\partial z}\right)+\frac{1}{r}\frac{\partial}{\partial r}\left(r\frac{k}{c_p}\frac{\partial h}{\partial r}\right)+S_h \tag{4}$$

The energy source (S_h) in the energy equation may be composed of three components, the first one is the Joule heating caused by arc resistance, the second term is the enthalpy which is transported by electrons due to the fact that velocity of electrons is generally much higher than heavy particles'[2], and the final term is optically thin radiation loss per unit volume. In DC arc model, the source will not change due to the fixed current. However, for the AC arc, direction and value of the current will change with time, the enthalpy which is transported by the electrons will be different. This is the major difference between AC and DC plasma arc model. And different energy sources are the key point of AC plasma arc model. The difference was not taken into account in the previous papers,[1,6,7] and the unsatisfactory results were obtained. The source in the energy equation can be expressed as follows:

$S_h = \frac{j_z^2 + j_r^2}{\sigma}+\frac{5k_B}{2e}\left(\frac{j_z}{c_p}\frac{\partial h}{\partial z}+\frac{j_r}{c_p}\frac{\partial h}{\partial r}\right)-S_R$, the ab in figure1 is cathode;

$S_h = \frac{j_z^2 + j_r^2}{\sigma}-\frac{5k_B}{2e}\left(\frac{j_z}{c_p}\frac{\partial h}{\partial z}+\frac{j_r}{c_p}\frac{\partial h}{\partial r}\right)-S_R$, the ab in figure1 is anode.

The radiation loss for argon plasma is taken from the study of D.L.Evans and R.S.Tankin[9].

In order to calculate the momentum source and energy source, current density and azimuthal magnetic field should be known first. So, it is necessary to solve the equations of electromagnetic field. In this study, three equations are defined in the generalized form (equation (5)) suggested by Patankar[10] for electric potential (V), radial and axial potential vector components (**Ar** and **Az**).

$$\frac{\partial(\rho\phi)}{\partial t}+\nabla\cdot(\rho v\phi)=\nabla\cdot(\Gamma_{\phi}\nabla\phi)+S_{\phi} \tag{5}$$

The equations in the generalized form of Patankar for the three scalars are given as follows:

Table I. Transport equations for the three user-defined scalars.

Conservation equations	Φ	Γ_Φ	S_Φ
Current (equation (6))*	V	σ	0
Axial vector potential (equation (7))*	$\mathbf{A_z}$	1	$_0\mathbf{j_z}$
Radial vector potential (equation (8))*	$\mathbf{A_r}$	1	$_0\mathbf{j_r}$-$\mathbf{A_r}$/r^2

*The general equation can be used to calculate the three scalars by taking the convection term equal to zero.

where, $_0$ is the permeability of vacuum and is given by the value of $4\pi\times10^{-7}$Hm^{-1}.

The current density can be deduced from the electric potential:

$$\begin{cases} j_z=-\sigma\left(\dfrac{\partial\phi}{\partial z}-v_r B_\theta\right) \\ j_r=-\sigma\left(\dfrac{\partial\phi}{\partial r}+v_z B_\theta\right) \end{cases} \tag{9}$$

Boundary conditions

Table II. Boundary conditions for the model

boundary	P/Pa	$\mathbf{v_z}$/ms^{-1}	$\mathbf{v_r}$/ms^{-1}	T/K	Φ/V	$\mathbf{A_z}$	$\mathbf{A_r}$
ab	-	0	0	T=3000	Equation(12)		
bc	-	0	0	T=3000			
cd	1atm	Δ	Δ	T=1000			
de	1atm	Δ	Δ	T=1000			
ef	-	0	0	T=1800	0		
fa	-						

Boundary conditions for the model of AC plasma arc are listed in Table II. Where, Δ represents that the value is derived from the internal computation, represents that the flux is zero. Symmetrical boundary condition is used for the axis a-f. No-slip conditions (zero velocities) are applied for the anode and cathode surfaces. For the boundary condition of electric potential, the current density distribution expressed by the equation (12) is imposed on the surface a-b, which is different with the DC plasma arc model.

$$J = \begin{cases} -2J_c(1-(\mathrm{r}/\mathrm{R_c})^2)\sin(2\pi\omega\,\mathrm{t}), r \le R_c \\ 0, r > R_c \end{cases} \quad (12)$$

where, R_c is the radius of the cathode spot, which is defined as:

$$R_c = \sqrt{I/(\pi J_c)} \quad (13)$$

And in this study, R_c is taken to be a constant which is corresponding to the maximum current. I is the total current in the system. J_c is the average current density, it is assumed to be 6.5×10^7 A/m^2[3].

No matter what kind of plasma arc, AC or DC, the major function of them is to supply heat for the bath or work-piece efficiently. In the previous researches about the DC plasma arc[11,12], four major mechanisms for the heat transfer from arc to the metal were taken into account: heat transfer by convection, Thompson effect, condensation of electrons, and heat transfer by radiation. The four different mechanisms for the heat transfer are also considered for the single-phase AC plasma arc here.

Results

The CFD commercial code FLUENT is used to solve the transport equations for the single-phase AC plasma arc model. The program-developing tools (user-defined-function and user-defined-scalar) are used to realize the coupling of the electromagnetic and hydrodynamic equations. Arc length is taken to be 10mm in this study. Electrical current should be dependent on the time, $I=200\cdot sin(2\pi\omega t)$ is adopted in this work. Where ω is the frequency of the AC current, 50Hz is used here. Uniform grid with minimum cell of 0.2×0.2mm^2 is adopted in the calculation, which is carried out for one and a half period.

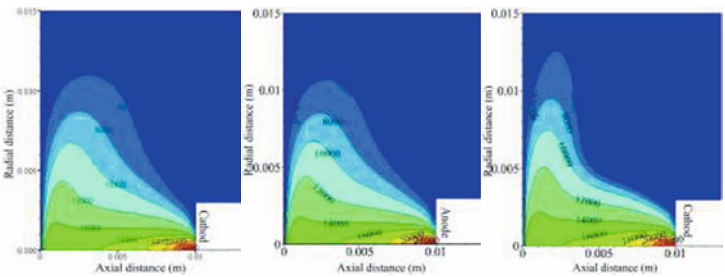

(a) t=0.005s (b) t=0.015s (c) DC arc

Figure 2. Temperature field of the AC arc at two specified times and DC arc.

Since the single-phase alternating current is time-dependent, the characteristics of the AC plasma arc will vary with time. So the distribution of temperature, velocity, electric potential of AC plasma arc will change all the time, while the direction of the current and polarity of the plasma arc change with the time periodically. Figure 2 shows temperature distributions of AC arc at t=0.005s and t=0.015s, corresponding to the maximum current in opposite direction, respectively. The temperature distribution of DC arc with the value of maximum current is also presented for comparison. As seen in the figure, the temperature distributions of the AC arc at different times are very similar with each other. Comparison between the calculated temperature distribution

with the DC arc shows that the shape of AC arc is similar with the DC arc's. Although the temperature distribution of the AC arc will change with the time, the highest temperature is always found at the central location closing to the graphite electrode. The highest temperatures are nearly the same at 0.005s and 0.015s.

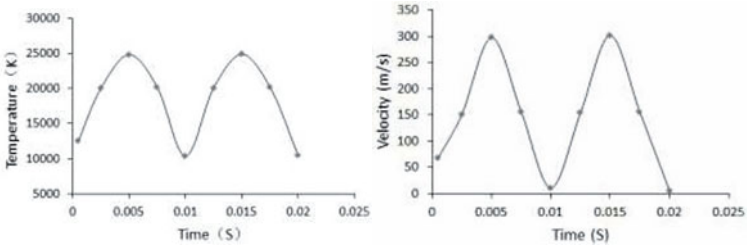

Figure 3. Highest temperatures and maximum velocities of AC arc at different times.

Figure 3 presents the predicted highest temperatures and maximum velocities of AC plasma arc at nine different times in a period. The current imposing on the electrode changed with time in sine form here. As shown in the figure, shape of the curve which composed of nine highest temperatures at different times is semi-sinusoidal. The transformation of AC arc temperature is connected with the change of current. The highest temperature of AC arc is varying periodically with time, just like the alternating current. And because the temperature has no direction, the period of temperature is half of the current's. Temperatures at 0.005s and 0.015s are the most highest which are corresponding to the maximum absolute values of current in a period. The shape of time-velocity curve is similar to the time-temperature curve. So, the law of the temperature is appropriate to the velocity of AC arc.

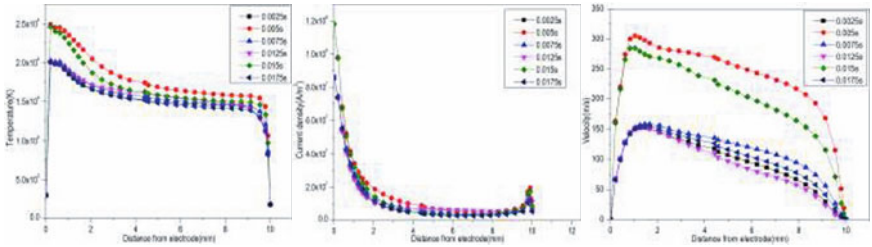

Figure 4. Simulated results of axial characteristics.
(a) temperature profiles, (b) current density profiles, (c) velocity profiles

Figure 4 presents the predicted results for the axial characteristics of AC arc at different times. As we can see from it, not like DC arc, the temperature of AC arc varies with time. As the only variable changing with time is current, so, we can say that, the temperature of AC arc varies with the change of currents, and greater the current, higher the temperature. Although the highest temperatures are changing with the time, distributions of the axial temperature of AC arc are similar to each other. For the characteristic of the AC electric current, we can know that the absolute values of current at four specified times (t=0.0025s, 0.0075s, 0.0125s and 0.0175s) are

the same. Just as expected, the predicted temperatures at the four times are almost in agreement with each other. In figure 4(b) and (c), the predicted results for the current density and plasma velocity along the symmetric axis are presented respectively. The results show that the law of the temperature is appropriate to the current density and the velocity of the AC arc. So, for the AC arc, although the direction of current will change, the characteristics will not change for the equal values of current.

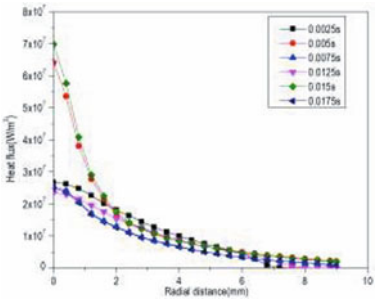

Figure 5. Heat flux on the bath surface.

The mechanism of heat transfer from arc to the melt surface is very complicate. The predicted heat flux from the AC plasma arc to the metal is presented in figure 5. As shown in figure 5, the greatest heat flux for AC arc appears at the central of arc, and the effective region of heating is very small, just around the central of arc. The heat flux of AC arc will vary with the time, and this is connected with temperature. The difference of the heat fluxes at different times is very evident, and higher current lead to higher heat flux. Although the direction of current will change with time, the heat fluxes will be similar as long as the absolute values of current are equal.

Conclusion

1. The characteristics of the AC plasma arc will vary with the time, for the current is time-dependent.
2. Although the temperature distribution of the AC arc will change with the time, the highest values of temperature, current density and plasma velocity are always found at the central location closing to the graphite electrode, and so do for the heat flux.
3. The highest temperature and velocity of AC arc are varying periodically with time, just like the alternating current. And the periods of them are both half of the current's.
4. Just like DC arc, greater the current, higher the temperature and velocity. The distribution law of temperature at different times is very similar to each other. And so it is with the current density and velocity.

Acknowledgements

The authors would like to acknowledge the financial support of National Natural Science Found of China (U1360201, 51174024).

References

1. J.A. Bakken, L. Gu, H.L. Larsen, and V.G. Sevastyanenko, “Numerical modeling of electric arcs,” *Journal of engineering physics and thermophysics*, 70 (1997), 530-543.

2. K.C. Hsu, K. Etemadi, and E. Pfender, "Study of the free- burning high- intensity argon arc," *Journal of Applied Physics*, 54 (1983), 1293-1301.

3. J. McKelliget, and J. Szekely, “Heat transfer and fluid flow in the welding arc,” *Metallurgical Transactions A*, 17 (1986), 1139-1148.

4. F. Lago, J. J. Gonzalez, P. Freton, and A. Gleizes, “A numerical modelling of an electric arc and its interaction with the anode: Part I. The two-dimensional model," *Journal of Physics D: Applied Physics*, 37 (2004), 883-897.

5. H.L. Larsen, G.A. Saevarsdottir, and J.A. Bakken, “Simulation of AC arcs in the Silicon Metal Furnace” (Paper presented at the 54th Electric Furnace Conference Proceedings, Dallas, Texas, 9 December 1996), 157.

6. G.A. Saevarsdottir, J.A. Bakken, V.G. Sevastyanenko, and L.Gu, “Modeling of AC arcs in submerged-arc furnaces for production of silicon and ferrosilicon,” *Iron & steelmaker*, 28 (2001), 51-57.

7. M.M. Moghadam, S.H. Seyedein, and M.R. Aboutalebi, “Fluid Flow and Heat Transfer Modeling of AC Arc in Ferrosilicon Submerged Arc Furnace,” *Journal of Iron and Steel Research International*, 17 (2010), 14-18.

8. G.J. Dunn, T.W. Eagar, “Metal vapors in gas tungsten arcs: Part II. Theoretical Calculations of Transport Properties,” *Metallurgical and Materials Transactions A*, 10 (1986), 1865-1871.

9. D.L. Evans, R.S. Tankin, “Measurement of emission and absorption of radiation by an argon plasma,” *Physics of Fluids*, 10 (1967), 1137-1144.

10. S. Patankar, *Numerical heat transfer and fluid flow* (Boca Raton. CRC Press, 1980).

11. J. Alexis, M. Ramirez, G. Trapaga, and P. Jönsson, “Modeling of a DC Electric arc furnace: Heat transfer from the arc,” *ISIJ international*, 40 (2000), 1089-1097.

12. R.T.C. Choo, J. Szekely, and R.C. Westhoff, “Modeling of high-current arcs with emphasis on free surface phenomena in the weld pool,” *Welding Journal*, 69 (1990), 346-361.

CFD Modeling and Simulation in Materials Processing 2016
Edited by: Laurentiu Nastac, Lifeng Zhang, Brian G. Thomas, Miaoyong Zhu, Andreas Ludwig, Adrian S. Sabau, Koulis Pericleous, and Hervé Combeau
TMS (The Minerals, Metals & Materials Society), 2016

SIMULATION OF HEAT TRANSFER IN SLAB CONTINUOUS CASTING MOLD AND NEW FORMATION MECHANISM OF SHELL HOT SPOTS

Zhaozhen Cai, Miaoyong Zhu

School of Materials and Metallurgy, Northeastern University, Shenyang, 110819, China

Keywords: Slab continuous casting, Mold, Heat transfer, Air gap, Mold flux film, Hot spots

Abstract

A mathematical model of simulating the heat transfer behavior of carbon steel solidifying in slab continuous casting mold was developed coupled with heat transfer media dynamic distribution behavior in shell/mold gap, such as liquid flux, solid flux, air gap, as well as mold/solid flux interfacial contact thermal resistance. The evolution characteristics of the distributions of mold flux, air gap formation, as well as the shell temperature field of carbon steel solidifying in a slab mold were described. Based on these, a new mechanism of shell hot spots formation in slab mold was proposed. The formation for shell wide face off-corner hot spot at mold upper and middle parts results from the thick mold flux film filling in shell/mold gap, while the lower part results from the thick air gap formation, and that of the narrow face just results from the thick mold flux film filling in the gap.

Introduction

Continuous casting is the most primary way of producing steel currently owing to its inherent advantages over ingot casting such as low cost, energy saving, flexibility of operation, and high quality cast product [1], and over 90% of steel in the world today is produced by this process. However, there are also numerous of defects often occurring in slabs surface and subsurface in practical continuous casting in steel plants, which are directly related to the thermal and mechanical behaviors of initial solidified shell in mold. Among these defects, the off-corner surface depressions and subsurface cracks, which results from the formation of hot spots on initial solidifying shell surface in mold, appear rather commonly. [2-4] Intending to reduce the occurrence rate of the defects, several studies have been conducted to investigate the shell thermal behaviors and the mechanisms of hot spots formation in shell surface in continuous casting mold in past decades by numerical simulation. [5-12]

Brimacombe et al. [5] studied the shell temperature evolution in a slab continuous casting mold by using a mathematical model coupled with the process of air gap formation in shell/mold gap with the shell deformation, and the formation mechanism of shell off-corner hot spots that resulted from the air gap formation in the regions was proposed. Kristiansson [6] also simulated the shell temperature filed in a billet mold by a two dimensional thermo-mechanical coupled model, and the hot spots formation cause was regarded as the reduced heat transfer in shell off-corners due to the air gap formation. Wang et al. [7, 8] studied shell thermo-mechanical behaviors in billet mold by using a gap-dependent heat transfer model to calculate the heat flux through the air gap, and the shell hot spots formation was also considered that they were resulted from the air gap formation. These previous works have a common point that the investigations on shell thermal behavior in mold did not consider the influence of mold flux film on the heat transfer

that the shell/mold gap just filled in the air gap. However, in practical continuous casting, the mold flux film in the gap has a great significant effect on shell heat transfer. [13-15] In order to consider the influence, Kim et al. [9] and Han et al. [10] studied shell temperature evolutions in beam blank and slab molds by developing finite element models with assuming uniform mold flux film of 100μm in shell/mold gap. Thomas et al. [11, 12] studied the shell temperature fields in slab and billet molds by developing finite element models based on the variation thickness of mold flux film in shell/mold gap along mold height. Nevertheless, both of them did not consider the distribution characteristics of the flux film along mold circumference that it was assumed uniformly along the circumference. Accordingly, the formation of shell hot spot in mold also attributed to the air gap formation. However, the practical continuous casting and several studies showed that the mold flux film in the mold both along mold circumference and height were nonuniform and affected the air gap formation and shell heat transfer in mold greatly. [14, 16, 17]
In present work, a two dimensional transient heat transfer model of simulating the strand-mold system heat transfer behaviors of carbon steel solidifying in slab continuous casting mold was developed coupled with shell deformation, in which the heat transfer behaviors of shell/mold gap were described in detail with the considerations of the gap size evolution, mold flux film dynamic distribution and air gap formation in it. Based on these, the characteristics of the mold flux film dynamical distribution, air gap formation, as well as the shell temperature field and the growth of a carbon steel solidifying in slab mold in a plant were analyzed, and a new mechanism for shell hot spots formation in slab mold was proposed by analyzing the evolution characteristics of shell surface temperature and the thermal resistances of mold flux and air gap in the shell/mold gaps of the wide and narrow faces.

Model descriptions

In our previous study [18], to describe the heat transfer process of shell solidification in a continuous casting mold in detail, a two dimensional slice-travel transient thermo-mechanical coupled model of a quarter of a strand-mold system were developed, as shown in **Fig. 1**.

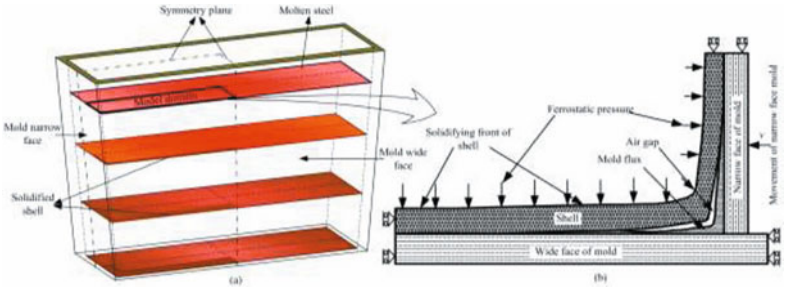

Fig. 1 Schematic of the shell thermo-mechanical simulation model for a slab mold: (a) the calculation domain, (b) transverse section of a slice

In this model, the shell heat transfer and stress evolution were predicted by a sequential coupling method. The heat transfers of strand and mold copper plate were governed by the two-dimensional transient heat transfer equation based on the strand surface and mold hot face heat transfer boundary conditions of the shell/mold gap heat flux obtained from the detailed

description of shell/mold gap heat transfer. The shell deformation and stress evolution were predicted by an Anand constitutive model [19, 20], and the mold copper plate deformation was neglected. The contact behavior between the shell and mold was set as rigid-to-flexible contact. The ferro-static pressure was loaded onto the shell solidification front using an algorithm that dynamically rejected the "liquid element" as the shell solidification proceeded.

For the description of the shell/mold gap heat transfer, the shell/mold gap was assumed to be fully filled by the mold flux film and air gap, and the area was not meshed. The gap size evolution was predicted by shell shrinkage and deformation within each time step as the shell moves down. The mold flux film in the gap was considered to consist only of liquid and solid flux, and the (liquid/solid) status was determined by both the shell surface temperature and its solidification temperature. The thickness of the film was determined by both the status of the mold flux and the shell/mold gap size. In accordance with practical continuous casting, the heat transfer of the shell/mold gap was divided into two modes according to the different heat transfer media used to fill it; specifically, the composition of mode I consisted of the liquid flux, the solid flux, and the mold/solid flux interfacial contact thermal resistance, and that of mode II consisted of the air gap, the solid flux, and the mold/solid flux interfacial contact thermal resistance. As an important part of the gap heat transfer [21, 22], the radiation heat transfers in the air gap and mold flux film were taken into account. The air gap formation, mold flux film distribution, and the corresponding thermal resistances around the mold circumference were calculated according to the mechanism of the same heat flux across the heat transfer medium layers based on the parameters of the shell surface and mold hot-face temperatures and the shell/mold gap size along mold circumference provided by the previous time-step of strand-mold thermo-mechanical behavior analyses. The more detailed calculation model was shown in our previous study [18].

Results and discussion

3.1 Mold flux film distribution and air gap formation in mold

Fig. 2 shows the predicted distribution characteristics of mold flux film in shell/mold gap around the shell off-corners at the distances of 100mm, 300mm, 500mm below meniscus and mold exit as the effect of above shell deformation characteristics. At the upper part of mold, the mold flux films both around shell wide and narrow faces decrease gradually from the corners to the midst. Nevertheless, the distributions are relatively uniform that the differences of the thicknesses between the corners and the midst are just 0.20mm and 0.32mm for the wide and narrow faces,

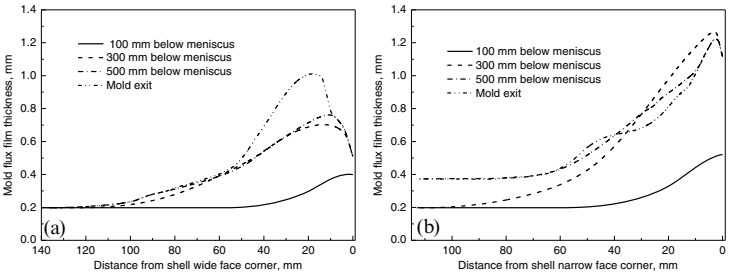

Fig. 2 Mold flux distribution around shell wide face corner (a) and narrow face corner (b)

respectively, when shell moves down to 100mm below meniscus. However, with the shell moving down continuously, the mold flux films completely solidify gradually from the corners to the midst, and thus the distributions show a trend that increase firstly and decrease then in the regions of 0–120mm and 0–70mm off the shell wide and narrow face corners respectively with the evolution of the shell/mold gap. The maximum differences of the thicknesses between the regions and the corresponding midst reach 0.81mm at mold exit and 1.07mm at 300mm below meniscus, respectively. It will greatly slow down the heat transfer of the off-corners.

Fig. 3 shows the predicted air gap distributions around the shell wide and narrow face corners. Under the casting conditions of the carbon steel, the air gap first forms in the shell corner at 160mm below meniscus and mainly concentrates in the regions of 0–20mm and 0–10mm off shell wide and narrow face corners, respectively. On the wide face due to lack of the compensation of mold wide face taper, the air gap grows continuously at mold upper and middle parts as the shell moves down, as shown in Fig. 3(a). When the shell moves down to the position of 550mm below meniscus, the air gap increases rather quickly. The maximum thickness of the air gap reaches 0.8mm at the corner.

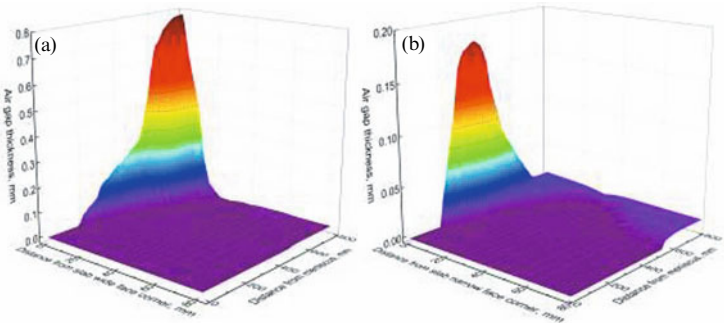

Fig. 3 Air gap distribution around shell wide face corner (a) and narrow face corner (b)

For shell narrow face, the air gap formation is quite different, as shown in Fig. 3(b). It mainly forms in the range of 160–450mm below meniscus, and is much thinner than that of wide face since the compensation of mold narrow face taper and more mold flux filling the gap restrain the formation. In the upper part of the mold, the air gap forms quickly and even exceeds that of the wide face. It reaches a maximum thickness of 0.17mm at 300mm below the meniscus, and then decreases sharply since the shell shrinkage slows down and the mold taper compensates. When shell moves down below 450mm from meniscus, the air gap becomes stable.

3.2 Shell surface temperature distribution

Fig.4 shows the surface temperature distributions of the solidifying shell near the corner along the height of mold. At the initial solidification stage, the shell surface temperature on wide face and narrow face is uniform. However, with the shell moving down, the heat transfers both around shell corner and off-corner slow down gradually since the thick mold flux film and air gap fill in the gap of these regions. When the shell moving down to 300mm below meniscus, the

hot spots form in the regions of 10–40mm both off shell wide and narrow face corners, and extend to the regions of 10–80mm and 15–60mm off the wide and narrow face corners when the shell moves down to mold exit, which the maximum temperature differences between the off-corners and the corresponding midst reach 120 ºC at mold exit and 129 ºC at 300mm below meniscus, respectively.

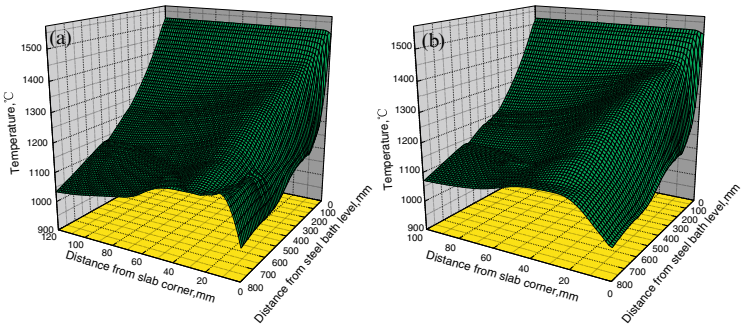

Fig.4 Shell surface temperature distribution at wide face (a) and narrow face corner(b)

3.3 New formation mechanism for shell hot spots

Fig. 5 shows the evolutions of the shell surface temperatures and the thermal resistances of mold flux and air gap around the wide and narrow face corners at various distances below meniscus. Because the generation of the mold/solid flux interfacial contact thermal resistance results from the mold flux film solidification shrinkage and deformation, the thermal resistance in this study was considered as a part of the mold flux thermal resistance. Thus, the mold flux thermal resistance in the figures consists both that of mold flux film and the mold/solid flux interfacial contact thermal resistance.

For the wide face, in accordance of the distribution characteristic of mold flux film in the gap, its thermal resistance also distributes first increase and then decrease from the corner to the midst in the mold, and therefore the peak value of the thermal resistance appears in the off-corner during the casting, as shown in Fig. 5(a). As the result of the mold flux thermal resistance such distribution characteristic, the shell off-corner heat transfer is greatly slowed down, and the hot spot gradually forms accordingly that the obvious higher shell surface temperature generates with a expanding temperature difference between the off-corner and the midst at the positions of 200–700mm below meniscus. During this process, although the air gap forms with a much greater thermal resistance around the corner, it is not the cause of giving rise to the shell off-corner form the hot spot due to the air gap formation region is too close to the corner that the two dimensional heat transfers of the corner counteract the temperature increase. When the shell moves down below 700mm from meniscus, the thick air gap spreads to the direction of the shell midst that the much greater thermal resistance reduces the heat transfer of the shell where closer to the corner more greatly, and a new and much serious hot spot forms at the mold exit. Hence, at the upper and middle parts of mold, the formation of shell wide face off-corner hot spot results from the thick mold flux film filling in the shell/mold gap, while it results from the thick air gap formation near to the mold exit.

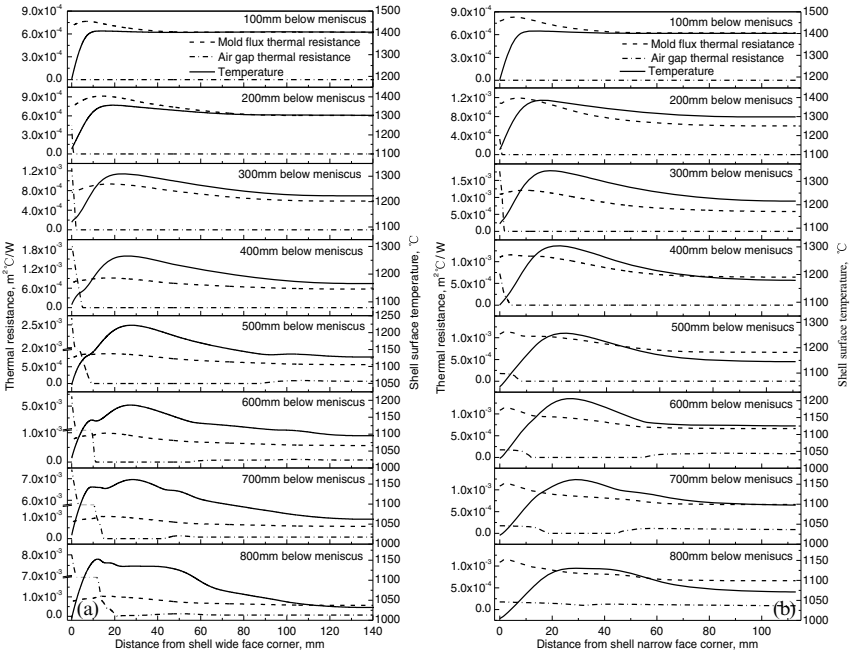

Fig. 5 The evolutions of mold flux and air gap thermal resistances in shell/mold gap and shell surface temperature around shell wide face corner (a) and narrow face corner (b)

As for the narrow face, as shown in Fig. 5(b), the off-corner hot spot formation mechanism has some differences. Since the air gap formation in shell narrow face is much closer to the corner that it just concentrates in the region of 0–10mm from the corner with thinner thickness, as seen from Fig. 4(b), the air gap does not have any effect on the shell off-corner heat transfer during the whole solidification process of shell in mold. Therefore, the formation of the hot spots in shell narrow face just results from the thick mold flux film filling in the shell/mold gap in the off-corner. Furthermore, since the maximum thickness difference of the mold flux film between the shell off-corner and the midst appears at 300mm below meniscus, the most serious hot spot forms at the position accordingly. It is rather different from the previous formation mechanism that considered the hot spots formation in shell wide and narrow face off-corners in the mold resulting from the air gap formation.

Conclusions

(1) Under the typical slab casting conditions of carbon steel, the thick mold flux film concentrates in 0–120mm and 0–70mm off the shell wide and narrow face corners, and the air gap first forms in shell corner and mainly concentrates in 0–20mm and 0–10mm off the corners in mold. The mold flux films around the wide and narrow face off-corners distribute first

increase and then decrease from the corner to the midst. The maximum thickness on shell wide face is 1.01mm at the mold exit, while on the narrow face is 1.27mm at 300mm below meniscus. The air gap on shell wide face grows continuously and increases at 550mm below meniscus, where it mainly forms in 160–450mm below meniscus on shell narrow face. The maximum thickness on shell wide face is 0.8mm at the mold exit, while on the narrow face is 0.17mm at 300mm below meniscus.

(2) Under the typical slab casting conditions of carbon steel, the hot spots form in the regions of 10–80mm and 15–60mm off the shell wide and narrow face corners with an expanding trend with shell moving down. The maximum temperature differences between the off-corners and the corresponding midst reach 120 °C at mold exit and 129 °C at 300mm below meniscus.

(3) The formation for shell wide face off-corner hot spot results from the thick mold flux film filling in the shell/mold gap at the mold upper and middle parts, while the lower part results from the thick air gap formation, and that of the narrow face just results from the thick mold flux film filling in the gap in the off-corner.

Acknowledgement

The National Natural Science Foundation of China (51404061) is acknowledged for supporting this work.

References

[1] J.K. Brimacombe, Metall. Mater. Trans. 24B (1993) 917-935.
[2] B.G. Thomas, W.R. Storkman, Modeling Casting Welding Proc. (1988) 287-297.
[3] B.G. Thomas, A. Moitra, R. McDavid, Iron Steelmaker 23 (1996) 57-70.
[4] Z.Z. Cai, W.L. Wang, M.Y. Zhu, Mater. Sci. Technol. Int. Conf. (2012) 61-72.
[5] A. Grill, K. Sorimachi, J.K. Brimacombe, Metall. Mater. Trans. 7B (1976) 177-189.
[6] J.O. Kristiansson, J. Thermal Stresses 7 (1984) 209-226.
[7] E.G. Wang, J.C. He, Z.K. Yang, H.G. Chen, Iron Steel 34 (1999) 25-27.
[8] E.G. Wang, J.C. He, Sci. Tech. Adv. Mater. 2 (2001) 257-263.
[9] K. Kim, H.N. Han, T. Yeo, Y. Lee, K.H. Oh, D.N. Lee, Ironmaking Steelmaking 24 (1997) 249-256.
[10] H.N. Han, J.E. Lee, T.J. Yeo, Y.M. Won, K.H. Kim, K.H. Oh, J.K. Yoon, ISIJ Int. 39 (1999) 445-454.
[11] Y. Meng, B.G. Thomas, Metall. Mater. Trans. 34B (2003) 685-704.
[12] C. Li, B.G. Thomas, Metall. Mater. Trans. 35B (2004) 1151-1172.
[13] S. Ozawa, M. Susa, T. Goto, R. Endo, K.C. Mills, ISIJ Int. 46 (2006) 413-419.
[14] R. Saraswat, D. M. Maijer, P. D. Lee, K. C. Mills, ISIJ Int. 47 (2007) 95-104.
[15] H. Nakada, M. Susa, Y. Seko, M. Nayashi, K. Nagata, ISIJ Int. 48 (2008) 446-453.
[16] K.C. Mills, A.B. Fox, ISIJ Int. 43 (2003) 1479-1486.
[17] Z.Z. Cai, M.Y. Zhu, Acta Metall. Sin. 47 (2011) 678-687.
[18] Z.Z. Cai, M.Y. Zhu, Acta Metall. Sin. 47 (2011) 671-677.
[19] K. Watanabe, M. Suzuki, K. Murakami, H. Kondo, A. Miyamoto, T. Shiomi, Tetsu-to-Hagané 83 (1997) 115-120.
[20] J.W. Cho, H. Shibata, T. Emi, M. Suzuki, ISIJ Int. 38 (1998) 440-446.
[21] J.W. Cho T. Emi, H. Shibata, M. Suzuki, ISIJ Int. 38 (1998) 834-842.
[22] Z.Z. Cai, M.Y. Zhu, Acta Metall. Sin. 45 (2009) 949-955.

CFD Modeling and Simulation in Materials Processing 2016
Edited by: Laurentiu Nastac, Lifeng Zhang, Brian G. Thomas, Miaoyong Zhu, Andreas Ludwig, Adrian S. Sabau, Koulis Pericleous, and Hervé Combeau
TMS (The Minerals, Metals & Materials Society), 2016

COMPUTATIONAL INVESTIGATION OF SPLASHING BEHAVIORS IN STEELMAKING CONVERTER

Qiang Li[1], Mingming Li[1], Mingxia Feng[2], Zongshu Zou[1]

[1]School of Materials and Metallurgy, Northeastern University
Heping District, Shenyang City, Liaoning Province, 110819, P. R. China

[2]Metallurgy Engineering College, Liaoning Institute of Science and Technology
High-tech Development District, Benxi City, Liaoning Province, 117004, P. R. China

Keywords: BOF, Splashing, Generation mechanism, Blowing number, Numerical simulation

Abstract

Splashing plays a key role in the kinetics of the steelmaking converter but not well understood. This work presents a numerical investigation on the generation of the splashing and introduces an evaluation approach for the qualification of the splashing in oxygen steelmaking converter. The generation mechanism of the droplets was explored by multi-fluid VOF simulation and the splashing rate was quantified based on the blowing number theory. The results show that two mechanisms, i.e. the direct ejection of individual droplets and the tearing of so-called "splash sheets" structure, simultaneously occur and attribute to the splashing. Blowing number fluctuates during process due to the oscillating nature of cavity, and an averaged value of 10.0 for blowing number is obtained under the present blowing condition.

Introduction

In Basic Oxygen Furnace (BOF) steelmaking process, supersonic oxygen jets impinge onto the molten bath surface with extremely high speed and cause the tearing of metal droplets from the bulk around the cavity surface, phenomenally referred as "spitting" or "splashing" [1]. Deo and Boom [2] reported that the generation of splashing stems from the impingement of the jet and the shearing action of the gas flow from the impact region when the jet strikes the metal surface and the gas is deflected upwards. Standish and He [3] observed two mechanisms of droplets generation through cold mode experiments, i.e. the direct ejection of the single droplet out of metal bulk around the cavity edge by so-called "dropping", and "large tears" of liquid producing from the cavity edge, in accompany with the direct ejection of some individual droplets, by so-called "swarming". Peaslee and Robertson [4] reported that the surface waves form finger like structure near the edge of the cavity, and finally are torn off due to the unstable structure of these metal fingers. This mechanism of droplets generation was also observed by Alam et al. [5] who studied the impingement of shrouded supersonic jet on a water surface by a developed volume of fluid (VOF) model in a two dimensional system. Most recently, Sabah and Brooks [6] have made an extensive literature review concerning the amount of droplets in the emulsion and found an observable discrepancy by different investigators and some arguments on the amount of droplets generated. Some experimental and theoretical studies [3, 5, 7-11] have also been performed to focus on the quantity and size distribution of the droplets, and their trajectory and the residence time in the slag. But to date, problems in sampling at high temperature, the interconnected nature

of slag and metal, and problems in scaling-up cold modeling or small-scale high temperature furnace modeling results to plant conditions involved with complex jets interaction [12], etc., means that there is only limited understanding of the knowledge to the generation rate and the residence time of metal droplets in emulsion [7]. Consequently, above-mentioned aspects on the droplets splashing must be solved before a comprehensive prediction model of oxygen steelmaking process is established.

The objective of this study is to numerically reveal the generation of metal droplets and their amount by a multi-fluid volume of fluid model developed in our previous studies [13-14]. The generation mechanism of droplets was visually presented and then expounded, and the generation rate of droplets was quantified on the basis of the "blowing number" theory [7].

Mathematical Model

Governing Equations

The tracking of the sharp gas-slag-melt interface was accomplished using the VOF approach firstly presented by Hirt and Nichols [15]. In this method, a variable, namely the volume fraction α of phase, is introduced for treating free boundary configurations of immiscible fluids. If the q^{th} fluid's (gas, slag, metal) volume fraction in the cell is denoted as α_q, the corresponding conservative equation can be expressed as follows:

$$\frac{\partial(\rho_q \alpha_q)}{\partial t} + \nabla(\alpha_q \rho_q \mathbf{u}) = 0 \tag{1}$$

where ρ_q and α_q are respectively the density (kg·m^{-3}) and volume fraction of phase q, and for the oxygen gas, it conforms to the relation $p=\rho RT$ due to the use of idea gas here.

In the VOF model, the different fluids are modeled by a set of momentum presented in Eqs. (2). The resulting velocity field is shared among the phases. The fields for all variables and properties are shared by the phases and represented volume-fraction-averaged values.

$$\frac{\partial}{\partial t}(\rho \mathbf{u}) + \nabla(\rho \mathbf{u}\mathbf{u}) = -\nabla p + \nabla \cdot \left[\mu_{\text{eff}} (\nabla \mathbf{u} + \nabla \mathbf{u}^T) \right] + \rho \mathbf{g} + f_\sigma \tag{2}$$

where $\boldsymbol{u}$ is the velocity vector (m·s^{-1}); p is the pressure (Pa); $\boldsymbol{g}$ is the gravity vector (m·s^{-2}); ρ is the density (kg·m^{-3}); μ_{eff} is the effective viscosity (Pa·s), $\mu_{\text{eff}} = \mu + \mu_t$.

$$\rho = \alpha_{\text{gas}} \rho_{\text{gas}} + \alpha_{\text{slag}} \rho_{\text{slag}} + \alpha_{\text{steel}} \rho_{\text{steel}} \tag{3}$$

$$= \alpha_{gas}\ \rho_{\text{gas}} + \alpha_{slag}\ \rho_{slag} + \alpha_{steel}\ \rho_{steel} \tag{4}$$

f_σ in Eq. (2) is the surface tension (N·m^{-3}) and calculated using the Continuum Surface Force (CSF) model developed by Brackbill et al. [16]. In the model, the surface tension effect is treated as body forces:

$$f_\sigma = \int_V \sigma\kappa\nabla\alpha dV = \sigma\kappa_p(\nabla\alpha_p)V_p \tag{5}$$

where V_P is the volume of cell P, and κ_P is the curvature calculated by:

$$\kappa_p = -\left(\nabla \cdot \hat{n}\right) = -\left[\nabla \cdot \left(\frac{\nabla\alpha}{|\nabla\alpha|}\right)\right]_p \tag{6}$$

where $\hat{n}$ is the unit vector normal to the surface.

The energy equation, also shared among the phases, is expressed as follows.

$$\frac{\partial(\rho E)}{\partial t} + \nabla \cdot \left[\mathbf{u}(\rho E + p)\right] = \nabla \cdot (\lambda_{\text{eff}} \nabla T) + S_h \tag{7}$$

where the energy E is treated as a mass-averaged variable. This also is applied to the temperature T (K).

$$E = \frac{\sum_{q=1}^{n} (\alpha_q \rho_q E_q)}{\sum_{q=1}^{n} (\alpha_q \rho_q)} \tag{8}$$

where E_q is based on the specific heat of that phase and the shared temperature for each phase. The source term S_h in Eq. (8) incorporates the contributions from the radiation as well as any other volumetric heat sources. $\lambda_{\text{eff}} = \lambda + \lambda_t$, is the effective thermal conductivity ($\text{W}\cdot\text{m}^{-1}\cdot\text{K}^{-1}$) and shared by all the phases, the same as other properties:

$$\lambda = \alpha_{gas}\lambda_{\text{gas}} + \alpha_{slag}\lambda_{slag} + \alpha_{steel}\lambda_{steel} \tag{9}$$

Turbulence Model

In this work, the standard k-ε model with compressibility correction was adopted. The transportation equations of turbulence kinetic energy (k) and the specific dissipation rate (ε) were solved as follows.

$$\frac{\partial(\rho k)}{\partial t} + \frac{\partial(\rho k u_i)}{\partial x_i} = \frac{\partial}{\partial x_j}\left[\left(\mu + \frac{\mu_t}{\sigma_k}\right)\cdot\frac{\partial k}{\partial x_j}\right] + G_k + G_b - \rho\varepsilon - Y_M \tag{10}$$

$$\frac{\partial(\rho\varepsilon)}{\partial t} + \frac{\partial(\rho\varepsilon u_i)}{\partial x_i} = \frac{\partial}{\partial x_j}\left[\left(\mu + \frac{\mu_t}{\sigma_\varepsilon}\right)\cdot\frac{\partial \varepsilon}{\partial x_j}\right] + C_{1\varepsilon}\frac{\varepsilon}{k}(G_k + C_{3\varepsilon}G_b) - C_{2\varepsilon}\rho\frac{\varepsilon^2}{k} \tag{11}$$

For the turbulent viscosity, μ_t, was modeled as follow:

$$\mu_t = C_\mu \rho \frac{k^2}{\varepsilon} \tag{12}$$

where, G_k represents the generation of turbulence kinetic energy due to the mean velocity gradients ($kg \cdot m^{-1} \cdot s^{-3}$). G_b is the generation of turbulence kinetic energy due to buoyancy ($kg \cdot m^{-1} \cdot s^{-3}$). Y_M represents the contribution of the fluctuating dilatation in compressible turbulence to the overall dissipation rate ($kg \cdot m^{-1} \cdot s^{-3}$), $Y_M=0$ for the incompressible fluid and $Y_M=2\rho\varepsilon M_t^2$ for the compressible fluid; M_t is turbulent Mach number, $M_t=k^{1/2}/a$; a is the sonic velocity ($m \cdot s^{-1}$), $a=(\gamma RT)^{1/2}$. $C_{1\varepsilon}$, $C_{2\varepsilon}$, $C_{3\varepsilon}$, σ_k, σ_ε and C are constants and their values are 1.44, 1.92, 0.8, 1.0, 1.3 and 0.9 respectively [17].

Numerical Solution Algorithms

In this study, a 150-ton top-blown oxygen steelmaking converter with an oxygen lance of six convergent-divergent nozzles was employed. Their geometrical configurations are shown in **Figure 1.** In order to reduce the computational cost, the calculated domain was simplified, and only one half of the converter was simulated. The geometrical parameters of the considered converter including the nozzles, the operating conditions are listed in **Table I**.

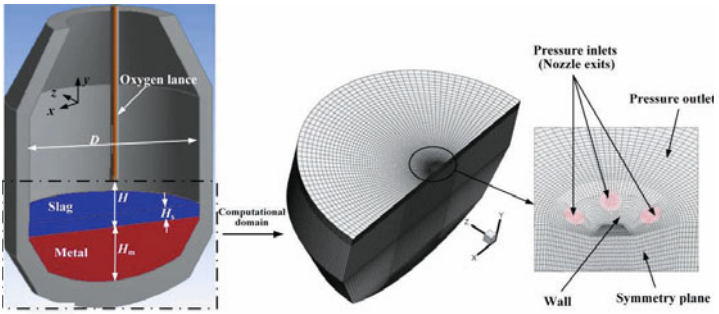

Figure 1. Schematic diagram of converter model and computational domain with grids

Table I. Geometrical parameters and operating conditions

Parameters	Value	Parameters	Value
Nozzle throat diameter d_*, (mm)	30	Converter temperature T_b, (K)	1873
Nozzle outlet diameter d_e, (mm)	43.4	Converter Capacity, (ton)	150
Number of nozzles N, (-)	6	Bath diameter D, (m)	5.685
Nozzle to nozzle angle θ, (°)	17.5	Melt height H_m, (m)	1.545
Mach number Ma, (-)	2.25	Slag height H_s, (m)	0.17
Designed pressure P_0, (Pa×101325)	11.56	Lance height H, (m)	1.2-1.8
Converter back-pressure P_b, (Pa×101325)	1	Operating pressure P, (Pa×101325)	$0.8P_0$, P_0, $1.2P_0$
Inlet oxygen temperature T_0, (K)	308	Oxygen flow Rate, Q ($Nm^3 \cdot h^{-1}$)	24210, 30283, 36871

The initial time step was 10^{-5} s and then was set to the adaptive scheme based on the limitation of a global Courant number of 1. The convergence criteria was set to 1×10^{-6} for the residual of energy while 1×10^{-3} for those of other dependent variables.

Results and Discussion

Mechanism of Droplets Generation

Figure 2 shows the transient shapes of the slag-metal bath surface in BOF during the incipient blowing process at lance height of 1.2m and normal operation pressure of P_0. The molten bath surface is relatively smooth and quiet and the jets just penetrate into the molten slag with slag splashing at the blowing time of 0.5s, as shown in **Figure 2**(a). As blowing proceeds, the molten slag is completely pushed away from the impact zone, metal is penetrated, surface waves form and is spread to all around. As a result, the cavity behaves oscillatory in the horizontal and vertical direction, and the oscillatory flow occurs in the molten bath (**Figure 2** (b) ~ (d)). Such oscillatory flow in the molten bath can also been proved by **Figure 3** where the velocity variation of a monitoring point inside the molten bath during the blowing process is plotted. Obviously, the velocity fluctuates sharply during the blowing process, which confirms that the BOF steelmaking process is unsteady and oscillatory. The same phenomenon was observed by our previous water model experiment and numerical study [13-14].

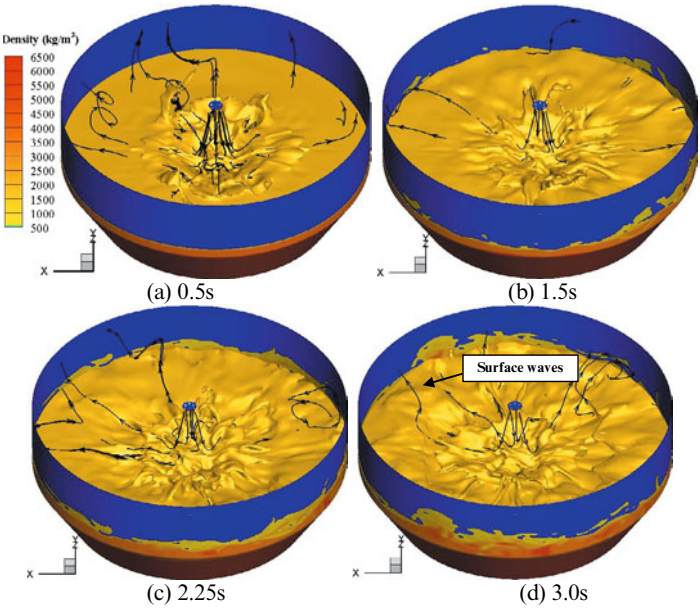

(a) 0.5s (b) 1.5s

(c) 2.25s (d) 3.0s

Figure 2. Profiles of the molten bath surface at different blowing moments for the lance height 1.2m and designed operation pressure P_0

The growth and propagation of surface waves are the basis and prerequisite for the splashing occurrence. Shabnam and Brooks [18] observed that so-called "splash sheets" form at the rim of the cavity based on their water model experiments. Such sheets rise up to a certain height until

become instable, and then fingers are formed which ultimately broke into droplets. **Figure 4** shows the typical splashing pattern obtained from the present numerical simulation at the lance height of 1.2m and operation pressure of P_0. The measured results by Sabah and Brooks [16] in a water model are also presented (as shown in **Figure 4**(a)) for comparison. The phenomena from two studies are encouragingly similar considering that the conditions involved are not the same and the present model is not perfect, e.g., it demands considerably refined mesh to reproduce small droplets normally with diameter in a range of 0.04~70mm. The present modeling results show two mechanisms of droplet splashing, i.e. the direct ejection of individual droplets out of metal body at the rim of cavity and crushing and tearing of "splash sheets" or "large tears" formed at the rim of cavity into several small droplets by deflecting gas flow (as shown in **Figure 4**(b)). Such two mechanisms stem from the ripples formed in the cavity surface. Small ripples results in the direct ejection of individual droplet, and the bigger ones for the generation of "splash sheets" or "large tears" [3]. The present simulation results show that both types of ripples can be produced simultaneously during blowing for the sake of oscillating nature of cavity.

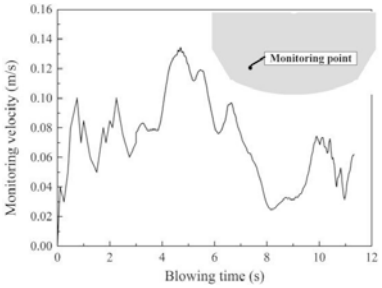

Figure 3. Velocity variation of monitoring point during the blowing at lance height 1.2m and operation pressure P_0

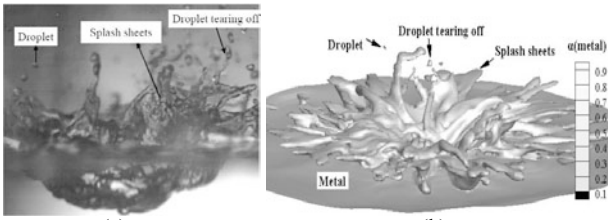

(a) (b)

Figure 4. Generation of splash droplets obtained from (a) high speed imaging by Sabah [7] and (b) present simulation

Rate of Droplets Generation

Even in nowadays it is extremely expensive and nearly impossible to reproduce all scales of droplets during blowing in BOF steelmaking process by numerical technology. Following

previous work [2], Subagyo et al. [7] proposed a "blowing number (N_B)" to assess the droplet generation based on the Kelvin-Helmholtz theory:

$$N_B = \frac{\rho_g u_g^2}{2\sqrt{\sigma g \rho_l}} \tag{13}$$

where N_B is a dimensionless parameter. ρ_g and ρ_l are the gas and liquid density respectively ($kg \cdot m^{-3}$). σ is the liquid surface tension ($N \cdot m^{-1}$). g is the gravitational acceleration ($m \cdot s^{-2}$). u_g is the critical velocity ($m \cdot s^{-1}$) of deflecting gas flow, as defined in **Figure 5**. The onset of splashing occurs once the N_B exceeds unity. **Figure 5** shows the variation of blowing number during blowing at the given lance height of 1.2m and operation pressure of P_0. It can be seen that the value of blowing number fluctuates during blowing attributing to the unstable characteristic of the molten bath and cavity. The oscillating nature of the cavity ultimately impacts the generation, amount and distribution of the splashing. An averaged value of 10.0 for blowing number is obtained under such a blowing condition.

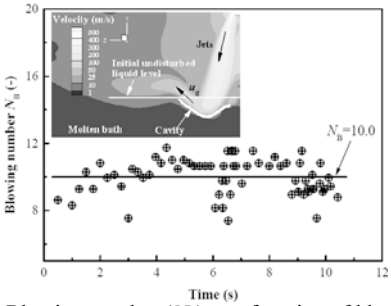

Figure 5. Blowing number (N_B) as a function of blowing time

Conclusions

An effort was paid to study the generation and quantification of the splashing metal droplets induced by the top-blown oxygen jets impinging on the molten bath in BOF steelmaking process by a developed multi-fluid volume of fluid model. The blowing number theory was utilized to quantify the splashing rate. The splashing are normally generated by the direct ejection of individual droplets at the rim of cavity and the tearing of so-called "splash sheets" like structure or "large tears" into several different sized smaller droplets by the deflecting gas flow. The two mechanisms of droplets generation simultaneously occur and attribute to the splashing during converter practice. The generation of droplets was assessed by blowing number theory, and the splashing was hence quantified. Blowing number and resulting blowing number fluctuates during blowing due to the oscillating nature of cavity. The typical blowing number is in the range of 7.8~12.1 at the present varying lance height operation.

Acknowledgements

The authors are grateful to the financial support by the National Natural Science Foundation of China (grant no. 51104037) and the Fundamental Research Funds of the Central Universities of

China (grant no. N120402010, N140204008).

References

1. Y. Tago and Y. Higuchi, "Fluid Flow Analysis of Jets From Nozzles in Top Blown Process," *ISIJ Int.*, 43(2) (2003), 209-215.
2. B. Deo and R. Boom. *Fundamentals of Steelmaking Metallurgy*, (London, UK: Prentice Hall International, 1993), 300-353.
3. N. Standish and Q. L. He, "Drop Generation due to an Impinging Jet and the Effect of Bottom Blowing in the Steelmaking Vessel," *ISIJ Int.*, 29(6) (1989), 455-461.
4. K. D. Peaslee and D. G. C. Robertson, "Model Studies of Splash, Waves, and Recirculating Flows within Steelmaking Furnaces," (Steelmaking Conference Proceedings, Iron and Steel Society, Warrendale, PA, 1994), 713-722.
5. M. Alam, J. Naser, G. Brooks, A. Fontana, "A Computational Fluid Dynamics Model of Shrouded Supersonic Jet Impingement on a Water Surface," *ISIJ Int.,* 52(6) (2012), 1026-1035.
6. S. Shabnam and G. Brooks, "Splash distribution in Oxygen Steelmaking," *Matal. Trans. B*, 46(2) (2015), 863-872.
7. Subagyo, G. A. Brooks, K. S. Coley, G. A. Irons, "Generation of Droplets in Slag-Metal Emulsuions Through Top Gas Blowing," *ISIJ Int.*, 43(7), (2003), 983-984.
8. Q. L. He and N. Standish, "A Model Study of Droplet Generation in the BOF Steelmaking," *ISIJ Int*., 30 (4) (1990), 305-309.
9. M. J. Luomala, T. M. J. Fabritius, E. O. Virtanen, T. P. Petteri and J. J. Härkki, "Splashing and Spitting Behaviour in the Combined Blown Steelmaking Converter," *ISIJ Int.*, 42(9) (2002), 944-949.
10. Subagyo, G. A. Brooks, K. S. Coley, "Residence Time of Metal Droplets in Slag-Metal Emulsions," *Can. Metal. Q.*, 44(1), (2005), 119-129.
11. G. Brooks, Y. Pan, Subagyo and K. Coley, "Modeling of Trajectory and Residence Time of Metal Droplets in Slag-Metal-Gas Emulsions in Oxygen Steelmaking," *Matal. Trans. B*, 36 (2005), 525-535.
12. M. M. Li, Q. Li, L. Li, Y. B. He and Z. S. Zou, "Effect of Operation Parameters on Supersonic Jet Behaviour of BOF Six-nozzle Oxygen Lance," *Ironmaking Steelmaking*, 41(4) (2014), 699-709.
13. Q. Li, M. M. Li, S. B. Kuang and Z. S. Zou, "Computational Study on the Behaviors of Supersonic Jets and Their Impingement onto Molten Liquid Free surface in BOF Steelmaking," *Can. Metall. Q.,* 53(4) (2014), 340-351.
14. Q. Li, M. M. Li, S. B. Kuang and Z. S. Zou, "Numerical Simulation of the Interaction between Supersonic Oxygen Jets and Molten Slag–Metal Bath in Steelmaking BOF Process," *Metall. Trans. B,* 46 (2015), 1494-1509.
15. C. W. Hirt and B. D. Nichols, "Volume of Fluid Method for the Dynamics of Free Boundaries," *J. Comp. Phys.,* 39, (1981), 201-225.
16. J. U. Brackbill, D. B. Kothe and C. Zemach, "A Continuum Method for Modeling Surface Tension,"*J. Comp. Phys.*, 100, (1992), 335-354.
17. B. E. Launder and D. B. Spalding: Lectures in Mathematical Models of Turbulence, Academic Press, London, (1972).
18. S. Shabnam and G. Brooks, "Splashing in Oxygen Steelmaking" *ISIJ Int*., 54(4) (2014), 836-844.

CFD Modeling and Simulation in Materials Processing 2016
Edited by: Laurentiu Nastac, Lifeng Zhang, Brian G. Thomas, Miaoyong Zhu, Andreas Ludwig, Adrian S. Sabau, Koulis Pericleous, and Hervé Combeau
TMS (The Minerals, Metals & Materials Society), 2016

SIMULATION OF AIR ENTRAINMENT IN HIGH PRESSURE DIE CASTING APPLICATIONS

Juergen Jakumeit[1], Herfried Behnken[1], Frank Schmidt[2], Julian Gänz[3], Bastian Thorwald[3], Michael Mathes[1]

[1]Access e.V., Intzestr. 5, 52072 Aachen, Germany
[2].Foundry Institute, RWTH-Aachen, Intzestr. 5, 52072 Aachen, Germany
[3]CD-adapco, Nordostpark 3-5, 52072 Aachen, Germany

Keywords: High pressure die casting, entrained air, mold filling simulation

Abstract

Since the computation of two-phase flow and solidification requires strong coupling, simulation of air entrainment in high pressure die casting applications is a challenge. The effects of surface tension, wetting angle and reduced melt flow due to solidification and air entrainment, as well as compression must be modelled with high precision.
To achieve these requirements, a finite-volume method featuring arbitrary polyhedral control volumes is used to solve flow and solidification strongly coupled. The volume-of-fluid approach is applied to capture the phase separation between gas, melt and solid in connection with a high-resolution interface-capturing scheme to obtain sharp interfaces between phases. Melt and air phase are considered to be compressible fluid. To model the resistance of the dendrite network to the melt flow, an additional source term in the momentum equation is implemented. At high fraction solid the flow is stopped completely.
This methodology was applied to predict air entrainment in high pressure die castings. Basic flow patterns were validated against casting trials using a simplified geometry, and a first industrial application is reported.

Introduction

High pressure die casting (HPDC) is an important manufacturing process for large, thin-walled geometries, especially in the automotive industry. A main disadvantage of HPDC is the entrainment of air, almost impossible to avoid completely due to the chaotic filling process. Entrained air makes HPDC parts non-heat-treatable. Air bubbles entrained under high pressure during solidification will cause HPDC parts to blister during solutionizing [1].
Simulation of the air entrainment is challenging because a two-phase flow of the filling process has to be computed strongly coupled with the calculation of the solidification process. Most commercial simulation programs use a one-phase approach to describe casting processes [2-5], and such programs are unable to handle correctly the air phase and its interaction with the melt.
A new approach to HPDC simulation is presented here, based on a three-phase simulation of casting processes, including the air, melt and solid phases. Both melt and air are considered as compressible fluids separated by a volume-of-fluid approach (VoF), including special treatment to keep the interface sharp. Reduced melt fluidity during the solidification process is handled by

a porous media approach to describe the flow through the dendrite network. At a critical solid fraction, the melt is stopped completely. This approach is implemented in the commercial casting simulation package STAR-Cast [6, 7].
Details of the simulation approach are given in the following chapter, and followed by a description of a number of simulation results: an optimization of plunger movement, prediction of flow pattern and air entrainment for a test-geometry and application to an industrial problem.

Theory

Simulation of the entire casting process is based on a finite-volume method using control volumes (CVs) of arbitrary polyhedral shape. The transport equations for mass, momentum, energy, and phase in integral form are applied to each CV, whereby the surface and volume integrals are approximated using the midpoint rule. Linear equation systems for each variable are solved using algebraic multi-grid iterative solvers. Mass conservation, pressure and velocity conservation are coupled via the SIMPLE algorithm. The transient term is discretized based on an implicit Euler-segregated concept. Details of discretization and the solution method are available in [7-10]. The conservation equation for total energy is solved for the solution variable temperature. For solidification modeling, the volume fraction of solidified liquid is determined using a tabulated fraction solid *vs*. temperature curve ($f_s(T)$). Latent heat L is released in proportion to the change in fraction solid ($L^*d(fs(T))/dT$). A realizable k-epsilon turbulence model in combination with a y+wall model is used to stabilize the chaotic flow, which has Reynolds numbers in the turbulent regime, and provide an additional degree of freedom for energy dissipation. Details of the methodology are presented in [9].
For correct calculation of air entrainment, the method used to track the motion of the free surface must provide a sharp interface. The volume of fluid (VOF) approach, in combination with a high resolution interface capturing (HRIC) scheme, is used to tackle the problem: the entire fluid domain is considered to be filled by a fluid, the properties of which vary according to the distribution of volume fractions of melt C_m, solid C_s and gas C_g ($C_m + C_s + C_g = 1$). The transport of melt, solid and gas is computed by solving transport equations for their volume fractions with a source term for the phase change from melt to solid. To achieve sharpness of the interface, an HRIC scheme [10, 11] is used, which typically resolves the interface within one cell.
The normal force due to surface tension is treated using the continuum surface force (CSF) model proposed by [12], which defines a volumetric source in the momentum equation expressed as:

$$S_\sigma = -\sigma \nabla \left(\frac{\nabla C_{nl}}{|\nabla C_{nl}|} \right) \nabla C_{nl}. \tag{6}$$

Flow resistance in the mushy zone is calculated assuming that the mushy zone acts like a porous medium. The fluid velocity resistance in the mushy zone can be approximated as a pressure drop [13]:

$$-\frac{\partial p}{\partial x_i} = \frac{\mu}{K}\vec{v} + \frac{C_E}{\sqrt{K}}\rho|v|\vec{v}, \tag{8}$$

where μ is the viscosity, K the permeability and C_E the Ergun's coefficient. Permeability can be deduced from the Kozeny-Carman equation [14] as $K = ((1-f_s)^3\lambda_2^2)/(180 f_s^2)$, where λ_2 is the secondary dendrite-arm spacing (SDAS).

The viscous porous resistance depends on the velocity of the melt and tends to zero as the velocity approaches zero. Hence, slight creeping of the melt is not hindered, especially if the melt is being pushed by a high force, as in the case of HPDC. To bring the melt to a complete stop, a flow-stop functionality was implemented. If the fraction solid is above a threshold value, the momentum equation is no longer solved for that particular cell. Flow stopped cells are of zero velocity (relative to the cell center velocity), and fluxes through all adjacent faces are also zero. Pressure remains constant at the value obtaining when the cell has been flagged to be stopped. Since the density of the melt depends on temperature, a mass compensation is needed to conserve the total melt mass. The flow-stop-mass-compensation functionality applies appropriate mass and energy sources to compensate for the unphysical mass change in stopped cells and maintains the total mass of each phase.

Casting trials using a simple test geometry

For the validation of the numerical approach, a simple rectangular plate of variable thickness was cast at the Foundry Institute of the RWTH Aachen. The geometry of the test case was designed to test numerical optimization of die cooling and the gating system. Both cooling channels and the main part of the gating system can be changed by additive manufacturing. Results from this optimization are not the topic of this work and will be published elsewhere. Here, we focus on flow pattern and air entrainment prediction in the geometry.
Fig. 1 shows the geometry used for the setup. The left-hand figure shows the entire geometry including part, gating system, dies, cooling channels and shot sleeve, while the right-hand figure only shows the melt region, including the runner, two plates, venting channels and overflow.

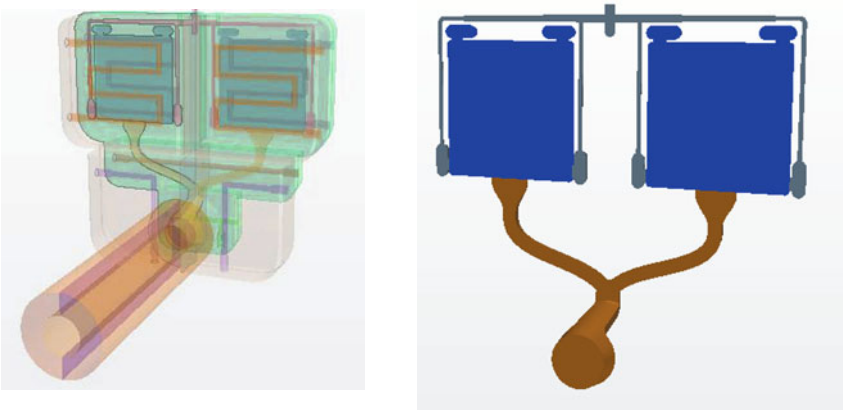

Figure 1: Geometry of the test case (left) with dies and shot sleeve; and on the right only the cavity which will be filled by melt.

The casting trials were performed on a high pressure die casting machine, Bühler H-630 SC, with a locking force of 7250 KN and a piston chamber length of 580 mm. Fig. 2 shows a photograph of one of the plates (left) and a computer tomography analysis of possible porosity (right). Both are taken from a casting of AlSi9 alloy at a casting temperature of 720 °C and a die

temperature of 250 °C, a piston filling speed of 0.74 m/s and an intesification pressure of 600 bar. From the surface roughness of the plate it can be deduced that two flow vortices form during filling (see Fig. 2, left) which result in a slight porosity at the center of the vortex (see Fig. 2, right).

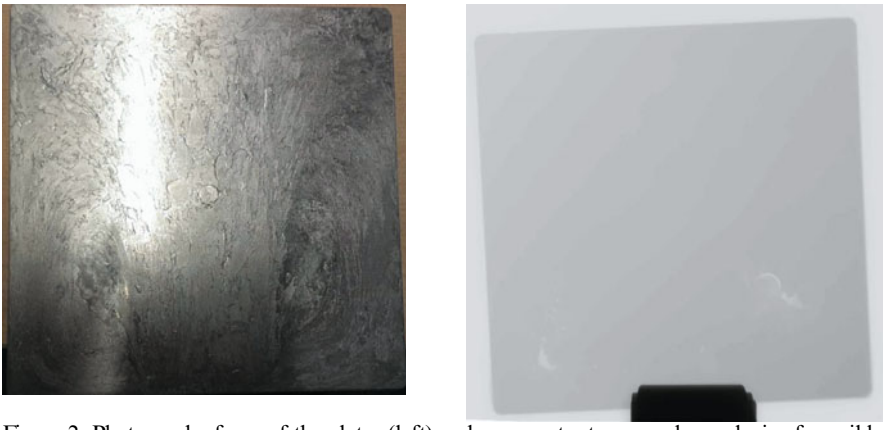

Figure 2: Photograph of one of the plates (left) and a computer tomography analysis of possible porosity (right).

Simulation results

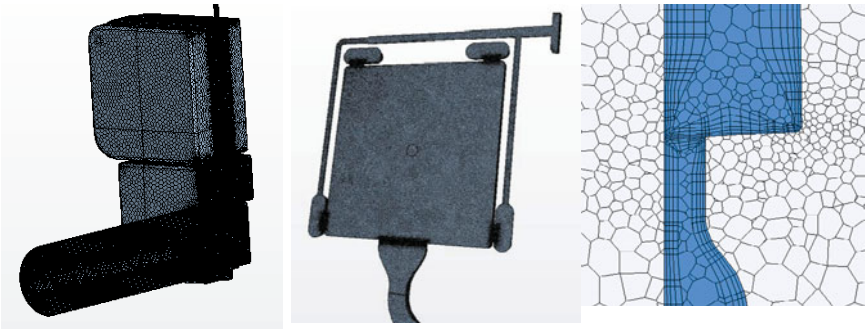

Figure 3: Mesh of the half geometry (left), a cut through dies and cavity (middle) and the prism layer in the melt region (right). The cavity mesh has approx. 900,000 cells.

Simulation setup

To accurately predict misruns, a fine mesh of the casting geometry is mandatory. A polyhedral mesh with prism layers at the surface of the melt region was used here. Even in thin regions a minimum of 7 cells was realized with this technology. Fig. 3 shows the mesh of the half geometry (left), a cut through dies and cavity (middle) and the prism layer in the melt region

(right). The material data of the AlSi9 alloy are from the STAR-Cast database. The simulation starts after the melt fills the piston chamber, with mold filling according to the shot curve of the experiment. The initial temperatures of the melt were set to 700 °C so as to take account of a cooling of the melt in the casting trial from the 720 °C pouring temperature before the plunger movement begins. The initial mold temperature is set to 250 °C, and initial pressure as well as the ambient pressure is at 1 bar. A heat transfer coefficient of 10000 W/m^{2}K is assumed between melt and die.

Optimized plunger movement

An important source of air entrainment is air from the slot sleeve entering the mold. To minimize the entrained air from the shot sleeve, the plunger must be moved in such a way that the shot sleeve is completely filled with melt without any wave braking or other splashing, which entrains air into the melt. Fig. 4 shows the amount of entrained air for a fast initial plunger movement and an optimized movement. Clearly, the optimized plunger movement significantly reduces the amount of entrained air. Details of the optimization will be published separately.

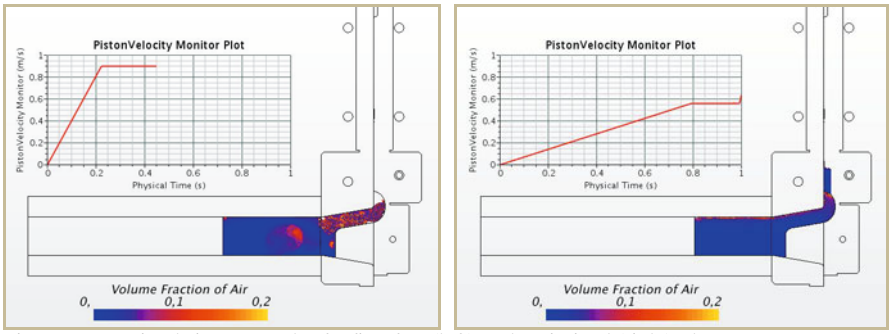

Figure 4: Entrained air as a result of a first fast (left) and optimized (right) plunger movement

Flow pattern and air entrainment prediction

Fig. 5 shows the developing flow pattern in the left plate. The top plots show the temperature on the melt, the bottom plots the velocity field. Two vortices form with an empty spot in the center of each vortex, which fills last. As Fig. 6 demonstrates, entrained air remains after filling at the center of the vortices. The air-entrained regions are not symmetrically placed: the position in the outer left vortex is lower than the position in the inner right vortex. Flow pattern and position of the vortex center with slight air entrainment agree well to experimental findings (Fig. 6 right and Fig. 2)

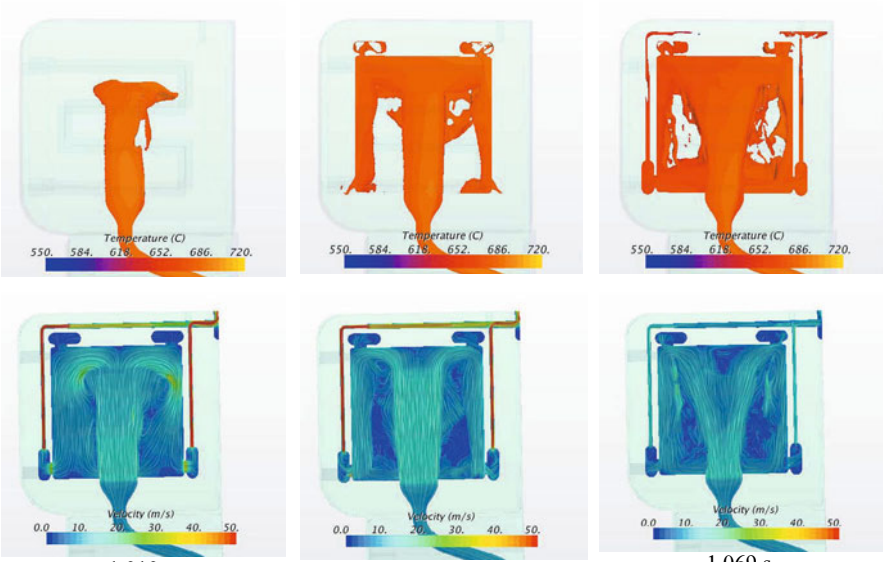

1.010 s 1.034 s 1.069 s

Figure 5: Developing flow pattern during the filling of the plates: Temperature on the mold and velocity distribution are plotted for 3 different time (1.010 s, 1.034 s, and 1.069 s from left to tight).

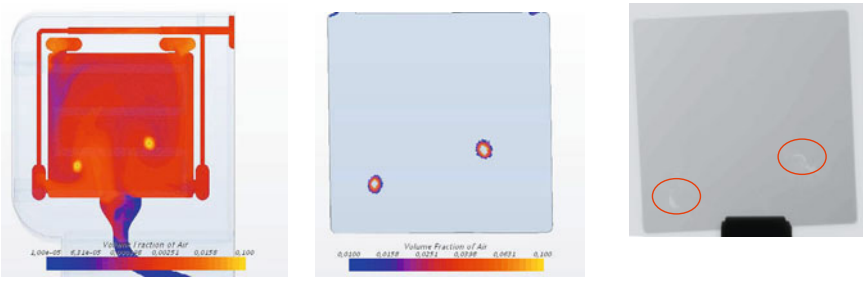

Figure 6: Entrained air after complete filling (volume fraction air) (left) and region with an air volume above 1 % (middle) compared to the experimental findings.

Remaining air in an industrial application

The industrial significance of the simulation approach described, which correctly considers the air as compressible gas, was demonstrated using a geometrically more complex industrial application. Fig. 7 (left) shows the geometry (application and industrial partner cannot be named). The impact of the pouring temperature on the amount of remaining air was investigated. As Fig. 7 (middle and right) demonstrates, a reduction of the casting temperature leads to a significant increase of the amount of entrained air. At the reduced pouring temperature, the melt enters the cavity at a temperature close to the liquidus temperature, and solidification occurs too fast to allow the entrained air to escape the cavity due to buoyancy.

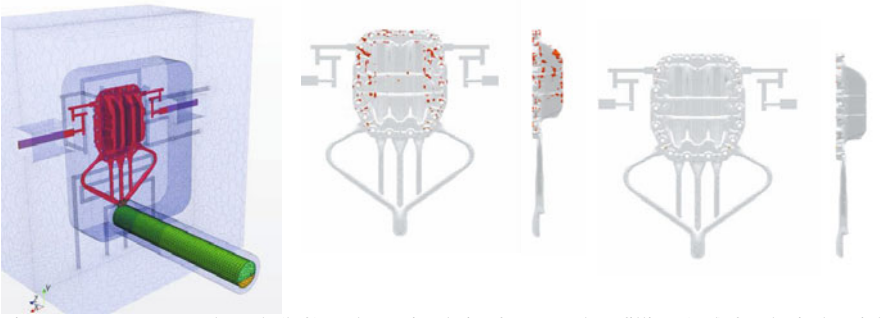

Figure 7: Geometry and mesh (left) and entrained air after complete filling (red) for the industrial application using an initial casting temperature of 640 °C (middle) and 680°C (right).

Conclusion and Summary

A new approach to simulating HPDCs, which correctly considers both phases, melt and air, as compressible media, is presented. This approach enables a detailed analysis of the entrainment of air in the casting. Demonstration of a successful optimization of the plunger movement is followed by a comparison of experimental findings of air entrainments with the simulation results for a simple test geometry. Good agreement between casting trial and simulation in terms of flow pattern and entrained air position was found. Finally, the approach was applied to an industrial application to demonstrate the applicability to complex geometries. The simulation demonstrates the expected increase in entrained air with reduced melt temperature.
Currently the approach is being extended to predict misruns and cold shots in HPDC applications.

Acknowledgement

The authors gratefully acknowledge the fruitful discussions with Santhanu Jana and Emir Subasic. The experimental work was supported by the German Research Foundation (DFG) and the authors would like to thank the German Research Foundation DFG for the kind support within the Cluster of Excellence "Integrative Production Technology for High Wage Countries".

CFD Modeling and Simulation in Materials Processing 2016
Edited by: Laurentiu Nastac, Lifeng Zhang, Brian G. Thomas, Miaoyong Zhu, Andreas Ludwig, Adrian S. Sabau, Koulis Pericleous, and Hervé Combeau
TMS (The Minerals, Metals & Materials Society), 2016

NUMERICAL SIMULATION OF THE MULTIPHASE FLOW IN THE SINGLE-TUNDISH SYSTEM

Shupei Liu, Bo Wang*, Zhiliang Yang, Shuai Feng, Kongfang Feng, Jinyin Xie, Jieyu Zhang
State Key Laboratory of Advanced Special Steel, School of Materials Science and Engineering, Shanghai University, Shanghai 200072, China
Keywords: Tundish, Flow control devices, Blowing, Numerical simulation

Abstract

The continuous casting tundish has evolved into a useful reactor for liquid steel refining. The appreciate flow control devices such as dam, turbulence inhibitor and gas blowing, helps to modify the pattern and minimize short circuiting and dead zone. In this paper, a commercial computational fluid dynamics (CFD) package FLUENT was used to predict the flow field under steady state in one-strand tundish. The effects of flow control devices, gas bottom-blowing flow rate on flow field and residence time distribution (RTD) were studied. The results show that the molten steel flow state in optimized tundish has been improved significantly. When the gas blowing position was 1950mm from inlet axis and argon flow rate was 0.3m^3/h, the average residence time of molten steel in the tundish was prolonged. And the volume fraction of dead zone in the tundish was reduced from 28.6% to 13.3%.

Introduction

The tundish in continuous casting operation is an important link between ladle (a batch vessel) and casting mould (a continuous operation). With the development of the continuous casting technology, there is a simple tundish excessive container storage and distribution of molten steel metallurgical reactor has developed into a number of functions for liquid steel refining. Thus a modern steelmaking tundish is designed to provide greatest opportunity for carrying out varieties metallurgical operations such as alloy trimming of steel, inclusion removal, calcium doped inclusion modification, superheat control, thermal and particulate homogenization, etc.[1].

Modern equipments include steel making furnaces and secondary metallurgy units form a compact and efficient production process. The increasing quality requirements in the steel industry causes that the new technological solution are still in exploration. The current state of this technology allows to cast a liquid steel into semi-finished products. However, it requires, the high quality of liquid steel introduced to the mould. The main role of the tundish is a distribution function [2]. The final metallurgical treatments are also performed in this unit.

Shaping the conditions of the process, we can acknowledge the effects of spontaneous phenomena during separation and inclusions flotation. For this purpose, the different fitting of tundish workspace (including dams, weirs and turbulence inhibitor) are used. It was known that the shape and placement of flow control devices in the workspace always affects the hydrodynamic and thermal conditions in the ladle [3, 4]. In recent years, the role of the tundish gas curtain technology in ultra-clean steel production caused widespread concern among metallurgy reserchers. That is the bubbling of argon gas from the tundish bottom in order to enhance the tundish capability to float out inclusions. Tundish blowing inert gas, to

form a channel air bag curtain, changes the flow field in the middle package. Bubbles rising during the capture of inclusions and improve the removal of inclusions in molten steel plays an important role in the purification. Yamanaka et al. [5] investigated the tundish using argon bubbling through porous plugs. They claimed 50% improvement in the removal of inclusions in the 50 to 100 m range. But in the middle of the bottom of the inflatable bag technology, the control parameters of blowing molten steel to improve the flow characteristics, the effect of inclusion removal study in depth is not detailed enough.

In this paper, using Eulerian-Eulerian the liquid-gas flow model, RTD and curves were numerically calculated. Exploration in the same locations with different flow rates of the flow behavior of the molten steel in the tundish, specifically identify reasonable argon gas flow rates and choose the best process parameters to improve tundish flow pattern of molten steel to improve the cleanliness of molten steel, so as to improve the slab quality.

Mathematical Modeling

The flow produced in a single-strand steelmaking tundish by an immersioned liquid steel stream is simulated. The single-strand tundish is equipped with an impact pad located at the bottom of the inlet shroud that is immersed in the liquid metal. Pouring liquid steel in the tundish through submerged shroud produces high turbulence intensity around the pouring point. To circumvent this, the tundish inner bottom wall is mounted with an impact pad placed below the ladle pouring point. The dimensions and the operating parameters of the tundish are summarized in table I.

Table I. Tundish design and operating parameters

Parameter	Value
Liquid steel level/mm	720
Tundish bottom length/mm	3755
Tundish bottom width/mm	620
Strand outlet diameter/mm	65
Shroud diameter/mm	105
Submergence depth of the shroud/mm	300
Volumetric flow rate, m^3/h	1.5, 0.9, 0.3

(a) Fluid and Turbulence Model

The bubbly flow was simulated using an Eulerian–Eulerian model [6] where steel liquid was considered as the primary phase and argon as the secondary one. The mathematical model is based on the assumptions of continuum suppose that demands the mean free path within the permissible limits [7]. Fluid is assumed as incompressible, Newtonian fluid to follow Boussinesq's approximation in density variation. The turbulence kinetic energy and intensity are assumed to be in equilibrium with the fluid flow and liquid state enthalpy. The governing equations are well addressed in the literatures [6, 8, 9].

(b) Tracer Dispersion Equation

Plotting of the RTD curve was possible by using a virtual tracer and introducing it to the numerical tundish model. In the presence of three dimensional velocity field u, v, and w with

no generation, the conservation of an added tracer concentration, C (kg/m^3), expressed in terms of the Cartesian coordinates. Tracer mass transfer equation shown as below:

$$(\frac{\partial C}{\partial t} + \nabla \bullet (U_C)) = \nabla \bullet ((\rho D_C + \frac{\mu_t}{Sc_t})\nabla \bullet (\frac{C}{\rho})) + S_C \quad (1)$$

In this equation, ρisthe density of mixed fluid, kg/m^3; i.e., mass per unit volume of tracer, kg/m^3; S_c, the volume of the source phase, is the remaining number of mass per unit time per unit volume of tracer, kg/(m^3•s); D_c, the tracer diffusion coefficient, in this paper takes 1.1 × 10^{-8} m^2/s; μ_t is the turbulent viscosity of molten steel, kg/(m•s); Sc_t is the tracer of turbulent Schmielt quasi number, The values used in the article is 0.9.

(c) Boundary conditions

All the equations were calculated simultaneously by commercial software FLUENT. Suitable boundary conditions for momentum transfer at all solid surfaces, including walls and bottom of the tundish, surfaces of impact pad, were those of non-slipping. The interface of slag and molten steel is considered as free surface. Normal gradients were imposed at all variables were all set to zero.

$$\frac{\partial u}{\partial z} = \frac{\partial v}{\partial z} = \frac{\partial k}{\partial z} = \frac{\partial \varepsilon}{\partial z} = w = 0 \quad (2)$$

Similar boundary conditions were established for turbulent kinetic energy and its dissipation rate. At the shroud exit, the mean velocity was assumed to be uniform though its cross section, and the other two perpendicular velocities were assumed to be zero. The turbulent kinetic energy and its dissipation rate were assumed to be uniform. At outlets, a pressure boundary condition was adopted. The density and viscosity of molten steel were assumed as constants: 6940 kg/m^3 and 0.06239 Pa·s.

At the gas inlet, the gas injection superficial velocity was specified from the gas flow rate, and the liquid volume fraction was set as zero. The density and viscosity of hot argon gas were assumed as constants: 0.342 kg/m^3 and 5.741×10^{-5} Pa·s.

Results and Discussion

The numerical simulations were carried out mainly for three cases: a bare tundish, a tundish using flow control devices and argon blowing at tundish bottom.

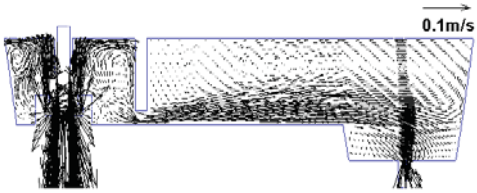

(a) Y=0

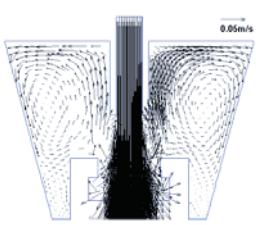

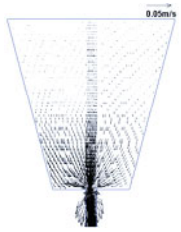

(b) X=-1.4815 (c) X=1.3765

Figure 1. Predicted velocity field in one half of the one strand bare tundish of:(a) longitudinal vertical at Y=0, (b) transverse vertical plane at X=-1.4815 and (c) transverse vertical plane at X=1.3765.

Figure 1(a), (b)and (c) show the predicted flow field in half of the one strand bare tundish system which represent the velocity field in XZ plane (central longitudinal vertical plane) at Y=0 and in YZ plane (central transverse vertical plane) at X=-1.4815(inlet stream) and X=1.3765(outflow stream), respectively. It can be clearly seen that molten steel from a high velocity and the impact of the ladle to the turbulence control device, a strong turbulence is controlled within the turbulent flow controller, high-speed flow of molten steel in the well mixed turbulent controller conducive inclusions grow collision. The bare tundishes were associated with considerable short circuiting, large dead volumes significant turbulence. Thus, which are potentially detrimental to the floatation of nonmetallic inclusions, so we should further optimize the tundish.

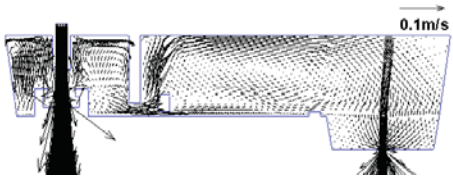

(a) Y=0

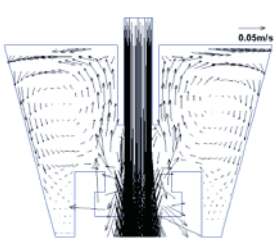

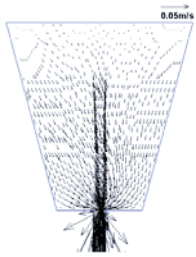

(b) X=-1.4815 (c) X=1.3765

Figure 2. Predicted velocity field in one half of the one strand tundish under weir dam control of:(a) longitudinal vertical at Y=0, (b) transverse vertical plane at X=-1.4815 and (c) transverse vertical plane at X=1.3765.

Figure 2(a), (b) and (c) show the predicted flow field in one half of the one strand with dam tundish system which represent the velocity field in XZ plane (central longitudinal vertical plane) at Y=0 and in YZ plane (central transverse vertical plane) at X=-1.4815(inlet stream) and X=1.3765(outflow stream), respectively. In order to eliminate short-circuit current and change the flow pattern of the tundish, retaining wall with deflector holes and double dams were setted in the tundish, which the low dam is seted behind the high dam and the top of low dam flush with the top of hole in the high dam. Such, which can eliminate short-circuit current, molten steel flow diversion hole according to the desired direction over the hole. It can be seen that the dam force the fluid of inlet stream to move towards free surface before transferred to the downstream side of the dam in the tundish, which can extend the mean residence time of molten steel and promote inclusion floating in the tundish, numerous studies show, by providing flow control means only removal of more than 50 m above inclusions effective, can't meet the requirements of high purity steel.

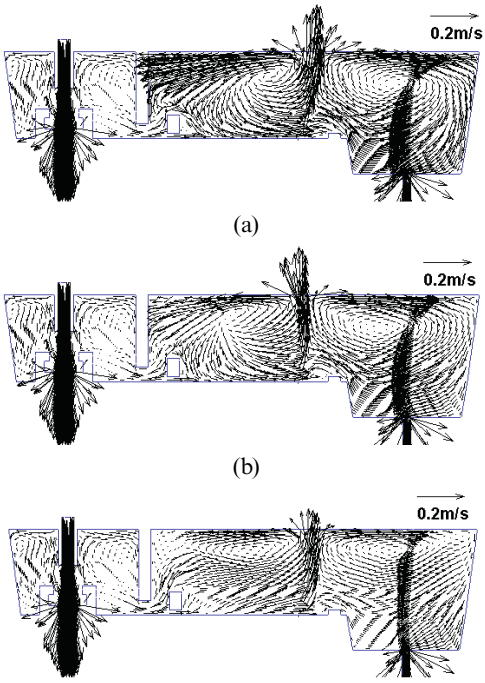

Figure 3. Predicted velocity field in half of the one strand tundish under different blowing rates (center section): (a) 1.5 m^3/h, (b) 0.9 m^3/h and (c) 0.3 m^3/h.

Figure 3 corresponds to tundish with gas bottom blowing, which the gas flow rate: (a)1.5 m^3/h, (b) 0.9 m^3/h and (c) 0.3 m^3/h, the gas blowing position is 1950 mm from inlet axis. The vector field of liquid steel flow were further changed after installing and activating the gas permeable barrier in the tundish also caused a steel circulation on both sides of the barrier, and a heavy mixing with high turbulence in the inject zone and has no obvious difference for these cases. The application of the gas injection system also cause an increase in liquid steel velocity, particularly in the region immediately adjacent to the gas permeable barrier. When gas was blowing from the bottom of tundish, the molten steel flow patter changes obviously, two backflows at each side of gas bubbles curtain are formed. One proceeds towards the inlet streams from the dam while another advances opposite and away from the inlet.

With higher flow rates of gas the large amount of bubbles ascending increased, and strong upward velocity of the molten steel flow is relatively large, increasing the turbulence of molten steel and promoting a higher stirring. Such, do not only reduces the effect of the capture of inclusions, and can easily lead to the floating steel which can result in slag entrapped into the steel, the molten steel secondary contamination, so level fluctuations are worse than the gas mainly exits the top surface. At the gas flow rate is 0.3 m^3/h that gas curtain were adopted can result in an decrease in liquid steel flow velocity, the reversed flow

are formed on both sides of the curtain which can decrease the dead volume regions and improve inclusions collision and rising, the steady upward flow are formed in the casting region which can prolong the residence time of the fluid in the tundish and improve the removal of inclusions.

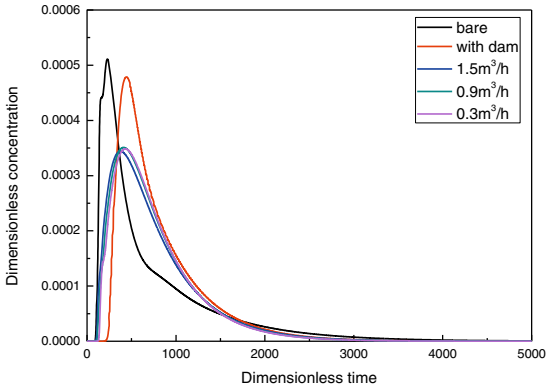

Figure 4. Residence time distribution in half of the one strand tundish under without gas bubbling and different blowing rates (center section): (a) 1.5 m^3/h, (b) 0.9 m^3/h and (c) 0.3 m^3/h.

Figure 4 shows the RTD curves for the tundish with different flow control devices. Analysis of RTD curves was shown in Table II. It is known that all the C curves in Figure 4 and Table II can be seen to be similar in their respective nature of variation. Though the average time (t_{av}) are much higher without gas bubbling and with dam compared to gas bubbling, the plug volume fraction was lower. In addition, we can see that with the blowing flow rates decreased, the average time were much higher, The volume fraction of dead zone in the tundish was reduced from 28.6% to 13.3% when the blowing flow rate is 0.3 m^3/h.

Table II. Analysis of RTD curves shown in figure 4

Tundish configuration	t_{min}, s	t_{peak}, s	t_{av}	V_p/V, %	V_d/V, %	V_m/V, %
Bare	153	229	781	20.2	28.6	51.2
With dam	306	445	819	22.0	14.9	63.1
1.5m^3/h	228	378	765	30.0	15.8	54.2
0.9m^3/h	250	412	762	33.0	13.9	53.1
0.3m^3/h	268	432	768	35.4	13.3	51.3

Conclusions

Numerical simulation and optimization of flow field in tundish were studied based on finite element analysis software. The results indicate that setting flow control devices can obviously improve flow situation of molten steel, and can enhance quality of continuous cast strand.

(1) With gas bottom-blowing in the tundish, the average residence time of molten steel in the tundish prolonged and the dead volume fraction decreased.

(2) Flow field were modefied for different gas flow rates: (a) 1.5 m^3/h, (b) 0.9 m^3/h and (c) 0.3 m^3/h. Based on the results, gas curtain were more available for controlling the flow pattern when the gas flow rate was 0.3 m^3/h. The volume fraction of dead zone in the tundish was reduced from 28.6% to 13.3%.

Acknowledgements

The authors gratefully thank the financial support received from Shanghai economic and information technology committee (CXY-2013-1).

References

1. Kumar A, Mazumdar D, Koria S C, “Modeling of fluid flow and residence time distribution in a four-strand tundish for enhancing inclusion removal,” ISIJ international, 48(2008), 38-47.

2. A. Kumar, S. C. Koria and D. Mazumdar, “An assessment of fluid flow modelling and residence time distribution phenomena in steelmaking tundish systems,” ISIJ international, 44(2004), 1334-1341.

3. Mazumdar D, Yamanoglu G, Guthrie R I L, “Hydrodynamic performance of steelmaking tundish systems: a comparative study of three different tundish designs,” Steel research, 68(1997), 293-300.

4. Lopez-Ramirez S, Morales R D, Serrano J A R, “Numerical simulation of the effects of buoyancy forces and flow control devices on fluid flow and heat transfer phenomena of liquid steel in a tundish ,” Numerical Heat Transfer: Part A: Applications, 37(2000), 69-85.

5. Yamanaka H, “Effect of Argon Bubbling in Tundish on Removal of Non-Metallic Inclusion in Slab,” Tetsu to Hagane, 69(1983), 213-230.

6. Reeks M W, “On the dispersion of small particles suspended in an isotropic turbulent fluid ,” Journal of fluid mechanics, 83(1977), 529-546.

7. Abbott M B, Basco D R, “Computational fluid dynamics-An introduction for engineers,” NASA STI/Recon Technical Report A, 90(1989), 51377.

8. Launder B E, Spalding D B, “The numerical computation of turbulent flows,” Computer methods in applied mechanics and engineering, 3(1974): 269-289.

9. Garcia-Hernandez S, Morales R D, Barreto J J, et al, “Numerical Optimization of Nozzle Ports to Improve the Fluidynamics by Controlling Backflow in a Continuous Casting Slab Mold,” ISIJ international, 53(2013): 1794-1802.

CFD Modeling and Simulation in Materials Processing 2016
Edited by: Laurentiu Nastac, Lifeng Zhang, Brian G. Thomas, Miaoyong Zhu, Andreas Ludwig, Adrian S. Sabau, Koulis Pericleous, and Hervé Combeau
TMS (The Minerals, Metals & Materials Society), 2016

CFD ANALYSIS OF BLAST FURNACE OPERATING CONDITION IMPACTS ON OPERATIONAL EFFICIENCY

Tyamo Okosun, Armin K. Silaen, Guangwu Tang, Bin Wu, and Chenn Q. Zhou

Center for Innovation through Visualization and Simulation
Purdue University Calumet
2200 169th Street
Hammond, IN 46323

Keywords: CFD, Blast Furnace, Combustion, Reacting Flow, Performance Optimization

Abstract

Blast furnaces are counter-current chemical reactors used to reduce iron ore into liquid iron. Hot reduction gases are blasted through a burden consisting of iron ore pellets, slag, flux, and coke. The chemical reactions that occur through the furnace reduce the iron ore pellets into liquid iron as they descend through the furnace. Experimental studies and live operation measurements can be extremely difficult to perform on a blast furnace due to the extremely harsh environment generated by the operational process. Computational Fluid Dynamics (CFD) modeling has been developed and applied to simulate the complex multiphase reacting flow inside a blast furnace shaft. The model is able to predict the burden distribution pattern, Cohesive Zone (CZ) shape, gas reduction utilization, coke rate, and other operational conditions. This paper details the application of this model to investigate the effects of coke size and porosity, iron ore pellet size, and burden descent speed on blast furnace efficiency.

Introduction

The efficiency of a blast furnace can be impacted by several factors. Significantly, the fuel required to operate the furnace at a given production rate of liquid iron can be influenced by the particle size and porosity of the coke charged into the furnace burden and the rate at which the burden descends through the furnace. In order to reduce operational costs, a considerable amount of effort has been made to reduce the coke rate of blast furnaces. A popular method currently in application is coke replacement by injected fuels, such as pulversized coal and natural gas. As injection rates rise to higher levels, it becomes crucial to attain an understanding of the physical phenomena occuring inside the blast furnace shaft. This understanding provides operaters with the ability to optimize the replacement of coke with injected fuels and maintain maximum cost efficiency [1, 2].

Iron ore and coke particles charged into the blast furnace experience gas-solid reactions as they descend through the shaft. The coke solution loss reaction in the shaft of a blast furnace under fixed tuyere operating condtions is the primary determinant of the coke rate. The solution loss can also be characterized as the degree of direct FeO reduction from the coupled reaction of FeO reduction and coke gasification. Because of this coupling, the reaction kinetics of iron ore and coke are interconnected and impact each other as well as the gas flow, thermal conditions, and overall conditions in the blast furnace.

A previous study examined the impacts of iron ore and coke reducibility on the operation of a blast furnace, finding that increased ore reducibility and low coke reactivity corresponded to decreases in furnace coke rate [3]. In order to manage the reactivity of coke, an examination of coke particle properties is necessary. In general, the size and quality of coke particles charged into blast furnaces are well controlled. However, variations in particle size can occur both unintentionally and intentiontally, leading to varied reduction rates and operating conditions inside the furnace shaft. Given the variety of operating conditions that can occur with increased fuel injection rates below the furnace shaft, it also becomes important to consider the rate at which the burden descends through the shaft. Variations in descent speed lead to radically different burden distributions which can greatly impact flow patterns and, by extension, reaction rates through the furnace shaft.

The research detailed in this paper explores the impacts of coke particle size, ore particle size, coke bed porosity, and burden descent speed on the operation of a blast furnace. An in-house CFD model was utilized to simulate the furnace at various operating conditions for this investigation. Results obtained from this study could provide guidance for the improvement of blast furnace efficiency, reduction of coke consumption, and decreases in CO_2 emissions.

CFD Model

A previously developed in-house CFD code, the blast furnace shaft simulator, was utilitzed to model gas flow and reaction phenomena inside the furnace [3]. The chemical reactions included in this model are detailed in previous publications [4]. The single interface unreacted shrinking core (URC) model is applied to represent iron ore reduction in this CFD simulation [5]. The complex process of iron ore reduction has been simplified to three rate control processes, namely, gas film resistance, diffusion resistance through the reduced iron shell, and intrinsic chemical reaction resistance at the metal-oxide interface. The expression for the reaction rate for one ore particle is expressed as Eq. 1.

$$R_i = \frac{4\pi r_0^2 (C_A - \frac{C_B}{K_{e,i}}) \times \frac{K_{e,i}}{(1+K_{e,i})}}{F + B_i + A_i} \quad (\frac{mol\ CO}{s}) \quad , i = 1 - 6 \qquad \text{Eq. 1}$$

Where the gas film resistance is: $F = \frac{1}{\beta_A} (\frac{s}{m})$, the diffusion resistance is:

$$B_i = \frac{r_0}{D_{e,i}} \times [(1 - f_i)^{-\frac{1}{3}} - 1] \ (\frac{s}{m}), \qquad \text{Eq. 2}$$

the intrinsic chemical reaction resistance is:

$$A_i = \frac{1}{k_i} \times (1 - f_i)^{-2/3} \times \frac{K_{e,i}}{(1+K_{e,i})} (\frac{s}{m}), \qquad \text{Eq. 3}$$

and the fraction of reduction f_i is defined as:

$$f_i = \frac{weight\ of\ oxygen\ removed\ from\ iron\ oxide}{weight\ of\ removable\ oxygen}, \qquad \text{Eq. 4}$$

r_0 is the radius of the iron ore, and the effective diffusivity is: $D_{e,i} = D_o \frac{\varepsilon_i}{\tau}$.

The porosities for each layer are [5]:

$$\varepsilon_{HM} = 0.008 + 0.992\varepsilon_o \quad \text{Eq. 5}$$

$$\varepsilon_{MW} = 0.122 + 0.878\varepsilon_o \quad \text{Eq. 6}$$

$$\varepsilon_{WF} = 0.435 + 0.565\varepsilon_o \quad \text{Eq. 7}$$

Where ε_o is the original ore porosity, as charged into the furnace, before any reactions. The tortuosity τ, is assumed to be 2 and $K_{e,i}$ are the equilibrium constants [6]. For each reaction step, the kinetic constant is:

$$k_i = k_{i,o} exp(\frac{-E_i}{RT_s}). \quad \text{Eq. 8}$$

Values for the frequency factors and activation energies for reduction reactions are adopted from prevalent literature [6].

Reactions R7 and R8 represent the two primary reactions experienced by coke in the blast furnace shaft. The first order irreversible assumption is made for these reactions. The kinetic diffusion model was applied to simulate chemical reactions at the lump coke inner surface [7]. The reaction rate for a single coke particle is described by Eq. 9.

$$R_i = \frac{4}{3}\pi r_p^3 \rho_i' \eta_1 A \quad (\frac{kg\,C}{s}) \quad , i = 7,8 \quad \text{Eq. 9}$$

The intrinsic chemical reaction rate is:

$$A = \rho_p A_g k_i \frac{RT}{M_r} \quad \text{Eq. 10}$$

Where ρ_p is the apparent density of the coke, A_g is the specific internal surface area of a given coke particle (assumed to be constant during reactions), and M_r is the molecular weight of reactant gas.

The diffusion rate is expressed as:

$$B = \frac{D_e}{r_p^2} \quad \text{Eq. 11}$$

Where r_p is the radius of the coke particle and D_e is the effective diffusion coefficient in the coke pores. The Thiele modulus is defined as:

$$\Phi = \frac{reaction\ rate}{internal\ diffusion\ rate} = \sqrt{\frac{A}{B}} \quad \text{Eq. 11}$$

The effectiveness factor without the gas film mass transfer is $\frac{3}{\Phi^2}[\frac{\Phi}{\tanh(\Phi)} - 1]$. The modified effectiveness factor that includes gas film resistance is:

$$\eta_1 = \frac{\eta}{1 + \frac{\Phi}{3} \times \frac{\frac{1}{\tanh(\Phi)} - \frac{1}{\Phi}}{Bi}} \quad when\ \Phi \leq 100 \quad \text{Eq. 12}$$

and $\eta_1 = \frac{1}{\Phi}$ *when* $\Phi > 100$

Where Bi is the mass transfer Biot number [8].

The effects of CO on chemical reaction constants are defined for reaction R7 as [9]:

$$k_7 = \frac{k_{co_2}}{1 + k_{co} P_{co}}. \qquad \text{Eq. 13}$$

The effect of H_2 on k_8 is assumed to be negligible and has such, $k_8 = k_{H2O}$ for reaction R8 [10]. It is also assumed that there is no reaction of coke when its temperature is lower than 700 °C.

Reaction R9 (flux decomposition) depends heavily on the pressure at which the reaction occurs. Additionally, the URC model is applied to this reaction. Reaction R10 is assumed to reach an equilibrium point above 1273 K [11]. Above the lower boundary of the cohesive zone, the direct reduction of solid FeO takes place in two steps, via reactions R3 and R7 or reactions R6 and R8 [12]. Due to this, direct reduction of solid FeO is not explicitly simulated. However, it is implicitly covered by the gas-solid reactions R3, R7, R6 and R8. Additionally, below the cohesive zone, the reactivity of coke increases and there is no significant amount of either H_2O or CO_2 present [13].

Results

Operating conditions from a previous research project were utilitized to conduct all simulations in this study. Furance size, productivity, and injected fuel rates were obtained from previously published work. The baseline case used in this project was validated against industrial data in a previous study [4].

Effects of Coke Porosity

The initial coke bed porosity for the baseline case is 0.45. To investigate the effects of coke porosity on furnace operation, simulations were run at coke porosity values varying by ±10% and ±20%. As the coke porosity increases, gas flow experiences less resistance in the shaft. As a result, pressure drop over the furnace falls and reduction gases have a lower residence time in the shaft. These higher flow velocities result in more rapid coke consumption through gas reactions, which in turn leads to a higher coke rate and average top gas temperature as shown in the left side of Figure 1. The right side of Figure 1 shows that the top gas CO utilization decreases as the coke porosity increases. H_2 utilization is also inversely proportional to the coke bed porosity.

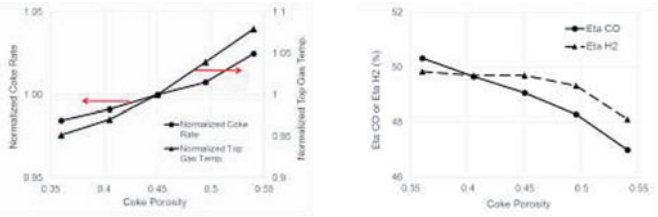

Figure 1. Coke rate and top gas average temperature vs. coke porosity (left) and CO and H_2 utilization vs. coke porosity (right)

The aforementioned variations in operating conditions at different coke bed porosities also result in a change in the shaft of the cohesive zone. As the coke bed porosity increases, the top of the cohesive zone rises, corresponding to the increased gas temperatures in the center of the furnace. The variation between cohesive zone shapes is shown in Figure 2.

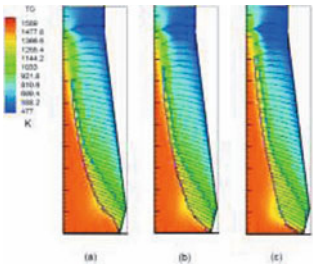

Figure 2. Contours of gas temperature for the -20% (a), baseline (b), and +20% (c) porosity cases. The cohesive zone is outlined in blue in each case.

Effects of Coke Particle Size

Coke particle size impacts furnace operation in a similar fashion. An increase in the size of coke particles leads to a higher void fraction in the coke bed. The left side of Figure 3 shows the effect of coke particles size on the coke rate and the top gas average temperature. In a similar vein to the results observed in the coke porosity cases, the coke rate and top gas average temperature both increase as the coke particle diameter increases. The top gas CO utilization falls as the coke particle diameter increases. However, the utilization of H_2 is inversely proportional to the particle size, as seen in Figure 3.

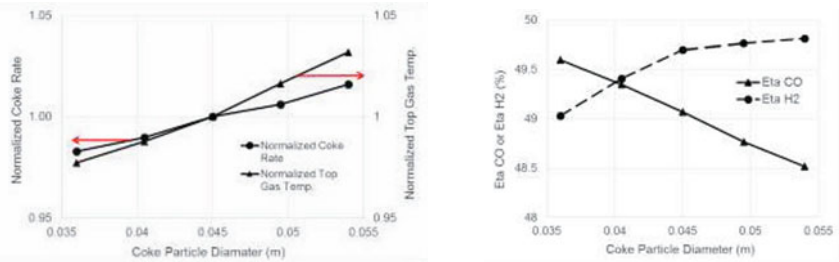

Figure 3. Coke rate and top gas average temperature vs. coke particle diameter (left) and CO and H_2 utilization vs. coke particle diameter (right)

Effects of Ore Particle Size

Iron ore particle size has a slightly different impact on the reactions inside the furnace shaft. Similar to the impact of coke particle size, an increase in ore particle size decreases the total porosity in the burden, allowing for higher velocity gas flow. However, as seen in Figure 4, the furnace coke rate remains relatively similar across all cases, while the top gas temperature experiences a steady decrease. Similar to the variation of coke particle size, increasing ore particle

size appears to have a negative impact on the utilization of CO and a slightly positive impact on the top gas H_2 utilization. This is likely due to the lower more rapid gas flow through the furnace bed as the particle size increases. Additionally, larger ore particles present a larger interfact at which reactions can occur.

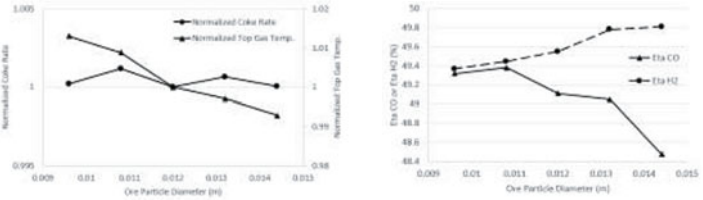

Figure 4. Coke rate and top gas average temperature vs. iron ore particle diameter (left) and CO and H_2 utilization vs. iron ore particle diameter (right)

Effects of Burden Descent Speed

The final parameter varied in this study was the burden descent speed. The rate at which burden descends through the furnace is dependent on the operating conditions below the furnace shaft. As such, it is not a direct input from furnace operators, but a burden that descends at differing speeds at along the furnace radius can lead to varied gas flow configurations and undesireable furnace operation. The burden descent speed parameter is defined as the ratio of the descent speed of the burden at the furnace center to the descent speed of the burner near the wall. Cases were run at descent speed ratios of 0.6, 0.7, 0.8 (baseline), 0.9, and 1.0. Figure 8 shows that as the rate of the descent speed is increased to 1, the coke rate reduces. As the descent speed ratio trends toward unity, the coke rate and top gas temperature decrease. Additionally, the pressure drop across the furnace increases as the ratio nears unity.

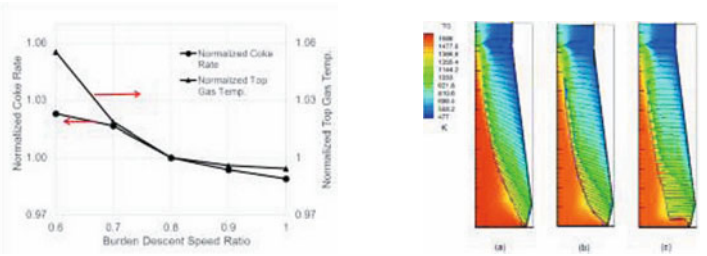

Figure 5. Coke rate and top gas average temperature vs. burden descending speed (left) and Contours of gas temperature for the 0.6 (a), baseline (b), and 1.0 (c) descent speed ratio cases (right).

The primary difference between these cases is the shape and location of the cohesive zone, shown by the blue outline in the right side of Figure 5. The radically different cohesive zones generated by varying the burden descent speed ratio change the flow patterns of gas through the packed bed of the furnace. The lower part of the cohesive zone becomes thicker as the burden descent speed ratio nears unity.

Table I details the coke rates and shaft pressure drops for each case simulated in the parametric study. In all the cases simulated, decreases in coke rate correspond to increases in the shaft pressure drop. In order to find an optimal operating condition for the furnace, both the pressure drop and the coke rate must be taken into account. Regardless of how much a given parameter can reduce the coke rate, if enough wind cannot be supplied to operate the furnace at the given conditions, it will be unfeasible as an optimization measure.

Table I. Tabulated results of comparative parametric studies

	Normalized Coke Rate	**Normalized Pressure Drop**
Coke Porosity		
-20%	0.984	1.328
-10%	0.991	1.174
Baseline (0.45)	1	1
+10%	1.007	0.892
+20%	1.025	0.764
Coke Particle Size		
0.036 m	0.983	1.174
0.041 m	0.99	1.062
Baseline (0.045 m)	1	1
0.05 m	1.006	0.965
0.054 m	1.016	0.946
Ore Particle Size		
0.0144 m	1	0.942
0.0132 m	1.001	0.976
Baseline (0.012 m)	1	1
0.0108 m	1.001	1.012
0.0096 m	1	1.022
Descent Speed Ratio		
0.6	1.023	0.965
0.7	1.017	0.988
Baseline (0.8)	1	1
0.9	0.994	1.1
1	0.989	1.135

Conclusions

The effects of coke particle size, coke bed porosity, and burden descent speed on blast furnace operation have been investigated. Coke porosity and coke particle size had, as expected, similar impacts on furnace. A 20% decrease in coke porosity resulted in a coke rate reduction of 1.6%, while a 20% increase in coke porosity resulted in a coke rate increase of 2.5%. Similarly, decreasing coke particle size resulted in up to a 1.7% coke rate reduction, while increasing the particle size resulted in a coke rate increase of 1.6%. Changing the ore particle size had little to no effect on the furnace coke rate in the ±20% range selected and presented only minor impacts on top gas temperature and pressure drop. Varying the burden descent speed ratio caused a significant change in the furnace coke rate, with a calculated coke rate reduction of 1.1%. It is important to note, however, that in all cases a reduction in the furnace coke rate corresponded to higher pressure drops (up to 33% more than baseline) over the furnace shaft. Because of this, it is necessary to take into account the wind rate that must be supplied by the blast if operation at conditions generating higher pressure drops is desired.

Acknowledgements

This research was supported by the American Iron and Steel Institute (AISI) and the U.S. Department of Energy (DOE) under Award No. DE-FG36-07GO17041. The authors would like to thank the support from the collaborators at ArcelorMittal-USA, ArcelorMittal-Dofasco, SeverStal, US Steel, US Steel - Stelco Inc., and Union Gas.

References

1. Y. H. Dang, S. M. Zhang, "Discussion on Low Fuel Rate and High PCI Rate of Blast Furnace Operation," *Iron and Steel*, 40 (2) (2005).
2. J. A. De Castro, H. Nogami, J. Yagi, "Numerical investigation of simultaneous injection of pulverized coal and natural gas with oxygen enrichment to the blast furnace," *ISIJ International*, 42 (11) (2005), 1203-1211.
3. D. Fu, Y. Chen, C. Q. Zhou, "Application of the Blast Furnace Shaft CFD Simulator," *Baosteel Academic Steel Conference 2013*, Shanghai, China, 10.
4. D. Fu, Y. Chen, C. Q. Zhou, "CFD Investigation of the Effects of Iron Ore Reducibility and Coke Reactivity on Blast Furnace Operation," *Proceedings of AISTech 2014*, Indianapolis, U.S.A., 9.
5. T. Murayama, Y. Ono, Y. Kawai, "Step-Wise Reduction of Hematite Pellets with CO-CO_2 Gas Mixtures," *Tetsu-to-Hagané*, 63 (7) (1977), 1099-1107.
6. Q. T. Tsay, W. H. Ray, J. Szekely, "The Modeling of Hematite Reduction with Hydrogen Plus Carbon Monoxide Mixtures: Part I. The Behavior of Single Pellets," *AIChE Journal*, 22 (6) (1976), 1064-1072.
7. The Iron and Steel Institute of Japan, *Blast Furnace Phenomena and Modelling* (New York, NY: Elsevier Applied Science Publishers LTD, 1987), 108-116.
8. J. B. Rawlings, J. G. Ekerdt, *Chemical Reactor Analysis and Design Fundamentals* (Madison, WI: Nob Hill Publishing, 2002).
9. S. Kobayashi, Y. Omori, "The Chemical Reaction Rate of the Solution Loss of Coke," *Tetsu-to-Hagané*, 63 (1977), 1081-1089
10. N. Miyasaka, N., S. Kondo, "The Rate of Cokes Gasification by Gas Consisting of CO_2, H_2O, CO, H_2, and N_2," *Tetsu-to-Hagané*, 54 (1968), 1427-1431.
11. H. Kokubu et al., "Effect of Humidified Blast on Blast Furnace Operation from the Viewpoint of the Softening and Melting Process of Ore Burdens," *Tetsu-to-Hagané*, 68 (15) (1982), 2338-2345.
12. W-K. Lu, "Chemical Reactions in the Blast Furnace as it Happens," *Proceedings of AISTECH 2004*, Volume I & II, 395-407.
13. G. Danloy, C. Stolz, "Shape and Position of the Cohesive Zone in a Blast Furnace," *Ironmaking Conference Proceedings*, 50 (1991), 395-407.
14. D. J. Harris, I. W. Smith, "Intrinsic Reactivity of Coke and Char to Carbon Dioxide, Steam, and Oxygen," *Twenty-Third Symposium (International) on Combustion*, 23 (1) (1991), 1185-1190.

CFD Modeling and Simulation in Materials Processing 2016

Microstructure Evolution

Session Chairs:
Hervé Combeau
Miaoyong Zhu

CFD Modeling and Simulation in Materials Processing 2016
Edited by: Laurentiu Nastac, Lifeng Zhang, Brian G. Thomas, Miaoyong Zhu, Andreas Ludwig, Adrian S. Sabau, Koulis Pericleous, and Hervé Combeau
TMS (The Minerals, Metals & Materials Society), 2016

VALIDATION OF A MODEL FOR THE COLUMNAR TO EQUIAXED TRANSITION WITH MELT CONVECTION

Mahdi Torabi Rad[1], Christoph Beckermann[1]

[1]Department of Mechanical and Industrial Engineering, The University of Iowa, 2402 SC, Iowa City, IA, 52242, USA

Keywords: Columnar-to-Equiaxed Transition, Melt Convection, Multi-phase/-scale Modeling, Recalescence, OpenFOAM

Abstract

Predicting the columnar-to-equiaxed transition (CET) in the grain structure of metal castings is still an important challenge in the field of solidification. One of the most important open questions is the role played by melt convection. A three-phase Eulerian volume-averaged model of the CET in the presence of melt convection is developed. The model is validated by performing simulations of a recent benchmark solidification experiment involving a Sn - 3 wt. pct. Pb alloy. The predicted cooling curves are found to be in a good agreement with the experimental measurements. After some adjustments to the grain nucleation parameters, the measured boundary between columnar and equiaxed grains is also well predicted.

Introduction

The transition from the elongated grains in the outer portions of a casting to more rounded ones in the center is called *columnar-to-equiaxed transition* (CET) [1]. Realistic modeling and simulation of the CET is still very challenging, because it requires one to simultaneously take into account numerous physical phenomenon at several length scales: heat/solute transfer, melt flow, nucleation of equiaxed grains, and growth of columnar and equiaxed grains into an undercooled melt.

In the past decade, there have been numerous modeling efforts to address this challenging problem. Most of these models are based on the pioneering work of Wang and Beckermann [2]. These authors developed a three-phase volume-averaged Eulerian solidification model, which accounts for phenomena such as: equiaxed dendritic growth, melt flow, micro-/macro-segregation, and transport of solid. Wang and Beckermann [3] and Martorano et al. [4] used a similar model to predict the CET in experimental castings. However, these efforts all neglected melt convection. Wu et al. [5] introduced a five-phase volume-averaged model for the CET in the presence of the melt convection. Their main motivation behind adding two additional phases was to more realistically incorporate the (columnar/equiaxed) dendrite morphology into the model. They have used this model to predict the CET in Al-Cu castings [6].

A benchmark solidification experiment, involving solidification of Sn-Pb alloys was performed by Hachani et al. [7, 8]. Carozzani et al. [9] simulated this experiment using a CAFÉ model. However, some discrepancies were observed between the measurements and the simulation results; especially, in the prediction of the recalescence and the boundary between the columnar and equiaxed grains. They attributed this to uncertainties in the nucleation law.

The main objective of the present study is to briefly introduce and, then, validate a three-phase Eulerian model for the CET in the presence of the melt convection. In the following, the equations of the model are shortly outlined for completeness. The model is then used to predict the cooling curves and the CET in the solidification benchmark experiment of Hachani et al. [4, 5].

The Multi-Phase/-Scale Model

The model we introduce here is a modified version of the model developed by Wang and Beckermann (WB) [2]. The model accounts for the CET in the presence of the melt convection by tracking the position of the columnar front. The solid is assumed to be stationary.

Conservation Equations

Energy Equation:

$$\frac{\partial T}{\partial t}+\nabla\cdot\left(g_l\overline{\boldsymbol{v}}_l T\right)=\alpha_0\nabla^2 T+\frac{h_{sl}}{c_0}\frac{\partial g_s}{\partial t} \tag{1}$$

where T is the temperature, g_l is the liquid fraction, $\overline{\boldsymbol{v}}_l$ is the average liquid velocity, α_0, h_{sl}, c_0 and $g_s\left(=1-g_l\right)$ are the thermal diffusivity, latent heat, specific heat and solid fraction, respectively.

Solute conservation equation for the solid:

$$g_s\frac{\partial\overline{C}_s}{\partial t}=\left(k_0\overline{C}_d-\overline{C}_s\right)\frac{\partial g_s}{\partial t} \tag{2}$$

where $\overline{C}_s$ and $\overline{C}_d$ are the average solute concentration in the solid and the inter-dendritic liquid, respectively, and k_0 is the partition coefficient.

Solute conservation equation for the inter-dendritic liquid:

$$\left(1-k_0\right)\overline{C}_d\frac{\partial g_s}{\partial t}=\left(1-g_s\right)\left(\frac{\partial\overline{C}_d}{\partial t}+\overline{\boldsymbol{v}}_l\cdot\nabla\overline{C}_d\right)+\frac{\partial}{\partial t}\left[g_e\left(\overline{C}_e-\overline{C}_d\right)\right]+\nabla\cdot\left[g_e\overline{\boldsymbol{v}}_l\left(\overline{C}_e-\overline{C}_d\right)\right] \tag{3}$$

where g_e is the extra-dendritic liquid fraction, and $\overline{C}_e$ is the average solute concentration in the extra-dendritic liquid.

Solute conservation equation for the extra-dendritic liquid:

$$g_e \frac{\partial \overline{C}_e}{\partial t} + \nabla \cdot \left(g_e \overline{\boldsymbol{v}}_l \overline{C}_e \right) = D_0 \nabla \cdot \left(g_e \nabla \overline{C}_e \right) + \left(\overline{C}_d - \overline{C}_e \right) \frac{\partial g_e}{\partial t} + \overline{C}_d \nabla \cdot \left(g_e \overline{\boldsymbol{v}}_l \right) + \frac{S_{ed} D_0}{l_{ed}} \left(\overline{C}_d - \overline{C}_e \right) \qquad (4)$$

where D_0 is the liquid mass diffusivity, S_{ed} is the interfacial area concentration, and l_{ed} is the diffusion length.

Mixture continuity and momentum conservation equations:

$$\nabla \cdot \left(g_l \overline{\boldsymbol{v}}_l \right) = 0 \qquad (5)$$

$$\frac{\partial}{\partial t} \left(g_l \overline{\boldsymbol{v}}_l \right) + \frac{1}{g_l} \nabla \cdot \left(g_l^2 \overline{\boldsymbol{v}}_l \overline{\boldsymbol{v}}_l \right) = -\frac{1}{\rho_0} g_l \nabla \overline{p} + \upsilon_0 \nabla^2 \left(g_l \overline{\boldsymbol{v}}_l \right) + \frac{\tilde{\rho}_l}{\rho_0} g_l \boldsymbol{g} - \frac{\upsilon_0}{K} g_l^2 \overline{\boldsymbol{v}}_l \qquad (6)$$

where ρ_0 is the reference density, $\overline{p}$ is the average pressure, υ_0 is the kinematic viscosity, $\tilde{\rho}_l$ is the liquid density, given by the Boussinesq approximation, i.e. $\tilde{\rho} = 1 - \beta_T \left(T - T_{ref} \right) - \beta_C \left(\overline{C}_e - C_{ref} \right)$, where, β_T and β_C are the thermal and solutal expansion coefficients, and T_{ref} and C_{ref} are the reference temperature and concentration, at which ρ_0 is determined; and K is the permeability of the mush, given by the Blake-Kozeny equation, i.e. $K = \lambda_2^2 g_l^3 \Big/ \left[180 \left(1 - g_l \right)^2 \right]$.

Supplementary Relations

Supplementary relations of the model are: 1) the liquidus line of the phase diagram [4], 2) an equation for the grain fraction [3], 3) the LGK growth model for the dendrite tip velocity [4], 4) a morphological equation for the interfacial area concentration [4], 5) an equation for the diffusion length [4], 6) the instantaneous nucleation law for the grain nucleation [4], and 7) an equation for tracking the columnar front. Due to space limitations, these models are not provided here.

Simulation of the Benchmark Solidification Experiment

Outline of the Experimental Conditions

Figure 1 shows the sketch of the experimental setup in Hachani et al. [7, 8]. The reader should consult these papers for more details on the experimental procedure. The corresponding material properties, boundary and initial conditions used in the present study are adopted from Carozzani et al. [9].

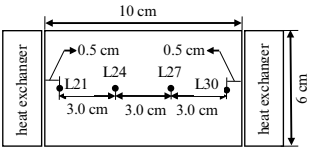

Figure 1. Sketch of the solidification benchmark experiment, performed by Hachani et al. [7, 8], along with the label and the location of the four thermocouples used in the present study to validate the present multi-phase/-scale model.

Numerical Simulations

We developed a parallel-computing in-house code on the OpenFOAM platform to solve the governing equations. In this section, we will only briefly introduce the interface-tracking algorithm that is required to solve these equations. The interested reader should contact the corresponding author for more numerical details.

Solving the equations of the model requires one to track the movement of the columnar front [4]. Here, we assume that these movements are perpendicular to the local isotherms; and then, the columnar front is tracked using the volume-of-fluid method (VOF) [10 and references therein].

Results and Discussion

Prediction of the Measured Cooling Curves

Figure 2 compares the measured cooling curves (empty squares) with the cooling curves predicted by the model (the blue lines) at four different locations shown if Figure 1. The overall agreement between the simulated and the measured temperatures is good.

The recalescence, recorded at position L21 in the experiment, is also well predicted by the model. This is shown in Figure 3, which is a close-up of the cooling curve in Figure 2 (a) around $t = 3500$ s. The grain/solid fractions (to be read from the right vertical axis) are shown by red lines. The liquidus temperature ($T_{liq} = 501.28$ K) and the nucleation temperature ($T_{nuc} = 498.3$ K) are shown by dotted lines. The liquidus temperature is taken from Carozzani et al. [9]; and the nucleation temperature is taken to be the minimum in the measured cooling curve before recalescence. The equiaxed grain density is $n = 10^6$ m^{-3}. We have chosen this value because it gives the best recalescence agreement with the experiment. Before the start of the solidification at this point, ($t < 3490$ s) there is an excellent agreement between the simulated and the measured temperatures. However, the predicted maximum recalescence temperature (=499.2 K) is 0.4 K lower than the measured one (=499.6 K). The reason for this under-prediction is not fully clear at this stage, but it might be because of the uncertainties in the equations used for the diffusion length, or the specific are concentrations. The authors are performing further investigations to clarify this. The outcome of these ongoing investigations will be used to improve the model for a better prediction of the recalescence temperature.

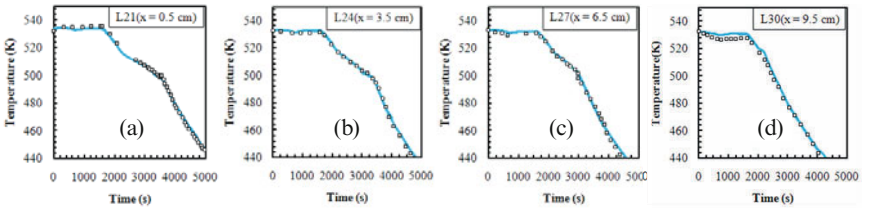

Figure 2. Comparison between the measured [7](symbols) and the simulated(blue lines) cooling curves for four different locations, shown in Figure 1: (a) x = 0.5 cm, (b) x = 3.5 cm, (c) x = 6.5 cm, (d) x = 9.5 cm. The distances are measured from the left boundary.

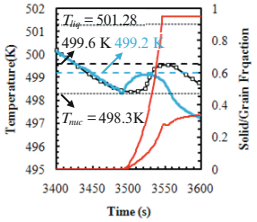

Figure 3. Close-up of the cooling curve shown in Figure 2(a), comparing the measured recalescence [7] (symbols) and the simulated recalescence (blue line), along with the solid/grain fractions (red lines, to be read from the right vertical axis). The dotted lines show the liquidus (501.3 K) and the nucleation (498.3 K) temperatures. The dashed lines indicate the measured (499.6 K) and simulated (499.2 K) recalescence temperatures.

Comparison with Model that Neglects Dendrite Tip Undercooling

Figure (4) compares the results of the model introduced in the present study (top row) with the results of a model that neglects dendrite tip undercooling and assumes Scheil type solidification. (bottom row). The reader is referred to Guo and Beckermann [11] for the equations of the latter model; for simplicity, this model is referred to in the following as the Scheil model. The red line in the top row is the columnar front. In the bottom row, this line is the mushy zone edge (i.e. isoline g_s = 0.001). The columns show the results at three different solidification stages. Next, we will compare the top and bottom rows of the figure to investigate the effect of tip undercooling.

At the early solidification stage (i.e. t = 2400 s), the predictions of the two models are shown in the first column of figure (4). Again, the contour plot at the top is the model presented here (which accounts for tip undercooling), and the contour plot at the bottom is the Scheil model (which does not account for the tip undercooling). The two contour plots are very similar. In both, the lead-rich heavier fluid moves downward along the solidification front, and generates a clock-wise rotating convection cell. In addition, the columnar front at the top is almost at the same position as the mushy zone edge at the bottom. These similarities indicate that the tip undercooling does not play a significant role at the early solidification stage.

At an intermediate solidification stage (i.e. t = 3500 s), the predictions of the two models are shown in the second column of figure (4). Close to the left wall, the two models have very different predictions: while the model introduced here predicts a solid-free zone over the left third of the cavity, the Scheil model predicts mush to present everywhere. The solid fraction patterns predicted by the two models over the right portion of the cavity are also somewhat different, with the Scheil model showing more pronounced channel segregates. These differences between the two models

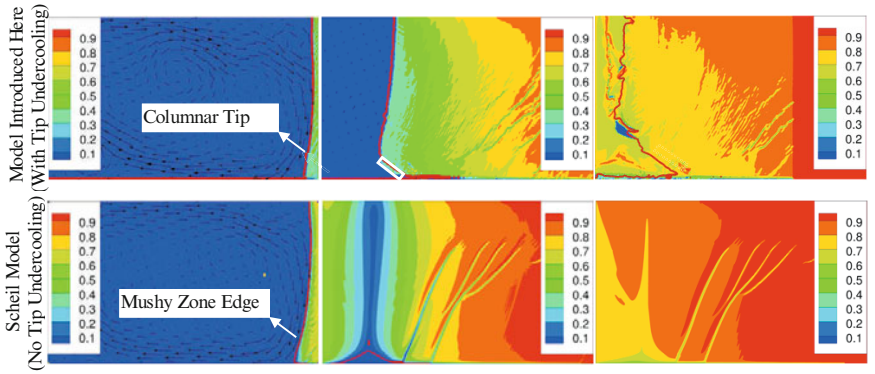

(a) $t = 2400$ s
Early Solidification Stage

(b) $t = 3500$ s
Middle Solidification Stage

(c) $t = 4000$ s
Late Solidification Stage

Figure 4(a-c). Comparison of the predictions of the model introduced in the present study (top row) with the Scheil solidification model (bottom row). Only the former one accounts for tip undercooling. The columns are, from the left: early, middle, and late solidification stages. The color is the solid fraction; and the black arrows are the flow velocity vectors. The red line in the top row is the columnar tip, and in the bottom row, it is the edge of the mushy zone (i.e. isoline $g_s = 0.001$). The inclined white box in the top middle contour shows the appearance of the first equiaxed grains in front of the columnar tip.

indicate that at the intermediate solidification stage, dendrite tip undercooling does play an import role.

At the late solidification stage (i.e. $t = 4000$ s), the predictions of the models are shown in the third column of figure (4). Close to the left wall, the Scheil model predicts slightly higher solid fractions, which can be attributed to this model predicting higher solid fractions at this location at earlier times. Other than this difference, the predictions of the two models are similar at the late solidification stage.

Prediction of the CET in the Presence of the Melt Convection

In figure (4), the contour plot in the second column of the top row indicates the location where the first equiaxed grains nucleate in front of the columnar tips (white box). These grains locally block the advance of the columnar tips. As solidification proceeds, more and more equiaxed grains nucleate ahead of the columnar front, until at t = 4000 s (third column), equiaxed grains are present everywhere to the left of the red contour line that indicates the columnar front. These equiaxed grains block the columnar front along its entire length, and the red contour line therefore indicates the location of the CET in the casting.

The preeicted CET line is superimposed on the mid-thickness grain structure observed in the experiment in Figure (5). The white line in the figure indicates the boundary between the columnar

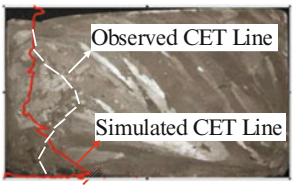

Figure 5. Simulated CET line (red) superimposed on the mid-thickness grain structure observed in the experiment [7]. The white line is an approximate indicator of the boundary observed between the columnar and the equiaxed grains in the grain structure.

and equiaxed grains observed in the experiment. It can be seen that the two lines are in reasonably good agreement. The reason for the slight disagreements at mid-height and at the bottom of the cavity are not entirely clear. The agreement can be expected to improve once the movement of equiaxed grains is accounted for in the model.

Conclusions

A three-phase Eulerian volume-averaged model for the CET in the presence of the melt convection is introduced. The model is validated by simulating the Sn - 3 wt. pct. Pb experiment of Hachani et al. [7]. The simulated cooling curves, including the recalescence at the location of one of the thermocouples, are in good agreement with the measurements. The results of the present model are compared with the results of a model where dendrite tip undercooling is neglected (Scheil model). The comparisons indicate that the role of tip undercooling is particularly noticeable at intermediate solidification stages. The position of the predicted CET contour is found to be in reasonably good agreement with the boundary between the equiaxed and columnar grains observed in the experiment. This agreement can be expected to improve once the movement of equiaxed grains is incorporated into the model.

References

1. J. A. Dantzig and M. Rappaz, *Solidification* (Lausanne, CRC Press, 2009), 430.

2. C.Y. Wang, and C. Beckermann, “Equiaxed Dendritic Solidification with Convection: Part I. Multiscale/Multiphase Modeling,” *Metallurgical and Materials Transactions A*, 27 (1996), 2754-2764.

3. C.Y. Wang, and C. Beckermann, “Prediction of Columnar to Equiaxed Transition during Diffusion-Controlled Dendritic Alloy Solidification,” *Metallurgical and Materials Transactions A*, 25 (1994), 1081-1093.

4. M.A. Martorano, C. Beckermann, and Ch.-A. Gandin, “A Solutal Interaction Mechanism for the Columnar-to-Equiaxed Transition in Alloy Solidification,” *Metallurgical and Materials Transactions A*, 34 (2003), 1657-1684.

5. M. Wu, A. Fjeld and A. Ludwig, "Modeling mixed columnar-equiaxed solidification with melt convection and grain sedimentation - Part I: Model description," *Computational Materials Science*, 50 (2010), 32-42.

6. M. Wu, A. Fjeld and A. Ludwig, "Modeling mixed columnar-equiaxed solidification with melt convection and grain sedimentation - Part II: Illustrative modeling results and parameter studies," *Computational Materials Science*, 50 (2010), 43-58.

7. L. Hachani, B. Saadi, X. Dong Wang, A. Nouri, K. Zaidat, A. Belgacem-Bouzida, L. Ayouni-Derouiche, G. Raimondi d, and Y. Fautrelle, "Experimental analysis of the solidification of Sn–3 wt. pct. Pb alloy under natural convection," *International Journal of Heat and Mass Transfer*, 55 (2012), 1986-1996.

8. L. Hachani, K. Zaidat, B. Saadi, X.D. Wang, and Y. Fautrelle, "Solidification of Sn-Pb alloys: Experiments on the influence of the initial concentration," *International Journal of Thermal Sciences*, 91 (2015), 34-38.

9. T. Carozzani, CH-A. Gandin, H. Digonnet, M. Bellet, K. Ziadat, and Y. Fautrelle, "Direct Simulation of a Solidification Benchmark Experiment," *Metallurgical and Materials Transactions A*, 44(2013), 873-887.

10. D. Hoang, V. Steijn, L. Portela, M Kreutzer, C. Kleijn, "Benchmark numerical simulations of segmented two-phase flows in microchannels using the Volume of Fluid method," *Computers & Fluids*, 86 (2013), 28–36.

11. J. Guo and C. Beckermann, "Three-dimensional simulation of freckle formation during binary alloy solidification: effect of mesh spacing," *Numerical Heat Transfer, Part A*, 44 (2003), 559–576.

CFD Modeling and Simulation in Materials Processing 2016
Edited by: Laurentiu Nastac, Lifeng Zhang, Brian G. Thomas, Miaoyong Zhu, Andreas Ludwig, Adrian S. Sabau, Koulis Pericleous, and Hervé Combeau
TMS (The Minerals, Metals & Materials Society), 2016

MODELING THE MULTICOMPONENT COLUMAR-TO-EQUIAXED TRANSITION OF ALLOY 625

Kyle Fezi, Matthew J.M. Krane

Purdue Center for Metal Casting Research
Purdue University School of Materials Engineering,
701 West Stadium Avenue,
West Lafayette, IN, 47906, USA

Keywords: CET, Macrosegregation, Alloy 625

Abstract

A numerical model has been developed to study the effect of columnar dendrite growth kinetics and solid grain movement on macrosegregation in static castings. The model solves continuum equations for mass, momentum, species, and energy conservation during multicomponent solidification. The columnar-to-equiaxed transition is modeled to explore its effect on macrosegregation of nickel alloy 625. The location of the CET and macrosegregation level of alloy 625 is affected by changing the thermal boundary conditions. As the heat transfer coefficient was increased the columnar volume fraction of the ingot increased and the macrosegregation level decreased.

Introduction

Typical as-cast microstructures consist of three different regions: the chill zone or the outer equiaxed zone, the columnar zone, and the inner equiaxed zone. The change in microstructure from columnar to equiaxed (CET) can impact the macrosegregation of the alloy, therefore understanding how the CET affects the chemical inhomogeneity is important. The microstructure can be altered through subsequent heat treatments and deformation processes however, the macrosegregation level will be unchanged. Other models that predict CET [1–4] do not consider either free-floating equiaxed particles or multicomponent solidification. Both of which may alter macrosegregation levels and the CET location of an ingot. In this study, a continuum mixture model which conserves mass, energy, species, and momentum is used to predict the CET location and corresponding segregation level. Columnar growth is modeled using the simplified LGK model. Equiaxed particles that nucleate in the undercooled liquid are free to move in the melt and settle to form a rigid mushy zone and block the growth of the columnar front. This model is coupled to a multicomponent solidification model of Ni alloy 625. Different thermal boundary conditions are used to alter the location of the CET and analyze the effect on the ingot macrosegregation.

Numerical Model

Continuum mixture model equations for continuity, momentum, species, and energy conservation are taken from Vreeman et al. [5,6], who included contributions from free-floating solid grains. These equations are discretized using the finite volume method and solved on a

staggered grid using the SIMPLER algorithm [7]. The nucleated equiaxed particles are free to move in the bulk liquid, but once a critical solid fraction, $g_{s,pack}$, is reached, the particles pack into a rigid mushy zone. The critical packing fraction is difficult to determine and is related to the size and morphology of the equiaxed dendrites and the direction and strength of the liquid flow [8]. The packing fraction has been observed to be below 30% [5,9] and for this study a value of 20% is used. The flow is driven primarily by thermal and solutal buoyancy effects and by density differences between the solid and liquid, and Stokes law is used for the relative velocity between the solid and liquid:

$$\vec{V}_s - \vec{V}_l = \frac{(1-g_s)}{18\mu_m}(\rho_s - \rho_l) d_{diam}{}^2 \vec{g}\,, \tag{1}$$

in which d_{diam} is the average particle diameter and μ_m is the mixture viscosity.

The growth of the columnar dendrites is modeled using a multiphase approach [10] in which a grain envelope separates the solid (*s*) and interdendritic liquid (*d*) from the extradendritic liquid (*l*) as in Figure 1. The growth of the grain envelope follows the simplified LGK model [11], in which only the solutal contribution to the undercooling is considered:

$$V^* = \frac{Dm(k-1)C_d}{\pi^2 \Gamma}\left[\left(\frac{\Omega}{1.5}\right)^{1.25}\right]^2, \tag{2}$$

where C_d is the interdendritic liquid composition, m is the slope of the liquidus line on the phase diagram, and $\Omega = \left(C_l^* - C_l\right)/C_l^*(1-k)$. The multicomponent columnar front velocity is approximated with the binary expression in equation (2), using Nb for the solutal undercooling since its partition coefficient, *k*, has largest deviation from unity.

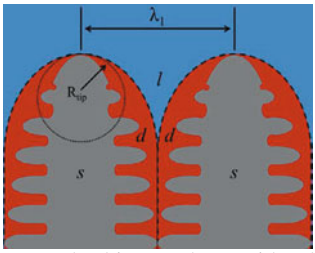

Figure 1: Schematic of the columnar dendrite envelope, with solid (*s*), interdendritic liquid (*d*), and extradendritic liquid (*l*), primary arm spacing (λ_1), and tip radius of curvature (R_{tip}).

The grain envelope grows at a rate determined by the tip growth velocity and the surface area of the grain envelope per unit volume, S_e, as given in equation (4) for a hexagonal array of dendrites [2]. The volume fraction of the grain envelopes (f_g) is the sum of the solid fraction (f_s) and the interdendritic liquid (f_d), or $f_g = f_s + f_d = 1 - f_l$.

$$\frac{\partial f_g}{\partial t} = -\frac{\partial f_l}{\partial t} = S_e V^* \tag{3}$$

$$S_e = f_l \frac{4\sqrt{\pi}(1-f_l)^{\frac{1}{2}}}{\sqrt{2\sqrt{3}}\lambda_1} \tag{4}$$

The primary dendrite arm spacing, λ_1, depends mainly on the columnar front velocity, the local temperature gradient, and the inter-dendritic liquid composition,

$$\lambda_1 = \sqrt{\frac{3}{G}}\left[\frac{8\pi^2 \Gamma D m_l C_d \left(1-\frac{1}{k}\right)}{kV^*}\right]^{\frac{1}{4}}.$$

Equiaxed grains nucleate with a fixed particle density in the undercooled liquid ahead of the columnar solidification front once a critical undercooling is reached. The columnar solidification front becomes blocked once the volume fraction of equiaxed particles reaches $g_{s,pack}$ and packs a control volume ahead of the columnar dendrite tips.

The columnar dendrites in the packed mushy zone slow the flow due to drag, which depends on the morphology and flow direction relative to the dendrite arms. For flow in the columnar mushy zone and high liquid fractions, the permeability model depends on the fluid flow direction as described by Felicelli et al. [12]. At low and intermediate liquid fractions, the permeability is determined based on the Blake-Kozeny model [13], which follows experimental data well in this range [14]. The permeability model switches from the orientation-dependent permeability models and the Blake-Kozeny at $g_l = 0.6$. For packed, equiaxed dendrites, the permeability follows the model given by Zick and Homsy for FCC arrangements at liquid fractions above 0.6 [14]: When $g_l < 0.6$, the Blake-Kozeny model is used with a permeability constant of 5.5×10^{-11} m^2.

An equilibrium solidification model is used to calculate the phase fractions, compositions, and temperature from the mixture enthalpy and compositions equations. At the start of solidification, the control volumes nearest the chilled wall are fully columnar dendritic structures. To track liquid and solid compositions and the columnar dendritic growth kinetics, the mixture composition equation is modified to incorporate the inter- and extradendritic liquid. In control volumes containing both columnar and equiaxed morphologies, solidification is governed by the columnar dendrite model.

The extradendritic liquid composition is assumed to be the mixture solute concentration, C_{mix}, during solidification, and the interdendritic liquid and solid exchange solute according to the equilibrium phase diagram. The columnar growth kinetics were derived for a binary alloy. In order to model a multicomponent alloy, a relationship between elemental segregation profiles must be established.

While performing a study for a ten component steel alloy, Schneider and Beckermann showed a linear relationship between the macrosegregation level of the alloying elements, $M^i = \left[\frac{1}{V_{casting}} \iiint_{volume} \left(\frac{C^i_{mix}}{C^i_{initial}} - 1 \right)^2 dV \right]^{\frac{1}{2}}$, and their partition coefficients [15]. Given this relationship, the local mixture composition of one element (C^1_{mix}) can be found as a function of another elemental composition (C^2_{mix}) and the partition coefficients of both elements using equation (5).

$$C^1_{mix} = C^1_{initial} + \left(\frac{k^1 - 1}{k^2 - 1} \right) \left(\frac{C^2_{mix} - C^2_{initial}}{C^2_{initial}} \right) C^1_{initial} \tag{5}$$

The equation for the liquidus surface temperature, $T_{LIQ}(K) = 1728 - 14.8365 + 75C_d^{Cr} - 16C_d^{Fe} - 524C_d^{Mo} - 1230C_d^{Nb}$, was taken from Yang et al. [16]. The two constants in the equation account for the liquidus temperature of pure Ni and the depression of the liquidus temperature due to the presences of trace elements that are treated as constant here. The Nb composition is calculated with the species transport equation in Vreeman et al. [5, 6] and the other elements which have an influence on buoyancy and T_{LIQ} are found from equation (5).

An axisymmetric standard case is developed for an alloy 625 ingot with a diameter of 50 cm (20 inches) and a height of 76.2 cm (30 inches). A symmetry boundary condition is applied at the centerline. The top of the ingot is insulated, while the side and bottom boundaries are a cooled by a constant heat transfer coefficient of 420 W/m^{2}K. The mold is assumed to start full of liquid with an initial temperature of 1710 K, which corresponds to a superheat of 73 K. The material properties of alloy 625 are listed in Table 1.

Table 1. Thermophysical properties of alloy 625.

Density [kg/m^3] [17,18]	8440	Nucleation sites [1/m^3]	3×10^5
Specific Heat [J/kg K] [17,18]	670	Free Floating Equiaxed Dendrite Diameter [m]	1.0×10^{-6}
Thermal Conductivity [W/m K] [17,18]	25.2	Packed Bed Equiaxed Dendrite Diameter [m]	1.0×10^{-4}
Thermal Expansion [1/K] [19]	1.28×10^{-4}	Diffusivity [m^2/s]	1×10^{-9}
Liquid Solutal Expansion [1/wt. fr.]	Cr: 0.201 Fe: 0.108 Mo:-0.184 Nb:-0.255	Latent Heat [J/Kg] [20]	2.9×10^5
Solid Solutal Expansion [1/wt. fr.] [15,19]	Cr: 0.199 Fe: 0.1199 Mo:-0.159 Nb: 0.0392	Eutectic Temperature [K] [16,17]	1430
Nucleation Undercooling [K]	3.0	Partition Coefficients	Cr: 1.04 Fe: 1.31 Mo: 0.83 Nb: 0.54

Results and Discussion

The model has been used to examine the influence of the solidification morphology on the macrosegregation level. A fully columnar solidification structure is compared to mixed columnar and equiaxed microstructures. The position of the CET changes with the thermal boundary condition. The all-columnar case has an overall macrosegregation level of 0.026 (M^{Nb} = 0.026) and Figure 2 shows the composition field. A depleted zone formed at the top of the ingot and at the outer, chilled surface. At the centerline, near the top of the ingot, a large enriched region formed, which corresponds to the last liquid to freeze. The flow is driven by negative thermal and solutal buoyancy, which moves the enriched solute down towards the centerline, enriching the bottom of the sump and depleting the top of the ingot.

Other cases were simulated over a range of thermal boundary conditions and included the columnar-to-equiaxed transition. The location of the CET, the flow field, the motion of the free floating particles, and the compositional field were all affected by the changes in outer wall heat transfer coefficient. The constant heat transfer coefficient at the side wall and bottom of the ingot was set to 220, 420, 520, and 720 W/m^{2}K. To compare the location of the CET for each case, the dimensionless CET position represented by the ratio of the volume of the ingot with columnar dendrites and the total ingot volume. The Nb macrosegregation number for the entire ingot is also calculated to compare the segregation levels for the four cases.

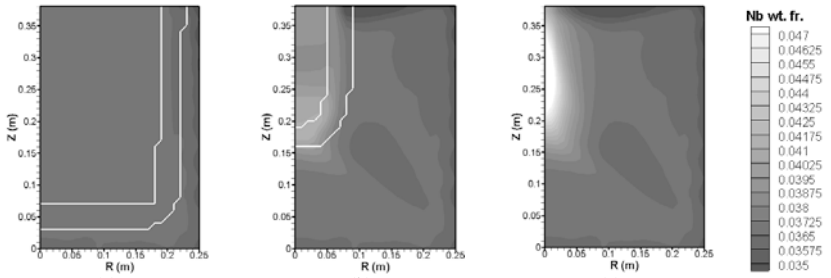

(a) (b) (c)

Figure 2. Nb composition fields for the fully columnar solidification structure showing the mushy zone with snapshots at (a) 8 min and 40 sec, (b) 54 min and 40 sec, and (c) 80 min.

When solid morphology is determined by the competition of free-floating equiaxed solid and columnar dendrites, a depleted region that is absent in the fully columnar case forms at the bottom of the ingot. Also, the location of the highest composition moves from the centerline to the top of the ingot. Equiaxed dendrites that nucleate near the columnar solidification front are depleted in solute are swept toward the bottom of the casting by the clockwise flow cell and settle there, forming a depleted region. In the equiaxed zone, the composition field is vertically stratified due to the particle settling.

Altering the thermal boundary conditions altered the CET position and the macrosegregation level. Increasing the heat transfer coefficient caused the CET position to move away from the bottom of the domain and shift closer to the centerline, with the exception of the extreme case of

720 W/m^{2}K, (Figure 3). For this very high heat transfer rate, the CET occurs very quickly. Although the segregation pattern is similar for each case, the overall segregation level decreases as the heat extraction rate increases. The columnar zone has a depleted region near the chill wall and at the top of the ingot. Also, the columnar zone has an enriched region at the top of the ingot near the CET. The equiaxed zone has a depleted region at the bottom and is vertically stratified, with increasing composition toward the top of the ingot. The results for the macrosegregation level and transition location are summarized in Figure 4.

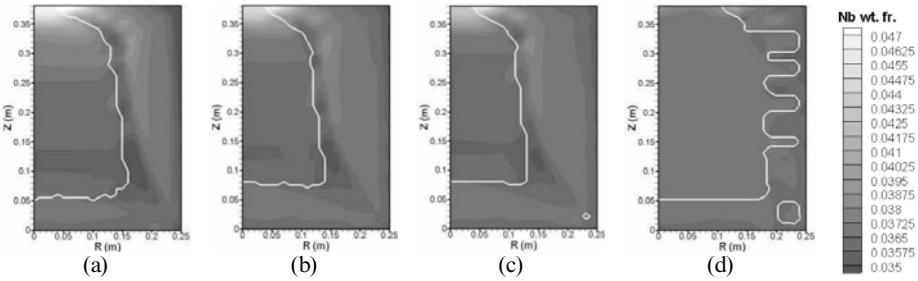

(a) (b) (c) (d)

Figure 3. Final Nb composition fields for heat transfer coefficients of (a) 220, (b) 420, (c) 520, and (d) 720 W/m^{2}K showing the macrosegregation pattern and the CET location with a solid white line.

The Nb macrosegregation number decreases with increasing heat transfer coefficient, because the solidification time decreases. The rejected solute has less time to be redistributed by the fluid motion in the liquid when the heat transfer coefficient is high. Increasing the heat transfer coefficient also increases the temperature gradient ahead of the solidification front, which increases the velocity of the columnar tips. Therefore the dimensionless CET position increases for increasing heat transfer coefficient, up to 520 W/m^{2}K. Increasing the heat transfer coefficient even further, to 720 W/m^{2}K, initiates the CET much earlier than in the previous cases. The very high heat extraction rate causes the entire domain to reach the undercooled nucleation temperature early on in the process and allows the equiaxed dendrites to grow before the columnar dendrites can reach the center. The equiaxed dendrites grew to fraction solid of 0.2 blocking the columnar dendrites, and causing an early CET. Figure 5 shows the temperature profiles across the radius at the ingot midheight (Z = 0.2m) for multiple times. The time between each temperature curve is 350 seconds. The temperature profile starts above the equiaxed nucleation temperature for about 10 minutes for both the 420 and 520 W/m^{2}K cases, but for the 720 W/m^{2}K case the temperature across the entire radius is below the nucleation temperature within the first 6 minutes. This lower

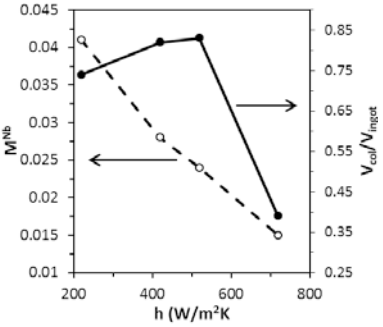

Figure 4. Macrosegregation and dimensionless CET location as a function of the heat transfer coefficient.

temperature causes much more nucleation of equiaxed particles early on in the process, blocking the columnar grains close to the chill. This result is reverses the trend observed in the first three cases and a previous study [2] and needs additional experimental support.

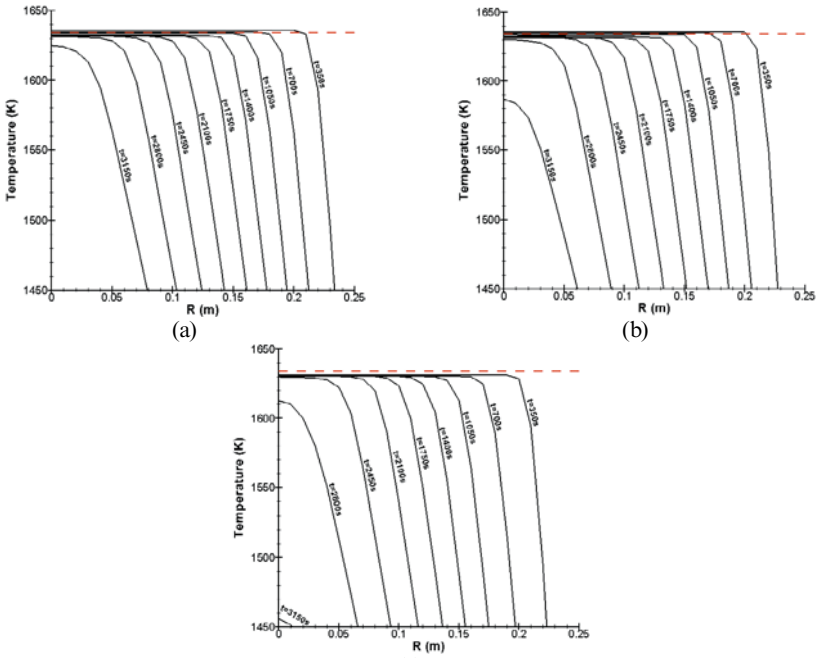

Figure 5. Radial temperature profiles showing the effect of the boundary condition on the thermal penetration depth for (a) 420, (b) 520, and (c) 720 W/m^{2}K. The red dotted line indicates the equiaxed grain nucleation temperature.

Summary

Several static castings of alloy 625 were analyzed, in which the solidification morphology and thermal boundary conditions were varied. The fully columnar case was compared to four mixed morphology cases with a columnar-to-equiaxed transition. The presence of equiaxed dendrites had a significant impact on the composition field. For the mixed morphology cases, the thermal boundary condition was varied. Smaller heat extraction rates lead to larger equiaxed zones and a smaller thermal gradient. Increasing the heat extraction rate from 520 to 720 W/m^{2}K caused a CET much closer to the outer wall due to the increased penetration depth of the boundary condition. The equiaxed zone in all of the cases was compositionally stratified in the axial direction, with a depleted region at the bottom of the equiaxed zone, due to the settling of solid grains. Validation of the numerical model is currently being conducted.

Acknowledgements

This research was funded by a gift from Precision Cast Corporation.

References

1. J.D. Hunt: *Mater. Sci. Eng.*, 1984, vol. 65, pp. 75–83.
2. C.Y. Wang and C. Beckermann: *Metall. Mater. Trans. A*, 1994, vol. 25, pp. 1081–93.
3. M.A. Martorano, C. Beckermann, and Ch. Gandin: *Metall. Mater. Trans. A*, 2003, vol. 34, pp. 1657–74.
4. M. Wu and A. Ludwig: *Acta Mater.*, 2009, vol. 57, pp. 5621–31.
5. C.J. Vreeman, M.J.M. Krane, and F.P. Incropera: *Int. J. Heat Mass Transf.*, 2000, vol. 43, pp. 677–86.
6. C.J. Vreeman and F.P. Incropera: *Numer. Heat Transf. Part B Fundam.*, 1999, vol. 36, pp. 1–14.
7. S.V. Patankar: *Numerical Heat Transfer and Fluid Flow*, Hemisphere Publishing, Washington DC, 1980.
8. I. Vusanovic and M.J.M. Krane: *3rd Int. Conf. Adv. Solidif. Process.*, 2011, vol. 27.
9. C.J. Vreeman, J.D. Schloz, and M.J.M. Krane: *J. Heat Transfer*, 2002, vol. 124, pp. 947–53.
10. C.Y. Wang and C. Beckermann: *Metall. Mater. Trans. A*, 1993, vol. 24, pp. 2787–2802.
11. J. Lipton, M.E. Glicksman, and W. Kurz: *Mater. Sci. Eng.*, 1984, vol. 65, pp. 57–63.
12. S D Felicelli, J C Heinrich, and D R Poirier: *Metall. Trans. B*, 1991, vol. 22, pp. 847–59.
13. S. Ganesan, C.L. Chan, and D.R. Poirier: *Mater. Sci. Eng. A*, 1992, vol. 151, pp. 97–105.
14. A.A. Zick and G.M. Homsy: *J. Fluid Mech.*, 1982, vol. 115, pp. 13–26.
15. M.C. Schneider and C. Beckermann: *Metall. Mater. Trans. A*, 1995, vol. 26, pp. 2373–88.
16. Wanhong Yang, Wei Chen, Keh-minn Chang, Sarwan Mannan, and John DeBarbadillo: in *Superalloys 2000*, T.M. Pollock, R.D. Kissinger, R.R. Bowman, K.A. Green, M. McLean, S. Olson, and J.J. Schirra, eds., TMS, 2000, pp. 75–84.
17. G Hoyle: *Electroslag Processes*, Elsevier Science Publishing Co. INC, New York, NY, 1983.
18. Special Metals Corporation: *INCONEL Alloy 625*, 2006.
19. T Iida and R Guthrie: *The Physical Properties of Liquid Metals*, Clarendon Press, Oxford, 1988.
20. H Jones: *Rapid Solidification of Metals and Alloys*, Institution of Metallurgists, London, 1982.

CFD Modeling and Simulation in Materials Processing 2016
Edited by: Laurentiu Nastac, Lifeng Zhang, Brian G. Thomas, Miaoyong Zhu, Andreas Ludwig, Adrian S. Sabau, Koulis Pericleous, and Hervé Combeau
TMS (The Minerals, Metals & Materials Society), 2016

PERFORMANCE OPTIMIZATION AND EVALUATION OF A 3D CA-FVM MODEL FOR DENDRITIC GROWTH OF Fe-C ALLOY

Weiling Wang[1], Sen Luo[1,2], Miaoyong Zhu[1]

[1]School of Metallurgy, Northeastern University, Shenyang 110819, China
[2]Ansteel research institute of vanadium & titantium (iron & steel), Ansteel Corporation, Panzhihua 610031, China

Keywords: Dendritic growth, Fe-C alloy, 3D CA-FVM model, 3D block-correction technique, Parallelization.

Abstract

Because of the tremendous computational cost of 3D (three dimensional) calculation of the dendritic growth, the parallel approach and the block-correction technique (BCT) are adopted to improve the efficiency of codes. Meanwhile, the accuracy of the codes is evaluated by comparing the present prediction with the analytical solutions to the fluid flow problem, LGK analytical results and the experimental measured columnar dendritic morphology and secondary dendritic arm spacing (SDAS, λ_2). The results show that the parallel Jacobi code with once 2D iteration in 3D BCT is proved to be the most efficient one among the codes compiled in the present work, accordingly is employed to simulate the 3D dendritic growth of alloys. The calculated velocities agree well with the results from the analytical equations. The predicted steady growth velocities of the equiaxed dendritic tip of Fe-0.82wt%C alloy by the present CA model agree with the 3D LGK analytical model as the anisotropy parameter is 0.04. Moreover, the present CA model shows some capability to predict the columnar dendritic growth during the directional solidification process of Fe-1.48wt%C alloy.

Introduction

With the increasing demand for simulating the dendritic growth of alloys closer to the actual case, the numerical simulation by the deterministic models such as the phase field (PF) model and the front tracking (FT) model and the stochastic models such as the cellular automaton (CA) model has been extended from two dimensional (2D) domain to three dimensional (3D) domain.
As the additional dimension is introduced, the computational cost boosts up significantly, especially in consideration of the melt flow, which is the most serious problem confronted by the model developers. Therefore, the algorithm optimization and the parallel computation are usually employed to improve the computation efficiency. The simulation of the dendritic growth in 3D was firstly realized with the PF model [1]. At first, considering the importance of the solidification interface to dendritic evolution, the adaptive-mesh approach with the much finer meshes at the interface and coarser meshes at the remain domain was usually used to reduce the computational cost of 3D PF models during the simulation of the dendritic growth of pure materials [2, 3]. With the development of computers, the parallel 3D PF models based on the message-passing interface (MPI) library become dominant to predict the dendritic growth with a reasonable computational efficiency [4]. The fundamental of the parallel approach is that the task is divided into several subdomains which are assigned to different processors and calculated

separately, meanwhile its continuity is guaranteed by the process communication, that is, the MPI approach. Moreover, the combination of the adaptive-mesh and the parallelization approach are usually combined to further improve the computational efficiency of PF models [5]. Similarly, Al-Rawahi and Tryggvason [6] implemented the 3D FT model on parallel computers using the MPI approach. Zhao and coauthors [7-10] realized the parallelization of their 3D CA-FVM (cellular automaton-finite volume method) model with discrete linear equations being solved by 3D TDMA (tri-diagonal matrix algorithm) by using the MPI approach. However, compared with other algorithms such as Jacobi, TDMA is intrinsically with the serial characteristic. Therefore, Eshraghi et al. [11, 12] introduced the 3D lattice Boltzmann method (LBM) with the complete parallelism to deal with transport equations and extended the computational scale of the 3D CA-LBM model to 3.6 billion cells. Moreover, another advantage of LBM is that it can deal with the fluid flow in the discontinuous regions well, compared with traditional CFD (computational fluid dynamics) approaches. Recently, the graphic processing unit (GPU) has been used to accelerate the calculation of the 3D PF model in large scale domains [13]. For the traditional methods such as FDM (finite difference method) and FVM still used in the simulation of the dendritic growth [7-10], except for the parallelism, some acceleration algorithms for the calculation of discrete equations should be considered to obtain an acceptable computational cost. For example, the block-correction technique (BCT) [14] can promote the convergence of the iterations of linear equations by methods such as TDMA and Jacobi and has been applied in the investigation of dendritic growth under the melt flow in 2D with CA approach by present authors [15, 16]. Therefore, its application in 3D will be expected, as well as its combination with the parallelization of the codes. Additionally, the accuracy of the 3D codes should be concerned to ensure their capability in predicting the 3D dendritic growth of alloys. The models for the dendritic evolution are customarily tested through the comparisons of the steady dendritic tip parameters [17, 18], the qualitative dendritic morphology [18] and the dendritic arm spacing (DAS)[7, 9, 10] with analytic models and experimental results. Taking the advantage of the superiority of the FT model, Al-Rawahi and Tryggvason [6] tested their model and flow solvers with respect to the analytical solutions for the Stefan problem of a sphere and for the flow over a simple cubic array of spheres. Although this concept is very constructive and novel, comparisons with solutions of Stefan problems cannot be transplanted to the CA model. It is mainly ascribed to that the isothermal solidification interface in Stefan problems should be explicitly tracked to consider the release of solidification heat there, which cannot be realized in the CA model. As a result, Yin et al. [19] employed analytical solutions of pure thermal and solute diffusion to validate the heat transfer and solute diffusion solvers in 2D, however neglected the test of the flow solver.

A 3D CA-FVM model focusing on the 3D dendritic growth of high carbon Fe-based alloys was developed in the consideration of the improvement of the computational efficiency and the model capacity [20, 21]. Compared with other works with traditional transport models [7-9], the present work employed both the 3D BCT and the parallelism to save the computational cost. The present paper will give a brief introduction of the first part of the work involving mainly seeking for the most efficient code to deal with the designed problems and evaluating the capability of 3D CA-FVM model in solving the transport problem and the dendritic evolution.

Model Description

Governing Equations

The governing equations for the inter- and exter-dendritic flows are given by:

$$\nabla \cdot (\rho \boldsymbol{U}) = 0 \tag{1}$$

$$\rho \frac{\partial \boldsymbol{U}}{\partial t} + (\rho \boldsymbol{U}) \cdot \nabla (\boldsymbol{U}) = -\nabla p + \nabla \cdot (\mu \nabla (\boldsymbol{U})) \tag{2}$$

where $\boldsymbol{U}$ is velocity vector, (u, v, w), ρ is density, μ is viscosity, and p is the hydrostatic pressure. The governing equations of solute transport are given by:

$$\frac{\partial C_l}{\partial t} + (\boldsymbol{U}) \cdot \nabla C_l = D \cdot \nabla^2 C_l \tag{3}$$

$$\frac{\partial C_s}{\partial t} = D \cdot \nabla^2 C_s \tag{4}$$

where C_s and C_s are solute concentrations in solid and liquid phases, respectively, and D is diffusion coefficient, which is the mean value of solid diffusivity, D_s and liquid diffusivity, D_l according to the solid fraction, f_s.

The governing equation of the heat transport is expressed as follows:

$$\frac{\partial T}{\partial t} + \boldsymbol{U} \cdot \nabla T = \alpha \cdot \nabla^2 T + \frac{L}{c} \frac{\partial f_s}{\partial t} \tag{5}$$

where T is temperature, α is thermal diffusivity, which is the function of the thermal conductivity, λ and the specific heat capacity, c, and L is solidification latent heat.

The convergence of transport equations should satisfy Eqs. (6) and (7):

$$\mathrm{Max}\left[\frac{\zeta_{i,j,k}^{n+1} - \zeta_{i,j,k}^{n}}{\mathrm{CT}} \right] < \chi \tag{6}$$

$$\mathrm{CT} = \begin{cases} 1 & \zeta_{i,j,k}^{0} >= 1 \\ \zeta_{i,j,k}^{0} & \zeta_{i,j,k}^{0} < 1 \end{cases} \tag{7}$$

where ζ represents field variables, including u, v, w, T and C, ζ^0 is on behalf of initial values of those variables, n is iteration steps, χ is a number far less than unity, CT is a constant dependent on ζ^0, and (i, j, k) denotes the serial number of the CA cell.

The Neumann configuration is used to deal with the evolution of the state of the CA cell. Accordingly, as the interface cell become solid, it will capture the liquid cells among its first nearest cells as the interface cells. The solute redistribution at the interface is given by:

$$C_s^* = k_0 C_l^* \tag{8}$$

$$C_l^* = C_0 + \frac{1}{m_l} \left(T^* - T_l + \Gamma \cdot wmc \right) \tag{9}$$

where C_l^* and C_s^* are equilibrium solid and liquid solute concentrations at solidification interface, respectively, k_0 is the equilibrium partition coefficient of the solute, C_0 is the initial solute content in the modeling domain, T_l is the equilibrium liquidus temperature, m_l is the slope of liquidus line in the equilibrium phase diagram of the alloy, Γ is the Gibbs-Thomson coefficient of Fe-C alloy, and T^* is the interface temperature. wmc is expressed in Eq. (10) [18]:

$$wmc = (3\varepsilon - 1)\cdot\left(\partial_x n_x + \partial_y n_y + \partial_z n_z\right) - 48\varepsilon\cdot\left(n_x^2\cdot\partial_x n_x + n_y^2\cdot\partial_y n_y + n_z^2\cdot\partial_z n_z\right) + 12\varepsilon\cdot Q\cdot\left(\partial_x n_x + \partial_y n_y + \partial_z n_z\right) + 12\varepsilon\cdot\left(n_x\cdot\partial_x Q + n_y\cdot\partial_y Q + n_z\cdot\partial_z Q\right) \quad (10)$$

where ε is the anisotropic degree of the surface energy, (n_x, n_y, n_z) is unit normal vector of the interface and is calculated according to the first-order derivative of solid fraction, f_s, such as $n_x=\partial_x f_s/[(\partial_x f_s)^2+(\partial_y f_s)^2+(\partial_z f_s)^2]^{0.5}$. The parameter Q is denoted as $Q=n_x^4+n_y^4+n_z^4$.
The evolution of the solidification interface is governed by the solute balance there, as expressed in Eq. (11) [7-10, 15, 16, 20, 21].

$$v_n C_1^* (1-k_0) = D_s \frac{\partial C_s}{\partial \boldsymbol{n}}\bigg|^* - D_l \frac{\partial C_l}{\partial \boldsymbol{n}}\bigg|^* \quad (11)$$

where v_n is normal growth velocity of solidification interface. The solute balance along three axes is separately calculated [15, 16]. The related physical property parameters of high carbon Fe-C alloy are listed in the previous paper [15, 16, 20, 21].

Performance Optimization

According to the basic concept of FVM, the transport equations in 3D are discretized into a uniform form:

$$a_P\varphi_P - a_W\varphi_W - a_E\varphi_E - a_S\varphi_S - a_N\varphi_N - a_B\varphi_B - a_T\varphi_T = b_P \quad (12)$$

where a, b and φ are the coefficient, the constant term and the variable of the discrete equation, and P, W and E, T and B and N and S represent the present cell, its west and east neighboring cells along x axis, top and bottom nearest ones along z axis, and north and south nearest ones along y axis. The basic concept of the BCT is to introduce a mean modification value to ensure the complete conversation in the each iteration [14], as shown in Figure 1.
The Parallel Patterns Library (PPL) and the namespace Concurrency in Microsoft Visual Studio 2010 C++ are used to parallelize the codes. The codes are run on the server with 40 CPU cores.

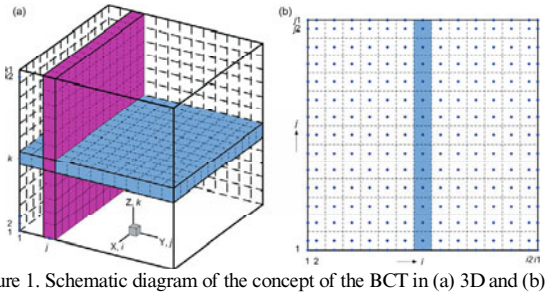

Figure 1. Schematic diagram of the concept of the BCT in (a) 3D and (b) 2D

Model Test

Transport Models

The computational efficiency of these codes is evaluated as they solve the designed melt flow problem, as illustrated in Figure 2(a) and (b). A fluid of the molten steel flows into the 201 μm ×

201 μm × 201 μm domain with the velocity of 0.001 m/s along x axis of at the left boundary, gets over the orthogonally arranged solid obstacles in the center of the domain and leaves at the right boundary, which belongs to the laminar category. The size of the block is 44 μm × 10 μm × 10 μm. Meanwhile, the domain is meshed into cells with the size of 1 μm × 1 μm × 1 μm. Except for the inlet and the outlet boundaries, other walls of the domain are symmetrical. The flow field at steady state is predicted with the SIMPLE algorithm. The number χ representing the convergence requirement is 0.001. As the 3D BCT is introduced, the computational cost of the serial TDMA code decreases from 92.62 h to 22.74 h, as shown in Figure 2(c). It is attributed to that the 3D BCT changes the convergence type of the iteration from the fluctuating one to a smooth one, according reduces the iteration steps. Subsequently, as the code is partially parallelized, the computational cost drops to 15.71 h. Such computational efficiency is still relatively high since TDMA is intrinsically serial. Therefore, Jacobi with much more parallel characteristic is employed to further improve the computational efficiency. The parallel Jacobi code with 3D BCT cost 8.67 h to get the convergence. According to the basic concept of BCT, the 2D iteration in 3D BCT is not necessarily required to be converged as the boundary condition is delivered into the computational domain. As the 2D iteration in 3D BCT in iterated once, the computational cost of the parallel Jacobi code reduces by 2.88 h. Moreover, as the compiling mode changes from debug to release, the computational cost of the parallel Jacobi code with once 2D iteration in 3D BCT reduces to an acceptable value, 2.60 h. Therefore, the parallel Jacobi code with once 2D iteration in 3D BCT is adopted to simulate the 3D dendritic growth of alloys in the present work.

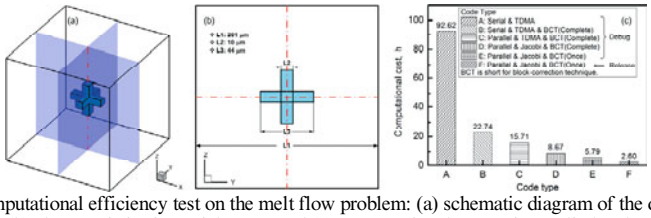

Figure 2. Computational efficiency test on the melt flow problem: (a) schematic diagram of the designed case, (b) characteristic sizes of the case and (c) computational costs of complied codes

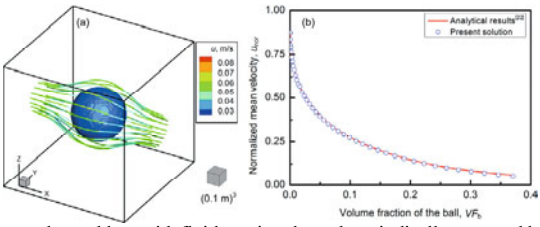

Figure. 3 Solution to the problem with fluid passing through periodically arranged balls: (a) the flow distribution around the solid ball and (b) comparison between the predicted normalized mean velocity, u_{nor} and the analytical results [22]

In order to evaluate the accuracy of the present fluid flow solver, the classical problem with flow passing through periodical arranged balls [22] is concerned. In order to impel the flow pass

through the gap between two adjacent balls with the size of L along x axis with the given average velocity $\overline{u}_0$, the driving force, that is, the pressure gradient β should be exerted. The normalized velocity u_{nor} representing the quantitative relationship between β and $\overline{u}_0$ changes with the volume fraction of the ball, VF_b. The fluid passes through the gap of 1.0 m between two adjacent balls with an average velocity of 0.1 m/s, as shown in Figure 3(a). The predicted functional relationship between u_{nor} and VF_b agrees well with the analytical result [22], as shown in Figure 3(b).

CA Model

The 3D LGK model without consideration of the thermal undercooling [17, 18] is adopted to evaluate the present CA-FVM model. The selection parameter of the dendritic tip, σ* used in the LGK model is determined to be 0.1273 corresponding to the anisotropy parameter of 0.04 according to the linearized solvability theory [23]. The cubic domain with the size of 201 μm × 201 μm × 201 μm meshed into (1 μm)^3 cells is used to simulate the single equiaxed dendritic growth of Fe-0.82wt%C alloy at the constant undercooling. The solute diffusion in solid phase is neglected in terms of the basic concept of the LGK mode. As the solidification time reaches the order of D/V^2 [18], the dendritic growth is assumed to be at steady state. Accordingly, the steady growth velocity and radius of the dendritic tip can be determined. Figure 4 shows the comparisons between the predicted steady growth velocity and radius of the dendritic tip and the analytical results as the undercooling changes from 3 K to 13 K. The predicted steady growth velocities of dendritic tip present good agreements with the LGK analytical results at the undercooling of 6-7 K. The steady tip radius is consistent with the analytical prediction at the undercooling of 6.5 K. Meanwhile, the difference between the prediction and the analytical data can be attributed to the mesh dependence of the CA model.

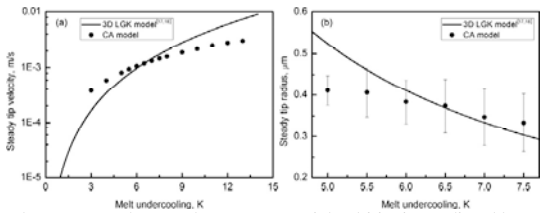

Figure. 4 Comparison between steady growth parameters of dendritic tip predicted by present CA model and the LGK analytical results: (a) the steady growth velocity and (b) the steady radius

Additionally, the unidirectional solidification processes of the high carbon steel presented by Jacobi and Schwerdtfeger [24] are adopted to evaluate the capability of present codes in predicting the columnar dendritic growth. The steel is simplified into Fe-1.48wt%C alloy. In the simulation, the nuclei are placed at the bottom domain according to the measured average primary dendritic arm spacing (PDAS, λ_1) [24] as listed in Table I. The cooling conditions are strictly in accordance with the experimental conditions with the given growth rate, R_d and the given temperature gradient, G, which are listed in Table I. Firstly, the columnar dendritic morphology of Fe-1.48wt%C at the cooling condition with R_d=0.51 m/h and G=5200 K/m (λ_1=540 μm) is predicted by the present CA-FVM model which agree with the experimental

result, as shown in Figure 5. The SDAS are measured as the columnar dendrites reach the top of the domain in the consideration of the dendritic coarsening and compared with the experimental measurements as listed in Table I. The predicted average SDASs shows some agreement with the experimental results, especially at R_d=0.51 m/h and G=7400 K/m.

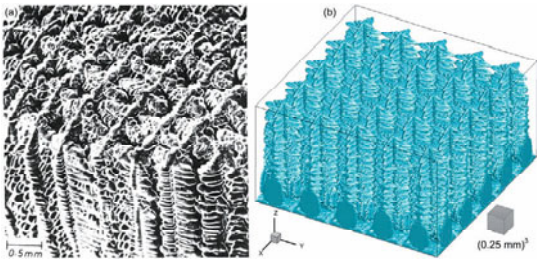

Figure. 5 Columnar dendritic morphology of Fe-1.48wt%C alloy during the unidirectional solidification: (a) the experimental observation [24] and (b) the predicted result

Table I Comparisons between the predicted SDASs and the experimental measurements[24]

R_d, m/h	G, K/m	$\lambda_{1,\,Mea}$, μm	$\lambda_{2,\,Mea}$, μm	$\lambda_{2,\,Cal}$, μm		
				MAX	MIN	AVE
0.25	5300	570	**150.0**	160.0	60.0	**110.0**
0.25	7000	370	**130.0**	170.0	75.0	**107.0**
0.51	5200	540	**110.0**	110.0	55.0	**77.0**
0.51	7400	320	**70.0**	90.0	45.0	**69.3**
0.75	8800	280	**80.0**	80.0	30.0	**52.0**

Conclusion

(1) With the introduction of the 3D BCT and the parallelism, the former serial TDMA code is gradually optimized to the parallel Jacobi code with once 2D iteration in 3D BCT with the computational cost reducing from 92.62 h to 5.79 h as it deals with the flow problem with the scale of 201^3. As the compile mode is changed from debug to release, the computational cost of this code become more acceptable. The solutions for the problem with the fluid passing through the gap between periodically arranged balls agree well with the analytical results.
(2) The predicted steady tip velocity and radius agree well with the LGK analytical model at the undercooling of 6-7 K. Moreover, the predicted columnar dendritic morphology of Fe-1.48wt%C alloy during the unidirectional solidification agrees with the experimental observation. The calculated SDASs agree with the experimental results, especially at the growth velocity of 0.51 m/h and the temperature gradient of 7400 K/m.

Acknowledgement

The authors sincerely acknowledge the financial support from National Natural Science Foundation of China No. 51404062 and Outstanding Talent Cultivation Project of Liaoning Province No. 2014029101 and Specialized Research Fund for the Doctoral Program of Higher Education of China No. 20130042120042.

References

1. A. Karma and W. J. Rappel, "Quantitative Phase-Field Modeling of Dendritic Growth in Two and Three Dimensions", *Physical review E*, 57 (4) (1998), 4323.
2. J. H. Jeong, N. Goldenfeld, and J. A. Dantzig, "Phase Field Model for Three-Dimensional Dendritic Growth with Fluid Flow", *Physical Review E*, 64 (4) (2001), 041602.
3. C. C. Chen and C. W. Lan, "Efficient Adaptive Three-Dimensional Phase-Field Simulation of Dendritic Crystal Growth From Various Supercoolings Using Rescaling", *Journal of Crystal Growth*, 311 (3) (2009), 702-706.
4. W. L. George and J. A. Warren, "A Parallel 3D Dendritic Growth Simulator Using the Phase-Field Method", *Journal of Computational Physics*, 177 (2) (2002), 264-283.
5. P. C. Bollada, P. K. Jimack, and A. M. Mullis, "An Adaptive Mesh Method for Phase-Field Simulation of Alloy Solidification in Three Dimensions", *IOP Conference Series: Materials Science and Engineering*, 84 (1) (2015), 012068.
6. N. Al-Rawahi and G. Tryggvason, "Numerical Simulation of Dendritic Solidification with Convection: Three-Dimensional Flow", *Journal of Computational Physics*, 194 (2) (2004), 677-696.
7. H.X. Jiang and J.Z. Zhao, "A Three-Dimensional Cellular Automaton Simulation for Dendritic Growth", *Acta Metallurgica Sinica*, 47 (9) (2011), 1099-1104.
8. X.F. Zhang and J.Z. Zhao, "Effect of Forced Flow on Three Dimensional Dendritic Growth of Al-Cu Alloys", *Acta Metallurgica Sinica*, 48 (5) (2012), 615-620.
9. X.F. Zhang, J.Z. Zhao, H.X. Jiang, et al., "A Three-Dimensional Cellular Automaton Model for Dendritic Growth in Multi-Component Alloys", *Acta Materialia*, 60 (5) (2012), 2249-2257.
10. X.F. Zhang and J.Z. Zhao, "Dendritic Microstructure Formation in A Directionally Solidified Al-11.6Cu-0.85Mg Alloy", *Journal of Crystal Growth*, 391 (2014), 52-58.
11. M. Eshraghi , S.D. Felicelli, and B. Jelinek, "Three Dimensional Simulation of Solutal Dendrite Growth Using Lattice Boltzmann and Cellular Automaton Methods", *Journal of Crystal Growth*, 354 (1) (2012), 129-134.
12. M. Eshraghi , B. Jelinek, and S.D. Felicelli, "Large-Scale Three-Dimensional Simulation of Dendritic Solidification Using Lattice Boltzmann Method", *JOM*, 67 (8) (2015), 1786-1792.
13. T. Takaki, "Phase-field Modeling and Simulations of Dendrite Growth", *ISIJ international*, 54 (2) (2014), 437-444.
14. Wenquan Tao, *Numerical Heat Transfer* (Xi'an: Xi'an Jiao Tong University Press, 2001), 280-283.
15. W.L. Wang, S. Luo, and M.Y. Zhu, "Numerical Simulation of Dendritic Growth of Continuously Cast High Carbon Steel", *Metallurgical and Materials Transactions A*, 46 (1) (2015), 396-406.
16. W.L. Wang, S. Luo, and M.Y. Zhu, "Dendritic Growth of High Carbon Iron-Based Alloy Under Constrained Melt Flow", *Computational Materials Science*, 95 (2014), 136-148.
17. J. Lipton, M. E. Glicksman, and W. Kurz, "Dendritic Growth into Undercooled Alloy Metals", *Materials Science and Engineering*, 65 (1) (1984), 57-63.
18. S.Y. Pan, M.F. Zhu, "A Three-Dimensional Sharp Interface Model for the Quantitative Simulation of Solutal Dendritic Growth", *Acta Materialia*, 58 (1) (2010), 340-352.
19. H. Yin, S.D. Felicelli, and L. Wang, "Simulation of A Dendritic Microstructure with the Lattice Boltzmann And Cellular Automaton Methods", *Acta Materialia*, 59 (8) 2011, 3124-3136.
20. W.L. Wang, S. Luo, and M.Y. Zhu, "Numerical Simulation of Three-Dimensional Dendritic Growth of Alloy Part I. Model Development and Test", *Metallurgical and Materials Transactions A*, (2015), Submitted.
21. W.L. Wang, S. Luo, and M.Y. Zhu, "Numerical Simulation of Three-Dimensional Dendritic Growth of Alloy Part II. Model Application to Fe-0.82wt%C alloy", *Metallurgical and Materials Transactions A*, (2015), Submitted.
22. A.S. Sangani and Acrivos A, "Slow Flow Through a Periodic Array of Spheres", *International Journal of Multiphase Flow*, 8 (4) (1982), 343-360.
23. A. Barbieri and J.S. Langer, "Predictions of Dendritic Growth Rates in the Linearized Solvability Theory", *Physical Review A*, 39 (10) (1989), 5314-5325.
24. H. Jacobi and K. Schwerdtfeger, "Dendrite Morphology of Steady State Unidirectionally Solidified Steel", *Metallurgical Transactions A*, 7 (6) (1976), 811-820.

CFD Modeling and Simulation in Materials Processing 2016
Edited by: Laurentiu Nastac, Lifeng Zhang, Brian G. Thomas, Miaoyong Zhu, Andreas Ludwig, Adrian S. Sabau, Koulis Pericleous, and Hervé Combeau
TMS (The Minerals, Metals & Materials Society), 2016

MULTISCALE MODELING OF THE SOLIDIFICATION STRUCTURE EVOLUTION OF CONTINUOUSLY CAST STEEL BLOOMS AND SLABS

Laurentiu Nastac[1], Mikko Kärkkäinen [2], Pilvi Hietanen[2], Seppo Louhenkilpi[2]

[1]The University of Alabama, Department of Metallurgical and Materials Engineering,
Box 870202, Tuscaloosa, AL, 35487, USA
[2]Aalto University, Department of Materials Science and Engineering,
PO Box 16200, FI-00076, Espoo, Finland

Keywords. Multiscale Modeling; Continuous Casting; Blooms and Slabs; Low Alloying Steels; Solidification Structure; Columnar-to-Equiaxed Transition.

Abstract

An efficient multiscale mesoscopic modeling approach capable of accurately predicting the formation of the solidification structure during the continuous casting (CC) process was developed. The modeling approach consists of integrating a macroscopic model (TEMPSIMU3D+IDS) with a stochastic mesoscopic solidification structure model (SolMicro).
The integrated model can predict the evolution of the grain morphology and the columnar-to-equiaxed transition (CET) and is compared against experimental measurements for low-alloyed steel blooms and slabs, with dimensions of T312mm x W372 mm x L31m and T280 mm x W1962 mm x L31m, respectively. The validated model was then applied to determine the effects of superheat on the solidification structure of CC processed steel slabs.

Introduction

The objective of this work was to apply a transient multiscale modeling approach to get insights into the effect of key processing parameters on the solidification structure evolution during continuous casting (CC) processing of steel blooms and slabs. The modeling approach consists of integrating a transient macroscopic model with a mesoscopic solidification structure model. The integrated model can predict the solidification structure evolution of both columnar and equiaxed morphologies and the columnar-to-equiaxed transition (CET). The integrated model can assist thus in achieving better control of the casting solidification structure in these cast products. Another objective of this work determine the effects of superheat, casting rate and heat extraction rate on the solidification structure of CC processed steel blooms and slabs.
The capabilities of the model include the effects of process parameters, such as casting rate, mold cooling conditions and casting size on the casting structure at both the macroscopic and the microscopic levels. Thus, grain size, grain morphology (dendritic columnar or equiaxed), grain direction and CET can be predicted [1-5]. Other capabilities of the developed model include the capability to analyze the effects of melt transients, typically observed in the CC process.

A schematic of the CC process and the longitudinal cross-section of a CC-processed casting are illustrated in Figure 1. Figure 2 presents a schematic diagram showing the coupling between the transient computational fluid dynamics (CFD) code (**TEMPSIMU3D+IDS**) and the casting solidification structure code (**SolMicro**) [1-5].

IDS (InterDendritic Solidification) [7] uses a thermodynamic substitution model alongside a magnetic ordering model, mass balance equations and Fick's law to calculate the phase fractions and compositions of the solidifying steel as a function of temperature. The following phases are simulated: proeutectoid ferrite, cementite, pearlite, bainite, martensite and various non-metallic phases in the form of precipitates and inclusions. Complete solute mixing in the liquid is assumed. The model is capable of calculating the temperature-dependent material properties and phase composition evolution of both low and high-alloy steels.

TEMPSIMU3D [8] uses a parallel modified Gauss-Seidel-Newton-Rhapson solver to calculate the temperature field of a CC steel slab or bloom in 3D. The boundary conditions for the heat transfer simulation are defined using a physical model of the casting machine, taking into account the cooling effects of air-mist sprays, contact rolls and heat radiation, and accounting for the Leidenfrost effect. Currently, **TEMPSIMU** accounts for the effect of turbulent flow on heat transfer using a fitting coefficient. This coefficient modifies the thermal conductivity of steel as a function of the solid/liquid fraction. The value of this coefficient has been investigated using FLUENT simulations [9]. Together, **TEMPSIMU3D and IDS** can model solidification-kinetics, heat transfer and micro- and macro-segregation phenomena during casting and solidification of commercial cast products processed by the CC technology.

CC casting dimensions are shown in Table 1. Control parameters of the CC process, such as casting speed, mold cooling and secondary cooling conditions are typical for processing of steel blooms and slabs. Thermal properties of the materials used in the simulations are shown in Table 2 and Table 3. The data used in the **SolMicro** code are shown in Table 4. The nucleation parameters C_0, C_1, and C_2 are explained in Ref. [3], p. 160. G_{cr} is the critical temperature gradient for equiaxed nucleation and is used a criterion for calculation of CET (Ref. [3], p. 173).

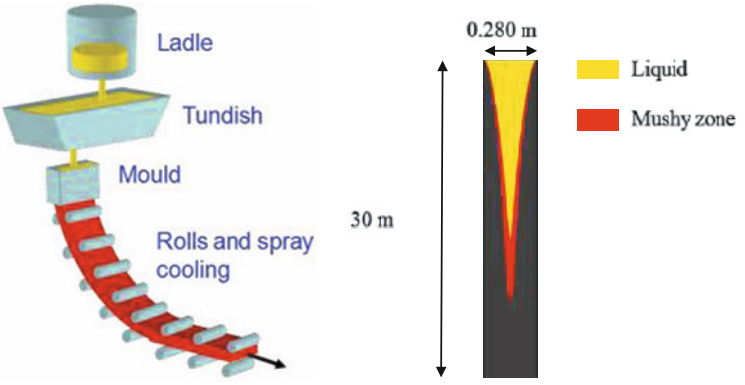

(a) (b)

Figure 1. (a) Schematic of the CC process [10] and (b) Longitudinal cross-section through a CC-processed slab (TEMPSIMU3D).

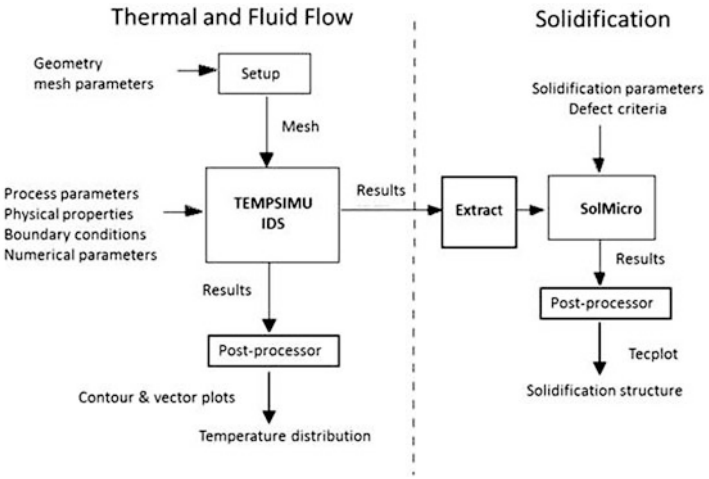

Figure 2. Coupling between **TEMPSIMU3D+IDS** simulation tools and **SolMicro** Stochastic Solidification Structure Simulator.

A special procedure was developed to compute and transfers all the transient information needed from the **TEMPSIMU3D+IDS** code to the **SolMicro** code including mushy-zone thermal gradients, cooling rates and solidification time.

As shown in Figure 2, the **TEMPSIMU3D+IDS** simulation code performs energy, momentum and solute transport computations to predict temperature, velocity and concentration distribution in the CC casting.

Then, from the transient temperature, concentration distributions computed by **TEMPSIMU+IDS** code, the **SolMicro** code computes the casting solidification microstructure evolution including grain morphology, grain size, and CET [6].

The **Extract** code computes and transfer all the information needed for the **SolMicro** simulator, including mushy-zone thermal gradients, cooling rates, and solidification time. The temperature history required by the **Extract** code is computed with the **TEMPSIMU** simulator. The additional solidification information required by **SolMicro** simulator is provided by **IDS** simulator.

Table 1. Boundary Conditions and Geometry for CC steel blooms and slabs

Model Conditions	Bloom	Slab A	Slab B
Casting width W[m]	0.372	1.974	1.962
Casting height, H[m]	0.312	0.279	0.279
Casting speed [m/min]	0.63	0.785	0.804
Mesh dimensions	47 x 40 x 613	50 x 20 x 617	50 x 20 x 617

Table 2. Thermal Properties of steel

Thermo-physical Property	Symbol	bloom	Slab A	Slab B
Density at solidus [kg m^{-3}]	ρ	7332	7318	7321
Thermal conductivity at solidus[W m^{-1} K^{-1}]	K	33.7	33.3	33.1
Liquidus temperature [C°]	T_L	1504	1505	1504
Solidus temperature [C°]	T_S	1453	1427	1422
Temperature of poured alloy [C°]	T_p	1559	1523	1548

Table 3. Enthalpy of steels (kJ/kg)

Temperature (C°)	Bloom	Slab A	Slab B
1600	1338	1329	1330
1500	1216	1206	1224
1400	930	922	923
1300	862	855	856
1200	795	788	789

Table 4. Data Used in Microstructure Modeling of steel

Solidification Kinetics Property	steel
Columnar nucleation parameters δN_c [nuclei m^{-2}]	$C_0 = 10^2$; $C_1 = 0$; $C_2 = 0$
Equiaxed nucleation parameters δN_e [nuclei m^{-3}]	$C_0 = 3.5 \times 10^5$; $C_1 = 3 \times 10^6$; $C_2 = 0$
Critical temperature gradient for CET, G_{cr} [K m^{-1}]	2000

Results and Discussion

The capability of the model to reconstruct CC bloom macrostructure was validated using measurements from a medium carbon Cr, Ni alloyed steel produced by OVAKO. Baumann (Sulfur) prints from the beginning, middle and end of a single heat were used to determine the location of the CET zone, as shown in figure 3. The modeled macrostructure for the top half of the CC bloom is shown in Figure 4. The model shows good agreement with the observed CET zone location.

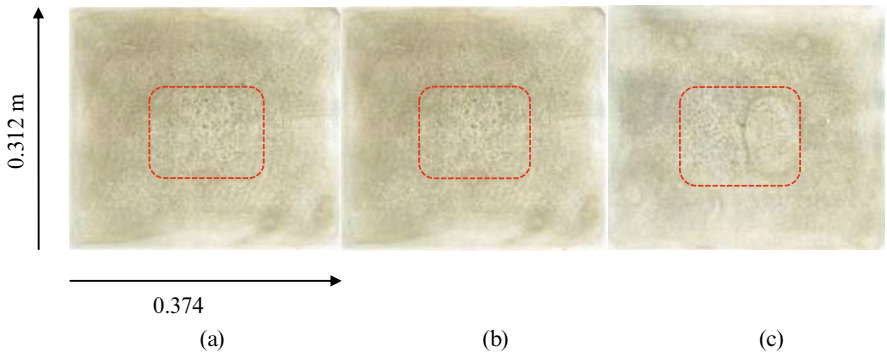

Figure 3. Baumann prints (Sulfur prints) of blooms at (a) start of cast, (b) center of cast, (c) end of cast highlighting the columnar-to-equiaxed transition.

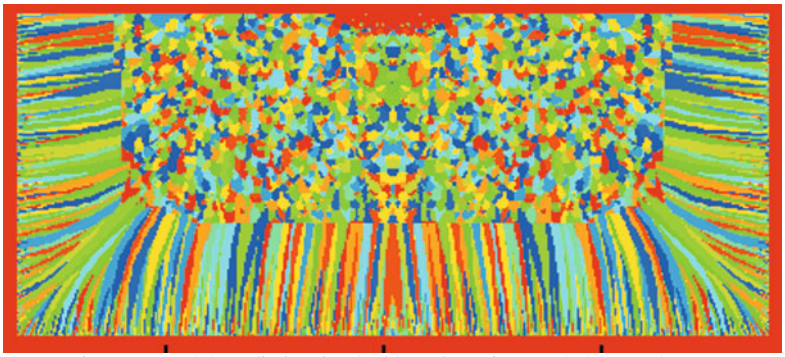

Figure 4. Model prediction for the bloom's grain morphology and CET.

The ability of the model to predict the slab macrostructure was validated using measurements from two slabs of a high-carbon medium-alloyed steel produced and analyzed by SSAB Europe Oy, Raahe. The slabs have similar composition but different values of superheat (45 K for slab B vs. 18 K for slab A). The ratio of different grain morphologies in the final macrostructures of the slabs is shown in figure 5.

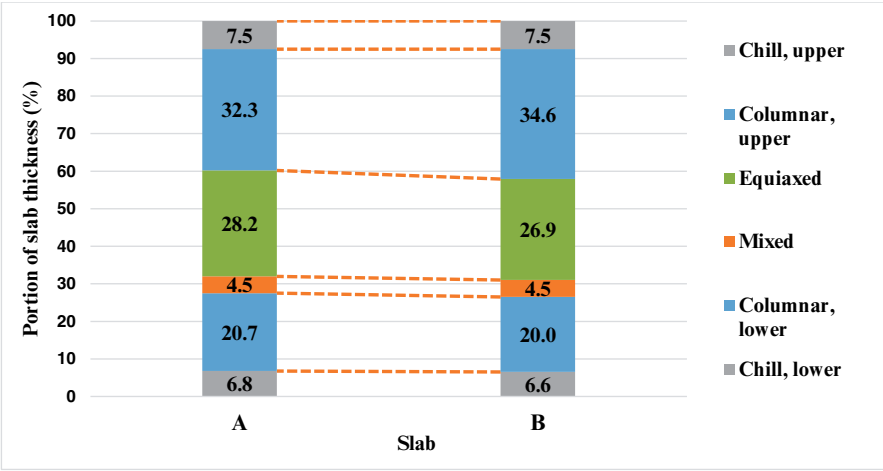

Figure 5. Experimental measurements of the grain morphology regions for slabs A and B.

The model predictions for the slabs A and B are shown in Figure 6. The measurements indicated 28.2% and 26.9% for the equiaxed grain region of the slab A and slab B, respectively. The model predicted an equiaxed-to-columnar ratio of 1:3 (~33% equiaxed grain region) for slab A and 1:3.3 for slab B (~30% equiaxed grain region). The predictions are in reasonable agreement with the experiments.

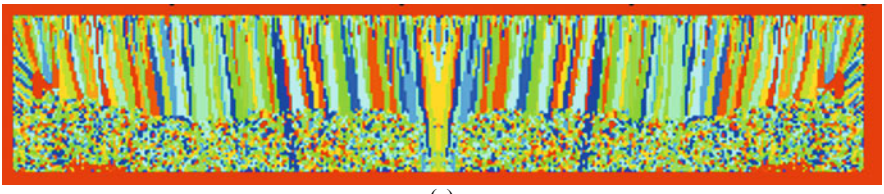

(a)

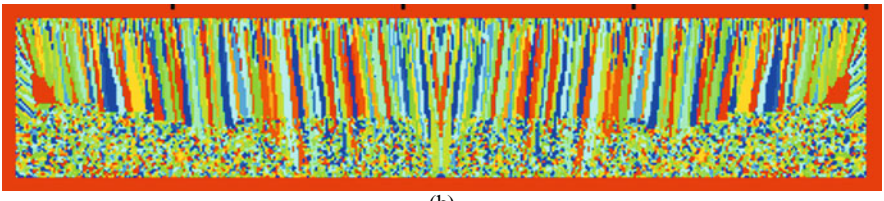

(b)

Figure 6. Model prediction for the slab's grain morphology and CET: (a) slab A and (b) slab B.

Conclusions and Future Work

An integrated multiscale transient modeling approach **TEMPSIMU3D+IDS** with **SolMicro**) was applied to simulate the solidification structure evolution during solidification of CC steel blooms and slabs. The integrated model was validated in terms of solidification structure against experimental data for CC processed steel blooms and slabs. The integrated modeling capability combined with prior production experience can be applied to determine the impact of casting conditions on the macrostructure behavior for different sizes of CC processed steel blooms and slabs and therefore it would potentially reduce the number of experimental trials needed in developing a new casting practice.
Future work will include additional model validation against experimental measurements in terms of grain size and CET for different steel alloys and for different sizes of blooms and slabs.

References

1. L. Nastac *et al.*, *Journal of Metals*, TMS, March 1998, pp. 30-35.
2. L. Nastac and A. Patel, Proc. of the Welding and Advanced Solidification Processes-MCWASP XI, Eds. C. Gandin and M. Bellet, TMS 2006, pp. 961-968.
3. L. Nastac, "Modeling and Simulation of Microstructure Evolution in Solidifying Alloys, Springer," Ney York, 2004 (ISBN 978-1-4020-7831-6).
4. L. Nastac, *Mat. Sc. and Tech.*, Vol. 28, No. 8, 2012, pp. 1006-1013.
5. L. Nastac, *Met Trans B*, Vol. 45B, 2014, pp. 44-50.
6. L. Nastac and D. M. Stefanescu, *Met Trans A*, Vol. 28A, 1997, pp. 1582-1587.
7. J. Miettinen, S. Louhenkilpi, H. Kytönen, and J. Laine, "IDS: Thermodynamic–kinetic–empirical tool for modelling of solidification, microstructure and material properties," *Math. Comput. Simul.,* Vol. 80, 2010, pp. 1536–50.
8. S. Louhenkilpi, M. Mäkinen, S. Vapalahti, T. Räisänen, and L. Laine, "3D steady state and transient simulation tools for heat transfer and solidification in continuous casting." *Mater. Sci. Eng. A,* Vol. 413-414, 2005**,** pp. 135–8.
9. P. Oksman, S. Yu, H. Kytönen, and S. Louhenkilpi, "The Effective Thermal Conductivity Method in Continuous Casting of Steel," *Acta Polytechnica Hungarica*, Vol. 11, No. 9, 2014, pp. 6-22.
10. S. Seetharaman, "*Treatise on Process Metallurgy, Volume 3: Industrial Processes*," Vol. 3. Newnes, 2013.

CFD Modeling and Simulation in Materials Processing 2016
Edited by: Laurentiu Nastac, Lifeng Zhang, Brian G. Thomas, Miaoyong Zhu, Andreas Ludwig, Adrian S. Sabau, Koulis Pericleous, and Hervé Combeau
TMS (The Minerals, Metals & Materials Society), 2016

NUMERICAL SIMULATION OF DENDRITIC GROWTH OF Fe-C BINARY ALLOY WITH NATURAL CONVECTION

Sen Luo[1,2], Weiling Wang[1], Miaoyong Zhu[1]

[1]Northeastern University; No.3-11 Wenhua Rd., Heping Dist.; Shenyang, Liaoning, 110819, China
[2]Ansteel Research Institute of Vanadium & Titantium (Iron & Steel)
No. 90 Taoyuan St., East Dist.; Panzhihua, Sichuan, 617000, China

Keywords: Dendritic Growth, Fe-C binary alloy, Natural Convection, Numerical Simulation

Abstract

Embedded the body force induced by the thermal and solutal gradient into the momentum conservation equation, a 2D CA-FVM model is developed for the numerical of dendritic growth with natural convection, and a numerical simulation is performed for the dendritic growth of Fe-0.82wt%C alloy in the presence of natural convection. The results show that the dendrite tip growth velocity is larger at the initial stage and rapidly decreases to steady-state value. The natural convection induced by the thermosolutal buoyancy is weak and promotes two vortexes flowing around the dendrite from the bottom to the top. With the further growth of dendrite, the natural convection is enhanced and four vortexes is developed between the dendrite arms. Also, the natural convection carries the heat and solute from the bottom to the top, resulting in promoting the downward dendrite branch growth and inhibiting the upward dendrite branch growth. Consequently, the asymmetries of the dendrite morphology, temperature and solute profiles are developed.

Introduction

The natural convection is an inevitable transport phenomenon during the solidification process of metallic alloys, due to the thermosolutal buoyancy under the gravity, and has effects on the dendritic growth and solute distribution.[1] The rejected solute during the dendritic growth is usually enriched in the interdendrtic region and can be also carried away by the natural convection. Thus, under the effects of the preferential flow in the interdendritic region induced by the natural convection, the channel segregation is tend to develop for the solidification of the metallic alloy, and has a great effect on the alloy properties. [2, 3] Therefore, basic understanding of the dendritic growth under the natural convection is very important for taking reasonable methods to control the solidification structure, in order to minimize the solidification defects and achieve the high quality alloy.

Cellular automaton (CA) method, as a popular probabilistic method, has been widely used in the field of computational modeling of dendritic growth in recent decades. In order to take the fluid flow effects into consideration, the momentum conservation equation should be coupled with the energy and species conservation equations. And the natural convection is usually included in the model for the dendritic growth by incorporating the thermal and solutal force into the momentum conservation equation. The traditional computational fluid dynamics (CFD) method, such as: finite difference method (FDM), finite volume method (FVM), and finite

element method (FEM), is the prior options for solving the Navier-Stokes (NS) equations and the continuity equation in the early research works. Yuan and Lee[4] incorporated the energy, mass and momentum conservation equations with the kinetics equations of dendritic growth to develop a cellular automaton (CA) model, where a projection algorithm[5] based on a staggered mesh is adopted for solving the NS equations using the FVM and a modified decentered square/octahedron algorithm[6] was implemented to explicitly catch the solid/liquid interface. Both the two- and three- dimension (2D and 3D) simulation are carried out to investigate the dendritic growth of Ni-Nb alloy with the forced and natural convection, and the difference between the 2D and 3D dendritic growth affected by the convection is clarified. Also the interdendritic flow and channel segregation during the unidirectional solidification of Pb-Sn alloy and Ga-In alloy are investigated using the 3D CA model. Shi *et al.*[7] established a 3D CA model by coupling Navier-stokes equations, the heat transfer equation and the solute convection and diffusion equation and investigated the dendritic growth with natural convection during the unidirectional solidification of NH_4Cl-H_2O solution. In recent years, Zhu *et al.* [8, 9] adopted the new and powerful CFD method, namely lattice Boltzmann method (LBM), to solve the fluid flow, heat transport and solute transport in their coupled CA-LBM model for the dendritic growth with fluid flow, and quantitatively investigated the dendritic growth in the presence of forced and natural convection. One of the most advantages of the model mentioned by the authors is that it has higher computational efficiency and better numerical stability for simulating the dendritic growth with complex fluid flow, when the solid fraction approaches the unity, than the model using the traditional CFD methods. But no matter which CFD method is adopted in the model, the most important thing is that the model should be capable of predicting the dendritic growth with fluid flow, especially for quantitative investigation.

In the present study, the previously developed 2D CA-FVM model[10] is extended to include the effect of thermal and solutal buoyancy and investigate the dendritic growth in the presence of thermosolutal convection.

Model Description

Momentum Conservation Equations

The Navier-Stokes equations for the incompressible fluid are given as followings:

Continuity equation:

$$\nabla \cdot \mathbf{U}=0 \tag{1}$$

Momentum conservation equation:

$$\rho \frac{\partial \mathbf{U}}{\partial t} + \rho \mathbf{U} \cdot \nabla \mathbf{U} = -\nabla p + \nabla \left(\mu \nabla \mathbf{U} \right) + F \tag{2}$$

where **U** is the velocity vector, ρ is the density, is the viscosity, p is the hydrostatic pressure, t is the time, and F is the additional force.

According to the Boussinesq approximation, the thermal and solutal buoyancy linearly change with temperature and can be incorporated into the momentum conservation equation as the additional force.

$$F = -\rho_0 g \left(\beta_t \left(T - T_0 \right) + \beta_c \left(C - C_0 \right) \right) \tag{3}$$

where g is the gravitational acceleration, ρ_0, T_0 and C_0 are respectively the reference density, temperature and composition, β_t and β_c are respectively the thermal and solutal expansion coefficients, and T and C are respectively the local temperature and concentration.

Species Conservation Equations

The Fick's law with convection is given by:

$$\frac{\partial C_e}{\partial t} + \xi \mathbf{U} \cdot \nabla C_e = D_e \cdot \nabla^2 C_e \tag{4}$$

where ξ is a constant related to the CA cell state (when the cell state is liquid or interface, ξ is 1; when the cell state is solid, ξ is 0), C_e and D_e are respectively the equivalent concentration and solute diffusion coefficient, and defined as followings:

$$C_e = C_s f_s + C_l f_l = C_l \left(1 - \left(1 - k_0\right) f_s\right) \tag{5}$$

$$D_e = D_s f_s + D_l f_l \tag{6}$$

where C_s and C_l are respectively the solid concentration and the liquid concentration, D_s and D_l are respectively the solute diffusion coefficient in the solid and liquid phase, and f_s and f_l are the solid fraction and liquid fraction, respectively.

Energy Conservation Equation

The energy conservation equation is given by

$$\frac{\partial T}{\partial t} + \xi \mathbf{U} \cdot \nabla T = \frac{\lambda}{\rho c_p} \nabla^2 T + \frac{L}{c_p} \frac{\partial f_s}{\partial t} \tag{7}$$

where T is the temperature, λ is the thermal conductivity, c_p is the specific heat, L is the latent heat.

Kinetics Equations for dendritic growth

Assuming the local equilibrium is reached at the solid/liquid (S/L) interface, the interface solute concentration and the normal velocity of the interface, V_n^*, are determined by the following equations:[11, 12]

$$C_s^* = k_0 C_l^* \tag{8}$$

$$V_n^* = \left(-D_l \nabla C_l + D_s \nabla C_s\right) \cdot \mathbf{n} \Big/ \left(C_l^* - C_s^*\right) \tag{9}$$

where C^*_l and C^*_s are respectively the local liquid and solid solute concentration at the S/L interface, k_0 is the equilibrium partition coefficient, and $\mathbf{n}=\nabla f_s$ is a normal vector of the solid fraction at the S/L interface.

Here, the equilibrium liquid concentration at the S/L interface can be determined by

$$C_l^* = C_0 + \left(T^* - T_l + \Gamma \kappa f\left(\varphi, \theta\right)\right) \Big/ m_0 \tag{10}$$

where C_0 is the initial solute concentration, T_l is the equilibrium liquidus temperature at the initial composition, T^* is the interface equilibrium temperature, m_0 is the liquidus slope, Γ is the Gibbs-Thomson coefficient, κ is the curvature of the S/L interface, and $f(\varphi,\theta)$ is a function describing the anisotropy of the interface energy, where θ is the angle of the preferential growth direction (crystallographic orientation) with respect to a reference axis, and φ is the angle of the normal to the interface with respect to the same reference axis (growth angle).

For cubic crystals, the anisotropy of the interface energy is four-fold and can be calculated as follow: [13]

$$f\left(\varphi, \theta\right) = 1 - \delta \cos\left(4\left(\varphi - \theta\right)\right) \tag{11}$$

where $\delta=15\varepsilon$ is the anisotropy coefficient, ε is the anisotropy degree of the surface tension.

In 2-D Cartesian coordinates, the growth angle is evaluated as the gradient of the solid fraction at the solid/liquid interface and given as follow[11, 12]:

$$\varphi = \arccos\left((f_s)_x \Big/ \sqrt{(f_s)_x^2 + (f_s)_y^2} \right) \tag{12}$$

The local interface curvature can be also derived from the gradient of the solid fraction as follow: [11, 12]

$$\kappa = \left[2(f_s)_x (f_s)_y (f_s)_{xy} - (f_s)_x^2 (f_s)_{yy} - (f_s)_y^2 (f_s)_{xx} \right] \Big/ \left[(f_s)_x^2 + (f_s)_y^2 \right]^{3/2} \tag{13}$$

where $(f_s)_x$ and $(f_s)_y$ are the first partial derivatives of solid fraction with respect to the (x, y) axes of the Cartesian coordinates, and $(f_s)_{xx}$, $(f_s)_{xy}$ and $(f_s)_{yy}$ are the second partial derivatives of solid fraction with respect to the (x, y) axes of the Cartesian coordinates.

Case Description

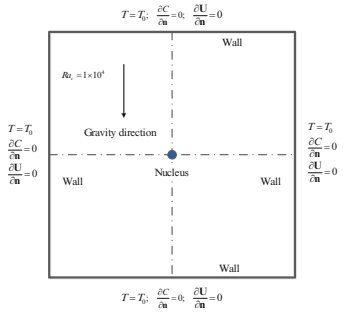

Fig. 1 Schematic diagram of calculation domain and boundary conditions

Table 1 Thermophysical parameters of Fe-0.82wt%C binary alloy[10, 15]

Property	Symbol	Fe-0.82wt%C	Units
Melting temperature	T_m	1809	K
Density	ρ_0	7020	Kg/m^3
Liquidus slope	m_0	-78.0	K/wt%
Conductivity	λ	33.0	W/(m·K)
Specific heat	C_p	824	J/(kg·K)
Latent heat	L	2.72×10^5	J/kg
Liquid mass diffusivity	D_l	$7.67\times10^{-6}\exp(-106000/RT)$	m^2/s
Solid mass diffusivity	D_s	$7.61\times10^{-6}\exp(-134564/RT)$	m^2/s
Partition coefficient	k_0	0.34	-
Thermal expansion coefficient	β_t	0.0002	1/wt%
Solutal expansion coefficient	β_c	0.011	1/K
Gibbs-Thomson coefficient	Γ	1.9×10^{-7}	K·m
Degree of anisotropy	ε	0.04	-

By coupling the momentum, species and energy conservation equations with the kinetics equations of dendritic growth, the 2D CA-FVM model is developed to predict the dendritic growth in presence of fluid flow, where the traditional CFD method, FVM, is adopted to solve the transport equations, based on the probabilistic method, CA. Meanwhile, the 2D CA-FVM has been validated with the modified 2D Ivantsov solutions [8] for dendritic growth with thermosolutal convection, and the good agreement has been achieved. Here, only the model capability is demonstrated. A square domain is assumed for the numerical simulation of the dendritic growth of Fe-0.82wt%C binary alloy with natural convection, and meshed into 401 × 401 cells with size of 0.7 m, which is proved to be fine enough to eliminate the mesh

dependency according to our previous study.[14] The calculation domain is schematically shown in **Fig. 1**, and the thermophysical parameters of Fe-0.82wt%C binary alloy used in the present simulation are listed in **Table 1**.

The four sides of the calculation domain are wall boundaries with constant temperature, zero-flux and non-slip for the heat, species and momentum transfer calculation, respectively. At the beginning of simulation, a nucleus with the composition of k_0C_0 and the crystallographic orientation of 0^0 with respect to the horizontal direction is assigned at the center of the square domain with the undercooled melt of 5K. Due to the thermal and solutal gradients under gravity, the thermosolutal convection will be developed with the dendritic growth and can be characterized by the thermal Rayleigh number , Ra_t, and the solutal Rayleigh number, Ra_c, respectively.

$$Ra_t = \beta_t \Delta T_c g l_c^3 / (\nu\alpha) \tag{14}$$

$$Ra_c = \beta_c \Delta C_c g l_c^3 / (\nu D) \tag{15}$$

where T_c, C_c is the characteristic temperature and solute concentration difference, l_c is the characteristic length scale for natural convection, ν is the kinetic viscosity and α is the thermal diffusivity.

Here, the solutal Rayleigh number is assumed to be 1×10^4 in the present study, and the heat Rayleigh number is simply determined by the relationship equation, namely, $Ra_t=\beta_t D/(\beta_c\alpha)Ra_c$, it seems to be more reasonable than the previous assumption that the heat Rayleigh number was same as the solutal Rayleigh number, [9, 10] because the thermal diffusivity of metallic alloys is 3~4 orders of magnitudes greater than the solute diffusivity.

Results and Discussion

Fig. 2 shows the predicted equiaxed dendrite morphology growing in an undercooled melt of 5K with the solutal Rayleigh number of 1×10^4, and the flow field with one vector in every 10×10 cells is overlapped on the dendrite morphology in order to clearly show the flow pattern. It can be seen clearly that with the dendritic growth, the solute is rejected and heat is released at the S/L interface, and the solutal and thermal gradient are established at the solidification front. Due to the effect of gravity, the thermosolutal convection is developed in the square domain, and the natural convection flows smoothly around the dendrite from the bottom to the top. The solute field and dendrite morphology are almost symmetrical, because the thermosolutal convection is weak at the early stage of dendritic growth. As the dendrite further grows, the solute is rejected and heat is released at the S/L interface continuously, and the natural convection induced by the thermal and solutal buoyancy under the gravity is gradually enhanced. Also, the solute concentration in the upper region is obviously larger than that of the lower region in the square domain, because the enhanced convection carried more solute from the lower region to the upper region. The solute boundary at the upward dendritic growth tip is thicker than that of the doward dendritic growth tip, and thus the lower solutal gradient will be formed in the upper region, resulting in the lower tip velocity of the upward growing branch in the upper region and higher tip velocity of the downward growing branch in the lower region. Consequently, the solute field and dendrite morphology become asymmetrical.

Fig. 3 shows the dendrite morphology and the streamlines in the square domain. It is notable that at the early stage of dendritic growth, there are two axial symmetrical vortexes, which flow upward around the dendrite and downward along the lateral sides of the square

domain. With the further growth of dendrite, the dendrite grows big enough to prohibit the upward flow directly crossing the horizontal dendrite branch, and four vortexes are developed between the dendrite arms. Also, the thermosolutal convection is enhanced by the thermal and solutal buoyancy, and has more significant effects on the dendritic growth.

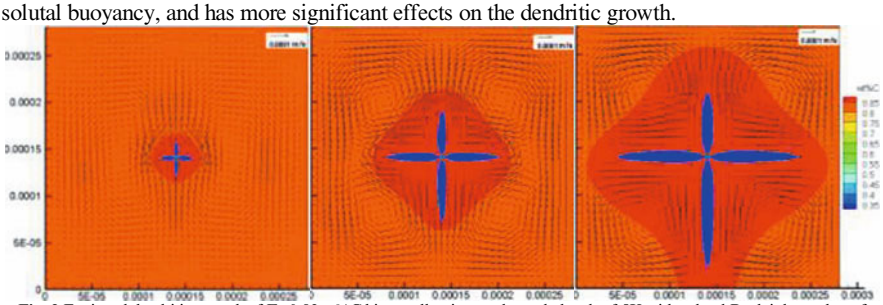

Fig. 2 Equiaxed dendritic growth of Fe-0.82wt%C binary alloy in a undercooled melt of 5K with solutal Rayleigh number of 1×10^4: (a) 0.1s, (b) 0.5s, (c) 1.0s

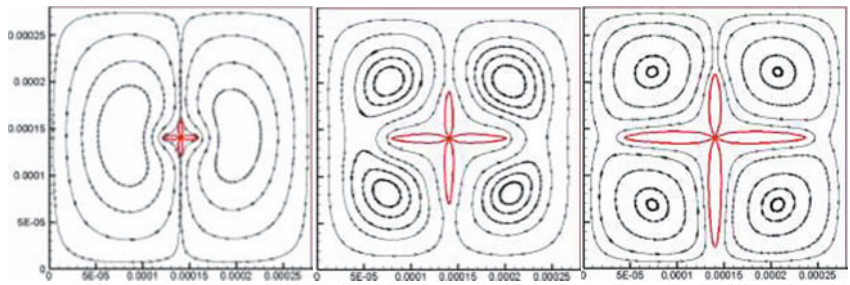

Fig. 3 Streamlines in the square domain with equiaxed dendrite growth of Fe-0.82wt%C binary alloy for different time with solutal Rayleigh number of 1×10^4: (a) 0.1s, (b) 0.5s, (c) 1.0s

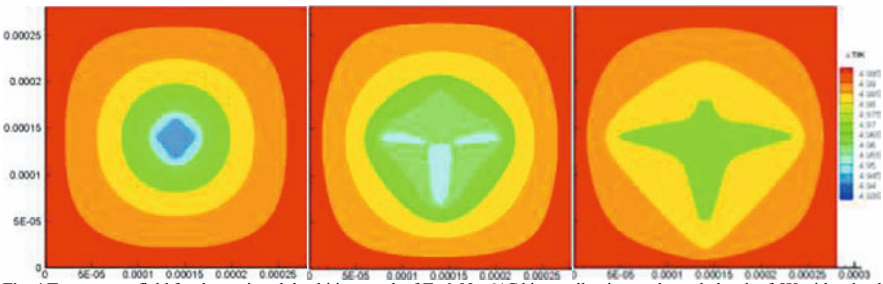

Fig. 4 Temperature field for the equiaxed dendritic growth of Fe-0.82wt%C binary alloy in a undercooled melt of 5K with solutal Rayleigh number of 1×10^4: (a) 0.1s, (b) 0.5s, (c) 1.0s

Fig. 4 shows the temperature field for the dendritic growth of Fe-0.82wt%C binary alloy. It can be seen that with the dendritic growth, the temperature around the dendrite becomes much higher than the melt temperature, because the heat is released at the S/L interface. At the early stage of the dendritic growth, the temperature field is almost symmetrical, because the natural

convection is weak and has a little effect on the temperature field. With the further growth of dendrite, under the effect of natural convection, the downward dendrite branch grows faster than the upward dendrite branch, resulting in more heat released by the downward growing branch and less heat released by the upward growing branch. Thus, the temperature field also becomes asymmetrical under the effect of the natural convection.

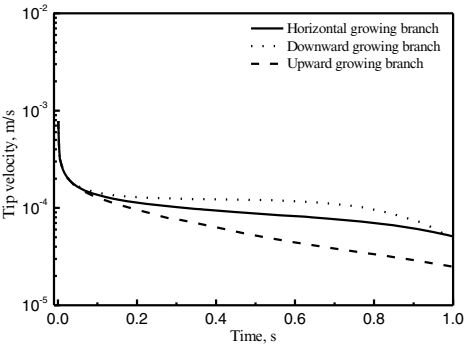

Fig. 5 Tip velocities of the equiaxed dendritic growth of Fe-0.82wt%C binary alloy in a undercooled melt of 5K with solutal Rayleigh number of 1×10^4: (a) 0.1s, (b) 0.5s, (c) 1.0s

Fig. 5 shows the tip velocities for the dendritic growth of Fe-0.82wt%C binary alloy. It can be seen that at the initial stage of the dendritic growth, the four dendrite branches have same high tip velocities and rapidly decreases, because the rejected solute and released heat at the S/L significantly inhibit the dendritic growth. As the dendrite grows further, the tip velocity gradually approaches the steady-state value. However, owing to the effects of the natural convection induced by the thermal and solutal buoyancy, the solute rejected by the downward growing branch is carried by the upward flow and enriched in the upper region. Thus, the tip velocity of the downward growing branch is larger than that of the upward growing branch, and the tip velocity of the horizontal growing branch has an intermediate tip velocity. Another phenomenon should be mentioned that at the later stage of the dendritic growth, the downward growing branch approaches the domain bottom and affected by the wall boundary. Thus, the tip velocity of the downward growing branch gradually decreases. This phenomenon can be released by the calculation domain enlargement.

Conclusions

By coupling the momentum, species and energy conservation equations with the kinetics equations of dendritic growth, the 2D CA-FVM model is developed to predict the dendritic growth in presence of fluid flow, where the traditional CFD method, FVM, is adopted to solve the transport equations, based on the probabilistic method, CA. The thermosolutal convection is taken into consideration by incorporating the thermal and solutal buoyancy induced by the temperature and solute concentration difference under the gravity into the momentum as an additional force term. A numerical simulation of the dendritic growth of Fe-0.82wt%C binary alloy in the presence of natural convection is performed, and the results show that for the undercooling of 5K and the solutal Rayleigh number of 1×10^4, the four dendrite branches grow with high velocities at the initial stage and rapidly the dendritic growth is significantly inhibited

by the rejected solute and released heat at the S/L interface, and gradually approaches the steady-state velocity. At the early stage, two vortexes are developed and respectively located on the left and right side of the dendrite. With further growth of dendrite, the natural convection is enhanced and has a significant effect on the dendritic growth. The tip velocity of the upward growing branch in the upper region is larger than that of the downward growing branch in the lower region, resulting in more solute and heat released at the S/L interface. Therefore, the solute field, temperature field and dendrite morphology become asymmetrical under the effects of natural convection.

Acknowledgements

The authors gratefully acknowledge the financial support of National Natural Science of China (No. 51404062), Specialized Research Fund for the Doctoral Program of Higher Education of China (No. 20130042120042) and Outstanding Talent Cultivation Project of Liaoning Province (No. 2014029101).

References

[1] M. Asta, C. Beckermann, A. Karma, *et al*., "Solidification microstructures and solid-state parallels: recent developments, future directions", *Acta Mater.*, 57(2009), 941-971.
[2] M. Medina, Y. Du Terrail, F. Durand, *et al.*, "Channel segregation during solidification and the effects of an alternating traveling magnetic field", *Metall. Mater. Trans.* 35B(2004), 743-754.
[3]S. N. Tewari, R. Tiwari, G. Magadi, "Mushy-zone rayleigh number to describe macrosegregation and channel segregate formation during directional solidification of metallic alloys", *Metall. Mater. Trans.* 35A(2004), 2927-2934.
[4] L. Yuan, P. D. Lee, "Dendritic solidification under natural and forced convection in binary alloys: 2D versus 3D simulation", *Model. Simul. Mater. Sci. Eng.* 18(2010), 055008.
[5] Kim J, P. Moin, "Application of a fractional-step method to incompressible Navier-Stokes equations", *J. Comput. Phys.* 59(1985), 308-323.
[6] W. Wang, P. D. Lee, M. McLean, "A model of solidification microstructures in nickel-based superalloys: predicting primary dendrite spacing selection", *Acta Mater.*, 51(2003), 2971-2987.
[7] Y. F. Shi, Q. Y. Xu, B. C. Liu, "Simulation and experimental research of melt convection on denrite morphology evolution" , *Acta Phys. Sin.* 60(2011), 126101.
[8] D. K. Sun, M. F. Zhu, S. Y. Pan, *et al.*, "Lattice Boltzmann modeling of dendritic growth in forced and natural convection", *Comput. Math. Appl*. 61(2011), 3585-3592.
[9] M. F. Zhu, D. K. Sun, S. Y. Pan, *et al*., "Modelling of dendritic growth during alloy solidification under natural convection", *Model. Simul. Mater. Sci. Eng.* 22(2014), 034006.
[10] W. L. Wang, S. Luo, M. Y. Zhu, "Dendritic growth of high carbon iron-based alloy under constrained melt flow", *Comput. Mater. Sci.* 95(2014), 136-148.
[11] L. Beltran-Sanchez, D. M. Stefanescu, "Growth of solutal dendrites: A cellular automaton model and its quantitative capabilities", *Metall. Mater. Trans.* 34A(2003),367-382.
[12] L. Beltran-Sanchez, D. M. Stefanescu, "A quantitative dendrite growth model and analysis of stability concepts", *Metall. Mater. Trans.* 35A(2004), 2471-2485.
[13] M. F. Zhu, D. M. Stefanescu, "Virtual front tracking model for the quantitative modeling of dendritic growth in solidification of alloys", *Acta Mater.* 55(2007), 1741-1755.
[14] S. Luo, M. Y. Zhu, "A two-dimensional model for the quantitative simulation of the dendritic growth with cellular automaton method", *Comput. Mater. Sci.* 71(2013), 10-18.
[15] W. L. Wang, S. Luo, M. Y. Zhu, "Numerical simulation of dendritic growth of continuously cast high carbon steel", *Metall. Mater. Trans.* 46A(2015), 396-406.

CFD Modeling and Simulation in Materials Processing 2016
Edited by: Laurentiu Nastac, Lifeng Zhang, Brian G. Thomas, Miaoyong Zhu, Andreas Ludwig, Adrian S. Sabau, Koulis Pericleous, and Hervé Combeau
TMS (The Minerals, Metals & Materials Society), 2016

LOCALIZED STRENGTHENING OF Al-BASED CASTING ALLOYS BY AUTOMATIZED OPTIMIZATION OF LASER HEAT TREATMENT

A. Ludwig, T. Holzmann

Chair of Simulation and Modelling of Metallurgical Processes,
Montanuniversitaet Leoben, Austria

Keywords: Al-alloys, Heat treatment, automatized Optimization

Abstract

The mechanic properties of many Aluminum alloys can be changed by a heat treatment and quenching procedure. If locally a strengthening of the alloy is needed, a localized heat treatment and quenching procedure may be an alternative to the energy intensive and costly treatment of the whole part. However, it is not obvious which process parameters are required in order to achieve the desired local strengthening. Thus, a numerical simulation of local heating and cooling in combination with predictions of the material constitution and thus local property changes is used for a multicriteria optimization approach where the desired local strengthening is defined as target function. The optimization scheme performs a series of process simulations where laser power and exposure time are varied automatically until the effective process is found which ensures sufficient local strengthening of the alloy.

Introduction

Castings made of Al-based alloys are often heat treated in order to improve their mechanical properties. This heat treatment happens in two steps. First, a supersaturated solid solution is obtained by heating up the casting to a certain temperature and then this state is conserved by rapid quenching back to room temperature. When this supersaturated solid solution is again heated up, but now mildly (if ever), different precipitations occur which hardens the material. In case of the AlSi7Mg0.5 alloy, which is focused on in the present work, the following precipitation sequence occurs from the quenched-in supersaturated solid solution upon heating: clusters with varying Mg and Si content, Guinier-Preston Zones (GP-Zones), beta'- and U1/U2-phases and the B-phase [1, 2, 3].

If strengthening of the material is only needed locally, energy and time could be saved by performing a local heat treatment. This might be especially efficient, if only one heating cycle is sufficient and self-quenching is used. Such a local heating is conceivable with different heat sources of which the laser is the most elegant, flexible and precise. However, when distinct material improvements are desired the power input, the beam diameter, the duration of heating and the necessary quenching strength are a prior unknown.

In this paper, an automatized optimization procedure is suggested that focus on short time local laser heating with quenching of an as-cast AlSi7Mg0.5 alloy in order to improve the strength of the material so that it can resist a prescribed loading.

Numerical Approach

Case of Loading

As starting point of this work, we have considered a simple rhombus-like plate casting with a centered hole. As case of loading the plate casting is considered to be fixed with a screwing connection at the center hole that is loaded with a prescribed mass, here of 360 kg that is acting on a ring area of 300 mm². The task of the optimization procedure is that the material property, namely the yield strength, should locally be improved by a laser heat treatment with subsequent quenching so that plastic deformation of the material can be avoided. If ideal elasto-plastic behavior is assumed and the local yield strength is given as $R_{p0.2}$, and the van Mises equivalent stress as σ^{eq}, then the condition of no plastic deformation can be written as

$$\Delta = R_{p0.2}(\vec{r}) - \sigma^{eq}(\vec{r}) \cdot S \geq 0, \tag{1}$$

where S represents a security factor. Condition Eq. (1) must be fulfilled at all positions, $\vec{r}$, in the whole casting, especially in the vicinity of the loaded area at the center hole. Due to the axis-symmetry of the case of loading we have considered only a segment of the plate casting for the stress analysis (and the heat treatment described later). The segment was chosen long enough so that the outer boundary conditions do not affect the stress evolution close to the center hole. Fig. 1 shows the considered segment together with the assume boundary conditions for the stress analysis. The stress analysis was done with OpenFOAM [4] solving for the divergence of the Cauchy stress tensor to be zero. The position-dependent yield stress and also the Young's modulus were taken from a MatCalc simulation as explained below.

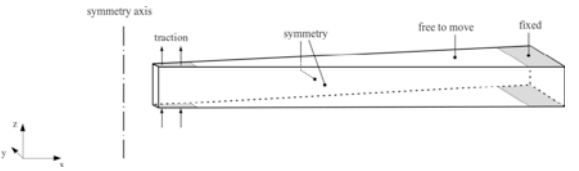

Figure 1. Wedge-shaped segment considered for the stress analysis. For the center hole a radius of 4 mm, for the segment a length of 200 mm and for the casting thickness 8 mm were chosen. An area at the outer fringe of the casting of 0.01285 m² was taken as fixed.

Heat Treatment

We have considered a Gaussian-shaped heat input of total power, P, for a certain time, t. Both, P and t are parameters which are subject to variations during the optimization procedure. P is varied between 500 and 8000 W and t between 1 and 105 s. Although a possible additional parameter to be varied, we have used a fix beam radius of $R = 15$ mm in this work. As initial condition, we started with the material at room temperature, used symmetry conditions at the wedge side faces and a heat transfer coefficient, h, with an ambient temperature, T_{amb} at top, bottom, left and right surface [5]. For the heating period, we took $h = 50$ W/m²/K with $T_{amb} = 293$ K, and for the quenching period $h = 15.000$ W/m²/K with $T_{amb} = 283$ K. As quenching period we always took 20 s. Fig. 2 shows a schematic draft of the heat source acting on the area around the center hole of the plate

casting. Note that the segment was chosen long enough so that the local heat treatment at the center never affects the outer boundary. For the time-depending temperature evolution in the plate we have solved the heat conductivity equation with OpenFOAM [4] using a heat conductivity of λ = 156 W/m/K, a heat capacity of c_p = 778 J/kg/K and a density of ρ = 2560 kg/m^3 for the considered AlSi7Mg0.5 alloy [6]. Note that the temperature-time curves at the six marked positions, which we call testing probes, were further used for the phase constitutive simulation.

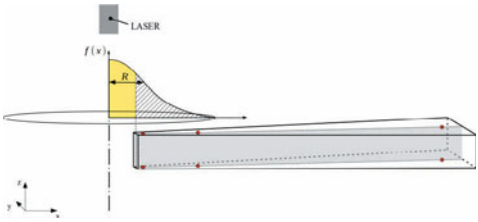

Figure 2. Schematic draft of the heat source. The non-hatched area below the Gauss-function defines the amount of energy being lost through the center hole.

The fact that a Gaussian-shaped laser beam at the center hole of the casting radiates most of its energy into the center hole could be avoided by using a ring-shaped laser beam. However, for the present investigation the exact shape of the laser beam is not of great importance as we are focusing on the strategy for the automatized optimization rather than on specific process details.

High laser power and long exposure time might lead to melting of the material. This has to be avoided. In the automatized optimization routine, parameter combinations where this happens are forbidden and excluded from the set of trials. A more sophisticated treatment of the melting problem is the introduction of two specific temperatures. At T_{off} the laser source is switched off and at T_{on} it is again switched on. The result of such an alternative off/on procedure is shown in Fig. 3. In the present numerical heat treatment this procedure is easy to implement. In practice, an empirical shutter or guided power-down technique applied at the laser control unit would be more adequate.

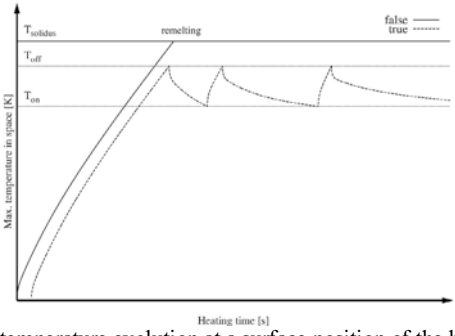

Figure 3. Possible temperature evolution at a surface position of the heated part. To avoid melting a temperature-guided shutter technique for the laser beam is tested.

Material Constitution Simulation

The evolution of the material constitution for the AlSi7Mg0.5 alloy during heat treatment and quenching was calculated at the six testing probes shown in Fig. 2 by using the commercial code MatCalc [7]. Based on a thermodynamic database and corresponding precipitation calculations, MatCalc also provide data on the yield strength and Young's modulus. However, for the heat treatment and quenching simulation the constitution of the as cast material has to be known as initial state. That's why we have performed a multicomponent Scheil solidification simulation [8] while MatCalc already calculates phase and precipitation evolution together with concentration profiles. Based on these results, the evolution of the material constitution during heat treatment and quenching is calculated using the temperature/time history at the before mentioned six testing probes. The final yield stresses and Young's moduli are then area-weighted interpolated, respectively extrapolated, onto the whole wedge-shaped segment. Such position-dependent mechanical properties are used in the stress analysis mentioned above.

Automatized Optimization Scheme

The task the automatized optimization should solve is to find a proper laser power and exposure time combination which is suitable to reach, at any point in the casting, a yield strength larger than the von Mises equivalent stress occurring during loading (Eq. (1)). This condition is fulfilled if the minimum difference between yield strength and von Mises equivalent is larger or equal to zero, that's

$$\delta_{out} = \min\{\Delta(\vec{r})\} \geq 0 \,. \tag{2}$$

If δ_{out} is larger than zero the local strengthening of the material by heat treatment and quenching is stronger than necessary. We thus chose $\delta_{out} = 0$ as target function for the optimization. That implies that no plastic deformation occurs with a minimum of heat treatment effort.

In the present study, we have used a gradient-based scheme from the open source optimization platform Dakota [9]. Fig. 4 shows the flow chart for the optimization scheme. As described above the process chain being addresses here consists of (a) casting and solidification; (b) local heat treatment and quenching; and (c) the case of loading. However, from a modelling point of view the chain has to be treated more detailed: (i) material constitution during solidification; (ii) material constitution during cooling to room temperature; (iii) temperature evolution during heat treatment and quenching; (iv) material constitution during heat treatment and cooling; (v) extraction of yield strength and Young's modulus; (vi) inter/extrapolation onto the 3D grid for stress analysis; (vii) 3D analysis of the case of loading. Steps (i) to (v) have to be done point-wise e.q. at the selected testing probes shown in Fig. 2. For points (vi) and (vii) all three dimensions are involved (3D). If the load analysis reveals $\delta_{out} = 0$ the optimum is found and the procedure stops. If not the procedure starts all over again with a new set of input parameter (for now laser power, P, and exposure time, t). The next (P, t)-input set is suggested by Dakota based on the above mentioned gradient-based scheme.

Actually, part (i) and (ii) could be placed out of the optimization loop, as the as-cast material is the bases for the local heat treatment procedure. However, we are currently working at a scheme where the solidification conditions will affect the local material constitution. Then casting temperature

or cooling conditions during solidification might also be possible inputs for an extended input set. In this more general case, part (i) and (ii) must be considered inside the optimization loop.

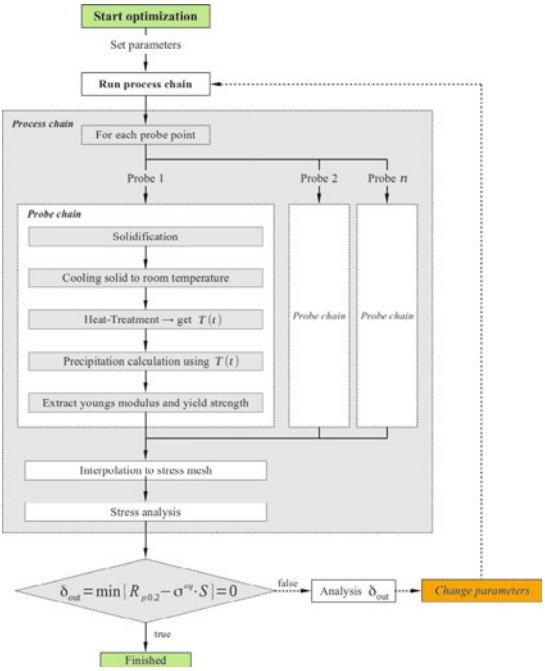

Figure 4. Flow chart of the automatized optimisation scheme.

Results and Discussion

The local heat treatment with quenching procedure results in the occurrence and growth of particular precipitations, which strengthen the material by increasing the yield strength. It is beyond the scope of this paper, to give further details on the mechanisms causing this increase. Fig. 5 shows the yield strength (here $R_{p0.2}$) depending on laser power and exposure time at the position where the maximum von Mises stresses occur. For lower laser power the local heating is not strong enough to reach a temperature level that favors the occurrence and growth of precipitations. Thus, the yield strength is the as-cast one (around 104 MPa). For higher laser power the yield strength increases to more than 130 MPa, whereby the shorter the exposer time the larger the power necessary to reach this increase. However, shortly after reaching the maximal level melting occurs and thus no data points are given any more.

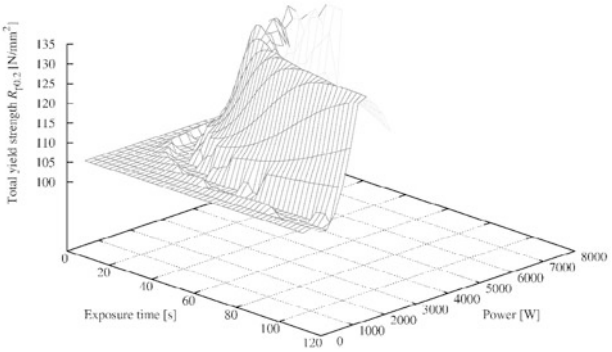

Figure 5. Strengthening of the material as function of laser power and heating time. For larger powers melting occurs and thus the power-time data set is cancelled.

In order to avoid melting at the casting surface, the shutter technique mentioned above with T_{off} = 793 K and T_{on} = 773 K was applied. Fig. 6 shows the corresponding yield strength surface. Now even higher laser powers for longer heating times are allowed without melting the material.

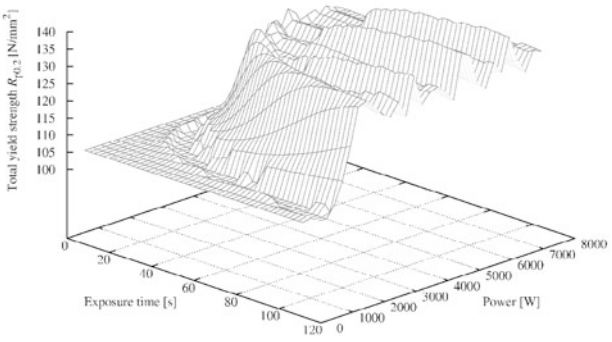

Figure 6. Strengthening of the material using the laser shutter technique according to Fig. 3.

As described above, in the present optimization scheme δ_{out} is the output quantity and P and t are the input quantities. The gradient-based optimization algorithm from Dakota suggests a new input data set (P, t) based on the actual value of δ_{out} and its gradient with respect to (P, t). Fig. 7 shows how the optimization scheme quite quickly finds the optimum, namely $\delta_{out} = 0$. Only 36 optimization loops were needed. Of course the scheme is generalizable and further variable parameter could be used as input data set.

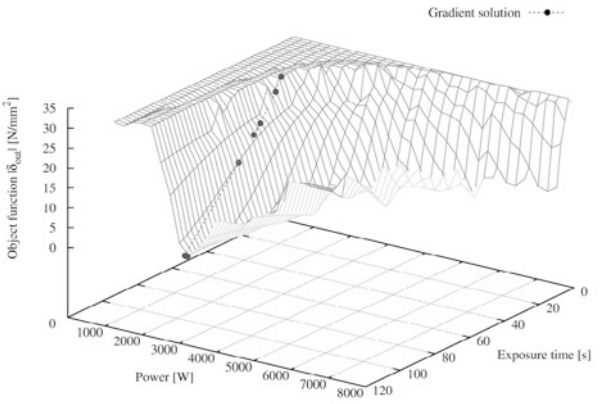

Figure 7. The target function, $|\delta_{out}(P, t)|$, evolves corresponding to the optimization strategy. For the presented case the minimum, $\delta_{out} = 0$, was found after 36 iterations.

Conclusion

In this paper, it was demonstrated that local strengthening of an as-cast AlSi7Mg0.5 alloy with a short time laser heat treatment might be possible. With an automatized optimization scheme the necessary laser power and exposure time was estimated to locally increase the yield strength so that the material can withstand a localized traction acting e.g. at a screwing connection without any plastic deformation. Beside a 3D heat transfer calculation and 3D stress analysis, the procedure uses predictions from the material calculator MatCalc, which are currently under validation. The proposed procedure has great potential as it might allow to account for casting features like casting temperature, cooling conditions, alloy composition, laser beam diameter and much more. Especially with the increased usage of robotics, it is conceivable that local laser heat treatment, preferable with self-quenching, might gain in importance. We think that the present paper is a significant step into that direction, as it shows how the suitable process parameters might be obtained. Energy and time saving might be the ultimate benefit of the proposed local strengthening of Al-based alloys.

Acknowledgement

Financial support by the Austrian Federal Government (in particular from the Bundesministerium fuer Verkehr, Innovation und Technologie and the Bundesministerium fuer Wirtschaft, Familie und Jugend) and the Styrian Provincial Government, represented by Oesterreichische Forschungs-foerderungsgesellschaft mbH and by Steirische Wirtschaftsfoerderungsgesellschaft mbH, within the research activities of the K2 Competence Centre on "Integrated Research in Materials, Processing and Product Engineering", operated by the Materials Center Leoben Forschung GmbH in the framework of the Austrian COMET Competence Centre Program, is gratefully acknowledged.

References

[1] R. Vissers, M.A. van Huis, J. Jansen, H.W. Zandbergen, C.D. Marioara, and S.J. Andersen, "The crystal structure of the β′ phase in Al-Mg-Si alloys," *Acta Mater.*, 55 (2007), 3815-23.

[2] A. Falahati, M.R. Ahmadi, P. Lang, E. Povoden-Karadeniz, P. Warczok, and E. Kozeschnik, „Thermo-kinetic computer simulation of precipitation and age-hardening effect in Al-Mg-Si alloys with arbitrary heat treatment," *Materials Science and Technology Conference and Exhibition 2011, MS and T'11*, (2011), 292-299.

[3] A. Falahati, E. Povoden-Karadeniz, P. Lang, P. Warczok, E. Kozeschnik, "Thermo-kinetic computer simulation of differential scanning calorimetry curves of AlMgSi alloys," *Int. J. Mater. Res.*, 101 (2010), 1089-96.

[4] http://www.openfoam.org/

[5] R. Vilums, "Implementation of Transient Robin Boundary Conditions in OpenFOAM," *Workshop Multiphysical Modelling in OpenFOAM, Riga, Latvia,* (2011), 39-40.

[6] DIN 1725: 3.2371

[7] http://matcalc.tuwien.ac.at/

[8] J.A. Dantzig, and M. Rappaz, *Solidification* (Lausanne, CH: EPFL Press, 2009), 396-401.

[9] https://dakota.sandia.gov/

CFD Modeling and Simulation in Materials Processing 2016

Casting with External Field Interaction

Session Chair:
Koulis Pericleous

CFD Modeling and Simulation in Materials Processing 2016
Edited by: Laurentiu Nastac, Lifeng Zhang, Brian G. Thomas, Miaoyong Zhu, Andreas Ludwig, Adrian S. Sabau, Koulis Pericleous, and Hervé Combeau
TMS (The Minerals, Metals & Materials Society), 2016

A HIGH-ORDER ACOUSTIC CAVITATION MODEL FOR THE TREATMENT OF A MOVING LIQUID METAL VOLUME

G S Bruno Lebon[1], Iakovos Tzanakis[2], Koulis Pericleous[1], Dmitry Eskin[2]

[1]Computational Science and Engineering Group;
The University of Greenwich; London, SE10 9LS, UK
[2]Brunel Centre for Advanced Solidification Technology (BCAST);
Brunel University; Uxbridge, Middlesex, UB8 3PH, UK

Keywords: Cavitation modeling, Ultrasonics, Light-metal alloys, Ultrasonic melt processing

Abstract

Ultrasonic cavitation significantly improves the downstream properties and quality of metallic materials. However, this technology has not been successfully transferred to the industry due to difficulties in treating large volumes of liquid metal. To improve the understanding of cavitation efficiency so that it can be applied to a moving melt volume, an improved cavitation model consisting of a high-order acoustics solver is applied to the two-phase problem of bubble breakup and propagation in the melt. Results from numerical simulations of the ultrasonic field and flow pattern in a launder are presented. The use of baffles to modify the flow pattern and amplify sound waves in a launder conduit is examined to determine the optimum configuration that maximizes the acoustic pressure amplitude in high cavitation activity regions.

Introduction

Significant improvements in the quality and properties of metallic materials have been observed after the materials have been subjected to ultrasonic melt treatment [1, 2, 3, 4]. These improvements, which are generally attributed to acoustic cavitation [5], include degassing of dissolved gases, improved wetting and the activation of inclusions by cleaning the solid-liquid interface, enhancing nucleation, and refining the grain structure of the solidified metal [6]. However, difficulties in transferring this promising technology to the industry still remain, particularly because the treatment of large volumes of liquid metal is still elusive. To circumvent these difficulties, a fundamental understanding of the gas bubble behavior in the treated melt, together with its coupling with the acoustic field, is required [7].

Bubble structures in sonicated liquid aluminium have been recently observed by X-ray tomography [8] and radiography [9, 10]. Cavitation-induced multiplication of nucleation sites due to secondary dendrite arms rupture has been observed by *in situ* radiography [10]. To predict the cavitation regions in which nucleation sites are induced within the liquid melt, a homogeneous model based on the full cavitation model of Singhal *et al.* [11, 12] have been applied to solve the acoustic pressures in a crucible by Nastac [13]. This model has been improved by Lebon *et al.* [14] to account for the large forcing amplitudes generally encountered in melt processing by employing the Keller-Miksis equation [15] to re-derive the net phase change in the bubble volume fraction equation.

In this paper, an improved version of the homogeneous model incorporating a high-order acoustic solver [16] is presented, together with comparison of measured acoustic pressures below a vibrating sonotrode in a water experiment. This model is then used in both water and aluminium to determine the effect of baffles separation on the pressure field.

Theory

Governing Equations

The wave equation in a moving fluid is expressed as the Navier-Stokes equations in perturbation form:

$$\frac{\partial \rho}{\partial t} + \nabla \cdot (\rho \boldsymbol{u}') = S_{mass}, \tag{1}$$

$$\frac{\partial (\rho u_i')}{\partial t} + \nabla \cdot (\rho \boldsymbol{u}' u_i') = S_{u_i'}, \tag{2}$$

where p is acoustic pressure, ρ is the fluid density, and $\boldsymbol{u}'$ is the perturbation velocity. The speed of sound c of the travelling medium is related to the acoustic pressure and density by $\partial p / \partial \rho \equiv c^2$. The source term S_{mass} contains mass sources. The forcing terms $S_{u_i'}$ contain velocity sources due to the vibrating solid surfaces.

Fluid flow is governed by the Reynolds-averaged Navier-Stoke (RANS) equations:

$$\frac{\partial \rho}{\partial t} + \nabla \cdot (\rho \boldsymbol{u}) = 0, \tag{3}$$

$$\frac{\partial (\rho u_i)}{\partial t} + \nabla \cdot (\rho \boldsymbol{u} u_i) = \nabla \cdot [(\mu + \mu_t) \nabla u_i] + S_{u_i}. \tag{4}$$

$\boldsymbol{u}$ is the fluid velocity, μ_t is the eddy viscosity and S_{u_i} are the momentum sources, including buoyancy. The standard $k - \varepsilon$ turbulence model is used for closure, together with an additional source term to account for turbulence generated due to bubble collapse [14].

The governing equation for the bubble volume fraction ϕ is:

$$\frac{\partial (\phi \rho_b)}{\partial t} + \nabla \cdot (\phi \rho_b \boldsymbol{u}) = \Gamma, \tag{5}$$

where $\Gamma = \Gamma_G - \Gamma_C$. Γ_G and Γ_C are the growth and collapse source terms respectively

When $p_{tot} < p_v$:

$$\Gamma_G = C_G \frac{\sqrt{k}}{\sigma} \rho_l \rho_b \left[\frac{2}{3} \left(\frac{1 + \frac{\sqrt{k}}{c}}{1 - \frac{1\sqrt{k}}{3\ c}}\right) \frac{p_v - p_{tot}}{\rho_l}\right]^{\frac{1}{2}} (1 - \phi), \tag{6}$$

and when $p_{tot} > p_v$:

$$\Gamma_C = C_c \frac{\sqrt{k}}{\sigma} \rho_l \rho_b \left[\frac{2}{3} \left(\frac{1 + \frac{\sqrt{k}}{c}}{1 - \frac{1\sqrt{k}}{3\ c}}\right) \frac{p_{tot} - p_v}{\rho_l}\right]^{\frac{1}{2}} \phi. \tag{7}$$

The subscripts l and b denote liquid and bubble properties respectively. The constants are C_G and C_C are 0.02 and 0.01 respectively. $p_{tot} = p_0 + p + \rho g h$ where p_0 is atmospheric pressure, g is the gravitational acceleration, and h is the depth below the free surface. k is the kinetic energy of turbulence.

Wave Equation Discretization

The computational meshes are fully staggered for the solution of equations (1) and (2). The scalar quantities acoustic pressure and volume fraction are stored in cell centers and velocity components are stored at cell faces [16]. Spatial derivatives are evaluated using the following 6-point stencil:

$$\frac{\partial f}{\partial x} = \frac{1}{\Delta x} \sum_{j=-2}^{3} a_j f\left[x + \left(j - \frac{1}{2}\right) \Delta x\right], \tag{8}$$

where the coefficients a_j are optimized to make the scheme exact to the fourth order [16].

Temporal integration is approximated as

$$\int_{-\frac{\Delta T}{2}}^{\frac{\Delta T}{2}} f(t)\, dt = \Delta t \sum_{m=0}^{3} b_m f(-m \Delta t), \tag{9}$$

where the coefficients b_m are optimized to make the scheme exact to the third order [16].

Problem Description

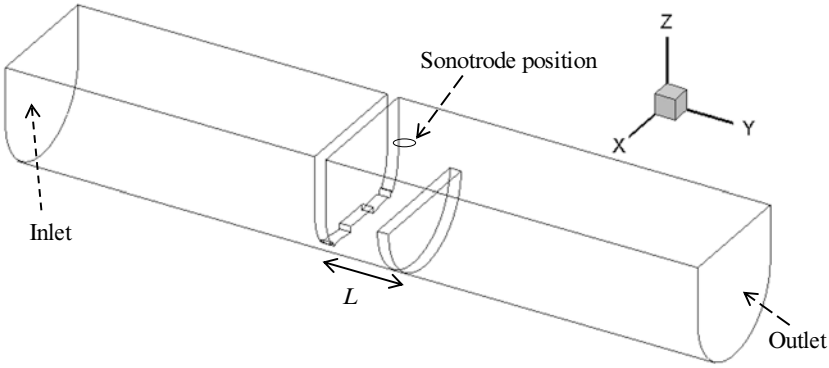

Figure 1. 50 cm x 9 cm x 8 cm launder. L denotes the length between baffles, of thickness 8 mm each. The sonotrode is immersed 1 cm into the free surface at the center of the domain.

The launder geometry is depicted in Figure 1: the same geometry is used for the computational model. The launder is 50 cm along y and 9 cm along x. The bottom section is a half cylinder of radius 4.5 cm. The liquid is filled up to a height of 8 cm from the bottom of the launder. The baffles have a thickness 8 mm. The lower opening of the low-y baffle is 2.0 cm, and the height of the high-y baffle is 2 cm. The sonotrode, of diameter 2 cm, is located at the centre of the domain and immersed 2 cm below the liquid free surface. The sonotrode displacement is varied from 1.0 μm to 2.0 μm; this displacement is prescribed to the sonotrode surface. The frequency of the forcing signal is 20 kHz.

Table 1. Material properties of liquid aluminium and water [1].

Material Property	Aluminium (700 ºC)	Water (20 ºC)
Sound speed c (m s^{-1})	4600	1482
Density ρ_l (kg m^{-3})	2375	1000
Dynamic viscosity μ (mPa s)	1.0	1.004
Surface tension (hydrogen interface) S (N m^{-1})	0.86	0.079
Vapour pressure p_{sat} (kPa)	0.000012	2.2
Bulk modulus K (GPa)	41.2	2.15

The distance between the baffles is varied as a function of the sound wavelength of the liquid medium. The wavelength λ of water at 20 kHz is 7.4 cm and for aluminium, the wavelength is 23 cm. The numerical simulation is run for each liquid for the following distances L between the baffles: 0.5 λ, 1.0 λ, and 1.5 λ. The material properties for both liquids are listed in Table 1. A case is also run without any partition. Pressure measurements are available at 3 points in the domain for the case of water with a separation of 1.0 λ, without bulk flow across the launder.

Results

Figure 2 and Figure 3 show the contour plots for bubble volume fraction and acoustic pressure along the axis of symmetry of the launder. The contours are at selected times within an acoustic cycle after which steady state conditions have been established. These contours depict results in water with the separation between baffles equal to 7.4 cm, the wavelength of sound at 20

kHz in water, and a prescribed sonotrode displacement of 1.0 μm. The Courant number for each simulation is set to 0.1.

The maximum variation in acoustic pressure is found below the sonotrode, between the two partitions. The largest bubble concentration is also located below the sonotrode, in the region of the expected conical bubble structure. Figure 3 also depicts the velocity contours along the symmetry plane, with the largest velocities recovered below the sonotrode as expected. The acoustic pressures in the low y region are lower than the pressures in the high y region, since the opening for the low-y baffle is much smaller than that of the high-y baffle.

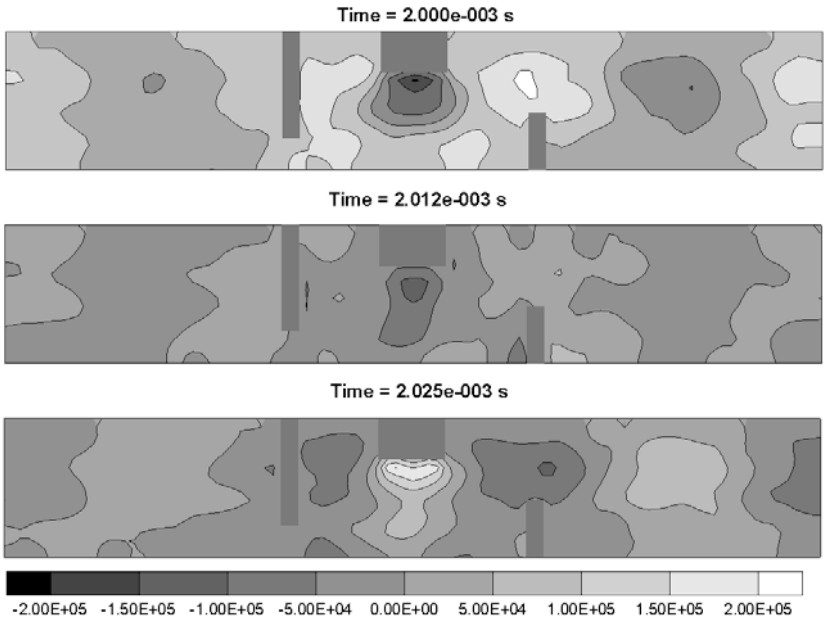

Figure 2: Acoustic pressures in water with $L = 1.0\ \lambda$ and sonotrode displacement = 1.0 μm.

Figure 4, Figure 5, and Figure 6 show the comparison of the computed root mean square pressures with the measured pressures at three points in the domain for four sonotrode displacements: 1.0 μm, 1.2 μm, 1.5 μm, and 2.0 μm. The three positions are all along the plane of symmetry of the launder and 4 cm below the free surface. Figure 4 is 2 cm below the sonotrode. Figure 5 shows values adjacent to the low-y baffle and Figure 6 shows values adjacent to the high-y baffle.

The numerical results are within an order of magnitude of one of the experimental values in each set. The discrepancy between the two measurement values at each point can be attributed to the large uncertainties in the probe calibration, resulting in uncertainties in the sensitivity values of each frequency calibration. The probe collects the pressure contributions with a large spatial resolution of 5 cm and along the whole surface of the probe tip, leading to an uncertainty in the measurement position.

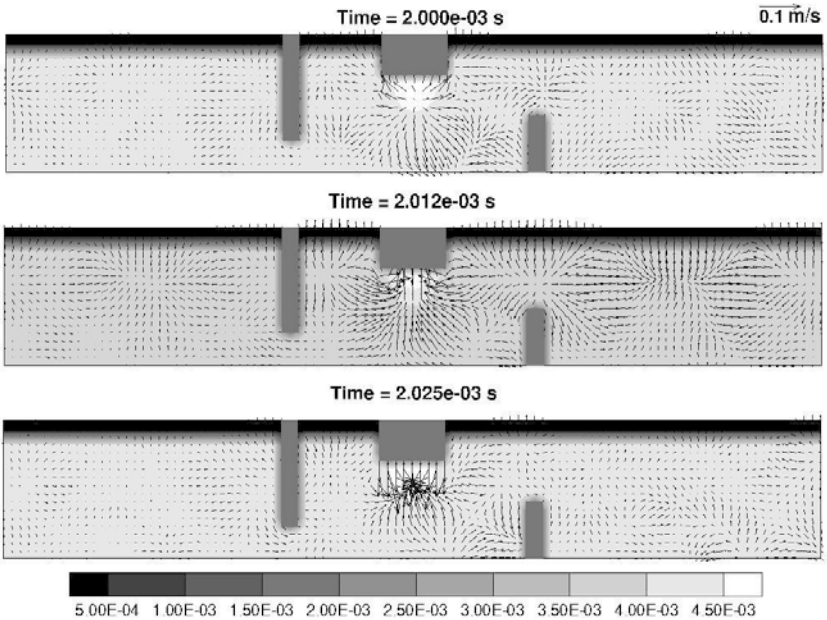

Figure 3: Bubble volume fraction for water with $L = 1.0\lambda$ and sonotrode displacement = 1.0 μm.

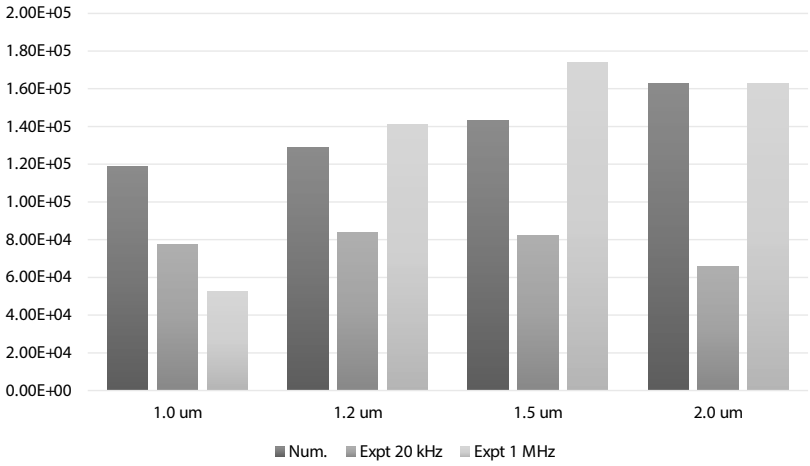

Figure 4: Comparison between computed root mean square (r.m.s.) acoustic pressures (Num.) with experimental values measured using a calibrated probe 2 cm below probe surface. Expt. 20 kHz corresponds to values using calibration at 20 kHz and Expt. 1 MHz corresponds to values using 1 MHz calibration.

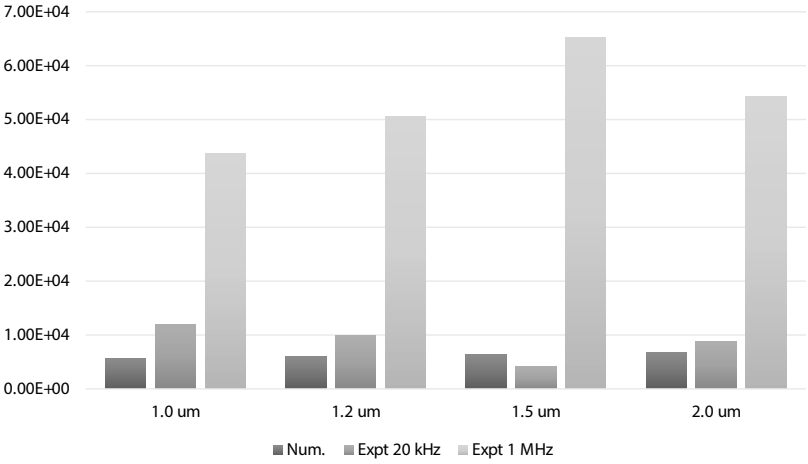

Figure 5: Comparison between computed r.m.s. acoustic pressures with experimental values measured with a calibrated probe 4 cm below the free surface outside the low-y baffle.

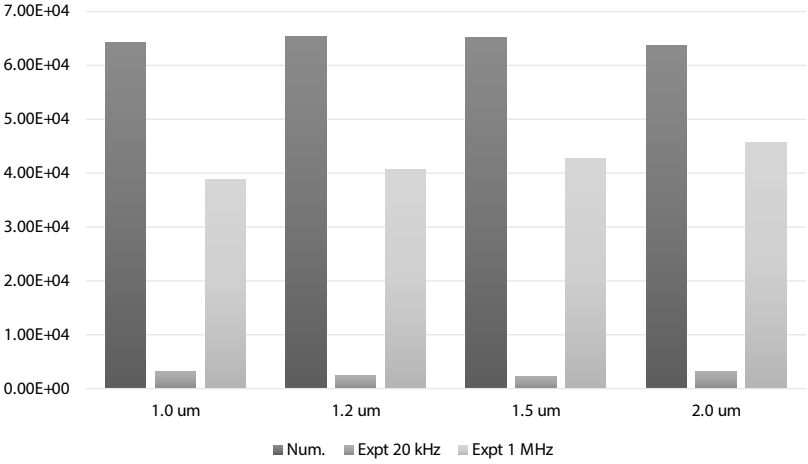

Figure 6: Comparison between computed r.m.s. acoustic pressures with experimental values measured with a calibrated probe 4 cm below the free surface outside the high-y baffle.

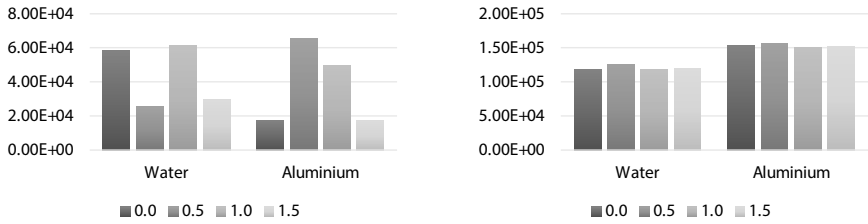

Figure 7: Change in computed r.m.s. acoustic pressure 2 cm below probe surface without partitions (0.0) and for three different partition separations (0.5, 1.0, and 1.5) for water and aluminium with sonotrode displacement set to 0.1 μm (left) and 1.0 μm (right).

Below the sonotrode (Figure 4), the measured high frequency pressure for the lowest amplitude, 1.0 um, is much smaller than for larger sonotrode displacements. This suggests that cavitation is not fully developed and the noise contribution for bubble cavitation is small. With larger sonotrode amplitudes, the contribution of pressure radiating from cavitating bubbles increases and becomes larger than the measured pressure at the forcing frequency, showing that noise from cavitation activity is larger than the prescribed sonotrode pressure.

Figure 7 shows the change in computed r.m.s. pressure in both water and aluminium for different baffle separations and two sonotrode displacements. For large sonotrode displacements of the order of 1.0 μm, the effect of the baffle separation negligible on the mean acoustic pressure. However, for small displacements of the order of 0.1 μm where the effect of acoustic shielding is negligible, the effect of baffles is more apparent. A resonant separation of 7.4 cm (1.0 λ) in water results in large acoustic pressures below the sonotrode. For aluminium, a separation of half a wavelength (0.5 λ) results in the largest acoustic pressure amplitude below the sonotrode. This implies that the forcing frequency and the various harmonics of the container geometry are important in designing a system to optimize the efficiency of the cavitation treatment.

Conclusions

A high-order acoustic solver, coupled with a cavitation model, for the ultrasonic treatment of liquid metals is presented in this study. The solver can predict the mean acoustic pressures in water. The effect of baffle distances in a launder is found to be important for small sonotrode displacements and negligible for large sonotrode displacements. The resonant frequency of the liquid container is therefore an important parameter in the design of an ultrasonic melt processing system when the effect of acoustic shielding is negligible.

Acknowledgement

The authors are grateful to the UK Engineering and Physical Sciences Research Council (EPSRC) for financial assistance for this research in contract number: EP/K00588X/1 and EP/K005804/1.

References

1. G. I. Eskin and D. G. Eskin, Ultrasonic treatment of light alloy melts, CRC Press, 2014.
2. J. Campbell, "Effects of vibration during solidification," *Int. Met. Rev.,* **26**, 71, 1981.
3. N. Alba-Baena and D. Eskin, "Kinetics of ultrasonic degassing of aluminum alloys," in *Light Metals 2013*, John Wiley & Sons, Inc., 2013, pp. 957–962.
4. G. Cao, H. Konishi and X. Li, "Mechanical properties and microstructure of SiC-reinforced Mg-(2,4)Al-1Si nanocomposites fabricated by ultrasonic cavitation based solidification processing.," *Materials Science and Engineering: A,* **486**, 1–2, 357–362, 2008.
5. G. I. Eskin, "Cavitation mechanism of ultrasonic melt degassing," *Ultrasonics Sonochemistry,* **2,** 2, S137–S141, 1995.
6. G. I. Eskin, G. S. Makarov and Y. P. Pimenov, "Effect of ultrasonic processing of molten metal on structure formation and improvement of properties of high-strength Al-Zn-Mg-Cu-Zr alloys," *Advanced Performance Materials,* **2**, 1, 43–50, 1995.
7. S. Komarov, K. Oda, Y. Ishiwata and N. Dezhkunov, "Characterization of acoustic cavitation in water and molten aluminum alloy," *Ultrasonics Sonochemistry,* **20**, 2, 754–761, 2013.
8. W. Xu, I. Tzanakis, P. Srirangam, S. Terzi, W. Mirihanage, D. G. Eskin and P. Lee, "In situ synchrotron radiography of ultrasound cavitation in a molten Al-10Cu alloy," in *TMS2015 Supplemental Proceedings*, Orlando, 2015.
9. H. Huang, D. Shu, Y. Fu, J. Wang and B. Sun, "Synchrotron radiation X-ray imaging of cavitation bubbles in Al–Cu alloy melt," *Ultrasonics Sonochemistry,* **21**, 4, 1275–1278, 2014.
10. J. Mi, D. Tan and T. Lee, "In situ synchrotron X-ray study of ultrasound cavitation and its effect on solidification microstructures," *Metallurgical and Materials Transactions B,* **46**, 4, 1615–1619, 2015.
11. A. Singhal, M. Athavale, H. Li and Y. Jiang, "Mathematical basis and validation of the full cavitation model," *Journal of Fluids Engineering,* **124**, 3, 617–624, 2002.
12. M. Athavale, Y. Jiang, H. Li and A. Singhal, "Application of the full cavitation model to pumps and inducers," *Int. J. Rot. Mach.,* **8**, 1, 45–56, 2002.
13. L. Nastac, "Mathematical modelling of the solidification structure evolution in the pressence of ultrasonic stirring," *Metall. Mater. Trans. B,* **42**, 6, 1297–1305, 2011.
14. G. S. B. Lebon, K. Pericleous, I. Tzanakis and D. Eskin, "A model of cavitation for the treatment of a moving liquid metal volume," in *Advances in the Science and Engineering of Casting Solidification: An MPMD Symposium Honoring Doru Michael Stefanescu*, Orlando, 2015.
15. J. B. Keller and M. Miksis, "Bubble oscillations of large amplitude," *The Journal of the Acoustical Society of America,* **68**, 2, 628–633, 1980.
16. G. Djambazov, C. H. Lai and K. Pericleous, "Staggered-mesh computation for aerodynamic sound," *AIAA Journal,* **38**, 1, 16–21, 2000.
17. B. E. Launder and D. B. Spalding, "The numerical computation of turbulent flows," *Computer methods in applied mechanics and engineering,* **3**, 2, 269–289, 1974.

CFD Modeling and Simulation in Materials Processing 2016
Edited by: Laurentiu Nastac, Lifeng Zhang, Brian G. Thomas, Miaoyong Zhu, Andreas Ludwig, Adrian S. Sabau, Koulis Pericleous, and Hervé Combeau
TMS (The Minerals, Metals & Materials Society), 2016

PROGRESS ON NUMERICAL MODELING OF THE DISPERSION OF CERAMIC NANOPARTICLES DURING ULTRASONIC PROCESSING AND SOLIDIFICATION OF Al-BASED NANOCOMPOSITES

Daojie Zhang and Laurentiu Nastac

The University of Alabama, Tuscaloosa, AL, 35487, USA, email: lnastac@eng.ua.edu

Keywords: Ultrasonic and electromagnetic stirring; Numerical modeling of dispersion of ceramic nanoparticles; 6061 nanocomposites; SiC nanoparticles; Molten metal processing; Unidirectional solidification.

Abstract

The metal-matrix-nano-composites (MMNCs) in this study consist of a 6061 alloy matrix reinforced with 1.0 wt. % SiC nanoparticles that are dispersed uniformly within the matrix using an ultrasonic cavitation dispersion technique (UCDS). A recently developed multiphase computational fluid dynamics (CFD) model is applied to study the effects of electromagnetic field from the induction coils and the magnitude of the fluid flow on the nanodispersion. The CFD model accounts for turbulent fluid flow, heat transfer and solidification, electromagnetic field as well as the complex interaction between the solidifying alloy and nanoparticles. SEM analysis was performed on the as-cast MMNC coupons processed via UCDS and confirmed the distribution of the nanoparticles predicted by the current CFD model.

Introduction

Micron-sized ceramic particle reinforcements are widely used in aluminum-based metal matrix composites (MMCs) which have high strength-to-weight ratios and enhanced mechanical and thermal properties including specific modulus, superior strength, stiffness, good wear resistance, fatigue resistance and improved thermal stability [1-4]. More recently, to overcome the counterpart that the ductility of the MMCs deteriorates with high ceramic particle concentration [5], more attention has been drawn to metal matrix nanocomposites (MMNCs), since the properties of metallic alloys reinforced by ceramic nanoparticles (with dimensions less than 100 nm) would be enhanced considerably while the ductility of the matrix is retained [6-12]. However, it is extremely difficult to obtain uniform dispersion of nano-sized ceramic particles in liquid metals due to their high viscosity, poor wettability in the metal matrix, and a large surface-to-volume ratio, which results in agglomeration and clustering [5]. Currently, several fabrication technologies including high-energy ball milling [9, 12], in-situ synthesis [8], electroplating [13], and ultrasonic technology (UST) [5, 6] are most commonly used, among which UST is supposed to be more reliable and cost effective.

Induction heating, which is a clean, energy-efficient and well-controllable melting process, is widely applied in metallurgical industry. During the process, the dominant electromagnetic field will generate heat (affecting the temperature field) and momentum (controlling the fluid flow field). Meanwhile, all these three fields may strongly influence one another, which may significantly complicate the problem [14]. An improved understanding of the heat and

electromagnetically driven flow mostly requires mathematical modeling, as experimental studies, especially for high temperature materials processing, may be restricted because of the physical and chemical properties of the melts [15].

During the solidification process, the particles will either be pushed or engulfed by the solidification front, among which particle pushing will always lead to segregation even clustering of the particulate reinforcement, which is undesirable as it results in non-homogeneous response and lower macroscopic mechanical properties. In general, it is considered that whether particles are pushed or engulfed during solidification depends on the velocity of the particle relative to the solidification front according to several previous models describing such particle engulfment and pushing phenomena [16-20].

In this study, ANSYS Fluent Dense Discrete Phase Model (DDPM) [21] was adapted. The DDPM accounts for turbulent fluid flow, heat transfer, electromagnetic forces, and complex interactions between the molten alloy and nanoparticles during the melting and unidirectional solidification processes. Based on the theory proposed by Ferguson, all of the nanoparticles are assumed to be engulfed by the solidification front and no entrapment will occur. The dispersion of SiC nanoparticles with different fluid flow intensities, and with and without induction stirring has been investigated in detail.

Model Description

The geometries of the electromagnetic field and CFD model are shown in Figure 1. 2D axisymmetric models are both applied to calculate the electromagnetic forces and the CFD related computations. The induction furnace is comprised of an Al_2O_3 crucible and 3 Cu induction coils. An electric current of 200A with frequency of 50 Hz is passed through the coils to induce eddy currents in the liquid Aluminium alloys. All material properties required for EM modeling are available in ANSYS Maxwell.

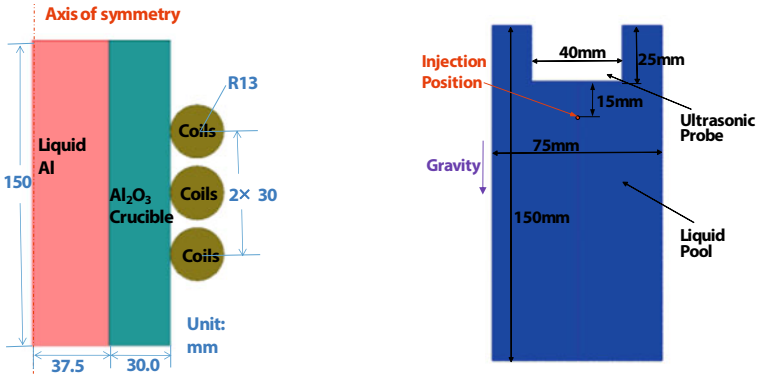

(a) Electromagnetic field

(b) CFD model

Figure 1. Geometry model.

The ultrasonic probe has a diameter of 40 mm. The liquid aluminium alloy is 6061. It has a density of 2685 kg/m3. The SiC nanoparticles with an average particle size of 55 nm and density of 3216 kg/m3 are treated as inert-particles. The mass flow rate of the SiC nanoparticles is 0.014 kg/s. Thus, 1.0 wt. % of SiC nanoparticles can be injected at about 15 mm beneath the ultrasonic probe for 1 sec. The multiphase CFD model accounts for turbulent fluid flow, heat transfer, and the complex interaction between the molten alloy and nanoparticles by using the ANSYS Fluent DDPM and k-ω turbulence model [21]. The CFD model is described in detail below.

Due to harmonic nature of EM field and induced eddy currents, the Lorentz force $\mathbf{F}_{Lor}$ can be decomposed into a steady and harmonic part that oscillates with double frequency. Because of much greater inertia times of melt in comparison to alternate EM field timescale, only the steady part of the Lorentz force is taken into account [22]. Assuming the fluid flow does not affect the electromagnetic field, the governing magneto-quasi-static equations for a material with constant magnetic permeability μ and constant Ohmic conductivity σ can be written as [23]:

$$\nabla \times \mathbf{H} = \mathbf{J} \tag{1}$$

$$\nabla \times \mathbf{E} = -\frac{\partial \mathbf{B}}{\partial t} \tag{2}$$

$$\nabla \cdot \mathbf{B} = 0 \tag{3}$$

The constitutive relations are:

$$\mathbf{B} = \mu \mathbf{H} \tag{4}$$

$$\mathbf{J} = \sigma \mathbf{E} \tag{5}$$

Thus the Lorentz force is calculated as:

$$\mathbf{F}_{Lor} = \frac{1}{2} \mathrm{Re}(\mathbf{J}^* \times \mathbf{B}) \tag{6}$$

where **J** is current density, **B** is magnetic flux density, **E** is electric intensity, **H** is magnetic field intensity, and $\mathbf{J}^*$ denotes the complex conjugate of the current density.

The fluid flow model, solidification model, particle tracking model, and solution procedure are presented in detail in [24, 25].

Simulation Results and Discussion

Figure 2 shows the electromagnetic force distribution interpolated on the Fluent finite volume mesh and fluid flow field in the induction furnace after 1.0s without ultrasonic stirring. As it can be seen, the electromagnetic forces mainly distribute in the skin layer due to skin effect. Also, the flow consists of two axisymmetric recirculating loops, consistent with the computed curl of the EM force field.

Figure 3 shows the fluid flow and particle distributions after 0.5s, 3.0s, and 20s, respectively, when the induction stirring is ignored.

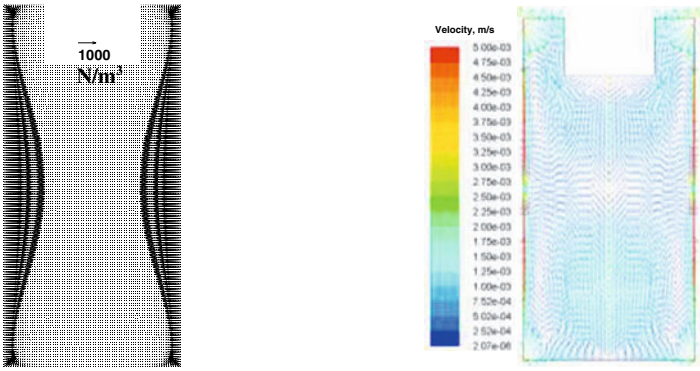

Figure 2. Electromagnetic force distribution (a) and fluid flow field (b) without ultrasonic stirring.

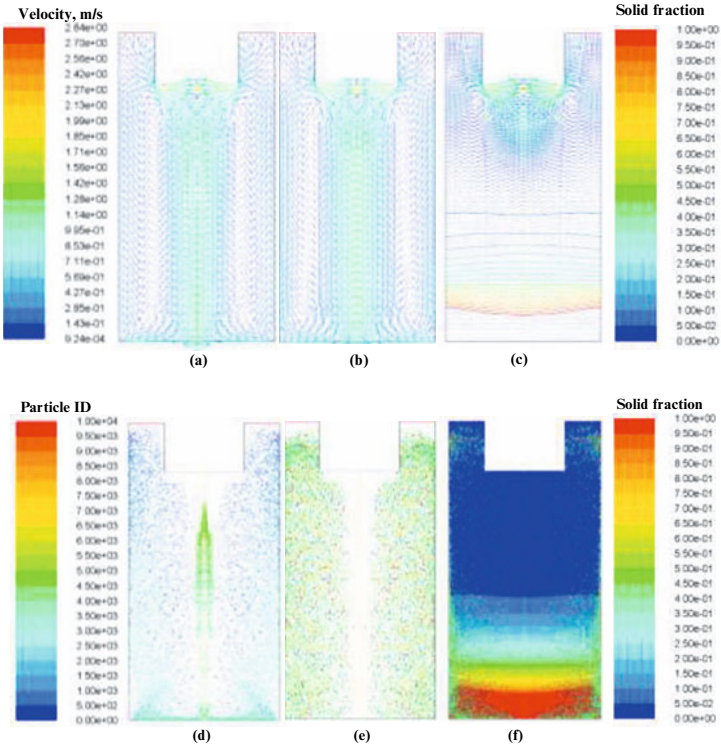

Figure 3. Fluid Flow and particle distributions (strong flow without induction stirring): (a) and (d) after 0.5s; (b) and (e) after 3.0s; and (c) and (f) after 20s.

It can be seen from Figure 3, the flow is much stronger at the center of the furnace. The fluid flow is damped in the mushy zone, where the particles will move relatively slow and stop moving in the solid (see Figure 3(c)). Also, at 3.0s, the particles have been dispersed pretty well from the bottom to the top, but a little more particles tend to stay near the wall, and fewer nanoparticles at the center where the flow is stronger, which indicates the nanoparticles couldn't disperse well in strong flows (see Figure 3(e)). Additionally, the particle distribution stays almost the same henceforth which means the distribution becomes stable. Then, the solidification process starts at 3.0s, and in order to model the unidirectional solidification process, all the walls except the bottom one are treated as adiabatic. After 20s, we can see that there are some agglomerations in the solid (see 3(f)) because the nanoparticles approaching the solid/liquid interface will be engulfed based on the assumption that the Brownian motion will dominate during the particle engulfment/pushing process.

When the induction stirring is taken into consideration, the fluid flow and particle distributions after 0.5s, 3.0s, and 20s are shown in Figure 4, respectively.

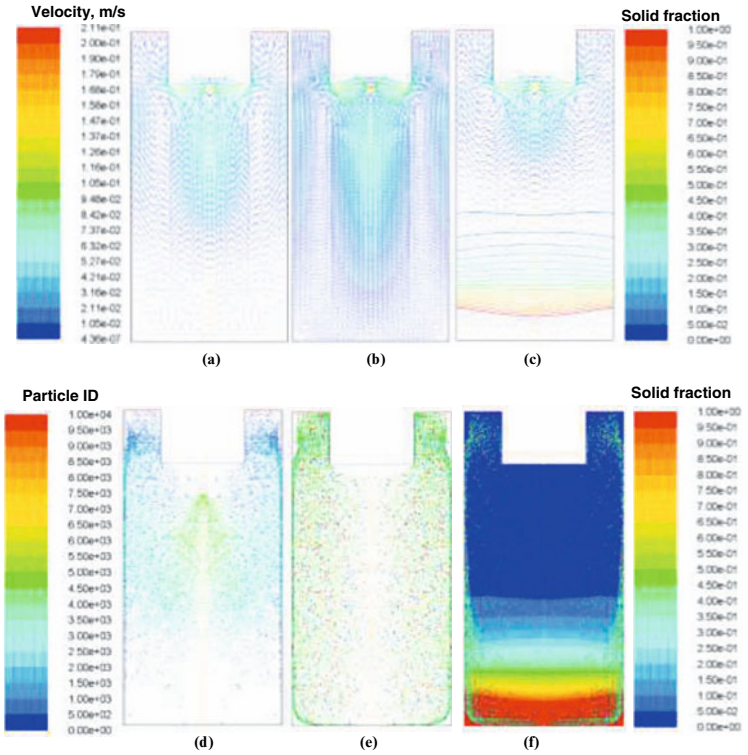

Figure 4. Fluid Flow and particle distributions (strong flow with induction stirring): (a) and (d) after 0.5s; (b) and (e) after 3.0s; and (c) and (f) after 20s.

Compared to Figure 3, the fluid flow pattern is basically the same, because the induced flow by induction stirring is relatively weak compared to that induced by ultrasonic stirring. But there are still some differences especially at the center of the furnace that the flow at the bottom becomes weaker than that at the top because of the induction stirring. It can also be seen that there are considerable number of particles in the center of the furnace, which indicates that the particle distribution becomes even better than before. It can be explained that induction stirring modifies the fluid flow, making it more uniform. When solidification starts, the fluid flow is damped in the mushy zone as well, and particles approaching the solidification front are captured. As it can be seen in Figure 4(f) that, after 20s, the nanoparticles are dispersed quite well throughout the metal matrix, which is also validated by SEM analysis [26, 27].

To investigate the effect of the magnitude of the fluid flow on the dispersion of nanoparticles, the velocity magnitude is changed to be 1/10th of the original one. Figure 5 shows the fluid flow and particle distributions (with induction stirring) after 3.0s, 20s, and 40s, respectively.

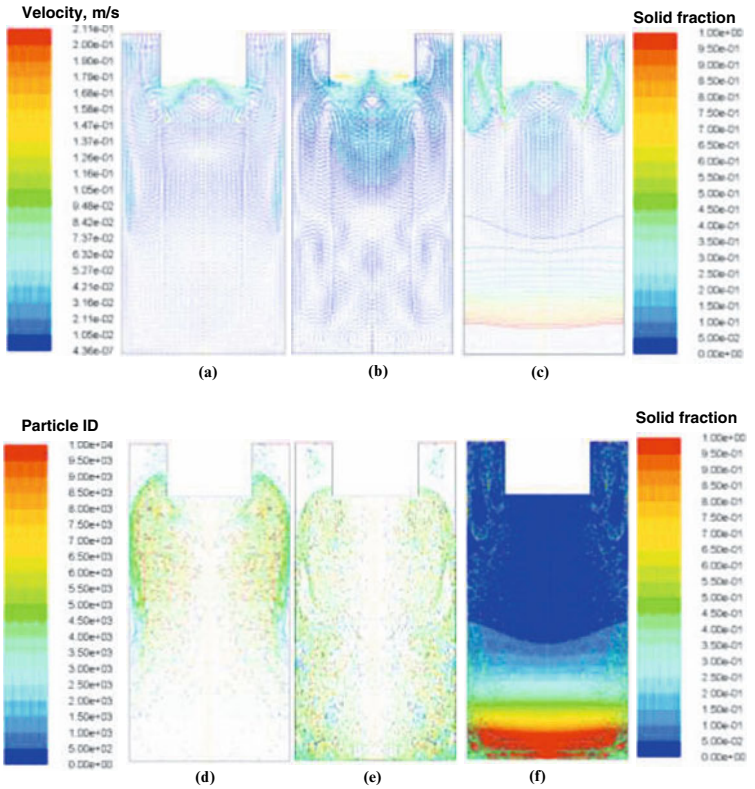

Figure 5. Fluid Flow and particle distributions (weak flow with induction stirring): (a) and (d) after 3s; (b) and (e) after 20s; (c) and (f) after 40s.

As the fluid flow is weaker, the particle dispersion is slower. And the flow fields after 3.0s and 20s are not exactly the same, because the flow after 3.0s is not fully developed yet. Besides, even the fully developed flow pattern is not as regular as before, that there are several recirculating loops, because the induction stirring, which cannot be neglected, is playing a major role on the fluid flow. When solidification starts, the fluid flow changes significantly because the induction stirring furnace is stopped. In addition, it can be observed that the flow pattern will become almost the same as that with a strong flow (see Figs. 4(c) and 5(c)).

After 20s, the distribution of the nanoparticles becomes stable, but there are much fewer particles at the top (around the probe) where fluid flow is relatively stronger. Also, more particles are captured by the mushy zone, and consequently fewer particles stay at the top (see Figure 5(f)). Lastly, it is pretty obvious that the particle distributions are not as good as those with a strong flow. Thus, It can be concluded that weak flow cannot disperse nanoparticles well enough during the ultrasonic and induction stirring processing.

Concluding Remarks

A magneto-hydro-dynamics model was developed in ANSYS Maxwell and ANSYS Fluent. The DDPM model coupled with the $k-\omega$ turbulence model was used to investigate the distribution of SiC nanoparticles into a 6061 matrix under ultrasonic and induction stirring and molten metal and unidirectional solidification processing conditions. It was determined that a strong flow can disperse the nanoparticles relatively well, especially when compared with a weak flow condition. Also, it was demonstrated that induction stirring can help improve the fluid flow characteristics, making the nanoparticle distribution even more uniform.

References

[1] J.W. Kaczmar, K. Pietrzak, W. Wlosinski. "The production and application of metal matrix composite materials," *Journal of Materials Processing Technology*, 106 (2000), 58–67.

[2] K. Durisinova, J. Durisin, M. Orolinova et al. "Effect of particle additions on microstructure evolution of aluminium matrix composite," *Journal of Alloys and Compounds*, 525 (2012), 137-142.

[3] C.H. William. "Commercial processing of metal matrix composites," *Materials Science and Engineering A*, 244 (1) (1998), 75–79.

[4] Y. Yang, J. Lan, X. Li. "Study on bulk aluminum matrix nano-composite fabricated by ultrasonic dispersion of nano-sized SiC particles in molten aluminum alloy," *Materials Science and Engineering A*, 380 (2004), 378-383.

[5] G. Cao, H. Konishi, X. Li. "Mechanical properties and microstructure of SiC-reinforced Mg-(2,4)Al-1Si nanocomposites fabricated by ultrasonic cavitation based solidification processing," *Materials Science and Engineering A*, 486 (2008), 357-362.

[6] J.H. Shin, H.J. Choi, M.K. Cho et al. "Effect of the inter face layer on the mechanical behavior of TiO_2 nanoparticle reinforced aluminum matrix composites," *Journal of Composite Materials*, 48 (1) (2014), 99-106.

[7] B. Dikici, M. Gavgali, Bedir. "Synthesis of *in situ* TiC nanoparticles in liquid aluminum: the effect of sintering temperature," *Journal of Composite Materials*, 45 (8) (2010), 895-900.

[8] A.A. El-Daly, M. Abdelhameed, M. Hashish et al. “Fabrication of silicon carbide reinforced aluminum matrix nanocomposites and characterization of its mechanical properties using non-destructive technique,” *Materials Science and Engineering A*, 559 (2013), 384-393.
[9] X. Jiang, M. Galano, F. Audebert. “Extrusion textures in Al, 6061 alloy and 6061/SiC_p nanocomposites,” *Materials Characterization*, 88 (2014), 111-118.
[10] J.H. Shin, D.H. Bae. “Effect of the TiO2 nanoparticle size on the decomposition behaviors in aluminum matrix composites,” *Materials Chemistry and Physics*, 143 (2014), 1423-1430.
[11] C. Borgohain, K. Acharyya, S. Sarma et al. “A new aluminum-based metal matrix composite reinforced with cobalt ferrite magnetic nanoparticle,” *Journal of Materials Science*, 48 (2013), 162-171.
[12] J.B. Ferguson, B.F. Schultz, P.K. Rohatgi et al. “Brownian Motion Effects on the Particle Settling and Its Application to Solidification Front in Metal Matrix Composites,” Light Metals TMS, 2014, 1383-1388.
[13] F.K. Sautter. “Electrodeposition of dispersion-hardened Nickel-Al2O3 Alloys,” *Journal of the Electrochemical Society*, 110 (1963), 557.
[14] M. Mach *et al.*, “Stirring of Liquid Steel in Crucible Induction Furnace,” *International Scientific Colloquium*, Riga (Latvia), 2006, 203-208.
[15] R. Schwarze, F. Obermeier, “Modelling of unsteady electromagnetically driven recirculating melt flows,” *Modelling Simul. in Mater. Sci. Eng.*, 12 (2004), 985.
[16] J.K. Kim and P.K. Rohatgi, “An Analytical Solution of the Critical Interface Velocity for the Encapturing of Insoluble Particles by a Movinb Solid/Lquid Interface,” *Metallurgical Materials Transaction A*, 29 (1998), 351-358.
[17] D.R. Uhlmann, B. Chalmers, and K.A. Jackson, “Interaction between Particles and a Solid-Liquid Interface,” *Journal of Applied Physics*, 35 (1964), 2986-2993.
[18] D.M. Stefanescu, A. Moitra, A.S. Kacar, and B.K. Dhindaw, “The Influence of Buoyant Forces and Volume Fraction of Particles on th Particle Pushing Entrapment Transition During Directional Solidification of Al/Sic and Al/Graphite Composites,” *Metallurgical Transactions A*, 21 (1990), 231-239.
[19] D. Shangguan, S. Ahuja, and D.M. Stefanescu, “An Analytical Model for the Interaction between an Insoluble Particle and an Advancing Solid Liquid Interface,” Metallurgical Transactions A, 23 (1992), 669-680.
[20] G. Kaptay, “Interfacial Criterion of Spontaneous and Forced Engulfment of Reinforcing Particles by an Advancing Solid/Liquid Interface,” Metallurgical Materials Transaction A, 32 (2001), 993-1005.
[21] Fluent 6.3: User’s Guide Manual Fluent Inc. and Ansys’s Fluent, (2006), http://ansys.com/.
[22] S. Spitans *et al*., “Numerical Modeling of Free Surface Dynamics of Melt in an Alternate Electromagnetic Field: Part I. Implementation and Verification of Model,” *Metall. Mater. Trans. B*, 44 (2013), 593-605.
[23] M. Pal, S. Kholmatov, P. Jönsson, “Numerical simulation of induction stirred ladle,” *COMSOL Users Conference*, Birmingham (USA), 2006.
[24] D. Zhang, L. Nastac, “Numerical modeling of the dispersion of ceramic nanoparticles during ultrasonic processing of aluminum-based nanocomposites,” *J. Mater. Res. Technol.*, 3 (2014), 296-302.
[25] D. Zang, L. Nastac, to appear in *IOP Conf. Ser.: Mater. Sci. Eng., June 2015, Presented at* Modeling of Casting, Welding, and Advanced Solidification Processes (MCWASP XIV), Awaji Yumebutai, Osaka (Japan), 2015.
[26] X. Liu, S. Jia, L. Nastac, “Ultrasonic Processing of A356-Nanocomposite Castings,” *Intern. Journal of Metal Casting (AFS)*, 8 (2014): 1-12.
[27] S. Jia, D. Zhang, L. Nastac, *J. Mater. Eng. Perform.*, ASM Intern., published online March 13, 2015, vol. 24, issue 6, June 2015, pp 1-9 (DOI: 10.1007/s11665-015-1467-4).

CFD Modeling and Simulation in Materials Processing 2016
Edited by: Laurentiu Nastac, Lifeng Zhang, Brian G. Thomas, Miaoyong Zhu, Andreas Ludwig, Adrian S. Sabau, Koulis Pericleous, and Hervé Combeau
TMS (The Minerals, Metals & Materials Society), 2016

Effects of Velocity-Based Packing Criteria on Models of Alloy Solidification with Free Floating Solid

A. Plotkowski[1], Matthew J. M. Krane[1]
[1]Purdue Center for Metal Casting Research; School of Materials Engineering; Purdue University; 701 W. Stadium Ave.; West Lafayette, IN 47907, USA

Keywords: Equiaxed solidification, finite volume, particle attachment

Abstract

In many solidification processes, particularly in the presence of grain refiner, solid grains initially form as free floating particles suspended within the liquid metal. As these grains continue to grow in number and size, their interactions cause them to form a permeable rigid solid structure. The majority of these models for equiaxed solidification assume that the transition from a slurry of particles to a rigid solid structure occurs at a fixed, uniform solid fraction. This approach does not include the influence of the local velocity field on the likelihood of packing. The present study investigates the effects of three different methods of including the solid particle velocity into packing rules and applies them to simulations of static castings. The advantages and disadvantages of these approaches are discussed in relation to the more common constant packing fraction model.

Introduction

Heat and mass transport during the solidification of molten alloys lead to ingot scale variations in composition, commonly termed macrosegregation. Due to the complex nature of the governing conservation equations, simulations are commonly used to gain understanding of the mechanisms for defect formation. In equiaxed solidification, these models are further complicated by free floating grains and their eventual coalescence, or packing, to form a rigid solid structure.

Two main types of equiaxed solidification models have been formulated. The first is the multi-phase approach proposed by Ni and Beckermann [1] including two [2,3], three [4,5], and five-phase variations [6]. These models either assume spherical grains or use supplemental relationships for the dendrite morphology within a spherical grain envelope. Packing occurs at a grain fraction 0.637, the density of close packed spheres [7]. The second type is the mixture model formulated by Vreeman et al. [8]. Mixture models use a lower packing fraction (expressed in volume fraction solid) that includes an implicit assumption about the grain morphology.

In both model types, the effect of the local velocity field on the attachment of free floating grains is neglected and packing occurs once a certain fraction of a control volume is occupied by solid grains. However, flow towards a packed interface will increase the likelihood of packing, while flow away from an interface will reduce it. Vusanovic and Krane [9] suggested an alternate packing model that bases the packing criteria on the state of control volumes in the downstream direction. That model is implemented here and compared to two variants.

Model Description

The solidification model used here is based on the continuum mixture formulation of the governing equations [10], with the modified momentum equations of Vreeman et al. [8]. The temperature formulation of the energy equation [11] is used with the source term linearization proposed by Voller and Swaminathan [12]. The governing equations are discretized and solved using standard finite volume techniques [13] using fully implicit time discretization on a Cartesian, uniform, structured, staggered grid. The species equations are discretized using the method of Vreeman and Incropera [14]. The free floating solid model calculates solid velocities using the definition of the mixture velocity, $\vec{V}$, and Stoke's law for spherical particles:

$$\vec{V} = f_s\vec{V}_s + f_l\vec{V}_l, \tag{1}$$

$$\vec{V}_s - \vec{V}_l = \frac{(1-g_s)}{18\mu_m}\Delta\rho d^2\vec{g}, \tag{2}$$

where f_s and f_l are mass fractions solid and liquid, $\vec{V}_s$ and $\vec{V}_l$ are the solid and liquid velocity vectors, g_s is the volume fraction solid, $_m$ is a mean viscosity, d is the particle diameter, and $\vec{g}$ is the gravitational vector. A uniform particle size of 20 m was used. The permeability of the rigid mushy zone, K, was modeled using the Blake-Kozeny relationship:

$$K = \frac{\lambda^2}{180}\frac{(1-g_s)^3}{g_s^2}, \tag{3}$$

where λ is the dendrite arm spacing, set here to 50 m. For the velocity control volumes, which are staggered from the main numerical grid, the permeability is calculated by first performing a linear interpolation of the solid fraction according to the recommendation of Kumar et al. [15].

In Vusanovic and Krane's [9] velocity based packing model, packing is based on the condition of the downstream cell. This idea is illustrated schematically in Figure 1a where the cell of interest packs if the downstream cell is packed and has a solid fraction above some critical value, $g_{s,c}$. If one of these conditions is not met, then the cell of interest does not pack.

The main difficulty in implementing such a model is determining which cells are downstream of the solid motion. Solid velocity is stored at the cell faces, and by definition, is equal to zero if the neighbor cell is packed. Vusanovic and Krane circumvented this problem by averaging the solid flow rates in each direction, then using the larger of the two resulting vectors to determine the *most* downstream cell. This model will be termed the average velocity method (AVM), in which the packing criteria are applied to only a single downstream cell. One obvious variation of the AVM is to consider both cells downstream from the averaged solid velocity vectors, and if either matches the conditions shown in Figure 1a, then the cell of interest packs. This model always considers two possible downstream cells and will be referred to here as the "average velocity, any cell" (AVA) method.

In both of these averaging methods, the existing non-zero mixture velocity information at the cell faces is neglected. Another method of determining downstream cells is to calculate an effective solid velocity of the equiaxed grains within the cell of interest, but near each of the cell faces. This calculation is performed using Equations 1 and 2 with the mixture velocity at each face but the solid fraction of the cell of interest. Then the logic shown in Figure 1 is applied to all of the downstream cells, which may include any number of neighboring control volumes, including extreme cases where none or all four are considered. This approach is termed the face velocity method (FVM).

To ensure smooth packing from cell to cell, $g_{s,c}$ is also applied as a constant packing fraction (CPF). The instantaneous solid fraction of the cell of interest when it becomes packed is termed the packing fraction, $g_{s,p}$, and for the velocity based models will vary throughout the domain, but always be less than or equal to $g_{s,c}$ due to this imposed upper limit. For the constant packing fraction (CPF) model used by Vreeman et al. [8], $g_{s,c}$ and $g_{s,p}$ are equal and constant throughout the domain. Packing is checked following convergence of the governing equations. The proposed packing schemes are compared using a simple static casting simulation. Figure 1b shows the system schematic with the boundary and initial conditions. The numerical grid was uniform and 80x80 cells except where noted.

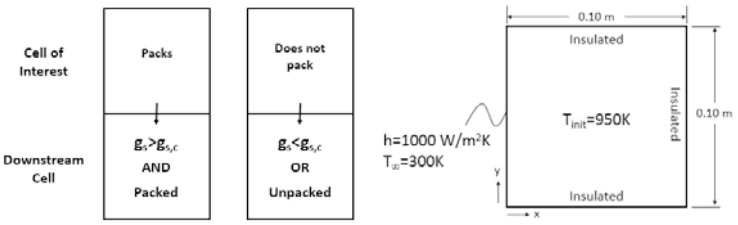

(a) *(b)*

Figure 1: Schematics for (a) the velocity based packing scheme and (b) system geometry and boundary conditions.

The alloy modeled was AA7050, with thermophysical properties taken from [16–19]. The model solved species equations for the quaternary Al-Zn-Cu-Mg system. An equilibrium thermodynamic model was used. The equation for the liquidus surface and the relevant partition coefficients were found using the Thermocalc™ TCAL1 database [20]. The liquidus is given by $T_{liq} = 933.15 + 0.63 - 174.16C_l^{Zn} - 271.55C_l^{Cu} - 494.68C_l^{Mg}$, where the temperature is in K, the composition in weight fraction, the first term is the melting temperature of pure aluminum, and the second accounts for additions of elements not tracked by the model (Zr, Fe, Si, Ti, Cr, and Mn). The relevant partition coefficients are $k^{Zn}=0.39$, $k^{Cu}=0.09$, and $k^{Mg}=0.29$.

Results and Discussion

Before considering the velocity based models, the CPF approach will be discussed as a baseline. Figure 2 shows Zn composition fields and flows predicted with the CPF model with packing fraction $g_{s,p}$=0.2 during and after solidification. The liquidus front proceeds from the left wall, and a counterclockwise buoyancy driven flow cell develops. For this alloy, the solute partitions

to the liquid. The first solid to attach to the cooling wall has the lowest composition in the domain, as the enriched liquid is advected from these first cells to pack and is replaced by fresh liquid nearer the nominal composition. The advection of solute from just inside the rigid mush continuously enriches the bulk liquid throughout the process, and so, the last liquid to freeze in the upper right corner has the highest composition. Additionally, the negative buoyancy of solute-depleted solid particles advected in the flow cell resists the up-flow at the right wall (Equation 2). Settling of these particles has an associated displacement of enriched liquid, further enriching the top layer of the casting.

Of particular note are the channel segregates which form as streaks in the composition field. The first of these appear directly on the cooling wall and are a result of individual cells packing prior to others. Advection of the liquid from these cells leaves behind depleted solid, and enriches the surrounding control volumes. The liquidus temperature of the neighboring cells is therefore depressed, lowering their fraction solid, and delaying packing. Flow around the first cells to pack also enriches control volumes in the lateral direction, allowing the channel to propagate into the casting. Channel segregates will be discussed further in the context of the velocity based methods below.

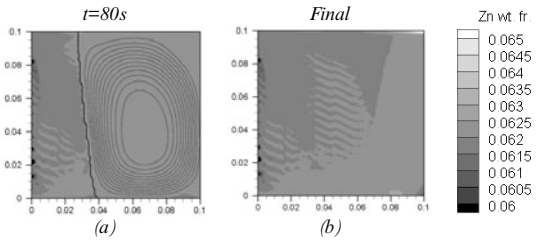

Figure 2: Composition fields for Zn for the constant packing fraction model (CPF) (a) during the process, showing counterclockwise streamlines and the packed interface, and (b) after solidification, for a packing fraction $g_{s,p}$=0.2.

One of the important implications of the velocity based packing models compared to the constant packing fraction approach is that the packing fraction ($g_{s,p}$) varies throughout the domain depending on the flow field, rigid interface geometry, and solidification conditions. Flow towards a packed interface and higher temperature gradients will favor lower packing fractions, while flow parallel to or away from a packing interface and lower temperature gradients favor higher packing fractions. Figure 3 shows the average and standard deviation of the packing fraction throughout the domain as a function of $g_{s,c}$ as predicted by the three velocity based schemes. The average packing fractions should be compared to a slope of unity representative of the constant packing fraction model, which would have a corresponding standard deviation of zero.

One aspect of Figure 3 to note is the relative values of the average packing fractions for the three velocity based models. In the AVM, only one velocity vector selects the downstream cell. In the AVA, both averaged velocity vectors are used (two downstream cells), increasing the likelihood of a cell meeting the requisite criteria. For the FVM, outward solid velocity from any of the four faces may trigger a packing event. In each case, the probability of a given cell packing is

increased relative to the CPF model, thereby decreasing the predicted average packing fraction. Similarly, the difference in standard deviation can be explained by the number of neighboring control volumes that may influence the packing of the cell of interest.

A more surprising trend is the maximum in the standard deviation with critical solid fraction. The initial increase is caused by the larger range of packing fractions that are allowed, since $g_{s,p}$ cannot exceed $g_{s,c}$. The eventual decrease is caused by natural limitation of the lower packing fractions, which tend to occur at the very beginning of the process when the solid fraction gradient is highest (i.e. it is most likely that a cell with a low solid fraction is neighboring a cell with $g_s > g_{s,c}$). For high critical values, the initial packing of the first few rows of control volumes is delayed slightly until the solid fraction gradient is lower, tending to discourage packing at low solid fractions.

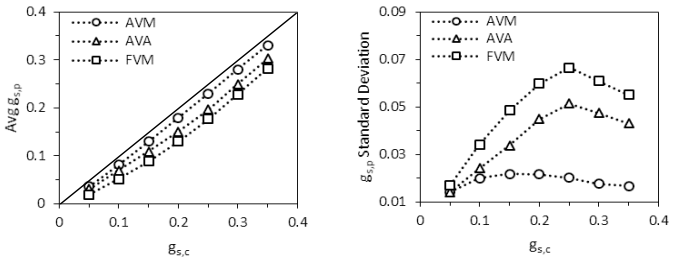

(a) *(b)*

Figure 3: Average predicted packing fraction and its standard deviation over the domain for each velocity based scheme as a function of the critical solid fraction.

Further comparison of the influence of three models on packing is made clear by the contour plots of resulting packing fractions throughout the domain, shown in Figure 4a for cases where $g_{s,c}$=0.2. First, the range of packing fractions exhibited by the different schemes matches the relative standard deviation values shown in Figure 3b. More interesting is the appearance of streaks in the packing fraction shown by the AVA and FVM, both of which consider any downstream control volume rather than just the *most* downstream control volume, as done in the AVM, where these streaks are not found. Furthermore, the packing fields correspond closely to the final composition fields (shown for Zn) as shown in Figure 4b.

The composition field is closely related to the packing fraction distribution through the permeability of the rigid mush. Macrosegregation is caused by the relative motion of solid and liquid of differing compositions. When a cell packs, the depleted solid becomes stationary, but the enriched liquid may be advected away, the ease of which is determined by Equation 3. For low packing fractions, the initial permeability of the rigid mush is fairly high, allowing enriched liquid to be advected away and replaced by fresh liquid at a composition nearer the nominal. At higher packing fractions, the permeability at the edge of the rigid mush is comparatively low, preventing significant fluid flow from occurring.

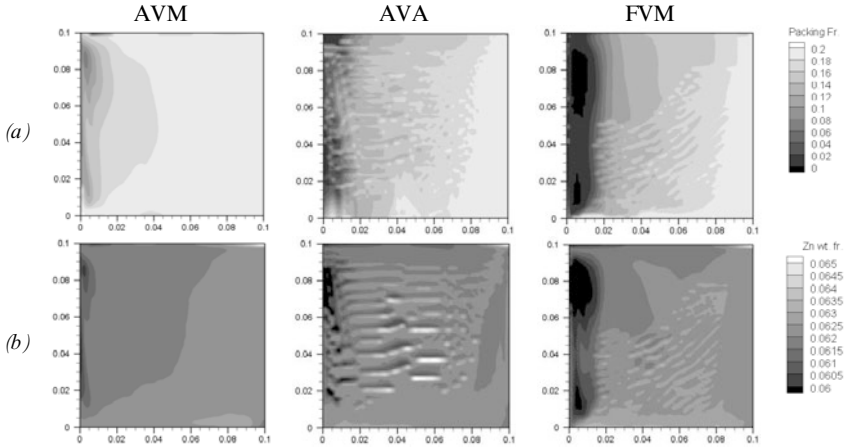

Figure 4: Contour plots of results from the three velocity based schemes with $g_{s,c}$=0.2 showing (a) predicted packing fraction distribution and (b) composition distribution.

The streaks in the composition field resemble channel segregates or freckles that have been reported both experimentally (e.g. [21]) and in simulations (e.g. [22]) of columnar solidification. These segregates form due to cells that pack at lower solid fractions jutting out from the solidification interface and affecting the flow around them. When one of these cells becomes packed earlier than the cells around it, the associated enriched liquid flows into neighboring cells in the downstream direction, to be replaced by liquid with a lower composition. The liquidus temperature, and therefore the fraction solid, of the enriched cells are reduced, tending to delay packing and becoming further enriched over time. Eventually these cells do become packed, but the next row of cells, similarly affected by the solute advection, are less likely to pack than their depleted neighbors, allowing the channel to propagate.

The formation of channel segregates is strongly affected by the packing model. The differences in packing are shown at an intermediate time in the process for the three packing models in Figure 5. The flow cell is rotating in a counterclockwise direction, flowing down the solidification interface. For the AVM, other than near the top of the domain, the strong down-flow along the solidification front mostly causes packing to proceed from the bottom up, as seen by the stepped shape of the packed interface. Any lateral flow in this case will likely be much weaker than the strong downward flow, so the selection of only the most downstream control volume in the packing model generally suppresses channel formation. In the AVA and FVM, since other downstream cells can trigger a packing event, weak lateral flows toward the packed interface can cause packing of cells that then jut out and affect the surrounding flow. These types of cells are apparent by the roughness of the packing interfaces on the order of the grid spacing in Figure 5 for the AVA and FVM when compared to the AVM. Once one of these cells pack, channel propagation may occur via the mechanism described above.

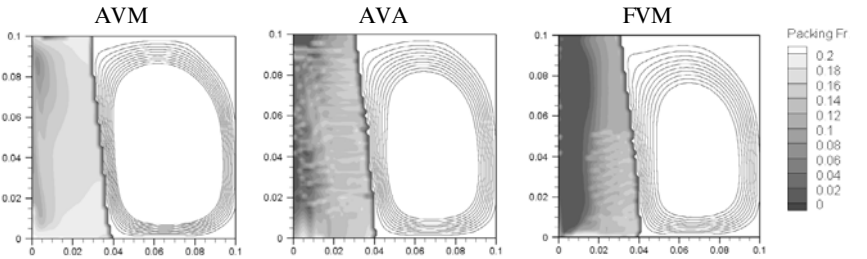

Figure 5: The effect of the fluid flow on the packing fraction, shown at time t=80s for the AVM with $g_{s,c}$=0.2.

Considering the strong effect of the packing models on channel segregate formation, it is tempting to use them as validation of one model over another. Unfortunately, segregates such as these have not been observed experimentally in equiaxed castings and there is reason to believe that they are a numerical artifact as illustrated by the results above and their extreme grid dependence (Figure 6). In the CPF model, as well as the AVA and FVM, the appearance, spacing, and composition of the channels is strongly dependent on the grid size. Only the AVM appears to achieve some level of grid independence, in which channels do not form at all.

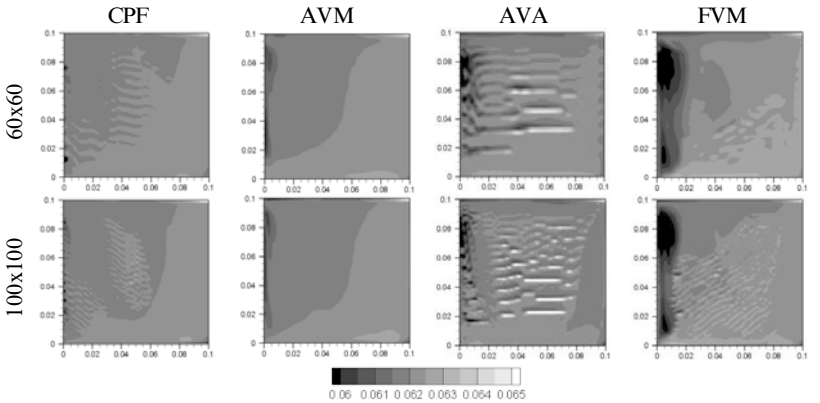

Figure 6: Grid dependence of channel segregates that appear in the AVA and FVM while the AVM is relatively grid independent. Contour is Zn wt. fr., the cases shown are for $g_{s,c}$=0.2.

Based on the plots in Figure 6, and assuming that channels are only a numerical artifact, at first it seems that the AVM performs the best, because channels do not form at all. However, the results presented here are for a specific domain geometry, material, and set of initial and boundary conditions. No channels form in the AVM because the interface between the rigid mush and the bulk liquid is mostly parallel to the local flow direction. Any change in cooling conditions or geometry may upset the balance of factors that suppress channel formation in this case, even for

the same material. Therefore, from the evidence given here, it is difficult to conclude that one particular packing model is more realistic than the others.

Conclusions

Three different velocity based packing schemes were presented for the modeling equiaxed solidification and compared to the constant packing fraction method for static castings of AA7050. Final macrosegregation distributions are strongly dependent on the packing model, but it is difficult to compare the relative worth of the various schemes. The extreme grid dependence of the development of channel segregates suggests that they are, at least in part, a numerical artifact. Future research should explore initiation and propagation of channel segregates in more detail to determine the origin of their numerical dependence, and include experimental validation.

References

1. J. Ni and C. Beckermann, *Metall. Trans, B*, 22 (1991), 349-361.
2. A. V. Reddy and C. Beckermann, in *Mater. Process. Comp. Age II,* V. R. Voller, S. P. Marsh, and N. El-Kaddah, eds. (1995), 89-102.
3. A. Ludwig and M. Wu, *Metall. Mater. Trans. A,* 33 (2002), 3673-3683.
4. C. Y. Wang and C. Beckermann, *Metall. Mater. Trans. A*, 27 (1996), 2754-2764.
5. C. Y. Wang and C. Beckermann, *Metall. Mater. Trans. A*, 27 (1996), 2765-2783.
6. M. Wu, A. Fjeld, and A. Ludwig, *Comput. Mater. Sci.*, 50 (2010), 32-42.
7. G. D. Scott and D. M. Kilgour, *J. Phys. D. Appl. Phys.*, 2 (2002), 863-866.
8. C. J. Vreeman, M. J. M. Krane, and F. P. Incropera, *Int. J. Heat Mass Transf.*, 43 (2000), 677-686.
9. I. Vusanovic and M. J. M. Krane, *IOP Conf. Ser. Mater. Sci. Eng.*, 27 (2012), 1-6.
10. W. D. Bennon and F. P. Incropera, *Int. J. Heat Mass Transf.*, 30 (1987), 2161-2170.
11. M. J. M. Krane in *ASM Handbk. Vol. 22B, Met. Process Simul.* (Materials Park, OH: ASM International, 2010).
12. V. R. Voller and C. R. Swaminathan, *Num. Heat Transf. Pt. B Fundam.*, 19 (1991), 175-189.
13. S. V. Patankar *Numerical Heat Transfer and Fluid Flow* (New York, NY: McGraw Hill, 1980).
14. C. J. Vreeman and F. P. Incropera, *Num. Heat Transf. Pt. B Fundam.*, 36 (1999), 1-14.
15. A. Kumar et al., *IOP Conf. Ser. Mater. Sci. Eng.*, 27 (2012), 1-8.
16. C. J. Vreeman: M.S. Thesis, Purdue University, 1997.
17. M. Lalpoor et al., *Mater. Sci. Eng. A*, 538 (2011), 2831-2842.
18. W. F. Gale, *Smithells Metals Reference Book 8th ed.* (New York, NY: Elsevier, 2004).
19. T. Iida and R. Guthrie, *The Physical Properties of Liquid Metals* (Oxford: Clarendon Press, 1988).
20. J. O. Andersson et al., *Calphad Comput. Coupling Phase Diagrams Thermochem.*, 26 (2002), 273-312.
21. N. Mori and K. Ogi, *Metall. Trans. A*, 22 (1991), 1663-1672.
22. I. Vusanovic and V. R. Voller, *Mater. Sci. Forum*, 790-791 (2014), 73-78.

CFD Modeling and Simulation in Materials Processing 2016
Edited by: Laurentiu Nastac, Lifeng Zhang, Brian G. Thomas, Miaoyong Zhu, Andreas Ludwig, Adrian S. Sabau, Koulis Pericleous, and Hervé Combeau
TMS (The Minerals, Metals & Materials Society), 2016

LARGE EDDY SIMULATIONS OF THE EFFECTS OF DOUBLE-RULER ELECTROMAGNETIC BRAKING AND NOZZLE SUBMERGENCE DEPTH ON MOLTEN STEEL FLOW IN A COMMERCIAL CONTINUOUS CASTING MOLD

Kai Jin[1], Surya P. Vanka[1], Brian G. Thomas[1], Xiaoming Ruan[2]

[1]Department of Mechanical Science and Engineering;
1206 W Green St.; Urbana, IL 61801, USA.
[2]Steelmaking Research Department, Research Institute Baoshan Iron &Steel Co., Ltd.;
889 Fujin Rd., Shanghai 201900, P. R. China.

Keywords: Continuous casting, Electromagnetic braking, Large eddy simulation

Abstract

In steel continuous casting, flow in the mold region is related to many quality problems such as surface defects and slag entrainment. An electromagnetic braking (EMBr) system is a method to control the steel flow field to minimize defects and capture inclusions. The position of the port of the Submerged Entry Nozzle (SEN) and the peak magnetic field both affect the performance of the EMBr. In the present work, an efficient multi-GPU based code, CUFLOW, is used to perform Large Eddy Simulations of the turbulent flow by solving the time-dependent Navier-Stokes equations in a domain that includes the slide gate, SEN and mold region. The computations were first validated by comparing the predicted surface velocity with plant measurements. Subsequently, eight LES simulations were conducted to study the effects of different EMBr values and SEN depths. The flow patterns in various regions are presented. The results show that applying EMBr greatly lowers top surface velocities and turbulent fluctuations.

Introduction

In the continuous casting process for making steel, electromagnetic devices are often used to modify the flow pattern in the mold region. The magnetic field can be either static (applying a DC current to electromagnets) or dynamic in which an AC current is applied. The static magnetic field in turn generates a Lorentz force field that acts against the flow. This type of configuration is therefore referred to as an electromagnetic braking (EMBr) system. Based on the DC electromagnet's shape and location, there are usually three types of magnetic field configurations [1]: local, single ruler and double-ruler [2–7]. The differences between these configurations are discussed elsewhere [1]. This work focuses on the double-ruler configuration that is widely used in industry and commonly known as Flow Control Mold (FC-Mold). In the FC-Mold, two rectangular magnets are placed across the entire mold width, with one positioned near the meniscus and the other below the nozzle port [1–7].

Owing to the hostile environment of the extremely hot molten steel, it is difficult to conduct experiments in real casters. Computational models are widely used [2–9] as tools to understand the physics of the process, and improve and optimize the operation. A large number of the previous numerical studies solved the Reynolds Averaged Navier Stokes (RANS) equations with

attention paid to the time mean flow behavior in the mold [2,3,7]. Recent developments in parallel computing technology have enabled high-fidelity Large Eddy Simulations (LES) to become feasible and have been recently performed by a few researchers to study the transient aspects of the turbulent fluid flow [4–6,9].

The FC-Mold EMBr arrangement followed in industry can affect both the mean flow behavior and the transient flow structure in the mold [5–7]. It also reduces the mean surface velocity and fluctuations normal to the free surface [2,3,5–7]. However, electromagnetic forces can also have an opposite effect on the overall flow if not used properly along with other parameters (e.g. submergence depth) [1]. With the same EMBr settings, different submergence depths may considerably change the effectiveness of local EMBr system [1]. However, to our knowledge not much attention has been paid to the effect of submergence depth and EMBr field distribution, especially for the widely used double-ruler magnetic field arrangement.

The effect of EMBr on the flow in mold has been previously studied, but the effects on the flow in the Submerged Entry Nozzle (SEN) have not been reported. Much of the work has been focused on the effects of an EMBr on the flow in the mold region without including the full SEN [2–5,8]. While some researchers have included the SEN in the computational domain, they have ignored the magnetic field above the steel-slag interface [6]. However, simulations with RANS have shown that a strong magnetic field modifies the mean flow inside the SEN and reduces its turbulent kinetic energy [7]. Therefore, high accuracy transient simulations must be conducted with inclusion of also the effects of the magnetic field on the nozzle flow.

The work presented here investigates the effect of submergence depth and EMBr on the turbulent flow in both SEN and mold regions of a real continuous caster of steel using LES. This paper first introduces the governing equations, then describes the computational models and numerical details. The model is then validated by comparing the predictions with plant measurements. The effect of submergence depth and EMBr on the flow field in the SEN, port, mold region and top surface are subsequently investigated. Finally, the important results are summarized.

Plant Measurements

Plant measurements of the magnetic fields and molten steel flow were conducted on the No. 4 caster at Baosteel, Shanghai in 2012. Top surface velocities of this conventional (230×1200 mm) continuous steel slab caster were measured with a device similar to Sub-meniscus Velocity Control (SVC) equipment. In the measurement, one end of a rod is connected to a pivot and the other end is dipped into the molten steel as shown in Figure 1. The molten steel flow impinges on the rod and induces a drag force that balances the weight of the rod and makes the rod rotate around the pivot by an angle θ. The angle is then converted into velocity of the molten steel. The SVC-like device probe was placed at quarter mold region parallel to the Wide Face (WF) of the mold and the measured steel surface velocity was recorded every 5 seconds in a 70-second time interval. The casting conditions and process parameters are given in Table I. Flow rate of the molten steel through the SEN into the mold was controlled by a slide-gate that moved between the geometric center and the Inside Radius (IR) side of the caster. For the experiments casting 1200mm wide slabs at 1.3m/min, the slide gate was 70% open, as shown in Figure 2. No argon gas was injected, and the EMBr system was also turned off during the experiment. The measured magnetic field strengths down the mold are shown in Figure 3.

Table I. Casting Parameters and Properties of the Steel

Process parameter	Value
Mold thickness (L_t)	230 mm
Mold width (L_w)	1200 mm*; 1300 mm
Slide gate opening area fraction	70%*; 80%
Submergence depth (d_{sub})	170 mm or 200 mm
SEN port downward angle	15°
Casting speed (V_c)	1.3 m/min*; 1.8 m/min
Steel density (ρ)	7000 kg/m^3
Steel dynamic viscosity ( )	0.0063 kg/(m·s)
Steel electrical conductivity (σ)	liquid steel 714000 S/m; solid steel 787000 S/m

* Casting conditions when plant measurements were done

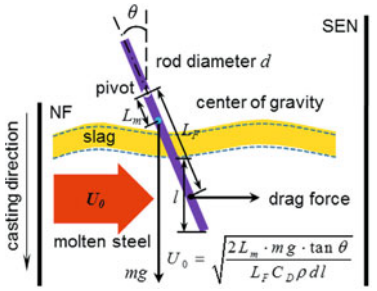

Figure 1. Schematic of SVC-like device

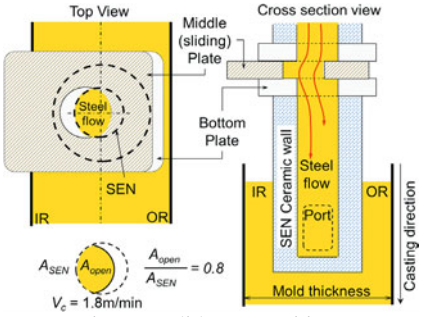

Figure 2. Slide gate position

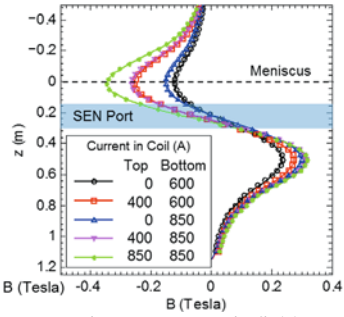

Figure 3. Magnetic fields

Governing Equations and Computational Model

A three-dimensional finite-volume computational model was applied to study the flow behavior in the caster. The governing equations and details of the model are discussed in this section.

Governing Equations for Fluid Flow

In LES, the dimensional filtered time dependent Navier Stokes equations given below are solved.

$$\nabla \cdot (\rho \mathbf{u}) = \dot{s} \tag{1}$$

$$\frac{\partial \mathbf{u}}{\partial t} + \mathbf{u} \cdot \nabla \mathbf{u} = -\frac{\nabla p}{\rho} + \nabla \cdot \left[\left(\nu + \nu_{sgs} \right) \left(\nabla \mathbf{u} + \nabla \mathbf{u}^T \right) \right] + \frac{\mathbf{F}_L}{\rho} \tag{2}$$

Here $\dot{s}$ is the sink term due to the solidifying shell, ρ is the molten steel density, $\mathbf{u}$ is filtered velocity, p is modified static pressure which includes the filtered normal stresses, $\mathbf{F}_L$ is the effect of the Lorentz force, ν is the kinematic viscosity of the molten steel and ν_{sgs} is the eddy viscosity that was computed from the coherent-structure Smagorinsky model (CSM) [10] also used in previous studies of fluid flow in steel casters with EMBr [6].

$$\nu_{sgs} = \left(C_s \Delta \right)^2 \sqrt{2 \left\| \mathbf{S} \right\|^2} \tag{3}$$

$$C_s^2 = C_{CSM}\left|\frac{Q}{E}\right|^{3/2}\left(1-\frac{Q}{E}\right) \quad \text{where} \quad Q=\frac{1}{2}\left(\|\mathbf{W}\|^2-\|\mathbf{S}\|^2\right) \quad \text{and} \quad E=\frac{1}{2}\left(\|\mathbf{W}\|^2+\|\mathbf{S}\|^2\right) \tag{4}$$

where is the filter width, **S** is the filtered rate-of-strain tensor, C_{csm}=1/22 is a model constant and **W** is the filtered vorticity tensor (also known as rate of rotation tensor). The CSM model incorporates the effect of anisotropy induced by the applied magnetic fields on the filtered scales [10]. Therefore, no additional terms are added.

In this work, the electric potential method is used to compute the Lorentz force $\mathbf{F}_L$. When a magnetic field **B** is applied to the moving conducting material (with electrical conductivity σ), an electric field is generated and the electrical current density **J** can be computed through Ohm's law given as equation (5) below. For a well conducting material the current conservation law is given by equation (6). Therefore, the electric potential Φ satisfies a Poisson equation (equation (7)) from which Φ is calculated. Then, Lorentz force can be computed following equation (8).

$$\mathbf{J}=\sigma\left(-\nabla\Phi+\mathbf{u}\times\mathbf{B}\right) \tag{5}$$

$$\nabla\cdot\mathbf{J}=0 \tag{6}$$

$$\nabla\cdot\left(\sigma\nabla\Phi\right)=\nabla\cdot\left[\sigma\left(\mathbf{u}\times\mathbf{B}\right)\right] \tag{7}$$

$$\mathbf{F}_L=\mathbf{J}\times\mathbf{B} \tag{8}$$

Note that both the molten steel and the solidified shell are conducting materials and therefore equations (5) to (8) need to be solved in both the liquid steel and shell region. Simply treating the shell as an insulated wall have been seen to lead to unrealistic flow unsteadiness in the mold [5,11]. In this work the above MHD equations are solved in the entire domain that includes the solid shell region.

Computational Methods, Mesh, and Boundary Conditions

The governing equations are solved with an in-house code CUFLOW [9,12–14] which utilizes Graphics Processing Units (GPU). Current version of the code was written using CUDA Fortran, and has been extended to be able to work on multiple GPUs in parallel through the Message Passing Interface (MPI) [14]. In CUFLOW, fractional step method is used to solve the continuity and momentum equations. Pressure and electric potential Poisson equations are solved efficiently by a V-cycle multigrid method, and red-black Successive Over Relaxation (SOR) on GPUs with over-relaxation parameter of 1.6. Details of the solution algorithm are available in reference [9,13,14]. The solver has been validated and used to study the effect of magnetic field in a lid-driven cavity [15] and the flow in the mold region of continuous casters of steel with and without EMBr [5,6]. As listed in Table II, seven simulations were carried out on the Blue Waters supercomputer.

A Cartesian grid of ~16 million finite volume cells (~4 mm cell size) is generated for the computational domain which includes slide gate, SEN and mold region. The domain ends at ~2.8 m below the meniscus. Solid shell is modeled only as an electrically conducting zone (fluid flow equations are not solved) and is included in the domain with a thickness found by the equation $h(\text{mm}) = 3[t(\text{s})]^{1/2}$.

The slide gate was 80% open for a casting speed of 1.8 m/min. The velocity at the SEN inlet is fixed to match the mass flow rate of the steel. At the outlet, a zero derivative boundary condition is applied. All other domain boundaries and the interface between the liquid steel and solidified shell are treated as no slip walls. For the MHD equations, insulated boundary condition was applied at all the boundaries of the computational domain.

Table II. List of the LES simulations

No.	V_c (m/min)	d_{sub} (mm)	Top coil current (A)	Bottom coil current (A)
1	1.8	170	0	0
2	1.8	170	0	850
3	1.8	170	400	850
4	1.8	170	850	850
5	1.8	200	0	0
6	1.8	200	0	850
7	1.8	200	400	850

Validation with Plant Velocity Measurements

In addition to the seven simulations listed in Table II, an 80 second LES simulation with a grid of ~15.5 million cells was conducted for the same casting conditions as the plant measurements. The u_x velocity parallel to WF, at the probe location (1 cm below the top surface and at the quarter mold region in the middle plane) was recorded. Figure 4 compares the measured u_x velocity against the predicted u_x velocity by the LES. Both LES simulation and the SVC-like measurements show that the flow direction was from narrow face (NF) to SEN with an average velocity of ~0.2 m/s. This good agreement between the computational model and the measurements provides support to the code results and demonstrate accuracy of the LES model.

Results and Discussion

Effect of Submergence Depth

Figure 5 shows contours of mean velocity magnitude |**U**| for different submergence depths (d_{sub}) at 1 cm below the top surface and at the center plane of the mold. In the top surface region, the region of high velocity is closer to the Outer Radius (OR) side of the mold. For d_{sub} = 170mm, the maximum velocity is ~0.45m/s. For d_{sub} = 200mm, the maximum top surface velocity is ~0.4m/s and the high velocity region is smaller. Overall, however, flow in the mold is not affected much by submergence depth, as both calculations show double roll flow patterns.

Effect of EMBr

Figure 6 shows the time averaged z-velocity in SEN on the symmetric plane for a submergence depth of 170mm. It is seen that increasing the magnetic field strength in the SEN causes a shorter jet. However, the size of the recirculation region below the sliding gate is not affected much by the magnetic field because the magnetic field strength field in the nozzle is relatively weak (<0.04T). Transient simulations in the mold region show two swirling vortices at the bottom of SEN for all cases except when the upper coil current I_{top} is 850A. The time-averaged flow field also shows two swirling vortices at the bottom of the SEN but only a small swirl for I_{top}=850A.

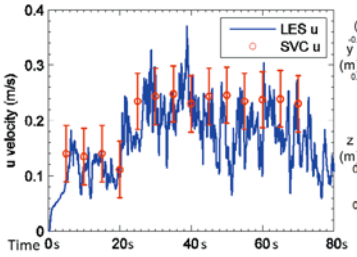

Figure 4. Compare with "SVC"

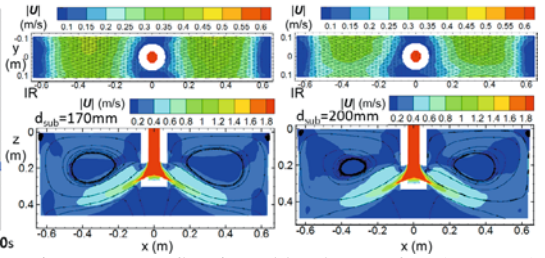

Figure 5. Mean flow in mold and top surface (no EMBr)

Figure 7 shows the time-averaged x-velocity (in/out of port) partway across the port at x = -0.045. A back flow region (where flow enters the port, towards the SEN inside) is seen near the top of port in all cases. With increasing magnetic field, the back flow region becomes larger and occupies almost half of the port when both coils have a current of 850A. The outward flow region is mainly at the bottom half of port, and the speed of the jet in the port increases with increasing magnetic field strength (due to smaller outflow area).

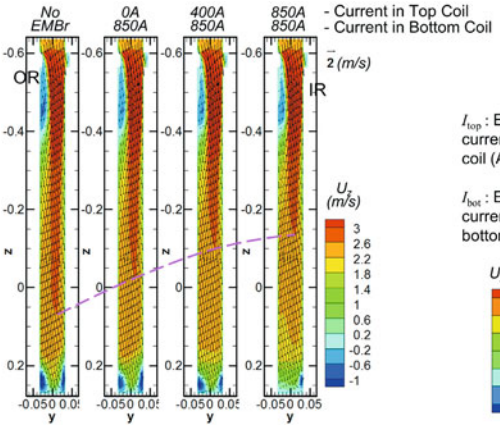

Figure 6. Mean velocity in SEN

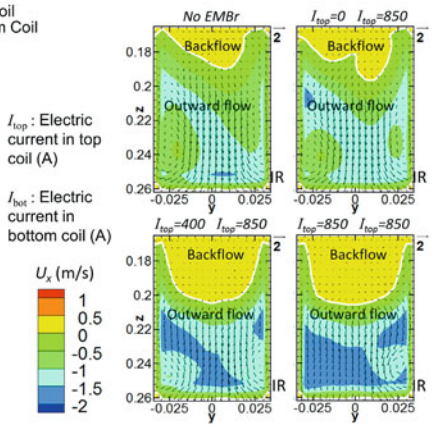

Figure 7. Backflow noticed in port

Contours of the magnitude of the time-averaged velocity in the middle y plane (y=0) for different magnetic fields (d_{sub}=170mm) are shown in Figure 8. With EMBr, thin regions of high velocity appear close to the side walls of the SEN, resulting in an M-shaped velocity profile in the x direction. This M-shaped profile is well known in channel flows with strong magnetic fields [16]. The jets exiting from the port are also thinner and stronger when the EMBr is used. The recirculation regions in the mold are more close to the jet which agrees with previous studies [6].

Figure 9 shows a typical snapshot of contours of velocity magnitude in a horizontal plane z = 0.01m (1cm below top surface). Without EMBr, the maximum velocity is ~0.5m/s and two vortices are seen near the SEN. High velocities and vertical flows at the steel-slag interface may lead to problems such as entrainment of slag. With EMBr (I_{bot}=850A) the top surface velocity

drops to ~0.05m/s. This low surface velocity may deliver less superheat to the meniscus region, leading to meniscus solidification, hook formation and entrapment of slag or inclusion particles [17]. Therefore, a weaker magnetic field that maintains the top velocity at around 0.2m/s would be better for this particular caster and casting conditions.

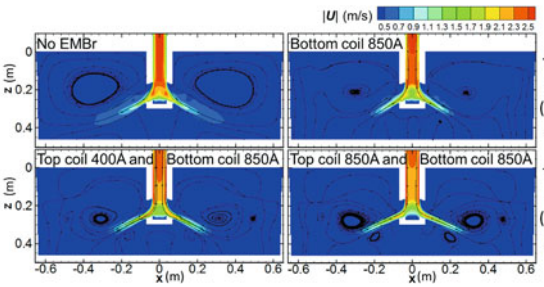

Figure 8. Velocity magnitude in mold and stream traces

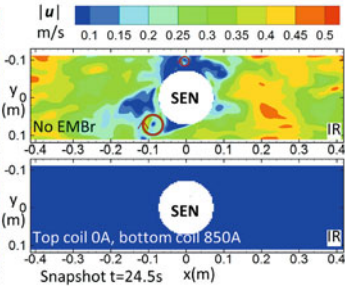

Figure 9. Flow near top surface

Conclusions

LES is used to study the effect of submergence depth and double-ruler EMBr on steel flow in SEN and mold region of a commercial steel caster. The predicted surface velocity history matches well with plant measurements. Applying strong EMBr across the nozzle in this system makes flow inside the SEN more uniform, and increases downward velocity along the walls (with strong EMBr) forming an M-shaped velocity profile in the lower part of the SEN. Application of the EMBr results in a tighter and faster jet in the mold cavity, which exits more towards the lower region of port with accompanying larger back-flow in the top. The recirculation regions in the mold become tighter and closer to the jet and newer smaller vortices form. Even with a high casting speed (1.8m/min) with no argon gas, holding the meniscus level at middle of the top ruler of the EMBr greatly lowers top surface velocity (to ~0.05m/s).

Acknowledgements

The authors thank the financial supports from the National Science Foundation (Grant No. CMMI 11-30882) and the Continuous Casting Consortium, Univ. of Illinois at Urbana-Champaign, USA. Thanks to Baosteel, Shanghai, P.R. China for providing the casting conditions and measurements. This research is also part of the Blue Waters sustained-petascale computing project, which is supported by the National Science Foundation (awards OCI-0725070 and ACI-1238993) and the State of Illinois. Blue Waters is a joint effort of the University of Illinois at Urbana-Champaign and its National Center for Supercomputing Applications. The authors also thank NVIDIA Hardware Grant Program for providing the GPUs for an in-house workstation.

References

1. B. Thomas and R. Chaudhary, “State of the Art in Electromagnetic Flow Control in Continuous Casting of Steel Slabs: Modeling and Plant Validation,” *6th Int. Conf. Electromagn. Process. Mater. EPM* (Dresden, Austria, 2009).

2. A. Idogawa et al., “Control of Molten Steel Flow in Continuous Casting Mold by Two Static Magnetic Fields Imposed on Whole Width,” *Mater. Sci. Eng. A*, **173** (1993), 293–297.

3. B. Li, T. Okane, and T. Umeda, “Modeling of Molten Metal Flow in a Continuous Casting Process Considering the Effects of Argon Gas Injection and Static Magnetic-Field Application,” *Metall. Mater. Trans. B*, **31** (2000), 1491–1503.

4. Y. Miki and S. Takeuchi, “Internal Defects of Continuous Casting Slabs Caused by Asymmetric Unbalanced Steel Flow in Mold,” *ISIJ Int.*, **43** (2003), 1548–1555.

5. R. Chaudhary, B. G. Thomas, and S. P. Vanka, “Effect of Electromagnetic Ruler Braking (EMBr) on Transient Turbulent Flow in Continuous Slab Casting Using Large Eddy Simulations,” *Metall. Mater. Trans. B*, **43** (2012), 532–553.

6. R. Singh, B. G. Thomas, and S. P. Vanka, “Large Eddy Simulations of Double-Ruler Electromagnetic Field Effect on Transient Flow during Continuous Casting,” *Metall. Mater. Trans. B*, **45** (2014), 1098–1115.

7. S.-M. Cho, S.-H. Kim, and B. G. Thomas, “Transient Fluid Flow during Steady Continuous Casting of Steel Slabs: Part II. Effect of Double-Ruler Electro-Magnetic Braking,” *ISIJ Int.*, **54** (2014), 855–864.

8. F. Li et al., “Simulation Research of Flow Field in Continuous Casting Mold with Vertical Electromagnetic Brake,” *ISIJ Int.*, **55** (2015), 814–820.

9. R. Chaudhary, “Studies of Turbulent Flows in Continuous Casting of Steel with and without Magnetic Field,” PhD Thesis, University of Illinois at Urbana-Champaign, 2011.

10. H. Kobayashi, “Large Eddy Simulation of Magnetohydrodynamic Turbulent Duct Flows,” *Phys. Fluids*, **20** (2008), 015102.

11. R. Singh, B. G. Thomas, and S. P. Vanka, “Effects of a Magnetic Field on Turbulent Flow in the Mold Region of a Steel Caster,” *Metall. Mater. Trans. B*, **44** (2013), 1201–1221.

12. S. P. Vanka, “2012 Freeman Scholar Lecture: Computational Fluid Dynamics on Graphics Processing Units,” *J. Fluids Eng.*, **135** (2013), 061401.

13. A. F. Shinn, “Large Eddy Simulations of Turbulent Flows on Graphics Processing Units: Application to Film-Cooling Flows,” PhD Thesis, Univ. of Illinois at Urbana-Champaign, 2011.

14. P. Kumar, K. Jin, and S. P. Vanka, “A Multi-GPU Based Accurate Algorithm for Simulations of Gas-Liquid Flows,” *Proc. 1st Therm. Fluids Eng. Summer Conf.* (American Society of Thermal and Fluids Engineers, New York City, August 9).

15. K. Jin, S. P. Vanka, and B. G. Thomas, “Three-Dimensional Flow in a Driven Cavity Subjected to an External Magnetic Field,” *J. Fluids Eng.*, **137** (2015), 071104.

16. R. J. Moreau, *Magnetohydrodynamics* (Springer Science & Business Media, 1990).

17. R. Liu et al., “Measurement of Molten Steel Surface Velocity with SVC and Nail Dipping during Continuous Casting Process,” *Sens. Sampl. Simul. Process Control* (John Wiley & Sons, San Diego, 2011).

CFD Modeling and Simulation in Materials Processing 2016

Smelting, Degassing, Ladle Processing, Mechanical Mixing, and Ingot Casting

Session Chair:
Adrian S. Sabau

CFD Modeling and Simulation in Materials Processing 2016
Edited by: Laurentiu Nastac, Lifeng Zhang, Brian G. Thomas, Miaoyong Zhu, Andreas Ludwig, Adrian S. Sabau, Koulis Pericleous, and Hervé Combeau
TMS (The Minerals, Metals & Materials Society), 2016

CFD MODELING OF A LADLE WITH TOP STIRRING LANCE

Haibo Ma[1], Xia Chen[1], Hoyong Hwang[2], Megan Pratt[3], Russel J. Mulligan[3], Bin Wu[1], Guangwu Tang[1] and Chenn Q. Zhou[1]

[1]Center for Innovation through Visualization and Simulation; Purdue University Calumet; 2200 169th Street; Hammond, IN 46323, USA
[2]ArcelorMittal Global R&D; 3001 East Columbus Drive; East Chicago, IN 46312-2939, USA
[3]ArcelorMittal Burns Harbor; 250 West U.S. Highway 12; Burns Harbor, IN 46304, USA

Keywords: stirring ladle, hot metal, CFD, multiphase flow, stirring

Abstract

Steel cleanliness is very important for the quality of final products. Stirring ladles have been widely used to ensure the good quality steel produced from liquid iron in steelmaking industry. Proper stirring is crucial for obtaining clean steel. In this study, three-dimensional computational fluid dynamics (CFD) technique is used to study the transient multiphase flow inside a working ladle at a steel plant. The study presents a comparison of three different methods to model multiphase flow, i.e. the volume of fluid (VOF) method, the Eulerian-Eulerian method, and the Eulerian-Lagrangian method. The simulation results are compared with experimental data obtained from a working ladle. The best simulation method, which gives the most accurate results within a reasonable amount of computational time, will be applied to optimize operating parameters under various conditions.

Introduction

In the steelmaking industry, secondary refining or secondary metallurgy is required for temperature homogenization, as well as ingredients adjustment, steel cleanliness, and other functions. A proper stir is very important for obtaining clean steel. The stirring ladle is widely used for steel cleanliness to ensure good quality of the product. Usually, a lance is immersed into the steel bath from top surface, the stirring gas is injected from nozzles, which are located at the bottom of the lance. With the stirring effect, the flow field of the steel bath is improved and high cleanliness efficiency is therefore guaranteed. Since there are both liquid phase (liquid iron and slag) and gas phase (stirring gas) existing in the ladle, thus, a multiphase model is required. Three different multiphase methods have been adopted in this study.

The VOF method can be used to simulate the two immiscible flows (liquid iron and slag) and the bubbles generated by the stirring gas [1, 2]. This method is able to capture the characteristics of the distinct interface between phases and the slag eye formation. The Eulerian-Eulerian method can obtain global information about gas phase. For instance, it can track the bubble velocity and concentration, but it cannot describe the formation process of bubbles [3]. The Eulerian-Lagrangian method treats gas bubbles as a discrete phase by employing the discrete phase model (DPM), while the Eulerian method is used to track the interface among the three phases in a ladle [4, 5, 6, 7].

Mathematical Models

The VOF method is based on the concept of solving one momentum equation for the multiphase mixtures, and characterizing different phases at the same computational volume at the same time by their volume fraction. A set of Navier-Stokes equations for an incompressible Newtonian flow was solved:

$$\frac{\partial}{\partial t}(\rho\vec{v}) + \nabla\cdot(\rho\vec{v}\vec{v}) = -\nabla p + \nabla[\mu(\nabla\vec{v} + (\nabla\vec{v})^T)] + \rho\vec{g} + \vec{F} \quad (1)$$

Since a particular control volume may be not entirely occupied by a single phase, the properties of mixture in Eq. (1) can be obtained from Eq. (2) and Eq. (3):

$$\rho = \alpha_q\rho_q + (1 - \alpha_q)\rho_q \quad (2)$$

$$\mu = \alpha_q\mu_q + (1 - \alpha_q)\mu_q \quad (3)$$

In the Eulerian-Eulerian method, similar to the VOF method, each phase is treated as an interpenetrating continuum, the concept of volume fraction is introduced, too. The momentum balance for phase q yields:

$$\frac{\partial}{\partial t}(\alpha_q\rho_q\overrightarrow{v_q}) + \nabla\cdot(\alpha_q\rho_q\overrightarrow{v_q}\overrightarrow{v_q}) = -\alpha_q\nabla p + \nabla\cdot\overline{\overline{\tau_q}} + \alpha_q\rho_q\vec{g} + I_q + \vec{F} \quad (4)$$

Here, $\overline{\overline{\tau_q}}$ is the q^{th} phase stress-strain tensor, μ_q and λ_q are the shear and bulk viscosity of phase q. The average interfacial momentum transfer rate I_q between two phases is based on the value of the exchange coefficient K_{pq} from the universal drag law. The drag coefficient C_D varies in different conditions:

$$C_D = \begin{cases} C_{D_{vis}} = \frac{24}{Re}(1 + 0.1Re^{0.75}), C_{D_{dis}} < C_{D_{vis}} \\ C_{D_{dis}} = \frac{2}{3}(\frac{d_p}{\lambda_{RT}})\,(\frac{1+17.67(1-\alpha_p)^{\frac{9}{7}}}{18.67(1-\alpha_p)^{\frac{3}{2}}})^2, C_{D_{vis}} < C_{D_{dis}} < C_{D_{cap}} \\ C_{D_{cap}} = \frac{8}{3}(1 - \alpha_p)^2, C_{D_{dis}} > C_{D_{cap}} \end{cases} \quad (5)$$

The Eulerian-Lagrangian method is a combination of VOF model and DPM model. For the liquid phase, a momentum source $\overrightarrow{F_b}$ is added to the continuous phase momentum Eq. (1) by examining the change in momentum of a particle as it passes through each control volume:

$$\frac{\partial}{\partial t}(\rho\vec{v}) + \nabla\cdot(\rho\vec{v}\vec{v}) = -\nabla p + \nabla[\mu(\nabla\vec{v} + (\nabla\vec{v})^T)] + \rho\vec{g} + \vec{F} + \overrightarrow{F_b} \quad (6)$$

Here, v is the fluid velocity. v_b, ρ_b and Q_b are the velocity, density and mass flow rate of argon bubble respectively, and Δt is the time step size. In order to include the effect of the discrete phase on the continuum phase, the two-way coupling is adopted. In the coupled method, the continuous phase flow pattern is impacted by the discrete phase, and vice versa.

For the discrete phase, the trajectory of each argon bubble is obtained by integrating the force balance on the bubble in each time step. The drag force, the buoyancy force, the virtual mass force and the force derived from the pressure gradient are taken into consideration in this study:

$$\frac{dv_b}{dt} = F_D(\vec{v} - \overrightarrow{v_b}) + \frac{\rho_b - \rho}{\rho_b}\vec{g} + \frac{1}{2}\frac{\rho}{\rho_b}\frac{d}{dt}(\vec{v} - \overrightarrow{v_b}) + \frac{\rho}{\rho_b}v_b\nabla v \quad (7)$$

Here, F_D is the drag force, C_D is the drag coefficient, which is a function of Reynolds number. Non-spherical particle drag model is introduced in present study [7]. In addition, the diameter bubbles is assumed to be a constant of 1.5 inches and the random walk model is considered to describe the chaotic effect of turbulence in the liquid iron.

Geometrical Model and Boundary Conditions

Figure 1 shows the three-dimensional model based on the drawings provided by the steelmaking plant. In order to purify the liquid iron, a tracer is introduced to measure the cleanliness process. The tracer is dropped from the top at the alloying chute position and then melted in the liquid iron. A sampling position is chosen to measure the tracer concentration in the liquid. By using the sampling data, the mixing process can be monitored.

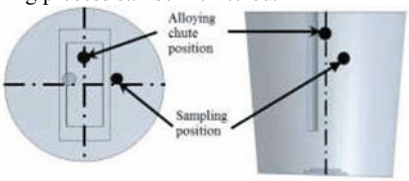

Figure 1. Computational geometry of the ladle.

Figure 2 shows the simulation domain of the stirring ladle. There are three phases in the VOF method and Eulerian-Lagrangian method, as shown in Figure 2(a). The yellow color area shows the liquid phase (liquid iron), and the blue color area represents the slag layer. The area above the slag phase is the gas phase. However, as for Eulerian-Eulerian method, each phase has its own momentum equation instead of sharing a single momentum equation with other phases. As a result, the number of phases may significantly affect convergence behavior in the Eulerian-Eulerian method. Since the present study is mainly focusing on the flow field and mixing process, a simplified calculation domain including liquid iron and argon gas was adopted in Eulerian-Eulerian model, as shown in Figure 2(b).

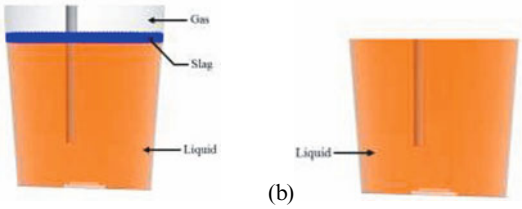

(a) (b)

Figure 1. Simulation domain. (a) VOF and Eulerian-Lagrangian; (b) Eulerian-Eulerian.

The no-slip boundary condition and standard wall function are applied at both bottom wall and side-wall for fluid flow. Also, the zero flux boundary condition is set at all the walls. All of the models are developed based on the platform of the software package ANSYS-Fluent 15.0. The time step is 0.0001 seconds, and the convergence criteria for all of the residuals are set to 10^{-3}.

Results and Discussions

Figure 3 shows the general recirculation flow patterns in a gas-stirred ladle at different time. The argon gas is injected into liquid iron through two nozzles located at the tip of the lance, then goes upward along the lance and expands as it rises. A part of the argon can escape from the slag layer, which may cause fluctuation of slag layer, the rest goes downward close to the side walls. Thus, two major large circulation loops can be observed at both sides of the lance. Moreover, since the lance is not in the middle of the ladle, the sizes of those two circulation loops are different from each other. The one that circulates in a much larger space corresponds to a larger

circulation loop than that the other one. The flow patterns simulated using three models a slightly difference from each other, all of them can predict the flow field inside the ladle.

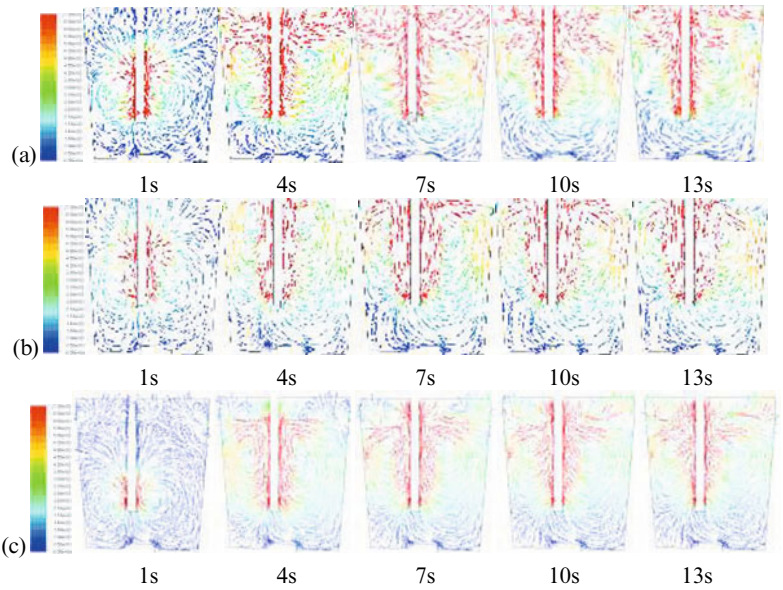

Figure 3. Velocity vectors distribution at different time. (a) VOF; (b) Eulerian-Eulerian; (c) Eulerian-Lagrangian.

Figure 4 indicates volume fraction of liquid iron. It can be seen that the fluid flow along the lance can generate more intensive turbulence due to higher velocity, the strong upward flow will break and push away the slag layer at the top of ladle consequently shown in Figure 4(a) and (c), and such open area at the slag layer is known as slag eye [8]. Furthermore, comparing Figure 4(a) with (b), the results are similar, but not identical. This is mainly because the domain applied in Eulerian-Eulerian method is not the same one used in VOF method. As a result, the different outlet conditions impact simulation to a certain extent.

Figure 5 shows the top view of slag eye at the quasi-steady state when the volume fraction of slag is lower than 0.01 [4]. According to Valentin et al. [9], as soon as a slag eye comes into existence, the inclusion length would be higher compared to those heats produced under a closed top slag. The size of slag eye affects the efficiency of desulphurization. The detailed slag eye sizes are tabulated in Table 1.

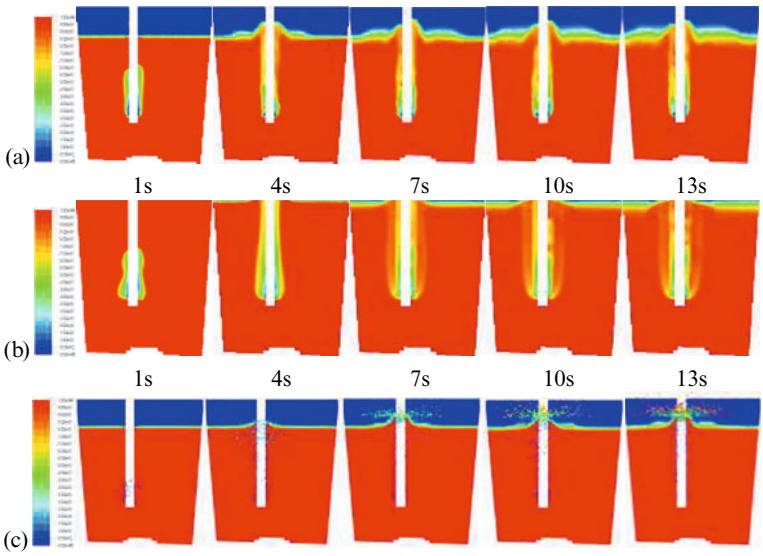

Figure 4. Volume fraction of liquid iron at different time. (a) VOF; (b) Eulerian-Eulerian; (c) Eulerian-Lagrangian.

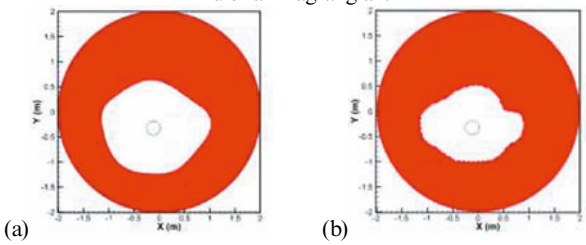

Figure 5. Top view of slag eye with 0.01 volume fraction of slag. (a) VOF; (b) Eulerian-Lagrangian.

Table 1. Detailed slag eye sizes in two methods

Parameter	VOF	Eulerian-Lagrangian
Length (X-direction) /m	2.17	2.05
Length (Y-direction) /m	1.87	1.54
Open ratio (Aslag/Aladle) /%	29	17

Table 1 shows that the slag eyes in two different methods are similar in general, although the one obtained from VOF method is much wider than that from Eulerian-Lagrangian method. Such phenomenon is corresponding to Figure 4(a) and (b), due to the assumption of bubble diameter in Eulerian-Lagrangian method. Therefore, it is critical to apply a proper diameter distribution

model for discrete phase in the Eulerian-Lagrangian approach to obtain a more reliable result which is in agreement with the reality.

Generally, the mixing time represents the mixing efficiency of a gas-stirred ladle. After the gas-stirring operation is accomplished, a certain amount of tracer will be injected into the ladle from a certain position. As the concentrations of the tracer in different locations have reached the equilibrium tracer concentration within 5%, the time from the beginning to then is defined as the mixing time [10]. Evidently, the shorter the mixing time, the better the mixing operation. A reasonable estimate of transient flow period can be deduced from the measured mixing times. Too short of a transient flow period may not at all show the kind of differential mixing times [11].

In order to simulate the mixing process, a quasi-steady state flow field is required. A comparison between Figure 3 and Figure 4 revels that it takes nearly 7 seconds for the ladle to be fully stirred by argon gas. To quantify the stir and mixing operation, three horizontal planes at different heights are chosen, as shown in Fig 6, and the area-weighted average velocity of each monitor plane at different time is calculated and shows in Fig 7.

Figure 6. Scheme diagram of three horizontal planes at different heights.

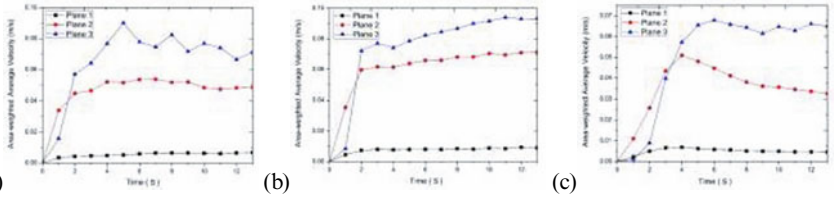

Figure 7. Area-weighted average velocity at different monitor planes. (a) VOF; (b) Eulerian-Eulerian; (c) Eulerian-Lagrangian.

Figure 7 demonstrates the typical stir behavior at different heights in a gas-stirred ladle. Within the first 2 seconds, the area-weighted average velocity of plane 2 is higher than the others. Because plane 2 is near the nozzles and argon gas injected with high flow rate has an intensive bubble plume, which introduces a high velocity in plane 2. As soon as argon gas reaches the slag layer, a strong interfacial behavior between liquid iron and slag will generate an open area at the slag layer, such interface impinges lead to more turbulent flow around plane 3. Thus, the area-weighted average velocity of plane 3 will exceed that of plane 2 after 3 seconds, while the bottom portion of the ladle remains inactive due to the less turbulence. Finally, when the two major circulation loops take place, the ladle has been fully stirred by argon gas, and the velocity of each plane changes a little. Therefore, the flow field of the gas-stirred ladle can be considered

steady after 10 seconds corresponding to Figure 7. In this study, the numerical simulations of mixing are based on the flow field at 13 seconds. The locations of two sample points are shown in Figure 8.

The results in Figure 9 show the quantification of mixing behavior when the mixing reaches 95% homogenization in the ladle. Figure 9 illustrates different peak positions of the two samples, likely caused by the significant turbulent fluctuations in the ladle. In addition, the concentration of sample 1 exceeds 100% in all of the three models, this phenomenon indicates that this region is full of solute-rich fluid before mixing is complete.

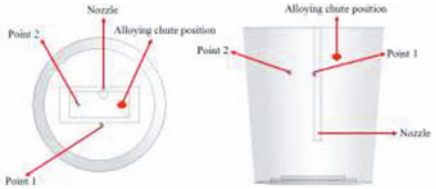

Figure 8. Monitoring sample points inside the ladle.

The concentration measured in sample 1 position returns to 100% around 2 minutes in both VOF method and Eulerian-Eulerian method, whereas the value measured in Eulerian-Lagrangian method will decrease to 100% after 4 minutes. This delay in mixing time may be caused by the inappropriate assumption of bubble size. Moreover, the peak value of sample 1 measured in the VOF method is higher than that of the Eulerian-Eulerian method, which may contribute to the formation and fluctuation of slag eye, since the slag layer was not taken into consideration in the Eulerian-Eulerian method.

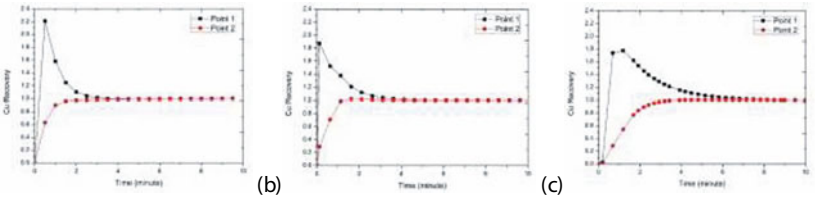

Figure 9. The 95% mixing time curve. (a) VOF; (b) Eulerian-Eulerian; (c) Eulerian-Lagrangian.

Conclusions

In this study, three different methods were utilized to simulate the transient multiphase flow field and interfacial behavior in a working gas-stirred ladle at a steel plant. The characteristics of the flow field and stirring process obtained were in reasonable agreement with experimental observations conducted in the steelmaking plant and other literature results.

The VOF method is recommended to simulate the motion of bubbles in a liquid and the tracking of any interface, but the small time step size must be adopted in order to obtain convergent solutions. The Eulerian-Eulerian method shows a lot of similarities comparing to the VOF method in terms of flow field and mixing behavior. However, the conservation equations in the

Eulerian-Eulerian method are independent and should be solved by each single phase, this treatment limits the number of secondary phases and convergence behavior, which significantly causes computing time and memories. Finally, the Eulerian-Lagrangian method is made considerably simpler when interactions between dispersed phases can be neglected, as presented in this study. Meanwhile, a few limitations should be taken into account. For instance, the bubble must be present at a fairly low volume fractions, usually less than 10–12%, and the bubble size distribution should be measured before modeling. And the most important, the simulation results depend heavily on the appropriate assumptions of force balance, breakup and coalescence mechanism of bubbles.

Acknowledgement

The authors would like to thank ArcelorMittal USA for offering this research opportunity, providing funding, and for conceptual guidance during the course of this work. The authors would also like to thank the Center of Innovation through Visualization and Simulation (CIVS) at Purdue University Calumet for providing all the resources required for this work.

References

1. M.V.S. Annaland, N.G. Deen, J.A.M. Kuipers, "Numerical simulation of gas bubbles behaviour using a three-dimensional volume of fluid method," *Chemical Engineering Science*, 11 (2005), 2999-3011.

2. S.S. Rabha, V.V. Buwa, "Volume-of-fluid (VOF) simulations of rise of single/multiple bubbles in sheared liquids," *Chemical Engineering Science*, 1 (2010), 527-537.

3. J.F. Domgin, P. Gardin, M. Brunet, "Experimental and numerical investigation of gas stirred ladles," (Paper presented at the 2nd International Conference on CFD in the Minerals and Process Industries, Melbourne, Australia, 1999).

4. H. Liu, Z. Qi, M. Xu, "Numerical Simulation of Fluid Flow and Interfacial Behavior in Three-phase Argon-Stirred Ladles with One Plug and Dual Plugs," *Steel Research International*, 4 (2011), 440-458.

5. D. Mazumdar, R.I.L. Guthrie, "An assessment of a two phase calculation procedure for hydrodynamic modelling of submerged gas injection in ladles," *ISIJ International*, 5 (1994), 384-392.

6. J. Aoki, B.G. Thomas, "Experimental and theoretical investigation of mixing in a bottom gas-stirred ladle," *AIST* 51 (2004), 61801.

7. A. Haider, O. Levenspiel, "Drag coefficient and terminal velocity of spherical and nonspherical particles," *Powder Technology*, 1 (1989), 63-70.

8. M. Peranandhanthan, D. Mazumdar, "Modeling of slag eye area in argon stirred ladles," *ISIJ International*, 11 (2010), 1622-1631.

9. P. Valentin, C. Bruch, Y. Kyrylenko, H. Köchner, C. Dannert, “Influence of the Stirring Gas in a 170‐t Ladle on Mixing Phenomena–Formation and On‐line Control of Open‐Eye at an Industrial LD Steel Plant,” *Steel Research International*, 8 (2009), 552-558.

10. S.M. Pan, Y.H. Ho, W.S. Hwang, “Three-dimensional fluid flow model for gas-stirred ladles,” *Journal of Materials Engineering and Performance*, 3 (1997), 311-318.

11. D. Mazumdar, R. Yadav, B.B. Mahato, “Transient flow and mixing in steelmaking ladles during the initial period of gas stirring,” *ISIJ International*, 1 (2002), 106-108.

CFD Modeling and Simulation in Materials Processing 2016
Edited by: Laurentiu Nastac, Lifeng Zhang, Brian G. Thomas, Miaoyong Zhu, Andreas Ludwig, Adrian S. Sabau, Koulis Pericleous, and Hervé Combeau
TMS (The Minerals, Metals & Materials Society), 2016

NUMERICAL SIMULATION ON MULTIPHASE FLOW IN THE TWO SIDE-BLOWN OXYGEN-ENRICHED COPPER SMELTING FURNACE

Liu Guanting, Liu Yan, Li Xiaolong, Zhang Ting-an
School of Materials and Metallurgy of Northeastern University, Key Laboratory of Ecological Untilization of Multi-metal Intergrown Ores of Education Ministry, Shenyang, 110819

Keywords: copper smelting, two side-blown, numerical simulation, multiphase flow

Abstract

In order to understand flow regularity and select oxygen lancer operating parameters of the two side-blown oxygen-enriched copper smelting process, commercial software Ansys/Fluent13.0 was used to simulate the flow characteristics of multiphase flow in the bath under different nozzle arrangement. The results showed that when the nozzle arrangement was compact, the stirring effect of gas was enhanced and the local velocity and turbulent kinetic energy of the fluid increased while the fluctuation of copper matte layer was intensified. Meanwhile, local gas holdup also increased, which caused uneven distribution of gas near the oxygen lacer. However, when the nozzle arrangement was sparse, the stirring strength decreased in the smelting zone. The flow fields obtained by PIV technology agreed well with the CFD results, which indicated that the numerical simulation results were reliable. The results above provided theoretical foundation for the further study on the two side-blown copper smelting process.

Introduction

Two side-blown copper smelting process is an efficient, energy-saving and environment-friendly copper smelting technology[1-3]. The melt in the bath is stirred by the oxygen-enriched air blown from the tuyeres on the two sides of the furnace, which causes the turbulent motion in the local area and then promotes the homogeneous dispersion of the material in the melt. Because the oxygen-enriched air is used to stir the slag layer, the mass and heat transfer between the melt and the material is strengthened, the dissolution of the matte in the slag is reduced and dynamics of the reaction in the melt is improved.

Recently, there are few basic studies of this technology and the flow state of the melt in the industrial bath is unclear, which leads to the great variation in the operating parameters of the oxygen lancers. Furthermore, the oxygen-enriched air is not fully used, which prolongs the smelting period, increases the energy consumption and restricts the optimization of this technology.

In the past few years，with the fast development of numerical simulation, CFD(Computational Fluid Dynamics) has become an effective method to reveal the flow properties of fluid[4-6] and the applications in the metallurgy industry have increased gradually[7-9]. In this paper, by means of numerical simulation, the

commercial software Ansys/Fluent13.0 was used to simulate the multiphase flow in the bath. The flowing law was revealed and the proper operation conditions of oxygen lancers were obtained, which provided theoretical foundation for the further optimization of the flow field and the mass, heat transfer in two side-blown copper smelting furnace.

Model establishment

Geometric model

Based on the geometry of an industrial copper smelting furnace, an 1:8 geometric model was established by using Gambit 2.4.6. The length of the model is 887mm, the height is 450mm and the maximum width is 324mm. The upper furnace body is ignored and there are 5 air inlet ports on each side of the furnace. The grids near the air inlets are refined and the number of the grids is 300 thousand. The generated mesh and geometry is shown in Figure 1.

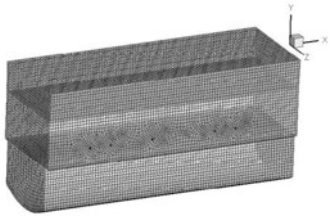

Fig.1 Mesh generated

Mathematical model

In this paper, the interaction between gas and liquid was simulated by using Euler model. Only fluid flow in the reactor was considered and energy transmission was ignored. Mathematical equations are as follows.

Continuity equation:

$$\frac{\partial}{\partial t}(\alpha_q \rho_q) + \nabla \cdot (\alpha_q \rho_q \vec{v}_q) = 0 \tag{1}$$

q=g, l, Where $\vec{v}_q$ is the velocity of q phase.

Momentum equation of gas phase and liquid phase:

$$\frac{\partial}{\partial t}(\alpha_g \rho_g \vec{v}_g) + \nabla \cdot (\alpha_g \rho_g \vec{v}_g \vec{v}_g) = -\alpha_g \nabla p + \nabla \cdot \bar{\bar{\tau}}_g + \alpha_g \rho_g \vec{g} + \sum \vec{F}_g \tag{2}$$

$$\frac{\partial}{\partial t}(\alpha_l \rho_l \vec{v}_l) + \nabla \cdot (\alpha_l \rho_l \vec{v}_l \vec{v}_l) = -\alpha_l \nabla p + \nabla \cdot \bar{\bar{\tau}}_l + \alpha_l \rho_l \vec{g} + \sum \vec{F}_l \tag{3}$$

$$\bar{\bar{\tau}}_q = \alpha_q \mu_q (\nabla \vec{v}_q + \nabla \vec{v}_q^T) + \alpha_q (\lambda_q - \frac{2}{3}\mu_q) \nabla \vec{v}_q \bar{\bar{I}} \tag{4}$$

Where $\bar{\bar{\tau}}_q$ is the stress tensor of q phase.

Standard k-ε Turbulence Model was chosen for simulating the turbulent flow.

Physical parameters and boundary condition

In this paper, the fluid was regarded as incompressible fluid and energy equation was

ignored, i.e. heat transfer was not considered. Wall condition was no-slip and heat insulating. Ambient atmospheric pressure was 101325Pa and gravity acceleration was 9.81m/s^2. Other physical conditions are shown in Table 1.

Table.1 Related parameters of the component

material	density kg/m^3	viscosity Pas
air	1.225	1.7894×10-5
water	1000	1.003×10-3

Velocity-inlet boundary condition was used for gas inlet and the velocity of gas was determined according to similarity principle[10-11]. Pressure outlet boundary condition was used for fluid outlet.

Model verification

Experimental conditions are as follows: in the air-water simulated system, nozzle angle is 7°, nozzle diameter is 3.7mm, nozzle arrangement is 1# which is shown in Figure 2 and gas flow rates are 17m^3/h, 20m^3/h, 23m^3/h and25m^3/h. The flow fields of section z=0m, which is shown in Figure 3, obtained by using PIV[12-13] in the water model experiment and commercial software Ansys/Fluent13.0 are shown in Figure 4.

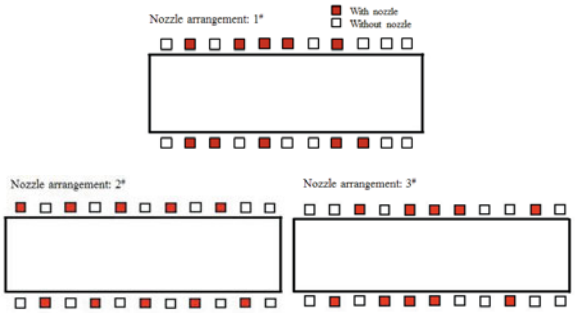

Fig. 2 Nozzle arrangement

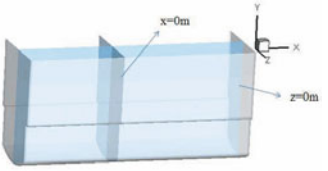

Fig. 3 The drawing show of each section

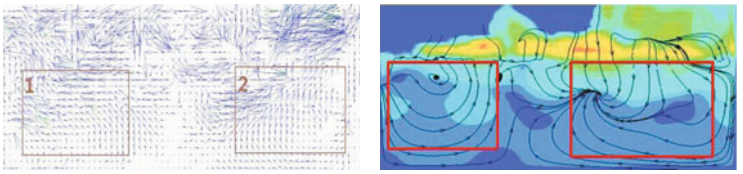

(a) Gas flow rate17m^3/h

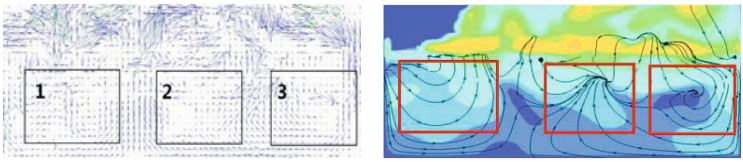

(b) Gas flow rate 20m^3/h

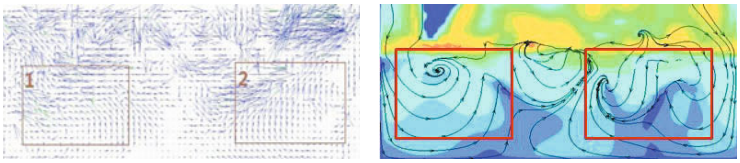

(c) Gas flow rate 23m^3/h

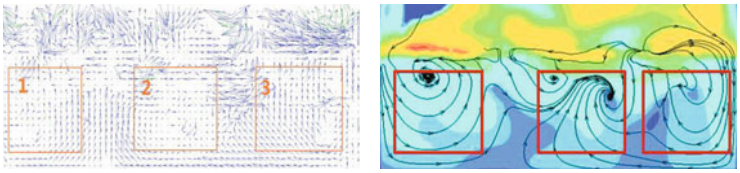

(d) Gas flow rate 25m^3/h

Fig. 4 The comparison of PIV flow fields and numerical simulation fields at the section z=0m under different gas flow rate

The flow fields on the left side are measured by PIV and the simulation results are shown on the right side. It can be concluded from the figure that the number and the location of swirls of the experiment results and simulated results is the same. The swirls are at the upper part of the furnace. The fluid in the lower part flows from two sides to the center and then flows upward. By comparing the pictures above, it can be concluded that the simulated results showed the accurate flow field and it is feasible to use this model to simulate the fluid flow in the two side-blown copper smelting reactor.

Results and discussion

Influence of nozzle arrangement on the flow field

Experimental conditions are as follows: the gas flow rate is 20m^3/h, nozzle diameter is 3.7mm, nozzle angle is 7° and nozzle arrangement is 1$^{\#}$, 2$^{\#}$ and 3$^{\#}$.

It can be seen from Figure 5 that with the 1$^{\#}$ nozzle arrangement, there are 3 swirls in the upper part of the bath and the flow velocity of the fluid is fast while the fluid in the lower part flows from two sides to the center steadily and the flow velocity is slow. The flow field and the velocity distribution are conductive to improve the stirring intensity of the smelting zone in the upper part and keep the copper matte layer in the lower part stable. When the nozzle arrangement is 2$^{\#}$, the fluid flows from the top to the bottom regularly and there exists no swirl, which makes the turbulent intensity weakened. With the 3$^{\#}$ nozzle arrangement, there also exist 3 swirls, but compared with the 1# nozzle arrangement, swirls are closer to the lower part of the bath, which

causes the fluctuation of the copper matte layer and decreases the grade of the copper matte.

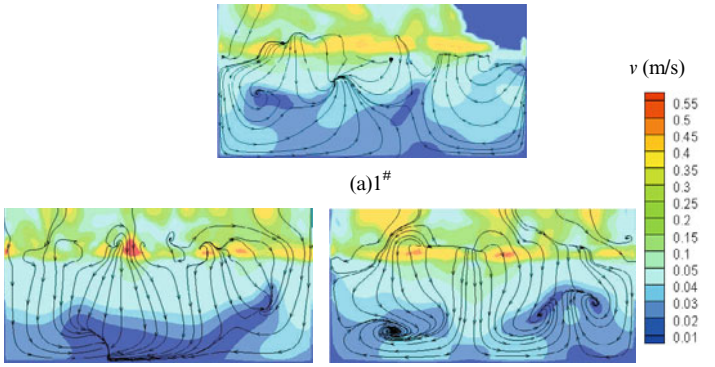

Fig. 5 The flow fields at the section z=0m under different nozzle arrangement

In addition, the flow field of the section x=0m was investigated. It can be inferred from the Figure 6 that with the 1# nozzle arrangement, there is a swirl in the central part, which strengthens the stirring effect in the smelting zone. Besides, a small swirl appears above the nozzle, which promotes entrainment and the uniform distribution of the material. With the 2# nozzle arrangement, the flow state causes the impact on the copper matte layer. With the 3# nozzle arrangement, the two closer swirls enhance the stirring intensity in the smelting zone, which is because the penetrating ability of the gas is improved when the nozzle arrangement is more compact.

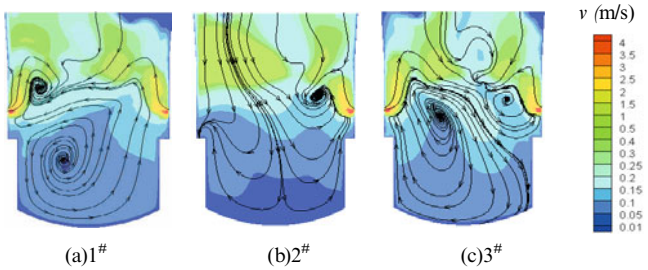

Fig. 6 The flow fields at the section x=-0m under different nozzle arrangement

By analyzing different nozzle arrangements, it can be concluded that when the nozzle arrangement is sparse, such as the 2# nozzle arrangement, there is no swirl and the flow velocity of the fluid is slow. In this case, the turbulent intensity of the fluid is weak, which goes against the mass and heat transfer in the smelting process. However, when the nozzle arrangement is too compact, the local flow velocity of the fluid is too fast, the area of dead zone becomes larger and the fluctuation of the copper matte layer is more violent, which indicates that the turbulent kinetic energy of gas increases and its ability of overcoming the liquid friction is stronger. Therefore, in order to keep the copper matte layer stable and the smelting intensity relatively strong, the better

nozzle arrangement is local compactness and global sparse, namely 1# nozzle arrangement.

Influence of nozzle arrangement on gas holdup

Figure 7 shows the distribution of gas holdup at the different sections of x axis direction. With the 1# nozzle arrangement, 3 peak values of gas holdup distribute in the furnace uniformly, with the 2# nozzle arrangement, the gas holdup decreases gradually from the left to the right and with the 3# nozzle arrangement, the gas holdup in the central part is higher than that of the two ends.

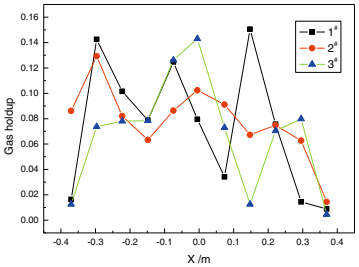

Fig.7 The gas holdup distribution of smelting zone under different nozzle arrangement

Based on the comparative analysis of the results, it can be concluded that the peak values appear at the sections near the compact nozzles because of the superposition effect of the adjacent gas column. Besides, the stirring effect of gas is improved when the nozzle arrangement is compact, which causes the appearance of the swirls. This is also the reason why there are 3 swirls with the 1# nozzle arrangement. When the nozzle is single arrangement, namely the 2# nozzle arrangement, the distribution of gas holdup is more uniform, but the stirring effect of gas is worse. With the 3# nozzle arrangement, because the nozzle arrangement is the most compact, there is massive gas in the center, which causes the peroxidation.

Furthermore, the gas holdup of the whole bath is investigated and the results are shown in the Figure 8. It can be inferred from the figure that with the 2# nozzle arrangement, the gas holdup is the highest, which indicates that the gas distribution is more uniform when the nozzle arrangement is sparse. In contrast, the gas holdup is the lowest with the 3# nozzle arrangement. This is because the two gas columns are closer, the friction between gas and liquid decreases and gas residence time decreases.

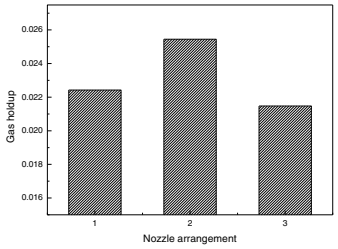

Fig. 8 The gas holdup of smelting zone under different nozzle arrangement

Influence of nozzle arrangement on wall sheer stress

The wall sheer stress on the wall of the bath reflects the scour effect of the melt on the furnace lining and the destruction of furnace lining caused by the recoil force of gas. Thus, the study of the wall sheer stress with different the nozzle arrangement is helpful to optimize the nozzle arrangement and prolong the life of furnace lining and oxygen lance. The simulated results are shown in the Figure 9.

It can be inferred from the figure that the wall sheer stress near the nozzles is higher and decreases gradually from the center to the periphery. This is because when the gas is blown into the melt, the resistance of liquid phase leads to sudden decrease of gas velocity and at the same time, the recoil force is produced at the opposite direction of the gas blowing, namely at the oxygen lance and the furnace lining around it, which causes the increase of the erosion of furnace lining. Moreover, the turbulent kinetic energy of melt around the nozzles increases and this also causes the increase of the wall sheer stress. In addition, when the nozzle arrangement is sparse, such as 2# nozzle arrangement, the area of high wall sheer stress is larger, so the compact nozzle arrangement is helpful to protect the furnace lining from eroding.

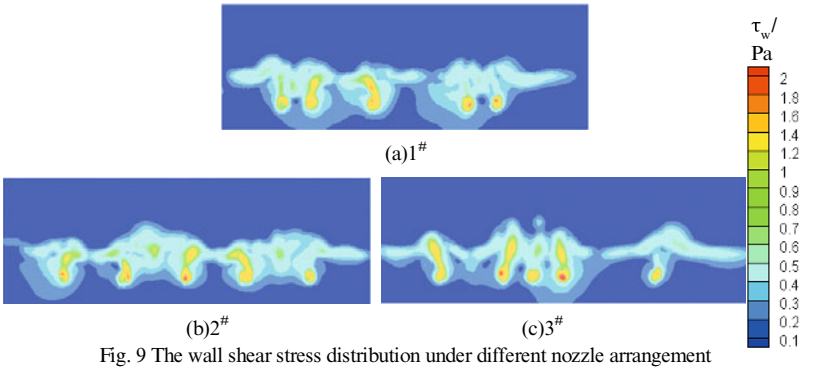

Fig. 9 The wall shear stress distribution under different nozzle arrangement

Conclusion

(1) The mathematical model of the multiphase flow in the two side-blown copper smelting bath was developed, where Eulerian model was used to simulate the flow process and standard k-ε model was used to simulate the turbulence. The accuracy of the model is verified by comparing the flow fields obtained by PIV technology and numerical simulation. Due the good arrangement between the PIV experimental date and numerical simulation results, it is feasible to use this model to simulate the multiphase flow in the bath.

(2) Adjacent nozzle arrangement enhanced the stirring effect of gas, which increased the velocity and turbulent kinetic energy, but the fluctuation of copper matte layer was also intensified and the increase of local gas holdup caused the uneven distribution of gas. Hence a too compact nozzle arrangement was inappropriate. However, if the nozzle arrangement was too sparse, the stirring strength would decrease and the erosion of the furnace lining around the oxygen lacer was more serious. Thus the optimal nozzle arrangement was local compactness and global sparse, namely 1#

nozzle arrangement.

The results provided theoretical foundation for the further optimization of the flow field and the mass, heat transfer in the two side-blown copper smelting furnace.

Acknowledgements

This research was supported by the National Natural Science Foundation of China (Nos.50974035, 51074047) and the NSFC (U1402271).

References

1. Ge XiaoMing, Wang Liangjv, "Plant practice of copper oxygen enrichment side-blowing bath smelting process," *Nonferrous Metals(Extractive Metallurgy),* 8 (2011): 13-16.

2. Huang Xiansheng, Wang guojun, "Practice of Jinfeng copper Co.Ltd. two side-blown bath smelting production," *China Nonferrous Metallurgy,* 6 (2008): 31-33.

3. Luo Yinhua, Wang Zhichao. "Plant Practice of Fubang oxygen—Enriched Side—Blown Bath Smelting Copper Furnace," *Nonferrous Metals(Extractive Metallurgy),* 7 (2013): 19-22.

4. Sokoliehin A. , Eigenberger G Lapin A. "Dynamical numerical simulation of gas-liquid two-phase flows," *Chemical Engineering Science,* 52(9)(1997): 611-626.

5. Torvikr, Svendsen H. F. "Modeling of slurry reactors．A fundamental approach," *Chemical Engineering Science,* 45(6)(1990): 2325-2336.

6. Jakobsen H.A., Svendsen H.E, Hiarbo K.W.. " On the prediction of local flow structures in internal loop and bubble column reactors using a two fluid model," *Chemical Engineering Science,* 17(5)(1993): 531—536.

7. Wilhelmi H. , Steiumetz. E. , Schlosscr G, Renz U, Hillemaeher. B. , Lange F. . " Flow simulation in bottom—blown metallurgical ladles(Flow simulation in bottom-blown metallurgical ladles)，" *Steel Research,* 62(11)(1991): 492-495.

8. ZHAN Shu-hua, LAI Chao-bin, HSIAO Tse-qiang. " CFD analysis of gas stirring behavior in side-blown metallic bath ，" *Journal of Central South University (Medical Sciences),* 34(2)(2003): 148-151.

9. LI Bao-kuan，HE Ji-cheng．" Numerical simulation on flow and mixing processes in bottom blown ladle ，" *Process Metallurgy&Miscellaneous,* 6(5)(1993): 359-363.

10. Xiao Xingguo, Xie Yunguo，*Foundation of metallurgical reaction engineering,* (Beijing, Metallurgical industry press, 1997), 5.

11. Zhu Miaoyong, HSIAO Tse-qiang. *Mathematical and physical simulation in refining process of steel,* (Beijing, Metallurgical industry press, 1998), 123.

12. Huchet F, Line A, Morchain, J. "Evaluation of local kinetic energy dissipation rate in the impeller stream of a Rushton turbine by time-resolved PIV," *Chemical Engineering Research and Design,* 87(4)(2009): 369-376.

13. Guida A, Nienow A W, Barigou M. "The effects of the azimuthal position of the measurement plane on the flow parameters determined by PIV within a stirred vessel," *Chemical Engineering Science,* 65(8)(2010): 2454-2463.

CFD Modeling and Simulation in Materials Processing 2016
Edited by: Laurentiu Nastac, Lifeng Zhang, Brian G. Thomas, Miaoyong Zhu, Andreas Ludwig, Adrian S. Sabau, Koulis Pericleous, and Hervé Combeau
TMS (The Minerals, Metals & Materials Society), 2016

3D CFD MODELING OF THE LMF SYSTEM

Laurentiu Nastac[1], Daojie Zhang[1], Qing Cao[1], April Pitts[1, 2], and Robert Williams[2]

[1]The University of Alabama, Department of Metallurgical and Materials Engineering,

Box 870202, Tuscaloosa, AL, 35487, USA, email: lnastac@eng.ua.edu

[2]Nucor Tuscaloosa, Tuscaloosa, AL, 35401, USA

Keywords: 3D CFD Modeling; Ladle Metallurgical Furnace; Molten Steel Processing; Fluid Flow Characteristics.

Abstract

A fully transient 3D CFD modeling approach capable of predicting the three phase (gas, slag, and steel) flows and behavior of the slag/steel interface in the argon gas bottom stirred ladle with two off-centered porous plugs (Ladle Metallurgical Furnace or LMF) was developed. The modeling approach consists of using a multiphase VOF-Level Set explicit model in conjunction with energy, momentum, and species transfer models as well as the k-epsilon realizable turbulence model with standard wall functions, and species transfer models available in ANSYS Fluent software. The CFD model can predict the evolution of Ar, steel and slag phases as well as the fluid flow characteristics during both the high-stirring and low-stirring conditions in the LMF system. The model predicted accurately the observed size of the slag eyes for both stirring conditions. The model was then applied to study the effects of key processing parameters including Ar flow rate, processing time, and depth of slag on the three phase flows and behavior of the slag/steel interface. The desulfurization process is also studied.

Introduction

The LMF is of enormous importance in steelmaking process, responsible for the homogenization of alloy elements and temperature, desulphurization, deoxidation, and inclusion removal. Inert gas is often injected into molten steel through the ladle bottom to produce bubbly plume flow, which is used to promote steel/slag interaction and chemical reactions, homogenize the composition of the melt. Because of the strongest heat/mass transfers in the bubbly plume region, it is significant to gain in-depth knowledge of the gas bubble flow in the gas-stirred system.

Currently, numerous studies on qualitative CFD simulations were developed to enhance ladle treatment operations before carrying out the expensive industrial trials. Many models of gas stirring in ladle metallurgy have been published in the past [1-4]. Ilegbusi *et al*. [5] presented a simple mathematical model the turbulent recirculating two-phase flow in gas-stirred systems for both air in water and nitrogen in steel. The air-water results compared well with established measurements of gas fraction and liquid velocities. Lou *et al*. [6] established a gas and liquid two-

phase flow model based on the Euler-Euler approach and investigated the influences of the interphase force including turbulent dispersion force, drag force, and lift force.

The interaction behavior between steel and slag is most important to control the ladle treatment and the properties of the final steel product. With incorporating the slag phase, the model of the gas-stirred ladle was improved to take three phases into account. Jonsson [7] used a two-dimensional three-phase model accounting for steel, argon and top slag to investigate the effect of viscosity on ladle-refining. It was concluded that a small change in slag composition can result in a large change in viscosity, leading to altered slag/steel mixing conditions. Lage JONSSN *et al.* [8] developed a three-phase model of a gas-stirred ladle and compared the calculated surface velocities for steel with the experimentally measured data. The three-phase model agrees significantly better with experimental data than the two-phase model that excluded the effect of the slag phase. It could also predict the amount of slag dispersed into the steel. Later, Li *et al.* [9] used the multiphase volume of fluid (VOF) method to simulate the transient three-phase flow in LMF and the effects of gas injection on the behaviors of slag layer. Even though many models have been developed to study the behavior of slag-steel interface, it is still not clear which model is the most appropriate. The effect of gas stirring and other operating parameters on the three phase flows is not yet clarified.

The objective of the present work is to develop a fully transient 3D CFD modeling approach in the argon gas bottom stirred ladle with two off-centered porous plugs. This model can predict the three phase (gas, slag, and steel) flows and behavior of the slag/steel interface. The model described reasonably well the observed size of the slag eyes for both the high-stirring and low-stirring conditions. The effects of key processing parameters including Ar flow rate, processing time, and depth of slag on the three phase flows and behavior of the slag/steel interface were also studied.

Model Description

The geometry of the LMF is shown in Figure 1. It has two off-centered plugs (diameter 92 mm). The initial thickness of the slag layer is 150 mm, and depth of the steel is 3.35 m. Two argon flow rates were used: 0.0281 m^3/s and 0.11238 m^3/s. The thermo-physical properties of the steel, slag and argon at 1800K are presented in Table I.

Table I. Thermo-physical properties of materials at 1800K

Steel		Slag		Argon	
Density, kg/m^3	Viscosity, kg/(m s)	Density, kg/m^3	Viscosity, kg/(m s)	Density, kg/m^3	Viscosity, kg/(m s)
7020	0.006	3500	0.03	0.568	2.125×10^{-5}

Governing Equations

The CFD model consists of using a multiphase VOF-Level Set explicit model in conjunction with energy, momentum, and species transfer models as well as the k-epsilon realizable turbulence model with standard wall functions, and species transfer models available in ANSYS Fluent [10].

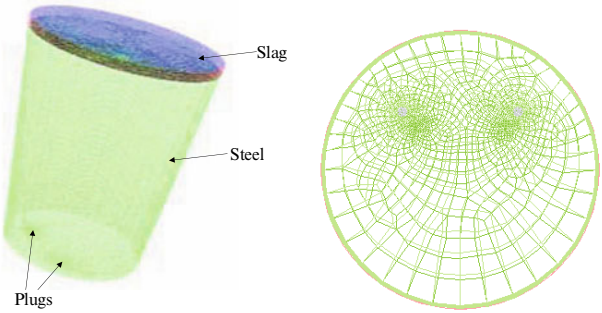

Figure 1. Meshed geometry of the LMF system.

The level-set function φ is defined as a signed distance to the interface. Accordingly, the interface is the zero level-set, $\varphi(x,t)$ and can be expressed as $\Gamma = \{x | \varphi(x,t) = 0\}$ in a two-phase flow system:

$$\varphi(x,t) = \begin{cases} +|d| & \text{if x} \in \text{the primary phase} \\ 0 & \text{if x} \in \Gamma \\ -|d| & \text{if x} \in \text{the secondary phase} \end{cases}$$

where d is the distance from the interface.

The evolution of the level-set function can be given in a similar fashion as to the VOF model:

$$\frac{\partial \varphi}{\partial t} + \nabla \cdot (\vec{v}\varphi) = 0 \tag{1}$$

where $\vec{v}$ is the underlying velocity field.

And the momentum equation can be written as

$$\frac{\partial}{\partial t}(\rho \vec{v}) + \nabla \cdot (\rho \vec{v}\vec{v}) = -\nabla p + \nabla \cdot [\mu(\nabla \vec{v} + \nabla \vec{v}^T)] - \sigma\kappa\delta(\varphi)\nabla\varphi + \rho\vec{g} \tag{2}$$

where $\delta(\varphi) = \dfrac{1+\cos(\pi\varphi / a)}{2a}$ if $|\varphi| < a$ and $a = 1.5h$ (where h is the grid spacing), otherwise $\delta(\varphi) = 0$. σ is the surface tension coefficient, and κ is the curvature of the interface.

The modeled transport equations for k and ε in the relizable k-ε model are

$$\frac{\partial}{\partial t}(\rho k) + \frac{\partial}{\partial x_j}(\rho k u_j) = \frac{\partial}{\partial x_j}\left[\left(\mu + \frac{\mu_t}{\sigma_k}\right)\frac{\partial k}{\partial x_j}\right] + G_k + G_b - \rho\varepsilon \tag{3}$$

$$\frac{\partial}{\partial t}(\rho\varepsilon)+\frac{\partial}{\partial x_j}(\rho\varepsilon u_j)=\frac{\partial}{\partial x_j}\left[\left(\mu+\frac{\mu_t}{\sigma_\varepsilon}\right)\frac{\partial\varepsilon}{\partial x_j}\right]+\rho C_1 S\varepsilon-\rho C_2\frac{\varepsilon^2}{k+\sqrt{v\varepsilon}}+C_{1\varepsilon}\frac{\varepsilon}{k}C_{3\varepsilon}G_b \quad (4)$$

where $C_1=\max\left[0.43,\frac{\eta}{\eta+5}\right]$, $\eta=S\frac{k}{\varepsilon}$, $S=\sqrt{2S_{ij}S_{ij}}$, and $S_{ij}=\frac{1}{2}\left(\frac{\partial u_j}{\partial x_i}+\frac{\partial u_i}{\partial x_j}\right)$.

In these equations, G_k represents the generation of turbulence kinetic energy due to the mean velocity gradient, calculated as

$$G_k=-\rho\overline{u_i'u_j'}\frac{\partial u_j}{\partial x_i} \quad (5)$$

G_b is the generation of turbulence kinetic energy due to buoyancy, calculated as

$$G_b=\beta g_i\frac{\mu_t}{\mathrm{Pr}_t}\frac{\partial T}{\partial x_i} \quad (6)$$

where Pr_t is the turbulent Prandtl number for energy, which is 0.85 for realizable k-ε model.

The eddy viscosity μ_t is computed from

$$\mu_t=\rho C_\mu\frac{k^2}{\varepsilon} \quad (7)$$

In the realizable k-ε model, C_μ is no longer constant as that in the standard k-ε model, but instead computed from

$$C_\mu=\frac{1}{A_0+A_S\frac{kU^*}{\varepsilon}} \quad (8)$$

where $U^*\equiv\sqrt{S_{ij}S_{ij}+\tilde{\Omega}_{ij}\tilde{\Omega}_{ij}}$, and $A_0=4.04$, $A_S=\sqrt{6}\cos\phi$.

The model constants are $C_{1\varepsilon}=1.44$, $C_2=1.9$, $\sigma_k=1.0$, and $\sigma_\varepsilon=1.2$.

The solute tranport of the Ca, Al, S, and O elements in both the slag and the steel phases were modelled using the species tranport equation avaialble in CFD Fluent via 2 mixture templates (see Fluent mannual for the solute tranport equations [10]). Each mixture template will have different thermo-physical properties. For example, the mass diffusivities of the above mentioned elements will be much lower in the slag than in the steel. The following reactions were modeled: (Ca)+[S]>(CaS) (reaction #1) and [Al_2]+[O_3]>[Al_2O_3]>(Al_2O_3) (reaction #2) where [] means steel and () denotes the slag). Ca will react with S at the metal-slag interface to form CaS that will

remain in the slag. Al will react with O to alumina precipiates in steel then move into the slag. This is modelled via a mass transfer rate at the slag/metal interface. The heterogeneous reaction #1 was modelled via an user defined function (UDF), which accounts for the kinetics of the reaction at both the bath metal/slag and the droplet slag/metal interfaces. The details of the reaction kinetics of these reactions can be found in [9]. The kinetics of droplet formation are described in [11]. The droplet size can be related to the turbulent energy and surface tension. The number of droplets can be calculated based on the Kelvin-Helmholtz theory (see Eq. (21) in [12]). The second reaction is homogeneous and it is modeled by the standard reaction kinetics interface available in Fluent. The values of the reaction kinetics coefficients related to the sulfur removal will be further validated and refined via experimental measurements at Nucor.

Initial and Boundary Conditions

Initially, the slag layer rests on top of the steel bath, and no argon blows through the porous plugs. The walls in the ladle are assumed to be smooth and non-slip. All the computations were done at 1800K. The inlet velocity of argon gas is calculated from [9]:

$$V_{in} = \frac{Q_L}{A} = \left(\frac{p_S T_L}{p_L T_S} \right) \frac{Q_S}{A}$$

where subscript L means ladle operating condition, and S is standard condition. T_S and T_L are solidus and liquidus temperature, respectively. A is plug area, and Q_S is argon gas flow rate at standard condition. An allowance is made for the escape of gas bubbles at the free surface.

Numerical Method

The calculations are conducted in transient solution mode using the PISO algorithm to solve the three phase flow problem. Variable time stepping method is used with minimum time step of 1e-05s and maximum time step of 0.01s.

Results and Discussion

Figure 2 shows the velocity vectors and the turbulent intensity profile of the mixture (slag, steel and argon) for a flow rate of 0.0281 m^3/s, which is the low flow rate case. Figure 3 shows the volume fraction profile for the Ar the middle cross section and for the slag (free surface). As it can be seen from these figures, the mixing is very strong (V>0.5 m/s) along the Ar path and become weaker (V~0.1 m/s) further from it. Figure 4 shows the velocity vectors and the turbulent intensity profile of the mixture (slag, steel and argon) for a flow rate of 0.11238 m^3/s, which is the high flow rate case. Figure 5 shows the volume fraction profile for the Ar the middle cross section and for the slag (free surface). As it can be seen from these two figures, the mixing is significantly stronger when compared with the low flow rate case (Figs. 2 and 3) (*i.e.*, V>1 m/s along the Ar path and V~0.5 m/s) further from it). Also, Figs 3b and 5b show the size of the open slag eye for the low and high flow rates, respectively. Their size are in reasonable agreement with the experimental

observations (See Fig. 6a). Figure 6b shows the S mass fraction profile in the steel phase at 100s for the high flow rate case. As it can be seen, the S removal is progressing well. The O was removed completely at this stage. The Al remnant in the steel melt was almost uniform and its value was about 0.003%.

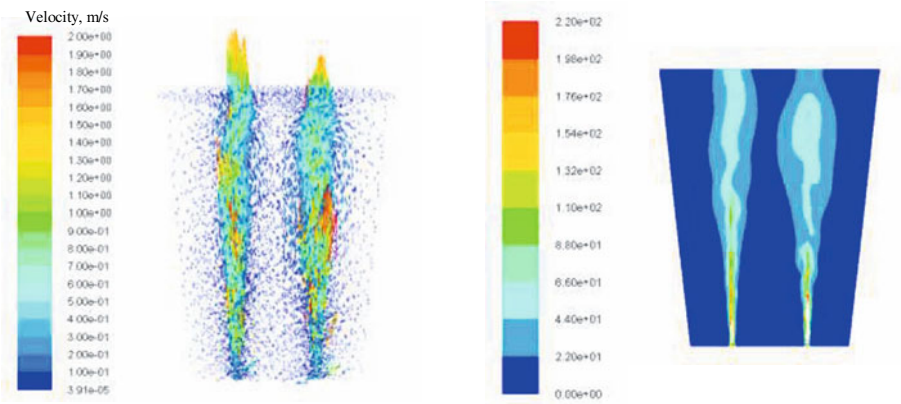

(a) (b)

Figure 2. Velocity vectors (a) and turbulent intensity profile (%) (b) after 448s for the low flow rate case.

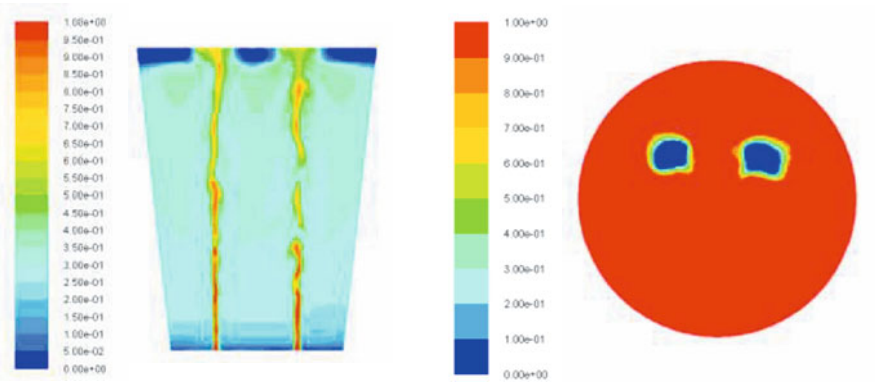

(a) (b)

Figure 3. Volume fraction profile for the Ar phase (a) and for the slag phase (b) after 448s for the low flow rate case.

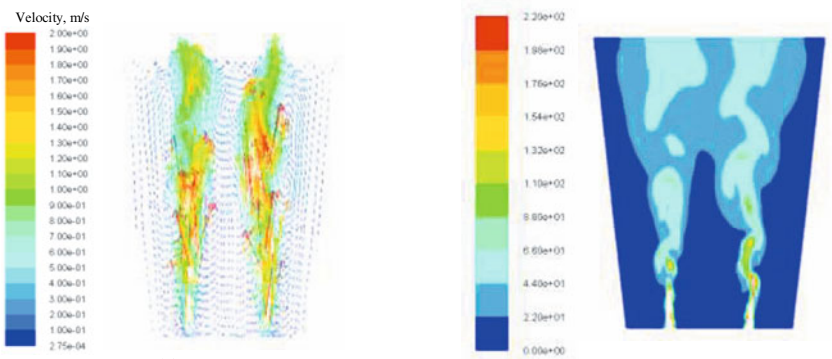

Figure 4. Velocity vectors (a) and turbulent intensity profile (%) (b) after 97s for the high flow rate case.

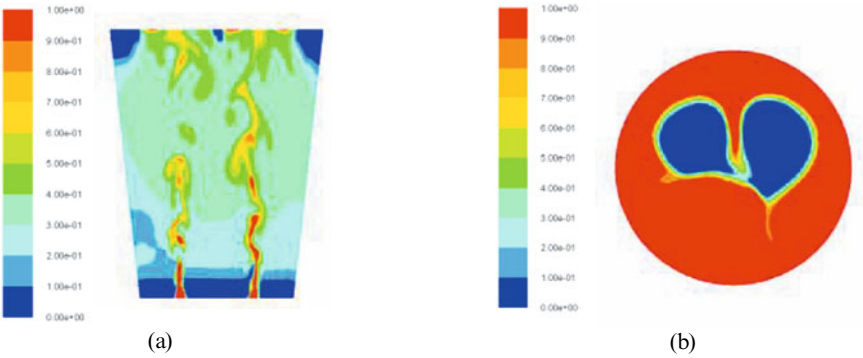

Figure 5. Volume fraction profile for the Ar phase (a) and for the slag phase (b) after 97s for the high flow rate case.

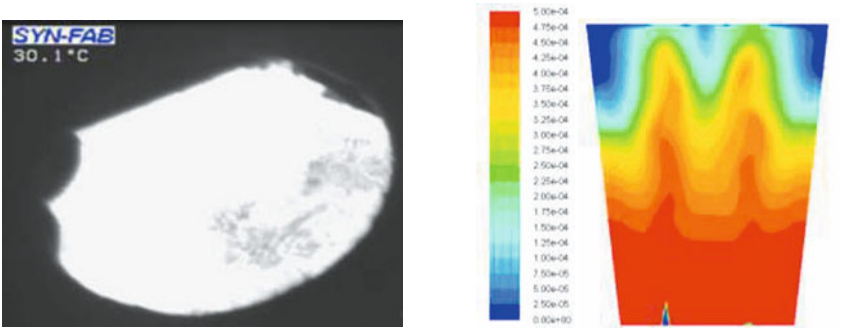

Figure 6. (a) Open slag eye observation during high flow rate case and (b) Mass fraction profile of sulfur in the steel phase after 100s for the high flow rate case.

Conclusions and Future Work

A fully transient 3D CFD modeling approach capable of predicting the fluid flow, solute transport and reaction kinetics in the LMF was developed in this study. The model can be used to predict the behavior of the metal/slag interface as well as the sulfur removal and deoxidation processing step during the high Ar stirring process. The reaction kinetics model for sulfur removal will be further validated and refined via experimental measurements at Nucor.

References

[1] D. Guo and G.A. Irons, "Modeling of Gas-Liquid Reactions in Ladle Metallurgy: Part II. Numerical Simulation," *Metallur. and Mater. Trans. B*, 31B (12) (2000), 1458-1464.

[2] P. Sulasalmi, A. Kärnä, T. Fabritius, and J. Savolainen,"CFD Model for Emulsification of Slag into the Steel," *ISIJ International*, 49 (11) (2009), 1661-1667.

[3] S.T. Johansen and F. Boysan. "Fluid Dynamics in Bubble Stirred Ladles: Part II. Mathematical Modeling," *Metallur. and Mater. Trans. B*, 19B (10) (1988), 755-764.

[4] E. Ramström, "Mass transfer and slag-metal reaction in ladle refining-a CFD approach" (Licentiate Thesis, Royal Institute of Technology, 2009), 1-31.

[5] O.J. Ilegbusi and J. Szekely, "The Modeling of Gas-bubble Driven Circulations Systems," *ISIJ Intern.*, 30 (9) (1990), 731-739.

[6] W.T. Lou and M.Y. Zhu, "Numerical Simulation of Gas and Liquid Two-Phase Flow in Gas-Stirred Systems Based on Euler-Euler Approach," *Metallur. and Mater. Trans. B*, 44B (10) (2013), 1251-1263.

[7] P.G. Jonsson, L. Jonsson and D. Sichen, "Viscosities of LF Slags and Their Impact on Ladle Refining," *ISIJ Intern.* 37 (5) (1997), 484-491.

[8] L. Jonsson and P. Jonsson, "Modeling of Fluid Flow Conditions face in a Gas-stirred Ladle," *ISIJ Intern.*, 36 (9) (1996), 1127-1134.

[9] B. Li, H. Yin, C. Q. Zhou, and F. Tsukihashi "Modeling of Three-phase Flows and Behavior of Slag/Steel Interface in an Argon Gas Stirred Ladle," *ISIJ Intern.*, 48 (12) (2008), 1704-1711.

[10] Fluent 6.3: User's Guide Manual Fluent Inc. and Ansys's Fluent, (2006), http://ansys.com/.

[11] B. Deo and R. Boom. *Fundamentals of Steelmaking Metallurgy*, London, UK, Prentice Hall Intern. 1993.

[12] Subagyo, G A. Brooks, K. S. Coley, and G A. Irons, "Generation of Droplets in Slag-Metal Emulsions Through Top Gas Blowing," *ISIJ Intern.*, 43(7), (2003), 983-989.

CFD Modeling and Simulation in Materials Processing 2016
Edited by: Laurentiu Nastac, Lifeng Zhang, Brian G. Thomas, Miaoyong Zhu, Andreas Ludwig, Adrian S. Sabau, Koulis Pericleous, and Hervé Combeau
TMS (The Minerals, Metals & Materials Society), 2016

APPLICATION OF CFD TO MULTI-PHASE MIXING IN THE METALS AND MINING INDUSTRIES

Duane Baker and Adam Blackmore

Hatch Associates
2800 Speakman Drive
Mississauga, Ontario, Canada

Keywords: CFD, Multi-phase, Euler-Euler, MUSIG, Mixing

Abstract

Mechanical mixing equipment is common in a wide variety of mining, metals and process applications, such as hydrometallurgical reactors, slurry tanks, oil storage tanks, etc. Computational Fluid Dynamics (CFD) has been applied successfully to single phase mechanical mixing problems for several decades and is established as a reliable design tool. As computational power and CFD codes have advanced there have been significant advances in multiphase modeling capabilities in particular improved models for dispersed bubbly flows.

This paper will provide an overview of the application of Multiphase CFD modeling to mechanical mixing problems; in addition, it will review the traditional single phase Multiple Reference Frame (MRF) and introduce advanced modeling techniques for dispersed bubbly flows often found in the mining and metals industries. Several examples on the application of CFD to industrial multiphase mixing problems will be shown.

Introduction

Mechanical mixing is a very important component of many mining and metals processes such as the Pressure Oxidation (POX) circuit of hydrometallurgical processing of mineral ores. A typical circuit is shown in Figure 1 below. It is worth noting that mechanical mixing is an important component in three of the vessels in this circuit: the upstream slurry mixing tank, the horizontal POX reactor, and the downstream slurry tank.

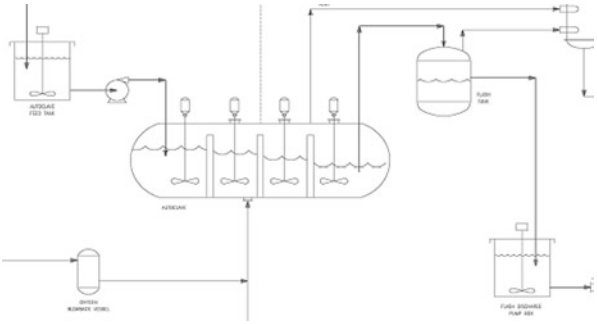

Figure 1 - Typical mining processing circuit

The design of these mixing components and the sizing of impellers, motors, baffles, supporting structures and other components can be accomplished by several methods which range from simple rules of thumb or design calcuations, scale-up from experimental results, use of advanced methods such as Computational Fluid Dynamics (CFD), or a combination of methods . The challenge in applying simple rules is that they can oversimplify the real industrial problem, including geometry, fluid properties, or other important features. The challenge of scale-up from experiments is that the geometry, fluid properties, Reynolds number, etc. are often idealizations of the real industrial problem. CFD has been developed since the 1980's and applied to many industries including the design of mechanical mixing components [1, 2].

A CFD model of a mixing system is often simplified by representing a complex multi-fluid, or fluid-solid system as a single phase fluid with representative properties and to simulate the inherent transient behaviour of the rotor and stator interaction as a steady flow [2, 3]. In this work we look at two cases which remove these simplifications. The first case is an air-water, large lab scale, mechanically agitated tank. The second is an air-water, small industrial-scale, mechanically agitated tank.

Multi-Phase Modeling Approach

The governing equations for a multi-phase flow are the continuity, momentum, and auxiliary scalar equations and jump conditions at the interface see for example full derivation and details in [4]. There are several approaches to modelling of multiphase flows which include: the direct solution and capturing of interface movement with a Volume of Fluid (VOF) or other method, Euler-Lagrange formulation, and Euler-Euler formulation see for example Wörner [4] and Ansys-CFX Theory Manual [5].

In theory, all multiphase problems could be solved with the direct approach or VOF method which resolves the interfaces between the phases. In practice, only simple structured and preferably steady problems can be solved with the full resolution of the interfaces. Further, for an engineering simulation, if all the details of the interface, it would result in too much information and a tremendous amount of post-processing would be required to obtain engineering quantities of interest; i.e., volume average void fraction (α_i), average interfacial area (A_i) average dispersed phase diameter, etc. The engineering approach for these problems is to apply volume averaging to the equations first and then solve for volume average quantities. The volume averaging approach, therefore, greatly simplifies the problem but, of course, results in the loss of a great many details, and therefore this closure information must be provided to solve the problem.

For the flows of interest in this work the multiphase regime is a dispersed gas phase interpenetrating in a continuous liquid phase and as such a practical modelling approach is the Euler-Euler method. Within the Euler-Euler framework there are various levels of sub-models for the multi-phase interactions. The simplest approach is the mono-disperse model where a pre-specified dispersed phase of a given size is solved in the whole domain. A further extension of is to solve in the domain for multiple size groups which in Ansys-CFX is called the MUSIG model see [5]

Application Examples

CASE 1: AIR-WATER LARGE LAB-SCALE MECHANICALLY AGITATED TANK

The dispersion and size distribution of air bubbles in a relatively large lab-scale mechanically agitated tank is analyzed to understand the modelling assumptions and to begin to develop best practices for mixing simulations of dispersed multiphase systems. The case chosen for this study is one from the open literature by Barigou and Greaves [6]. The key features of this case are that it is relatively large scale, the system is air dispersed in water at room temperature, the geometry is a standard vertical cylindrical tank with a standard Rushton radial impeller. The geometry is shown in Figure 2. The geometry of both the tank and the impeller is symmetric about a 180° plane, and given the rotating impeller and rotating flow field, only a half model with periodic boundary conditions was solved, as shown in the figures. The key feature of the measurements is that detailed bubble size distributions were taken at more than 30 locations in the tank.

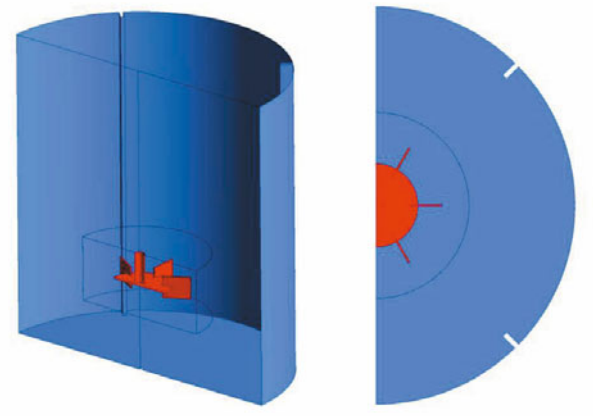

Figure 2 - CFD model of the tank geometry

The conditions chosen for comparison are a moderate air injection rate of 0.00438 m^3/s with impeller rotation speeds of 180 RPM and 270 RPM and a high air injection rate of 0.00687 m^3/s with impeller rotation speeds of 180 RPM, 285 RPM and 385 RPM, for a total of five cases. The velocity contours and the in-plane component of the velocity vectors are shown on the left side in Figure 3 to Figure 7. The Sauter Mean Diameter (SMD) is shown on the right in the figures and compares the experimental values at specific points to the simulation results. When looking at the velocity contours and in-plane vectors, the figures show a strong radial flow outward from the impeller and a classical two-loop circulation pattern. The bottom loop from the radial impeller to the tank walls down to the bottom and back to the bottom of the impeller and the top loop up to the top surface and then back down to the top of the impeller. There were unfortunately no velocity measurements in the published work to compare. As expected the higher impeller speeds have a higher radial velocity.

For the moderate air injection rate the comparison of the measured and the MUSIG multiphase CFD Sauter Mean Diameter (SMD) bubble size is shown in Figure 3 for the 180 RPM case and Figure 4 for the 270 RPM case. For the 180 RPM experiment the range of SMD is 1.54-4.48 mm. The range of SMD for the CFD simulation is 1.5-5 mm. The smallest bubbles are in the region leaving the radial impeller where the fluid velocity and shear is high and therefore bubble break-up is dominant. The largest bubbles are in the region about half way up the tank in the region where fluid velocity turns downward into the impeller eye where fluid velocity and shear are low and coalescence is dominant.

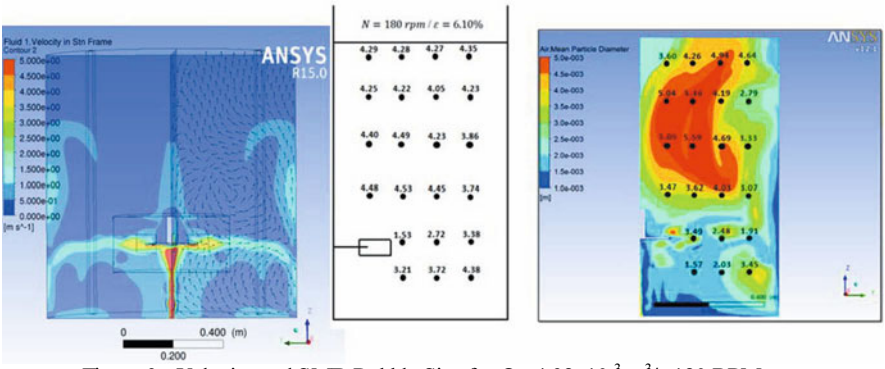

Figure 3 - Velocity and SMD Bubble Size for Q= 4.38x10^{-3} m^3/s 180 RPM case

For the 270 RPM experiment, the range of SMD is 1.29-4.55 mm. The range of SMD for the CFD simulation is 1.0-5 mm. The smallest bubbles are smaller than the 180 RPM case and are in the region leaving the radial impeller, where the fluid velocity and shear are high and, therefore, bubble break-up is dominant. The largest bubbles are in the region about half way up the tank near the axis. The large bubbles are confined to a smaller region than for the 180 RPM case where fluid velocity and shear are low and coalescence is dominant. Overall the higher impeller speed case has a higher velocity and shear in the entire domain, and as a result, there is an expected increase in break-up.

The main observation for the 270 RPM case is that the range of SMD is the correct order of magnitude in the CFD simulation. The second observation, when we compare the experiments and the CFD simulation, is that the trend of SMD is correct, both qualitatively and quantitatively, as one follows the path of a fluid particle through the two loops of the radial impeller. The most important observation is that the trend of lower SMD for the 270 RPM case, as compared to the 180 RPM case is well predicted by the CFD simulation as shown in Table 1. Overall the CFD simulation compares well to the experimental results. As a result, Euler-Euler multiphase is expected to be a very useful tool for studying process variations in such a dispersed air-water system.

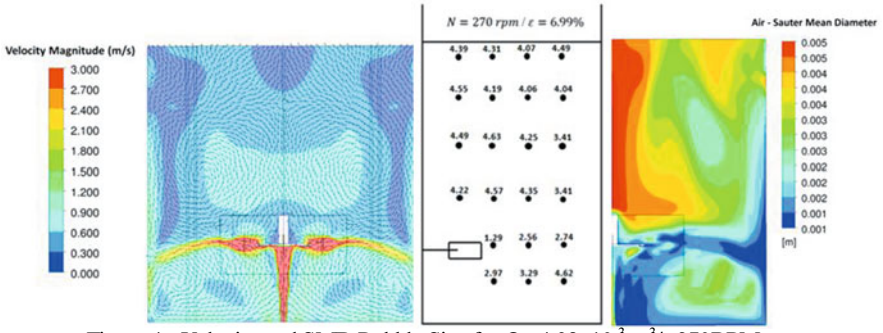

Figure 4 - Velocity and SMD Bubble Size for Q= 4.38x10^{-3} m^3/s 270RPM case

For the high air injection rate the computed velocities and comparison of the measured and the CFD prediction of Sauter Mean Diameter (SMD) bubble size is shown in Figure 5 for the 180 RPM case, Figure 6 for the 285 RPM case, and Figure 7 for the 385 RPM case. For the 180 RPM experiment the range of SMD is 1.54-4.48 mm. The range of SMD for the CFD simulation is 1.5-5 mm. The smallest bubbles are in the region leaving the radial impeller where the fluid velocity and shear is high and therefore bubble break-up is dominant. The largest bubbles are in the region about half way up the tank in the region where fluid velocity turns downward into the impeller eye where fluid velocity and shear are low and coalescence is dominant. For the 285 RPM experiment the range of SMD is 2.1 - 4.56 mm. The range of SMD for the CFD simulation is 1.5-4.5 mm. For the 385 RPM experiment the range of SMD is 1.41 - 4.30 mm. The range of SMD for the CFD simulation is 1.2-4.5 mm. The summary of volume average SMD for all runs is given in Table 1. The trend of deceasing bubble diameter with increasing impeller speed is well predicted. The trend of increasing bubble diameter with increasing air injection is also well predicted. The MUSIG model does, however consistently under predict the bubble diameter.

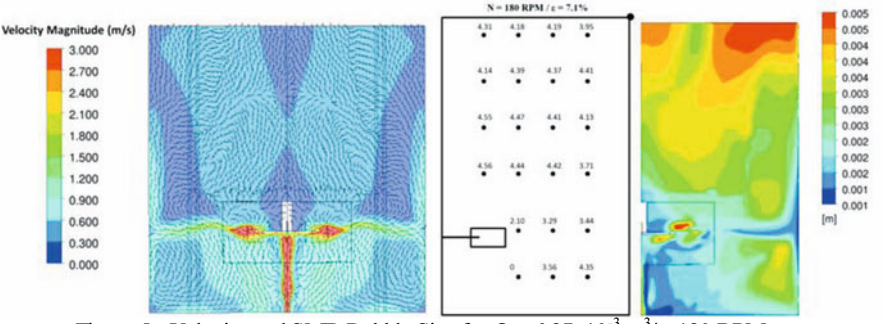

Figure 5 - Velocity and SMD Bubble Size for Q = 6.87x10^{-3} m^3/s, 180 RPM case

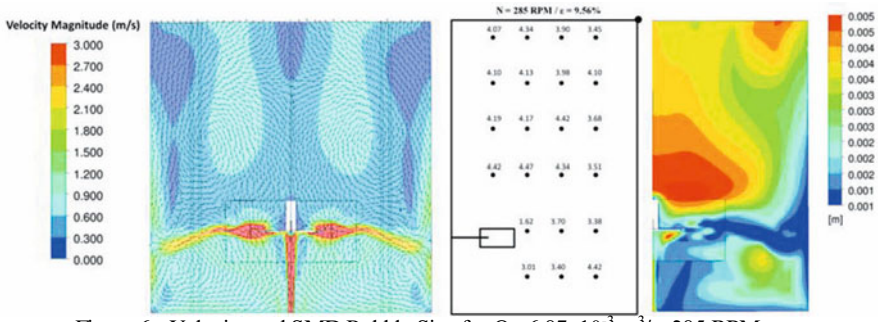

Figure 6 - Velocity and SMD Bubble Size for Q= 6.87x10^{-3} m^3/s, 285 RPM case

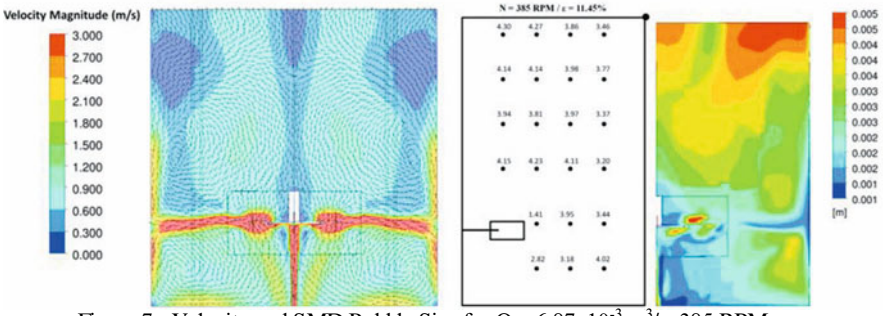

Figure 7 - Velocity and SMD Bubble Size for Q = 6.87x10^{-3} m^3/s, 385 RPM case

Table 1 - Comparison of experimental and CFD simulation results of mean bubble size

Air Injection [10^{-3} m^3/s]	**Speed [rpm]**	**Experimental [mm]**	**CFD [mm]**
4.38	180	3.84	3.19
4.38	270	3.72	3.05
6.87	180	4.06	3.23
6.87	285	3.80	2.86
6.87	385	3.71	2.39

CASE 2: AIR-WATER INDUSTRIAL SCALE MECHANICALLY AGITATED TANK

The dispersion of air bubbles in a small industrial scale air-water system is analyzed to better understand the modelling assumptions and best practices for multiphase CFD simulations. The key features of this case are that it is of a small but practical tank geometry, a Rushton radial impeller and a simple vertical air inlet under the impeller are used, and only global or integral

measurements are made such as impeller torque, flow visualization, etc. A steady Euler-Euler multiphase simulation was conducted in CFX V12.1 for which the geometry and boundary conditions for the simulation are shown in Figure 8.

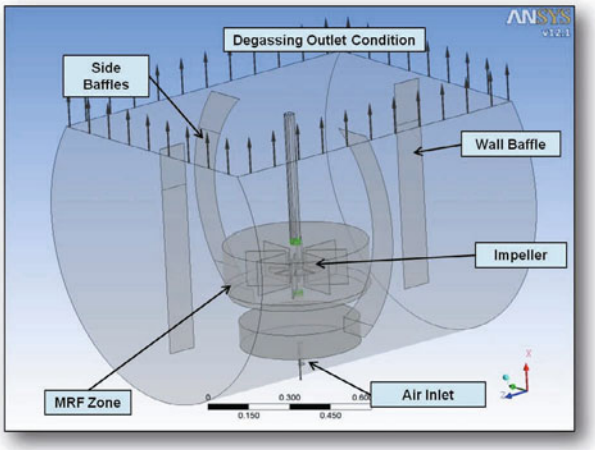

Figure 8 - CFD model and boundary conditions for the industrial air-water dispersion tank case

The problem physics, equations solved, and solver settings for this case are nearly identical to those used in Case 1 and, therefore, this case serves as an ideal practical complement at larger scale. In addition to the advanced homogenous MUSIG model treatment for the dispersed phase used previously, a mono-dispersed fixed diameter Euler-Euler model was used as well. The main objective of the experiment and CFD analysis was to determine the effect of dispersed gassing on the impeller torque and power input for a simple system. The traditional approach, without advanced CFD modelling is to design for a specified torque or power of the continuous fluid (water in this case) and then multiply this by a K-factor, where K=1.0 for an ungassed operation, Nicolle et al. (2008).

The quantitative experimental and CFD results are shown in
Figure 9. A qualitative comparison of the flow visualization in the experiment and the MUSIG CFD simulation is shown in Figure 10. Both the 3.6 mm bubble Euler-Euler and the MUSIG model Euler-Euler simulations under-predict the impeller torque for all air flow rates. The trend of decreasing torque with increased air flow rates is relatively well captured. The agreement is good for both models, but at higher gassing rates, is significantly better for the MUSIG model. This result is somewhat expected as the MUSIG model is able to account for the change in break-up and coalescence rates with increased air-flow. The qualitative comparison in Figure 10 is also excellent, especially given the difficulty of visualizing an air-water system.

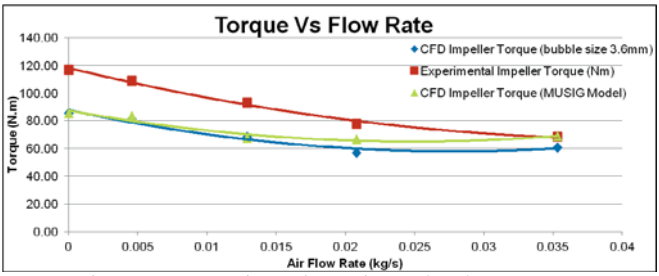

Figure 9 - Comparison of experimental and CFD torque

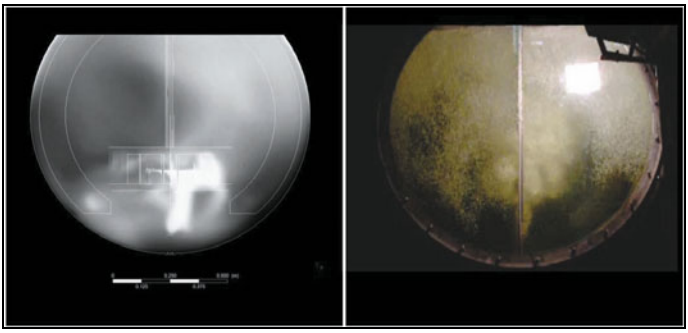
Figure 10 – Comparison of the CFD (left) and experimental (right) results

CONCLUSIONS

The two CFD mixing simulations have provided an introduction to the use of advanced CFD modelling techniques for typical mixing applications in mining and metals. The examples shown have been specifically chosen as they demonstrate the approaches and challenges as one moves from simple steady, single phase CFD simulations to multiphase problems. The examples were also chosen to provide experimental measurement data to allow a comparison to the CFD results. The CFD results were shown to give good agreement to the measurements available.

References

1. Ferziger, J. & Peric, M. Computational Methods for Fluid Dynamics, 2nd Edition, 2001
2. Marshal, L. & Bakker, A. Computational Mixing, 2002
3. Nicolle, M., Nel, G., Plikas, T., Shah, U., Zunti, L., Bellino, M., & Pieterse, H. (2009). Mixing System Design for the Tati Activox Autoclave. The Southern African Institute of Mining and Metallurgy, 2009.
4. M. Wörner, A Compact Introduction to Numerical Modeling of Multiphase Flows, Forschungszentrum Karlsruhe, FZKA 6932, 2003
5. Ansys-CFX, Theory Manual, V15, 2013
6. Barigou, M. & Greaves, M. Bubble Size Distributions in a Mechanically Agitated Gas-Liquid Contactor. Chemical Engineering Science, vol. 4, pp. 2009-2025, 1992

CFD Modeling and Simulation in Materials Processing 2016
Edited by: Laurentiu Nastac, Lifeng Zhang, Brian G. Thomas, Miaoyong Zhu, Andreas Ludwig, Adrian S. Sabau, Koulis Pericleous, and Hervé Combeau
TMS (The Minerals, Metals & Materials Society), 2016

NUMERICAL STUDY AND EXPERIMENTAL VALIDATION OF MULTIPLE POURING PROCESS IN A 438-t STEEL INGOT

Zhenhu DUAN, Houfa SHEN, Jinwu KANG and Baicheng LIU

Key Laboratory for Advanced Materials Processing Technology, Ministry of Education, School of Materials Science and Engineering, Tsinghua University, Beijing 100084,

Keywords: Multiple pouring, Solidification, Macrosegregation, Heavy ingot

Abstract

In the present work, a ladle-tundish-mould model throughout the whole multiple pouring (MP) process is proposed to describe the carbon distribution in the tundish and solidification process in the mould. The water analog experiment was carried out to simulate the carbon transportation and diffusion in the liquid steel in the tundish based on similarity rules. The experimental results were compared to the predicted results in a good agreement. The carbon distributions along three transverse sections in the riser of 438-t steel ingot were measured and found to be in good agreement with the simulated results, proofing the macrosegregation model. In addition, different pouring processes including the original MP process and delayed MP technique were considered to investigate their effects on the final macrosegregation of ingot. The results show that the delayed MP process has greater effects on the reduction of the positive segregation in the riser and in the centre region of ingot than the traditional MP.

Introduction

At present, the large steel ingots are still used in the production of the high-cost and high-quality sections such as the pressure vessels required for the nuclear power generation [1]. The macrosegregation is the main defect in large steel ingots. With the increasing size of ingots, the segregation degree in ingots is more severe. Recently, many numerical models have been developed to predict the macrosegregation quantitatively. Beckermann and coworkers [2, 3] were the first to present the multiphase models that account for the melt convection and the solid movement. Ludwig and coworkers developed a series of multiphase models [4, 5]. Combeau and coworkers [6, 7] presented a multiphase and solidification model, which describes the morphology of the equiaxed grains and their motion. These models offer a better understanding the mechanisms of the formation of macrosegregation. However, these models were just applied to the industrial steel ingots without considering the filling process in the tundish and mould. As large steel ingots of 300~600 tons concerned, few researchers have attempted to take both the mold filling and solidification process into account. The numerical simulation in a 360 ton steel ingot was carried out by Liu et al, whereas the filling in the tundish and mould should be introduced in detail [8]. A marked reduction of macrosegregation was obtained in the ingot body for 570 tons steel ingot produced by MP process [9]. The MP process of a 292 ton steel ingot was simulated by Tu et al, and the favorable initial carbon distribution in the mould was found after MP process [10].

This article presents a model to investigate the carbon mixing behavior in the tundish and mould. The effects of the different MP processes on the final macrosegregation of the large steel ingot have been understood. Especially, the water analogy and industrial experiments were carried out to validate the present the mathematical model.

Mathematical models

A CFD model and a continuum macrosegregation model were ultilized in the simulation of MP process and solidification process of the ingot. The CFD turbulence transportation model based on multi-phases and VOF methods treats unsteady, turbulent and gas-liquid two phase flow, as shown in Table1. In addition, the continuum macrosegregation model was incorporated into the filling transportation model to simulate the filling and solidification process in the mould listed in Table 2.

Table 1. The mathematical model for conservation equations for the tundish filling

Mass	$\rho\frac{\partial a_q}{\partial t}+\rho\bar{\mathrm{u}}\cdot\nabla\cdot a_p=0$	(1)
Momentum	$\frac{\partial\rho_m\mathrm{u}}{\partial t}+\nabla\cdot(\rho_m\mathrm{uu})=-\nabla p+\nabla\cdot(\mu_{eff}\nabla\mathrm{u})+\rho_m g$	(2)
Realizable k-ε	$\frac{\partial\rho_m k}{\partial t}+\nabla\cdot(\rho_m\mathrm{u}k)=\nabla\cdot\left(u+\frac{u_{eff}}{\sigma_k}\right)\nabla k+G_k-\rho_m\varepsilon$ $\frac{\partial\rho_m\varepsilon}{\partial t}+\nabla\cdot(\rho_m\mathrm{u}\varepsilon)=\nabla\cdot\left(u+\frac{u_t}{\sigma_\varepsilon}\right)\nabla\varepsilon+\rho_m C_1 E\varepsilon-\rho_m C_2\frac{\varepsilon^2}{k+\sqrt{\nu\varepsilon}}$	(3)
Energy	$\frac{\partial\rho_m T}{\partial t}+\nabla\cdot(\rho_m\mathrm{u}T)=\nabla\cdot(\frac{k_{eff}}{c_p}\nabla T)$	(4)
Species	$\frac{\partial\rho_m C}{\partial t}+\nabla\cdot(\rho_m\mathrm{u}C)=\nabla\cdot(D_{eff}\nabla C)$	(5)

Table 2. Mathematical model for the macrosegregation in the mould

Mass	$\nabla\cdot\mathbf{u}=0$	(6)
Momentum	$\rho\frac{\partial\mathbf{u}}{\partial t}+\rho\nabla\cdot(\mathbf{uu})=-\nabla p+\mu_l\nabla^2\mathbf{u}-\mu_l K^{-1}\mathbf{u}+\rho_b\mathbf{g}$	(7)
Density in buoyancy term	$\rho_b=\rho[1-\beta_T(T-T_0)-\beta_C(C_l-C_0)]$	(8)
Energy	$\frac{\partial T}{\partial t}+\nabla\cdot(\mathbf{u}T)=\frac{k}{\rho c_p}\nabla^2 T+\frac{L}{c_p}\frac{\partial g_s}{\partial t}$	(9)
Species	$\frac{\partial C}{\partial t}+\nabla\cdot(\mathbf{u}C)=\nabla\cdot(g_l D_l\nabla C)+\nabla\cdot[g_l D_l\nabla(C_l-C)]-\nabla\cdot[\mathbf{u}(C_l-C)]$	(10)
Permeability	$K=\frac{\lambda_2^2}{180}\frac{g_l^3}{(1-g_l)^2}$	(11)
Temperature and liquid concentration	$T=T_m+m_l C_l$	(12)
Solid volume fraction and temperature	$g_s=\frac{1}{1-k_p}\frac{T-T_l}{T-T_m}$	(13)

Experiment Process and Parameters

a) Water analogy experiment

In present water analog experiment, the parameters of the experiment and real production as well as the real size of the different parts in the measured system are referred in [11]. The methylene blue in the water was ultilized to simulate the carbon species in the liquid steel during MP process. The pouring system and sensors used are shown as in Figure 1(a) including the tundish, mold, ladle, the connected tubes and the measurement devices.

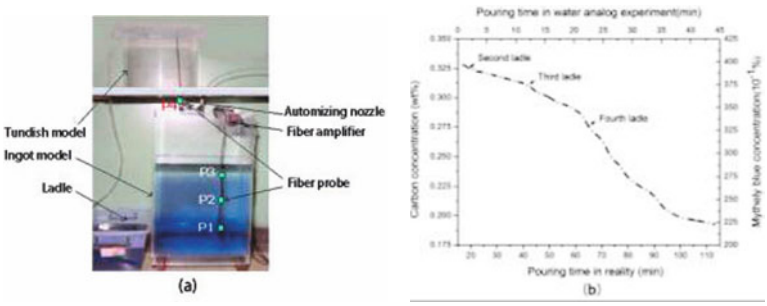

Figure 1. The water analogy experiment, (a) the apparatus,
(b) the measured solute concentration at the outlet of tundish

The Figure 1(b) shows the solute variation with times at the outlet of the tundish. The result shows that the varied curve generally presents the decreasing trends. During the pouring of the ladle- 2 to the final one, the current measured concentration at the outlet of tundish is higher than current ladle concentration. During the drainage stage, the concentration at the outlet is still higher than that of the current ladle solute concentration, the reason can be explained by that concentration of the former ladle is higher than that of the current ladle. At the nearly end of pouring process, the concentration is close to the current ladle concentration. In addition, the other factors of for each ladle, such as concentration, weight, and pouring time, have an important impact on the concentration variation at the outlet of tundish. For example, if the last ladle volume is larger than the current one, the concentrations maybe lower than the current measured values. If the whole pouring time is larger than the current value, the concentration may become more even than the results as shown in Figure 1(b) because more fully solute mixing behavior would occur in tundish.

b) Industrial 438-t ingot experiments

A 438-t steel ingot was cast and analyzed by the steel plant of CITIC Heavy Industries Co., Ltd. The carbon concentration was measured at the positions as shown in the Figure 4(d). It should be noted that the riser of ingot was cut for microstructure analysis after forging. The average diameter of ingot is 3689mm. The height of ingot is 4095mm. The pouring temperature was 1580°C and the pouring time was about 5700s. Four ladles were poured in succession from the

tundish to mould for the production of steel ingots with average Fe-0.26%C. The weight of the molten steel in each ladle was 90t, 90t, 105t and 155t respectively, and the carbon concentrations from the first to the forth ladle are 0.33%, 0.30%, 0.26% and 0.20%, respectively.

Numerical Simulation and Validation

In the present simulation, the heat transfer coefficients at the interfaces of the mould/ingot and mould/ambient were assumed as constant values of 1000 and 100$Wm^{-2}K^{-1}$, respectively. A small heat transfer coefficient of 5 $Wm^{-2}K^{-1}$ was used at the interface between the casting and powder at the mould top. The time step was set up 0.01 seconds in the tundish filling and fluid flow simulation. The time step was set up 1 second in the mould filling process and then 2 seconds at the later stage of the solidification simulation.

a) The tundish results and discussion

Figure 2 presents the carbon distribution in the tundish at different times. In the holding stage as shown in Figure 2(a) and (b), the molten steel with lower C concentration is transferred to the corners of the tundish, and several swirls with the high C distribution form in the middle of the tundish. When it comes to the draining stage, the bath level in the tundish decreases to the lowest critical height as shown in Figure 2(c). The carbon distribution is almost the same and remains higher than that of molten steel from the last ladle.

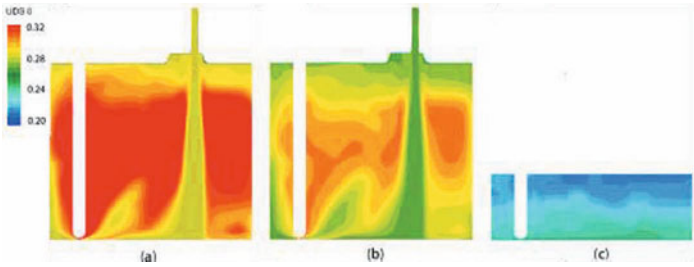

Figure 2. The carbon distribution in the tundish at times. (a) At time of 1700s for ladle-2, (b) at time of 3000s for ladle-3, (c) at time of 5500s for ladle-4

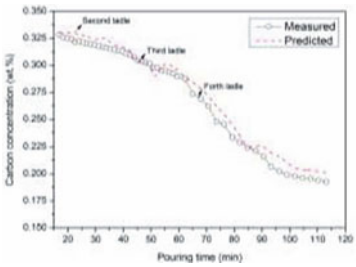

Figure 3. The comparison between the predicted and measured carbon variation curves at the outlet of the tundish

Figure 3 presents the comparison between the predicted and measured carbon variation curves at the outlet of the tundish. There are some fluctuations for the predicted carbon concentration when the transition between two ladles, while the measured curve descends continuously. The possible reasons contributing to the differences between two curves are as following: First, the predicted values are averaged across the outlet section of the tundish, while measured values are at only one point nearly the outlet of tundish. Second, both simulation results probably have measured or model calculation errors leading to the discrepancy. Generally, the simulation results are generally in good agreement with the measured data, both showing similar tendencies.

b) The mould results and discussion

Figure 4(a-b) shows both the filling and the solidification processes at different times in the mold. The carbon distribution pattern takes on a kind of V-shape with the deepest height of about 1 m in the upper region of mold. The carbon distribution gradually decreases from the center to the side in middle of the mold. Finally, the initial carbon distribution in the mould, after MP process, is obviously low in the hot top section. Figure 4(c-d) shows the carbon distribution evolution and the fluid flow during the solidification stage after the pouring process. High carbon distribution is noticed at the lowest bottom of the ingot. With the solidification proceeding, the carbon distribution in the center of the liquid steel increases, and finally the serious positive segregation is noticed in the hot top region of the ingot.

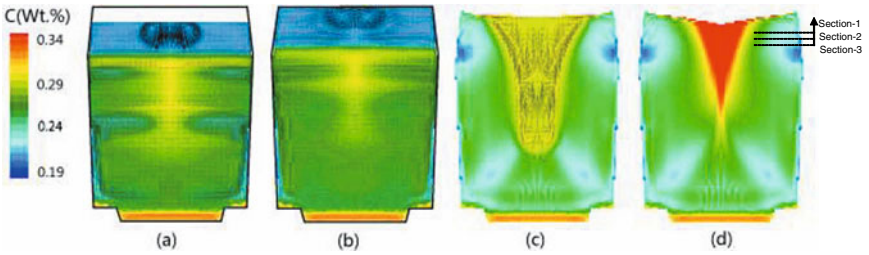

Figure 4. The carbon distribution in the mould with different times, (a) 5100s, (b) 5700s, (c) 100000s, (d)final moment

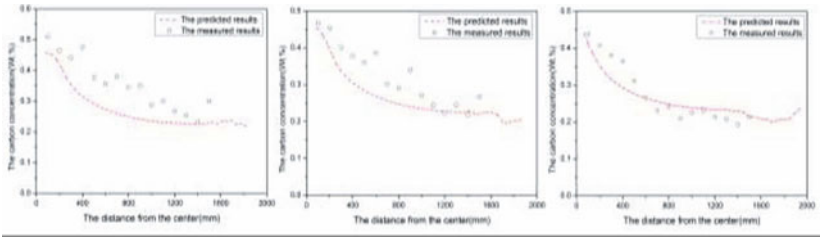

Figure 5. Measured and predicted carbon concentration
(a) Section-1, (b) section-2 and (c) section-3

Figure 5 shows the comparison between the predicted and measured result of carbon segregation along the transverse sections (1~3) of the ingot hot top as illustrated in Figure 4(d). The predicted positive segregation around the center region is underestimated as compared to the experimental results. The possible reasons for the discrepancy are: first, the macrosegregation model was considering only the thermal-solutal convection, heat transfer and the solidification shrinkage, without considering the motion of equiaxed grains; second, the uncertainties in the boundary conditions, such as the heat transfer coefficients at the interfaces of mold/ingot, air/mold, and the material physical properties of density, specific heat, and viscosity.

However, the agreement between the predicted and the measured carbon concentrations can be generally considered good. Thus, the present developed mathematical models can be utilized to simulate the macrosegregation of the large steel ingot with MP process with reasonable accuracy.

The comparison between the original MP and improved MP

In this section, the validated MP model was ultilized to investigate the effect of an improved MP process on the macrosegregation in the 438-t steel ingot. The improved MP technique can be described as the delayed-pouring technique between the ladle changes. In the present case, three ladles were used in MP process, with the nominal carbon concentration of 0.44% and three ladles concentration of 0.49%, 0.44%, and 0.37%, respectively. There was a delay of 20 hours between the second and the last ladle. The result is compared with that of the original MP technique. It should be noted that the result of the original MP process can be obtained from Ref[12].

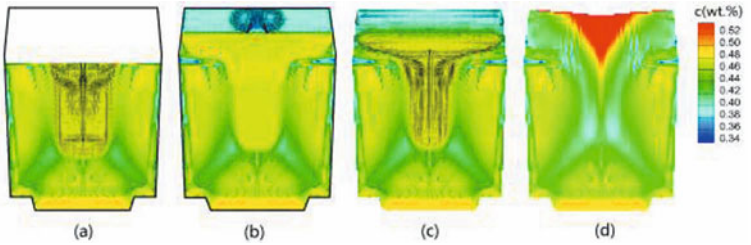

Figure 6. The carbon distribution in 438-t steel ingot with delayed-pouring process,
(a) 61000s, (b) 80000s, (c) 110000s, (d) final stage

Figure 6 shows the solutal and flow field at different times in the improved case. After the second ladle is poured, the ingot body nearly has been completed and then an interval of 20 hours was set after the second ladle. It should be noted that the delayed time and carbon concentration of last ladle become the key parameters to adjust to control the macrosegregation. As shown in Figure 6(a) at the time of 61000s, it can be seen that the steel in the mould has been solidified and with the preferable segregation patterns in the solidified section of the ingot body. Negative segregation forms in the two sides of the lower section of ingot body and mostly other section are nearly the nominal concentration of about 0.44%. The carbon distribution is almost homogeneous in the remaining melt. With solidification processing, the negative segregation in the bottom becomes more serious after the interval of 20 hours as shown in Figure 6(b). In addition, the interface of the solidified section and molten steel shows the negative segregation because the top solidified surface captured the low carbon molten steel from the last ladle.

Figure 7 shows the comparison of the carbon distribution profile along the centre line between the two cases. At the time of nearly complete filling process, as shown in Figure 7(a), the molten steel in the hot top with lower carbon concentration is deeper in case-2 than that in case-1. Case-2 presents fluctuations, while case-1 presents straight line profile in ingot body centre line. At time of 6000s after the MP process, the carbon value generally is lower in case-2 than that in case-1. Finally, the maximal positive segregation is shifted into the top riser in case-2, which means that the positive segregation in the riser is greatly reduced by improved MP.

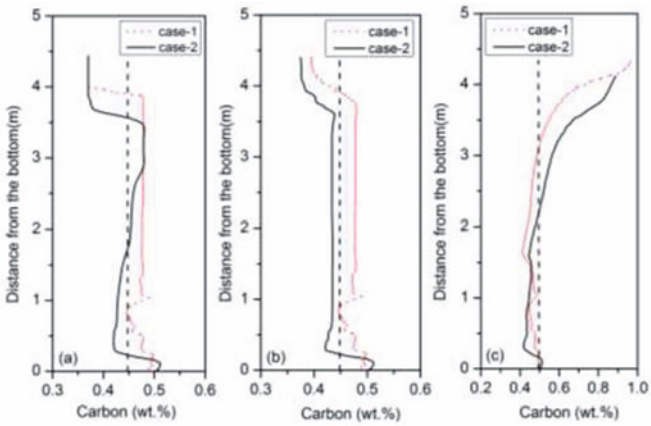

Figure 7. The comparison of the carbon distribution along the centre line of ingot,
Case-1: improved MP, case-2: tradition MP,
(a) 80000s, (b) 86000s, (c) final moment

Through above the comparison, the improved technique can release the positive segregation in riser and centre region of ingot greatly, however, the other factors such as the delay times, ladle concentration, and the ladle pouring time have a great impact on the macrosegregation in ingot.

Future studies should be considered the selection of the optimal parameters in order to control the macrosegregation in ingots effectively.

Conclusions

A ladle-tundish-mould model has been presented in order to simulate the macrosegregation in heavy steel ingot. The performance of the model in the prediction of macrosegregation with MP process was evaluated based on results from the water analog experiments and an industrial experiment of the 438-t steel ingot. The model was applied to simulate the solidification and pouring process of the 438-t steel ingot. The positive segregation was predicted in the hot top and negative segregation in the two sides of the bottom. An improved MP process using the delayed-pouring technique was simulated and compared with traditional MP process. The results show that the improved MP can release the positive segregation in the riser or the centre region much more greatly as compared to the traditional MP and the negative segregation in the two sides of ingot bottom located closer to the centre region.

Acknowledgments

This work was financially supported by the National Basic Research Program of China (No. 2011CB012900) and the National Science and Technology Major Project of the Ministry of Science and Technology of China (2012ZX04012011).

References

1. Tanaka Y, Sato I. Development of high purity large forgings for nuclear power plants. *Journal of Nuclear Materials,* 2011, 417(1-3):854-859.
2. Wang C Y and Beckermann C. A Multiphase Solute Diffusion Model for Dendritic Alloy Solidification. *Metallurgical Transaction A*, 1992, vol 24A, 1993-2787.
3. Wang C Y, Beckermann C. Equiaxed dendritic solidification with convection: part I. multiscale/multiphase modeling. *Metallurgical and Materials Transactions A*, 1996, 27(9):2754-2764.
4. Ludwig A and Wu M. Modeling of Globular Equiaxed Solidification with a Two-Phase Approach. *Metallurgical and Materials Transactions A*, 2002, vol 33A, 3673.
5. Ludwig A and Wu M. Modeling the Columnar-to-Equiaxed Transition with a Three-Phase Eulerian Approach. *Materials Science and Engineering A*, 2005, 413-414, pp109-114.
6. Combeau H, Zaloznik M, Hans S, and Richy P E, Prediction of macrosegregation in steel ingots: Influence of the motion and the morphology of equiaxed grains. *Metall. Mater. Trans. B.* 40 (2009).
7. Combeau H, Kumar A, Zaloznik M. Modeling of equiaxed grain evolution and macrosegregation development in steel ingots. *Transactions of the Indian Institute of Metals*, 2009, 62(4-5):285-290.
8. Liu D R, Sang B G, Kang X H, et al. Numerical simulation of macrosegregation in large multiconcentration poured steel ingot. *International Journal of Cast Metals Research*, 2010, 23(6):354-363.
9. Mankichi T. Development of large size high quality steels and their future prospects as “near net shape” material. *Transactions ISIJ*, 1985, 25:97-105.

10. Tu W T, Zhang X, Shen H F and Liu B C. “The numerical simulation on multiple pouring process for 292 ton steel ingot”. *China Foundry,* 2014, Vol 11, No.1.
11. Kang J W, Dong C, Hao X K, Nie G et al, Water Analog experimental method for the diffusion and distribution alloy elements in liquid steel during ingot filling process. *ISIJ International*, 2014, 54, No.2, pp.275-280.
12. Duan Z H, Shen H F, Liu B C, A Numerical Study of the Effect of Multiple Pouring on Macrosegregation in a 438-Ton Steel Ingot. *Acta Metallurgica Sinica (English Letters),* Vol 28, Issue 9 (2015), Page, 1123-1133.

CFD Modeling and Simulation in Materials Processing 2016
Edited by: Laurentiu Nastac, Lifeng Zhang, Brian G. Thomas, Miaoyong Zhu, Andreas Ludwig, Adrian S. Sabau, Koulis Pericleous, and Hervé Combeau
TMS (The Minerals, Metals & Materials Society), 2016

3D CFD MULTICOMPONENT MODEL FOR COLD SPRAY ADDITIVE MANUFACTURING OF TITANIUM PARTICLES

*Muhammad Faizan-Ur-Rab[1], Saden H. Zahiri[2], S. H. Masood[1], M. Jahedi[2], R. Nagarajah[1]

[1]Swinburne University of Technology; 545 Burwood Road, Hawthorn; Melbourne, Victoria, 3122, Australia
[2]CSIRO Manufacturing Flagship; Gate 5 Normanby Road, Clayton; Melbourne, Victoria, 3168, Australia

Keywords: cold spraying, titanium particles, computational fluid dynamics (CFD), additive manufacturing three dimensional multicomponent model

Abstract

Cold spray is a solid state additive manufacturing process in which high-velocity gas is used to accelerate metal particles toward a metallic or non-metallic substrate. After impact, particles deform plastically and consolidate onto the substrate's surface. Development of a 3D multicomponent model for cold spray assists with the understanding of the complicated events that underlie particle deposition and bond formation. A k-ε type computational fluid dynamics (CFD) multicomponent model has been developed to compute the state of the supersonic gas impinging onto the substrate in the presence of surrounding air. A holistic approach is implemented to determine the gas properties from the stagnation zone, through the nozzle to the substrate surface, as well as the trajectories, velocity and temperature distribution of powder particles accelerated by this flow. The 3D CFD model is a valuable tool for optimizing cold spray process conditions, development of novel materials and nozzle design for cold spray additive manufacturing.

Introduction

The cold spray process is an emerging additive manufacturing technology in which small solid state powder particles are accelerated through high-velocity inert gas within the de Laval nozzle and impinges onto the substrate material for deposition [1]. The kinetic energy of the particles in the presence of supersonic jet causes the solid state bond formation between particle and substrate [2], which can be used for coatings and additive manufacturing of bulk structures. The complex adiabatic shear phenomenon [3] assists the particle to establish good bond with the substrate material without undergoing any melting of powder particles. The schematic diagram of typical cold spray process is shown in Figure 1. In traditional additive manufacturing process, powder particles are first melted and then deposited layers by layers [5]. The cold spray process differs from traditional additive manufacturing in that there is no melting involved and particles deposited onto the substrate material to establish coatings are free from oxidation, residual stresses and thermal defects. This provides an opportunity for cold spray to be implicated for oxygen-sensitive materials such as titanium. Another benefit of cold spray process as novice additive manufacturing process over traditional additive manufacturing process is the size limit of the part to be manufactured. The cold spray process can be performed in an open space at an

ambient environment conditions. On the contrary, almost all traditional additive manufacturing processes require closed enclosure to avoid oxidation with the environment air.

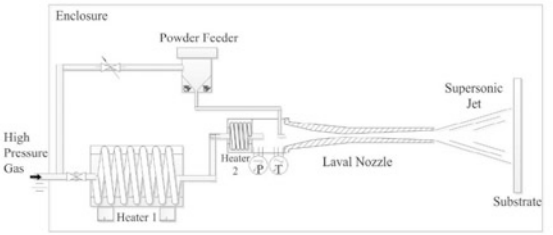

Figure 1. Schematic diagram of cold spray process [4]

The state of in-flight powder particles in their trajectories through the cold spray de Laval nozzle throughout the cold spray process is of great importance for optimization of cold spray process conditions and properties of deposited material. For instance, it is a known fact that particles must achieve a certain velocity called critical velocity [6] for successful deposition and bond formation with the substrate material. Many studies [7, 8] explained the complex solid state bond formation event of particle undergoing adiabatic shear instability with the help of numerical models. Most of these studies used axisymmetric 1D or 2D [9, 10] numerical methods with limited information about upstream particle detailed. Recently, R. Lupoi [11] experimentally measured the deposition efficiency of commercially pure (CP) titanium powder grade 2 on an aluminum 6082-T6 tube specimen, with four different cold spray nozzle designs. The author compared the experimental data with the 2D numerical model but the cold spray 2D numerical model was incapable of predicting the acceleration process accurately and realistically. The author suggested the need of more robust numerical model to capture cold spray supersonic jet and particle state.

An earlier validated three dimensional model for cold spray supersonic jet successfully predicted the state of accelerating gas holistically through the cold spray de Laval nozzle impinging onto the substrate [4]. In another study of cold spray 3D multicomponent model [12], the state of cold spray supersonic jet was presented realistically using nitrogen and air. The 3D model was calibrated and validated against experimentally measured substrate temperature. The aim of this study is to further elaborate the scope of earlier developed gas phase 3D CFD multicomponent model by introducing titanium particle acceleration from the injection point to the moment of impact onto the substrate. Keeping in view of the wide interest of additive manufacturing industry, titanium powder particle is considered for injection in cold spray 3D multicomponent model.

Numerical Analysis

A two equation k-ε type three dimensional turbulence model was developed to simulate the titanium particles trajectory in a cold spray supersonic jet. The flow in cold gas dynamic spray is considered as steady-state supersonic turbulence flow with heat transfer during the flow process. A commercially available density based solver ANSYS^{TM} CFX®v14.5 is utilized under steady state conditions, as it better conforms to compressible flow at supersonic regimes. For

multicomponent model, transport equations are solved for velocity, pressure, temperature and other quantities of the fluid. In this study high pressure nitrogen accelerating through de Laval nozzle has been coupled with surrounding air to simulate the cold spray process realistically.
The CFD computational grid, surrounding domain and boundary conditions for the present study are similar to an earlier study [12]. The details of experimental set-up can be found elsewhere [4]. The established computational domain and nozzle dimensions are shown in Figure 2. The hexahedral mesh elements approach was adopted to develop an acceptable structured mesh and its details can be found elsewhere [12].

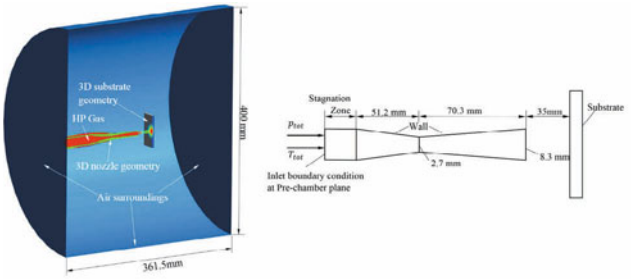

(a) (b)

Figure 2. Three dimensional presentation of cold spray nozzle, high pressure nitrogen, titanium substrate and surrounding air domains, (b) Schematic diagram of cold spray type 27 TC nozzle with dimensions [12].

A total pressure p_{tot} and total temperature T_{tot} as inlet boundary conditions were specified at the pre-chamber plane of high pressure gas domain for better convergence rate. The direction of the inlet velocity vector was normal to the boundary. Opening boundary condition was chosen for all cylindrical domains surrounding surfaces because it allows gas to cross boundary surfaces in either direction. The interaction between gas and solid was assumed to be frictionless, which was equivalent to the free-slip wall boundary conditions [13]. The adiabatic wall boundary condition was specified for nozzle pre-chamber inlet plane in order to prevent heat transfer across the wall boundary. The mechanical and thermal properties of the tungsten carbide (WC) nozzle and titanium substrate were assumed to be isotropic.
Particle transportation model was implemented using discrete phase modeling algorithm with Lagrangian particles tracking technique. It calculates the acceleration of particulate flow of a given size material in carrier gas as well as surrounding fluid. The available CFD tool ANSYS™ CFX® has been widely accepted in previous studies [14] to simulate cold spray particle flow and in this study, same tool is used to further extend the capability of earlier developed 3D multicomponent model [12]. Particle temperature at the injection point within the stagnation zone was 25°C with initial velocity of 10 m/s. Particles injection point into the cold spray upstream was chosen at 60 mm from the start of the convergent section of the nozzle which was approximately same as the particle injection location of commercially available KINETKS® 4000 cold spray system. The shapes of injected titanium particles were considered to be spherical with particle size distribution as shown in Figure 3. This particle size distribution has been used

previously in an experimental study [15]. The interaction between solid particle and gas is fully coupled and involves intensive momentum and heat transfer.

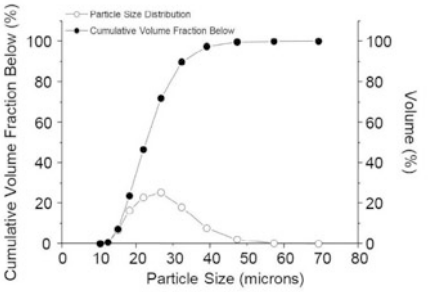

Figure 3. Particle size distribution for a commercial purity (CP) titanium powder [15].

The aerodynamic drag force F_D on a particle is very important in cold spray process and depends upon the velocity difference between the particle and the carrier gas velocity [16, 17]. The drag force is given by:

$$F_D = \frac{1}{2} C_D \rho_F A_F |U_F - U_P| (U_F - U_P) \quad (1)$$

where C_D is the drag coefficient, ρ_F is the density of fluid, A_F is the effective particle cross-sectional area, U_F is the fluid velocity and U_P is the particle velocity. The drag coefficient is a complex function of Reynolds Number Re which must be determined from experiment [16]. In cold spray process, the volume ratio of solid particles to carrier gas is low [16, 17]. Therefore Schiller-Naumann [18] drag correlation as shown in equation (2), for flow past a sparsely distributed spherical particle in a jet best describes the cold spray particle flow. This drag coefficient has been used earlier for cold spraying of fine spherical ceramic particles in order to study the effect of stand-off distance [14].

$$C_D = \max\left(\frac{24}{Re}(1 + 0.15\, Re^{0.687}), 0.44\right) \quad (2)$$

The heat transfer for a spherical particle in fluid is defined using the Ranz-Marshall correlation [19]. For solid particles, in cold spray process, where heat transfer occurs mainly due to convection. Convective heat transfer can be expressed as,

$$Q_C = \pi\, d_P\, \lambda_F\, Nu\, (T_F - T_P) \quad (3)$$

where d_P is particle diameter, λ_F is the thermal conductivity of the fluid, T_F and T_P are fluid temperature and particle temperature, respectively, and Nu is the Nusselt number.

The collision of particles with the nozzle wall was assumed to be frictionless, considering no erosion of nozzle wall by the particle. The particle surface roughness was also considered negligible. The particle-particle collision was incorporated into the multicomponent model using stochastic particle-particle collision proposed by Frank *et al.* [20]. The governing equations of

the flow, particle transport model and boundary conditions at inlet, surrounding domains and wall are summarized in Table I.

Table I. Numerical analysis conditions

Terminology	Classification	Condition
Flow	a. Heat Transfer	Total energy
	b. Turbulence model	k-ε two equation model
Particle	a. Transport Model	Lagrangian particle tracking
	b. Drag coefficient (C_D)	Schiller Naumann
	c. Heat transfer	Ranz Marshall
Boundary condition	a. Inlet	Total pressure (p_{tot}), Total temperature (T_{tot})
	b. Surrounding	Opening condition
	c. Walls	Free-slip
	d. Solid nozzle and substrate interface with fluid	Monte Carlo radiation model

Results and Discussions

The cold spray 3D multicomponent model was used to estimate the state of titanium particles as per spray conditions listed in Table II. The cold spray condition 1 was selected to examine the performance of earlier developed 3D multicomponent model in terms of particle temperature, velocity and particle location just before the impact, compared with condition 2. In a preliminary study of condition 1, 2500 titanium particles were injected into the cold spray gas stream to achieve a dilute mixture of titanium particles and gas. However, for condition 2, an increased sample of 5000 [17] titanium particles were injected into the cold spray gas stream. Both conditions well predicted the state of injected titanium particles.

Table II. Cold spray conditions to estimate state of titanium particles

Cold Spray Condition	Temperature (°C)	Pressure (MPa)	Propellant Gas	Standoff (mm)
1	800	3.0	Nitrogen	35
2	550	1.4	Nitrogen	35

Temperature of Titanium Particles

The temperature history of all injected titanium particles for cold spray condition 1 is shown in Figure 4(a). The thermal state of injected particles can be estimated holistically from the point of injection in stagnation zone, through the nozzle throat, at nozzle exit and to the point of impact onto the surface of substrate. It is reflected from the 3D model outcome that random size particle injection changes particle temperature in the presence of cold spray jet. For instance, within the stagnation zone, temperature of most of the particles reached close to the inlet temperature of 800°C. However, in the divergent section where carrier gas cools due to expansion, many particles synchronized with the propellant gas temperature within the range of 490°C to 750°C, as shown in Figure 4(a). Similar trend can be observed for cold spray condition 2 within the

particle temperature range of 220°C to 420°C as shown in Figure 4(b). In a previous 2D study of cold sprayed stainless steel powder, Li *et al.* [21] reported the similar behavior of change of particle temperature.

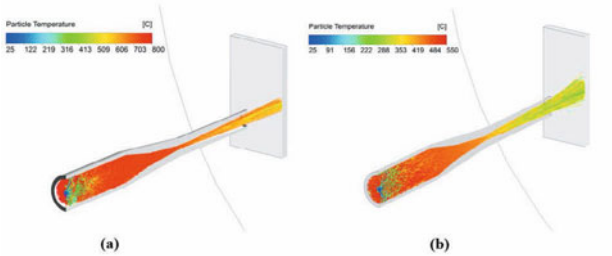

Figure 4. Cross section of 3D simulation of titanium particle temperature holistically from injection point to the location of impact for condition (a) 800°C and 3 MPa and condition (b) 550°C, 1.4 MPa.

Velocity of Titanium Particles

In cold spray process, velocity of particle is an important point of discussion. It has been well understood that particle travelling at or above critical velocity [6] can successfully deposit and create a bond with substrate material. The 3D model velocity predictions of titanium particle are shown in Figure 5. The velocity of particles for condition 1 reached to 840m/s from the injected velocity of 10m/s as shown in Figure 5(a). It is also interesting to learn that in both conditions 1 & 2 particles were aligned with the nozzle axis after passing through the throat. However, in stagnation zone collision of particles with the nozzle wall can be seen clearly. It can cause clogging and in severe case it can block the nozzle throat. This has been addressed previously in real deposition process but with limited published investigations [22]. The available 1D or 2D cold spray models have paid little attention to this phenomenon [9,10].

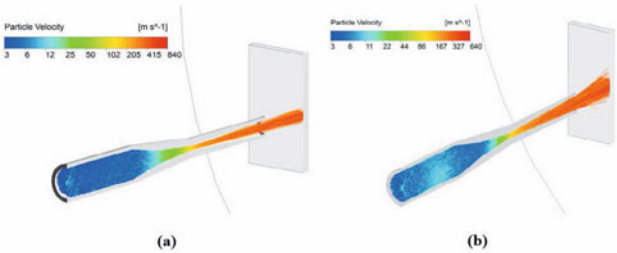

Figure 5. Cross section of 3D simulation of titanium particle velocity holistically from injection point to the location of impact for (a) 800°C and 3 MPa and (b) 550°C, 1.4 MPa.

The 3D model velocity estimation for condition 2 as shown in Figure 5(b) demonstrated the decline in particle speed in comparison with condition 1. This is because of lower pressure and

temperature at inlet for condition 2. The condition 2 confirms the large spread of cold spray plume at nozzle exit and outside the nozzle.

Location of Titanium Particle at Impact

The position of all titanium particles at the moment of impact for the two spray conditions is shown in Figure 6. It can be observed that location of particles for condition 1, as shown in Figure 6(a), were denser at the jet center when compared to condition 2 in Figure 6(b). The 3D model also recognized some asymmetry in the location of impact for condition 2, as shown in Figure 6(b). For two different cold spray conditions, the 3D model prediction of cold spray jet spread with respect to jet center is 2mm to 3mm for condition 1, and 5mm to 6mm for condition 2, as shown in Figure 6(a) and 6(b) respectively.
The locations of titanium particles in Figure 6 show that the position of deposition for individual particle is not symmetrical. The reason could be diversion of particles from their trajectories after collision and bouncing with the nozzle wall. These preliminary 3D model results identified the area for future investigations of asymmetric deposition of cold spray particles.

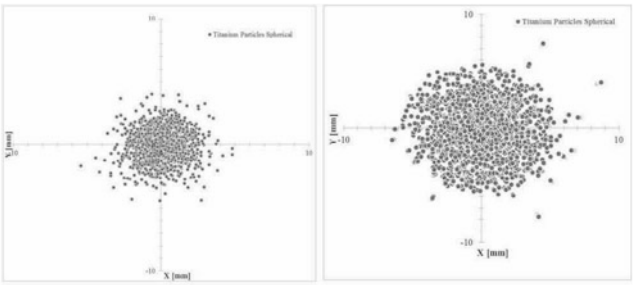

(a) (b)

Figure 6. Estimated location of titanium particles at the moment just before the impact with respect to jet center for (a) 800°C and 3 MPa and (b) 550°C, 1.4 MPa.

Conclusion

A 3D model has been developed for cold spray additive manufacturing process. In cold spray, particles travel with supersonic speeds to establish a bond with substrate material and bulk structures can be produced. Spherical shape titanium particles were injected in validated cold spray jet model. The state of titanium particle in terms of temperature, velocity and location just before the impact were analyzed for two cold spray conditions. The developed 3D model has well predicted the titanium particle state in terms of temperature, velocity and particle location. The 3D model estimation for particle location is an economical method and it could be difficult to achieve this information through experimentation. The cold spray model for particle could benefit the cold spray additive manufacturing industry as a visual tool that include cold spray process optimization, better nozzle designs and powder material behavior.

References

1. Papyrin et al., *Cold Spray Technology*, (United Kingdom, UK: Elsevier, 2007).
2. M. Fukumoto et al.,"Effect Of Substrate Temperature On Deposition Behaviour Of Copper Particles On Substrate Surfaces In The Cold Spray Process", *J. Therm. Spray Technol.* 16 (5-6) (2007), 643-650.
3. M. Grujicic et al., "Adiabatic Shear Instability Based Mechanism For Particles/Substrate Bonding In The Cold-Gas Dynamic-Spray Process", *Mater.Des*. 25 (8) (2004), 681-688.
4. S.H. Zahiri et al., "Development Of Holistic Three-Dmensional Models For Cold Spray Supersonic Jet", *J. Therm. Spray Technol*. 23 (6) (2014), 919-933.
5. S.H. Masood, "Introduction to Advances in Additive Manufacturing and Tooling", S. Hashmi, Ed., Comprehensive Materials Processing,Vol. 10 (Elsevier Science Direct, 2014), 1-2.
6. A. Moridi et al., "A Hybrid Approach To Determine Critical And Ersion Velocities In The Cold Spray Process", *App. Surf. Sci*. 273 (1) (2013), 617-624.
7. W.-Y.Li et al., "Effect Of Standoff Distance On Coating Deposition Characteristics In Cold Spraying", *Mater. Des*. 29 (2) (2008), 297-304.
8. T. Hussain, "Cold Spraying Of Titanium: A Review Of Bonding Mechanism, Microstructure And Properties", *Key Engg. Mater.* 533 (2013) 53-90.
9. S. Rahmati et al., "The Use Of Particle/Substrate Material Models In Simulation Of Cold-Gas Dynamic –Spray Process", *J. Therm. Spray Technol*. 23 (1) (2014), 530-540.
10. S. Li et al., "A Numerical Investigation Of The Cold Spray Process Using Underexpanded And Overexpanded Jets", *J. Therm. Spray Technol*. 21 (1) (2012), 108-120.
11. R. Lupoi, "Current Design And Performance Of Cold Spray Nozzles: Experimental And Numerical Observations On Deposition Efficiency And Particle Velocity", *Surf. Engg*. 30 (2014) 316-322.
12. Muhammad Faizan Ur Rab et al., "Developemnt Of 3D Multicomponent Model For Cold Spray Process Using Nitrogen And Air", *Coatings* 5 (4) (2015),688-708.
13. A. Kumar et al., "Simulation Of Cooling Of Liquid Al–33 Wt.% Cu Droplet Impinging On A Metallic Substrate And Its Experimental Validation", *Acta Materialia.* 58 (1) (2010), 122-133.
14. Doo-Mann Chun et al. "Effect Of Stand-Off Distance For Cold Gas Spraying Of Fine Ceramic Particles (<5μm) Under Low Vacuum And Room Temperature Using Nano-Particle Deposition System (NPDS)", *Surf. Coat. Technol.* 206 (8-9) (2012), 2125-2132.
15. Zahiri et al., "Characterization Of Cold Spray Titanium Supersonic Jet", *J. Therm. Spray Technol.* 18 (1) (2009), 110-117.
16. CFX Solver Theory Guide, release 15 (Pittsburgh, PA: ANSYS, Inc., 2013), 155.
17. B. Samareh et al., "A Three-Dimensional Analysis Of The Cold Spray Process:The Effects Of Substrate Location And Shape", *J. Therm. Spray Technol.* 16 (1) (2007), 634-642.
18. L.Schiller et all., *VDI Zeits,* 13(1) (1933), 318.
19. W. E. Ranz et al.,"Evaporation From Drops", *Chemical Engg. Proc*.48 (1) (1952), 141-146.
20. CFX Solver Theory Guide , release 15 (Pittsburgh, PA: ANSYS, Inc., 2013), 249.
21. Li et al.,"Optimal Design Of Cold Spray Nozzle By Numerical Analysis Of Particle Velocity And Experimental Validation With 316L Stainless Steel Powder", *Material and Design.* 28 (7) (2007), 2129-2137.
22. R. Lupoi et al., "Powder Stream Characteristics In Cold Spray Nozzles", *Surf. Coat. Technol.* 206 (1) (2011), 1069-1076.

CFD Modeling and Simulation in Materials Processing 2016
Edited by: Laurentiu Nastac, Lifeng Zhang, Brian G. Thomas, Miaoyong Zhu, Andreas Ludwig, Adrian S. Sabau, Koulis Pericleous, and Hervé Combeau
TMS (The Minerals, Metals & Materials Society), 2016

NUMERICAL SIMULATION OF EFFECT OF DIFFERENT ELECTRODES ON MAGNETIC FORCE AND FLOW FIELD OF PURE ALUMINUM MELT

Qixin Wang[1], Xiang Wang[1], Zhishuai Xu[1,2], Ning Pei[1] ,Yongyong Gong[1,2*], Qijie Zhai[2]
[1]College of Science, Shanghai University, 99 Shangda Road, 200444 Shanghai, China
[2]Shanghai Key Laboratory of Modern Metallurgy &Materials Processing, Shanghai University, Shanghai 200072, China
*corresponding author

Keywords: ANSYS; numerical simulation; electrodes; solidification structure

Abstract

Using the finite element software ANSYS, the effect of different ways of electrodes of pulse electric current on magnetic force and flow field of pure aluminum melt was theoretically studied. The results indicate that the electromagnetic force on the melt and the induced flow distribution are significantly different with different electrode applying manners. The analysis of numerical simulation provides a scientific basis for the further explanation of the mechanism of electric pulse refinement of metal solidification structure.

Introduction

The metal structure of fine uniform equiaxed grains have excellent processing and mechanical properties. In recent years, the environmental protection has been introduced into the materials science with ecological environment material presented. From the perspective of environmental protection material, physical fields which refined grain structure have become the ideal processing techniques. In solidification grain refine technology via physical fields, the current treatment technology is the most frequently used. The treatment of metal melt by DC current, AC current [1-4] and high intensity pulse current [5-7] has been studied. Kequan Chen etc. [8~9] and Jie Li [10] studied the effect of different electrode applying manner on the solidification of metal. In this paper, the influence of different ways of electrodes of pulse electric field on the electromagnetic field and flow field of the pure aluminum melt is studied based on the method of finite element numerical simulation.

Analytical model

The electromagnetic field theory is described by a set of Maxwell's equations.

Maxwell's equations is used in the finite element simulation of the electromagnetic field:

$$\nabla \times \vec{H} = \vec{J} + \frac{\partial \vec{D}}{\partial t} \tag{1}$$

$$\nabla \times \vec{E} = \frac{\partial \vec{B}}{\partial t} \tag{2}$$

$$\nabla \bullet \vec{D} = \rho \tag{3}$$

$$\nabla \bullet \vec{B} = 0 \tag{4}$$

Lorenz force on a charged particle in electromagnetic field is given by:

$$\vec{f} = \mu_0 \vec{J} \times \vec{H} \tag{5}$$

Where,

$$\vec{J} = \sigma\left(\vec{E} + \vec{v} \times \vec{B}\right) \tag{6}$$

In the flow field analysis, it is assumed that the fluid mass is conserved, and there is continuity equation:

$$\nabla \bullet \vec{v} = 0 \tag{7}$$

In addition, the momentum equation needs to consider the role of electromagnetic force:

$$\frac{\partial\left(\rho_l \vec{v}\right)}{\partial t} + \left(\rho_l \vec{v} \bullet \nabla\right)\vec{v} = -\nabla \vec{p} + \eta_{eff} \nabla^2 \vec{v} + \vec{f} \tag{8}$$

In all of the above formulas, $\vec{E}$ is the electric field intensity, $\vec{B}$ is the magnetic induction intensity, $\vec{D}$ is the dielectric density, $\vec{f}$ is the electromagnetic force, $\vec{H}$ is the magnetic field intensity, $\vec{J}$ is the current density, $\vec{p}$ is the pressure, t is the time, η_{eff} is the viscosity coefficient, μ_0 is the permeability of material, ρ_l is the density of the metal melt, ρ_0 is the density of volume charge, σ is the conductivity of material, v is the velocity of the metal melt.

Table I. Material parameters for numerical simulation

	Resistivity（Ωm）	Relative permeability
Al（660℃）	2.42×10^{-7}	1
Electrode	1×10^{-6}	1
Air（25℃）	-	1

ANSYS finite element analysis is carried out by Maxwell equation, Lorentz law and Joule law. In this paper, we make the following assumptions:①The physical parameters do not change with temperature;②The influence of the flow of the aluminum liquid on

the electromagnetic field is ignored;③The metal liquid is the incompressible Newton fluid. Table 1 shows the material parameters for numerical simulation.

This paper uses three-dimensional model. Figure 1. shows solid mesh division of the melt and different electrodes applying manner. In order to reduce the computation quantity and guarantee the quality of the grid, the grids need to be controlled artificially. The electromagnetic field is intensive in the vicinity of the electrode and the skin depth, and the magnetic field gradient is large, so the grid of these regions is appropriately fine, and the other area can be coarse. The current pulse propagation inside the melt will induce an electromagnetic field in the outer space. Therefore, a layer of air is arranged outside the melt in the simulation. The magnetic vector potential method is used to analysize magnetic field and solid hexahedral element SOLID97 is used for harmonic electromagnetic field analysis. FLUID142 solid hexahedral element Flow field analysis is used for flow field analysis.

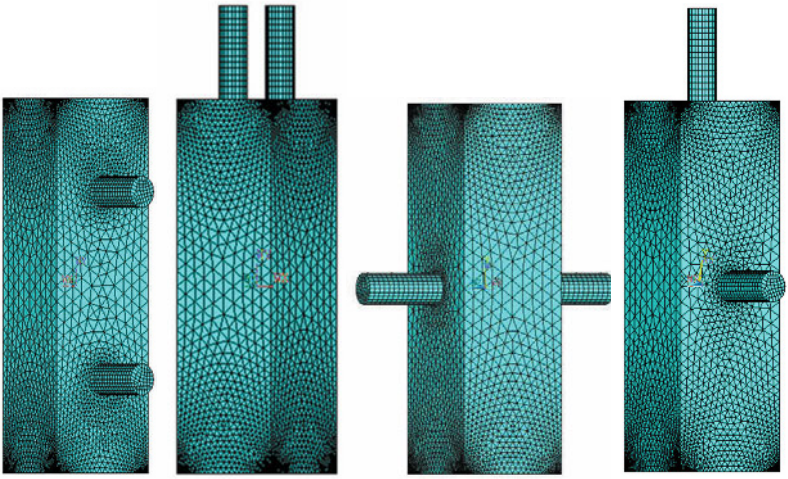

(a) (b) (c) (d)

Figure 1. Solid mesh division of the melt and different electrodes applying manner.

Imposed boundary conditions and loads are: The magnetic field is required to be coupled with the VOLT degree of freedom, and the voltage at the cathode section is defined as 0. Then magnetic lines parallel boundary conditions at the outermost layer of air is set as: $AZ=0$. The pulse current is approximated as a sine wave in a single cycle：

$$i(t)=I\sin(\omega t+\varphi) \tag{9}$$

$$i(0)=0 \tag{10}$$

Where, I is pulse peak.

First, the magnetic field analysis is performed, and the electromagnetic force is applied to the flow field, finally the flow field analysis is performed.

Electromagnetic Force Analysis

Figure 2. shows that the electromagnetic force distribution diagram of the vertical section of the melt in the different electrodes applying manner under certain conditions. Zhishuai Xu [11] demonstrated that the current density plays an important role in the solidification microstructure refinement, and the electrode is located in the region of the rapid increase in current density by experiment. According to the equation (5), when the other conditions are fixed, the greater the current density, the greater the electromagnetic force in the region can be found. It can be seen from It can be seen from Figure 2. that the electromagnetic force which is radial is the largest in the electrode, and mainly focused on the surface of the melt. The current flows from the top of the anode to the cathode through the melt. When current is applied to the metal melt, melt surface can generates the oscillating electromagnetic force. Crystal nucleus shaken off on the wall by the electromagnetic force drift into the melt forming a large number of free nucleus, resulting in the solidification structure refinement.

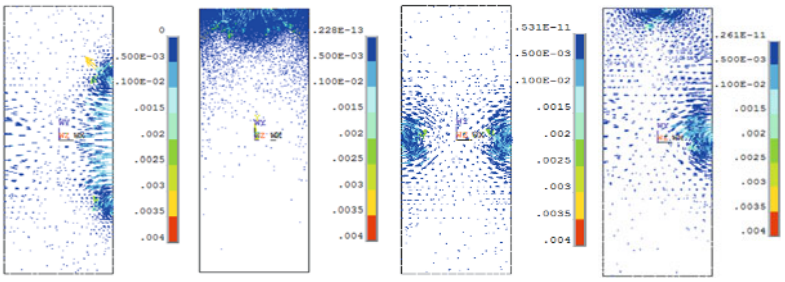

(a) (b) (c) (d)

Figure 2. Electromagnetic force distribution

Flow Field Analysis

Figure 3. shows that the flow field distribution diagram of the vertical section of the melt in the different electrodes applying manner under certain conditions. The melt flows under the action of electromagnetic force from the electrodes to the other parts which is helpful to the uniform distribution of grains fallen down from the wall by the electromagnetic force, increasing the internal nucleation rate, refining the metal solidification structure, homogenizing the temperature gradient, changing the temperature field, reducing the internal defects and improving the physical properties.

Figure 3a. shows that a general circulation is formed near the electrodes, and the flow field is relatively uniform. Figure 3b. shows that the flow field is only located near the

electrode, and a large part of the melt is not flowing. The grains dropped by the electromagnetic force are difficult to drift to the lower part of the melt. Figure 3c. shows that the flow velocity is significantly larger than the other three methods, the flow of the melt is obvious and the flow field is more uniform. Figure 3d. shows that there is a general circulation respectively in the upper and lower parts of the melt and the flow of the melt is obvious, but the flow velocity is small, which cannot make the grain drift effectively.

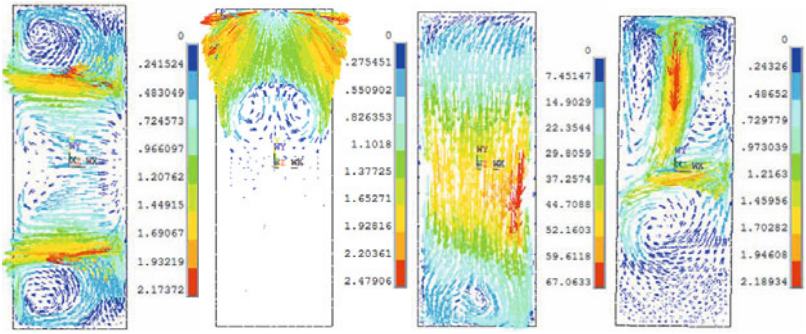

(a) (b) (c) (d)

Figure 3. Flow field distribution

Discussion

Kequan Chen etc. discovered that copper and aluminum alloy solidification structure refinement effect is very good with the opposite electrode which is inserted from the side wall. Jie Li confirmed that the use of parallel electrode method is the best way to optimize the pulse current processing in the same pouring process and current parameters. The conclusion are given based on the experiments. Based on the numerical simulation results, we can indicate that the electromagnetic force on the melt and the flow distribution are significantly different with different electrodes applying manner. The electromagnetic force is basically the same with different electrodes applying manner, but the distribution and direction is different. The numerical value and the flow direction of the flow field are very different. The flow velocity in the third electrode insertion method has significantly higher. The analysis shows that the electromagnetic force can make the crystal nucleus dropped down from the wall and transformed into the free crystal nucleus and can promote melt flow. Then the free crystal nucleus will flow together with the flowing melt as a result of uniform distribution of grains inside the melt and increasing of the internal nucleation rate. The flow which is generated by the action of electromagnetic force can uniform the temperature distribution and the temperature gradient, prevent the free crystal nucleus remelting and help the growth of the crystal nucleus. The flow has a great effect on refining the solidification structure of metals. The third electrode applying manner has a good effect on refining the solidification structure based on the analysis of numerical simulation, which were testified by experiment from Kequan Chen.

Conclusions

The effect of different electrodes applying manner on magnetic force and flow field of pure aluminum melt were investigated with the ANSYS in this paper. The simulation results indicate that the manner of the opposite electrode which is inserted from the side wall can produce more uniform and a wider range of flow field distribution. The analysis of numerical simulation provides a scientific basis for the further explanation of the mechanism of electric pulse refinement of metal solidification structure.

Acknowledgements

The authors gratefully acknowledge the financial supports from the National Basic Research Program of China (973 program) (Grant No.2011CB012902) and the National Natural Science Foundation of China (Grant Nos.11304194 and 50574056)

References

[1] R. W. Smith. “Electric field freezing,” Journal of Materials Science Letters, 1987, 6:643-644.
[2] A. K. Misra. “Effect of Electric Potentials on Solidification of Near Eutectic Pb-Sb-Sn Alloy,” Materials Letters, 1986, 4(3):176-177.
[3]H. Li, X. F. Bian, X. F. Liu, et al. “Influence of Current Density on Structure and Properties of Al Alloy,” Special Casting and Nonferrous Alloys, 1996(3):8-10.
[4] N. M, M. C. Flemings, “Modification of Solidification Structures by Pulse Electric Discharging,” ISIJ International, 1990, 30(1):27-33.
[5] H. C. Yan, G. H. He, B. L. Zhou, “Effect of Pulse Current on the Solidification Structure of Sn-Pb Alloy,” Acta Materialia Sinica, 1997, 33(4):352 -358.
[6] B. T. Zi, BA Q. X. Ba, CUI J. Z. Cui, et al. ,“The Solidification Structure of LY12 Aluminum Alloy with High Density Pulse Electric current,” special Casting and Nonfer rous Alloys, 2000, 4:4-6 .
[7] M. Gao, G. H. He, F. Yang, et al., “effect of strong electric current pulse on the properties of casting ZA27 alloy,” Chinese Journal of Materials Research, 2009, 16(1): 72-76.
[8] X. Z. Qing, C. H. Wang, Z. Y. Liao, et al., “effect of different electrode applying manner on Al-Si alloy solidification,” Journal of Inner Mongolia University of Science and Technology, 2012, 31(3): 279-283.
[9] K. Q. Chen, H. C. Wang, X. Z. Qing, et al., “Effect of Ways of Electrodes on Pure Copper Solidification Structure,” J. of Anhui University of Technology: Natural Science, 2013 (1): 11-15.
[10] J. Li, “Mechanism and Application of Metal Solidification Structure Refinement by Electric Current Pluse,” Shanghai：Shanghai University, 2009.
[11] Z. S. Xu, “The Effect of Parameters and Application Process on the Solidification Structure treated By Pulsed Electromagnetic Fields,” Shanghai: Shanghai University, 2014.

CFD Modeling and Simulation in Materials Processing 2016

Poster Session

CFD Modeling and Simulation in Materials Processing 2016
Edited by: Laurentiu Nastac, Lifeng Zhang, Brian G. Thomas, Miaoyong Zhu, Andreas Ludwig, Adrian S. Sabau, Koulis Pericleous, and Hervé Combeau
TMS (The Minerals, Metals & Materials Society), 2016

GAS-SOLID FLOW AND INJECTED GAS DISTRIBUTION IN OBF ANALYZED BY DEM-CFD

Zeshang Dong[1], Jingsong Wang[1], Jinzhou Liu[1], Xuefeng She[1], Qingguo Xue[1], Lin Lin[2]

[1]State Key Laboratory of Advanced Metallurgy, University of Science and Technology Beijing, Beijing 100083, PR China
[2]School of Mechanical Engineering, University of Science and Technology Beijing, Beijing 100083, PR China

Keywords: Oxygen blast furnace, DEM-CFD coupling mathematical model, Shaft gas injection, Gas-solid two phase flow, Gas penetration, Impact factors

Abstract

DEM-CFD coupled mathematical model of oxygen blast furnace (OBF) is established. Then it is applied to study the gas-solid flow in OBF. The effects of burden motion state, particle size, auxiliary tuyere size and the ratio of injected gas flow rate to total gas flow rate on the injected gas distribution were investigated in detail. The results show that there are 4 moving regions in the OBF. The high particles velocity corresponds to the high porosity in furnace, so the injected gas can penetrate into the center in moving bed more easily than fixed bed. Both decreasing particle size and increasing auxiliary tuyere area will increase the injected gas ratio at the edge, but decrease at the center. Calculation results also prove that the ratio of injected gas flow rate to total gas flow rate is crucial for the injected gas distribution in the furnace.

Introduction

In response to global warming, steel enterprises have to try to reduce the blast furnace (BF) carbon consumption. Oxygen blast furnace (OBF) as a new ironmaking process, was initially proposed by Wenzel [1] in 1970. Then some industrial experiments have been carried out, such as ULCOS in Europe [2] and experiment OBF in Japan [3]. These industrial tests proved the feasibility and advanced of this ironmaking process. DEM-CFD model [4] can be used for studying the gas-solid system such as BF. The utilization rate of the shaft injected gas of OBF is considered to be so important to realize the energy conservation and emissions reduction. The effect of injected gas flowrate, furnace profile and shaft tuyere position on the gas permeation has been studied [5-6]. But the specific manifestations of these factors are different. In previous studies some factors, especially the particle size and burden motion state were not taken into account. In connection with our previous cold model study [5], in this work the OBF DEM-CFD model is used for investigating the injected gas behavior in a large scale model. Then the basic characteristics of gas-solid flow in OBF is obtained. The difference of injected gas permeation distance between moving and fixed bed is studied. The influence of particle size, auxiliary tuyere size, ratio value of injected gas flowrate to total gas flowrate on gas permeation are examined.

Model Description

Discrete element method

Particle motion is described by Newton's second law. The model consists of spring and dashpot in the normal direction, spring, dashpot and slider in the tangential direction [7]. At any time t, the governing equations for particle i can be written as follows.

$$m_i \frac{d\mathbf{v}_i}{dt} = \sum_j (\mathbf{F}_{cn,ij} + \mathbf{F}_{dn,ij} + \mathbf{F}_{ct,ij} + \mathbf{F}_{dt,ij}) + m_i \mathbf{g} + \mathbf{F}_{pf,i} \quad (1)$$

$$I_i \frac{d\boldsymbol{\omega}_i}{dt} = \sum_j (\mathbf{M}_{t,ij} + \mathbf{M}_{r,ij}) \quad (2)$$

Where m_i, $\mathbf{v}_i$, and $\boldsymbol{\omega}_i$ are the mass, translational and rotational velocities of particle i, respectively. I_i is the moment of inertia of particle i. The forces involved are: the particle-fluid interaction force $\mathbf{F}_{pf,i}$. The normal and tangential contact forces $\mathbf{F}_{cn,ij}$ and $\mathbf{F}_{ct,ij}$, damping forces $\mathbf{F}_{dn,ij}$ and $\mathbf{F}_{dt,ij}$. The torque $\mathbf{M}_{t,ij}$ which is generated by the tangential force, and $\mathbf{M}_{r,ij}$ commonly known as the rolling friction torque.

Governing equations for gas phase

The DEM-CFD coupling module uses the existing Eulerian-Eulerian multiphase model. The conservation equation of solid part is not calculated by the CFD, but by the DEM. Then the solid particle data is transmitted to CFD. The gas phase was described by equations (3) and (4).

$$\frac{\partial \varepsilon \rho}{\partial t} + \nabla \bullet (\rho \varepsilon \mathbf{u}) = 0 \quad (3)$$

$$\frac{\partial \varepsilon \rho \mathbf{u}}{\partial t} + \nabla \bullet (\rho \varepsilon \mathbf{u}\mathbf{u}) = -\nabla p + \nabla \bullet (\mu \varepsilon \nabla \mathbf{u}) + \rho \varepsilon \mathbf{g} - \mathbf{S} \quad (4)$$

Where ε, ρ, $\mathbf{u}$, μ, and p denote the void fraction, density, velocity vector, viscosity and pressure of a fluid, respectively. The interaction force between fluid and particles was taken into account by the momentum sink S. The species transport governing equation (5) including CO and N_2 is added for considering the injected gas penetration behavior.

$$\overrightarrow{J_i} = -(\rho D_{i,m} + \frac{\mu_t}{Sc_t}) \nabla Y_i \quad (5)$$

Where Sc_t is the turbulent Schmidt number ($\frac{\mu_t}{\rho Sc_t}$ where μ_t is the turbulent viscosity and D_t is the turbulent diffusivity). The default Sc_t is 0.7.

Particle–Fluid Interaction

Porosity and particle motion state in a packed bed are obtained by DEM analysis. The pressure drop is expressed by the multidimensional Ergun's equation for a packed bed. The drag force on the individual particles is calculated using the Ergun and Wen & Yu [8-9] drag model.

Simulation Conditions and Procedure

The geometry and computational grid used in this work is shown in Figure 1. It doesn't include the hearth bottom which contains hot liquid. The furnace is axisymmetric, so only half of it is selected. The slot model's size is 0.4 m width which is set to at least 4 particles diameter [10].
The simulation is started with the random generation of coke and ore particles without overlaps. The volume ratio of ore and coke is 1:1. For representing the BF operation, the particles are removed at a specified rate from the raceway and added back onto the top in order to keep the burden surface constant. Then the coupled calculation starts. Pure N_2 is blown from the hearth tuyere, CO is from shaft tuyere. When the top CO concentration keeps constant, stop calculating. Coke and ore particle parameters are listed in **Table Ⅰ**.

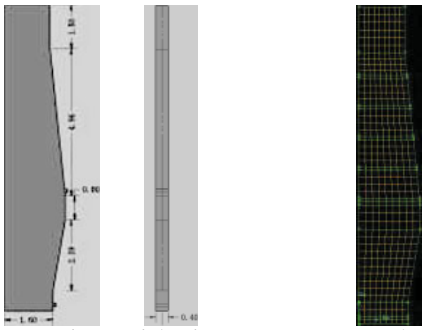

Front view Right view Mesh
(a) (b)

Figure 1. (a) BF geometry used in this work (m); (b) Computational grid for gas phase solution.

Table Ⅰ. Particles properties and conditions used in this work

Variables	Base
Particle shape	Spherical
Number and diameter(mm) of	Variable
Coke and ore particle density	1100,
Material Poisson's ratio	0.25
Material shear modulus (pa)	1.0×10^{8}
Particle-particle/wall restitution	0.3
Particle-particle/wall static friction	0.4
Particle-particle/wall rolling friction	0.05
DEM Time step (s)	5×10^{-5}

The determination of solid discharging rate in the simulation is based on the modified Froude number Fr_S [11] at the BF throat. The parameter for gas flowrate is determined according to the Reynolds number [4] at the BF throat.

$$Fr_S = \frac{\rho}{\rho_S - \rho} \bullet \frac{u_s^2}{gR} \tag{6}$$

$$\mathrm{Re} = \frac{2R\rho U_f}{\mu} \tag{7}$$

Where U_S, U_f, ρ_S, ρ is the particle descending velocity, gas superficial velocity, burden bulk density and gas density at the furnace throat. In practical BF [4], the Fr_S is around 10^{-8}-10^{-9}, U_f is about 2-3 m/s, and the Reynolds number is about 10^3-10^4. In order to reduce the DEM calculation time, the burden descending velocity is accelerated. This treatment has been found to be acceptable in a BF [10]. In this work, the Fr_S is set to 1.44×10^{-5}, the gas superficial velocity is kept at 2.5 m/s, correspondingly the Reynolds number is 1.67×10^4. The total gas flowrate is about 1500 L/s. Some simulation conditions are shown in **Table II**. The shaft tuyere size under No.3 is 100×400 mm if there is no special notes.

Table II. Simulation conditions

Particle diameter (mm)	Shaft tuyere size	No.	N_2 flowrate-V (L/s)	CO flowrate-U (L/s)	Particle motion	U/(U+V)
100	100×400	1	1200	300	Moving bed	0.2
	100×400	2	1000	500	Fixed bed	0.33
	(50~200)×400	3	1000	500	Moving bed	0.33
	100×400	4	900	600	Moving bed	0.4
	100×400	5	600	900	Moving bed	0.6
	100×400	6	300	1200	Moving bed	0.8
80, 60, 40	100×400	7, 8, 9	1000	500	Moving bed	0.33
-	100×400	10	1000	500	Empty	0.33

Simulation Results

Model validity

Figure 2 is the CO concentration distribution level in the shaft part under No.3 case. There is a horizontal black line at the 1 m above the shaft tuyere level as shown in Figure 2(a). The CO concentration on this line is shown in Figure 2(b). Figure 2(a) shows that injected gas can penetrate close to the center with the increase of the shaft position. This phenomenon is interpreted as eddy diffusion effects [6], which is caused by the gas irregular turbulent diffusion in the radial direction. Figure 2(b) shows the gas can easily penetrate to the center without the bed resistance. This simulation result is consistent with the cold model result [5].

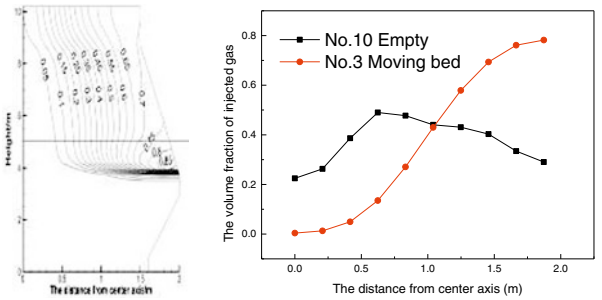

(a) (b)

Figure 2. Injected gas distribution in the shaft

Figure 3 shows the granular flow schematic under steady state: (1) Two-dimensional physical model result [12], (2) Mathematical model result (No.3). It proves that the difference of burden descending behavior between OBF and TBF is little. It can also be divided into four regions in OBF: (1) Stagnant zone, (2) Plug flow region, (3) Converging flow zone, (4) Quasi-stagnant zone. The above phenomenon is basically in consistent with the literature [10, 12] results.

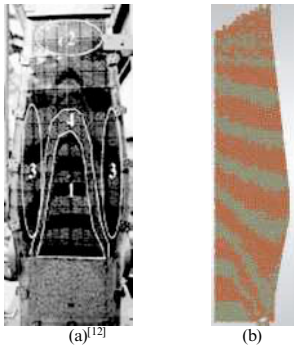

(a)[12] (b)

Figure 3. Particle movement characteristics in BF

Particle move state and its effects on the gas permeability

Figure 4 shows the gas infiltration in the shaft parts under No. 2 and No. 3 cases. It is assumed that the zone where the injected gas volume fraction is below 0.05 is the rising gas dominant area. From Figure 4 it can be seen that radius of this region is 0.68 m in fixed bed, 0.41m in moving bed. In moving bed this area decreases significantly. This phenomenon has been explained in the following reason [4], the porosity distribution is related to the flow of particles: the high velocity corresponds to the high porosity. Generally, the region with the high porosity must derive from the fast motion of particles. This is a good explanation of why the injected gas is more difficult to penetrate in fixed bed which owns the higher burden resistance.

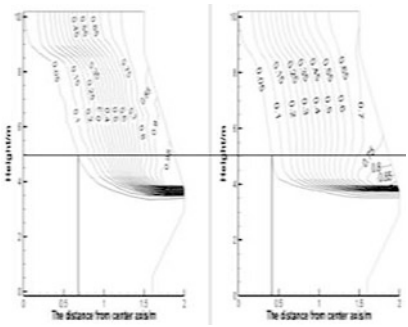

(No.2) (No.3)

Figure 4. Gas infiltration in the shaft parts under the different conditions

The influence of particle size on gas permeability

Figure 5 shows the gas diffusion at 1 m above the shaft tuyere level under different particle size conditions. The U/(U+V) is 0.33 under above cases. It can be seen that the change relationship between injected gas concentration at edge and center is reciprocal. When the particle size is reduced, the injected gas concentration of central region decreased, but increased at the edge. This is mainly because the more particles, the more gas flow channel, the injected gas can easily spread around. It causes that horizontal inertial force of the injected gas decreases rapidly. In addition the lift force from the rising gas prevents the injected gas from diffusing to the center zone, so it gathers on the edge. Into practice there are more particles in the BF, so it will be more difficult for injected gas to penetrate to the center, injected gas is easily gathered near the shaft wall. It will bring bad effect on the gas utilization and preheating burden in shaft, but as mentioned before the eddy diffusion effects will alleviate the adverse impact.

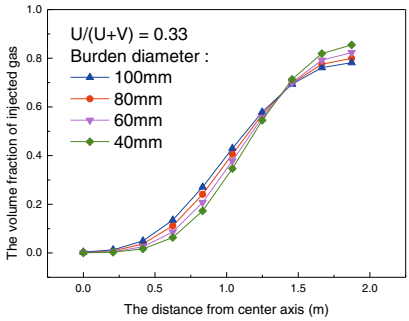

Figure 5. Gas penetration under different radius of burden 1m above the auxiliary tuyere

The influence of auxiliary tuyere size of gas penetration

Figure 6 shows the gas distribution under different tuyere size 1m above the auxiliary tuyere. With the increase of blast kinetic energy the injected gas can be more deeply into the shaft center area. The effect of blast kinetic energy is not significant in previous cold model results [5]. This is mainly because the stability of experiment equipment, measurement error and accuracy. The gas concentration difference at the edge under above conditions is bigger than concentration difference near the center zone. So the effect of blast kinetic energy on the gas concentration on the edge is much bigger than the center. This is different with the influence of particle size (Figure 5). If the injected gas amount is stable, the gas is more easily to gather near the shaft wall under the lower gas velocity. So in practice, the blast kinetic energy can be increased to improve the depth of penetration of the injected gas.

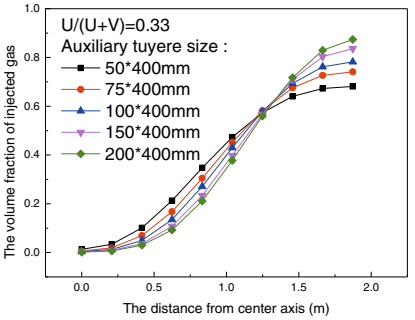

Figure 6. Gas penetration under different tuyere size 1m above the auxiliary tuyere

The influence of U/(U+V) on the injected gas penetration

Figure 7 shows the influence of U/(U+V) on the injected gas distribution at 1m above the auxiliary tuyere. The total amount (U+V) of the furnace gas remain unchanged. This result is similar with the cold model result [5]. Relative to the effect of particle size (Figure 5) and tuyere size (Figure 6), the value of U/(U + V) is a decisive role for the injected gas distribution in the furnace. If the tuyere size remains the constant, the injected gas horizontal total momentum increases with the increase of flowrate. In summary under the constant tuyere size condition if the injected gas flowrate increases, the penetration of the gas can be improved to a great extent. The heat utilization and chemical utilization of the injected gas can be improved also. But considering the BF operation, the numerical value of U/(U+V)remains at about 0.5 is optimal.

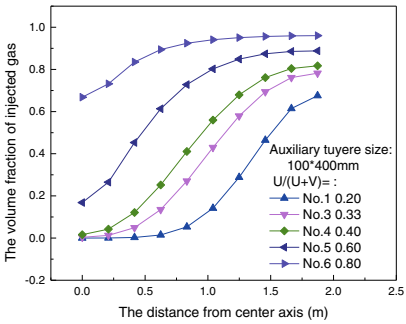

Figure 7. Influence of U/(U + V) on the injected gas distribution in the shaft

Conclusions

(1) The burden descending in OBF can also be divided into four regions. The injected gas is more difficult to penetrate in fixed bed than in the moving bed.
(2) Both reducing the particle size and gas velocity will make the gas concentration increased at the shaft edge and decreased at center. But the impact effect is different: the effect of gas velocity on the edge zone gas concentration is more obvious than center. The influence of particle diameter on each part is similar.
(3) Calculation results also prove that the ratio of injected gas flowrate to total gas flowrate is crucial for the injected gas distribution in furnace.

Acknowledgements

The authors are gratefully acknowledge the support of the Key Project of National Natural Science Foundation of China (No. 51134008).

References

1. W. Wenzel., GER, 2030468.1[P]. 1970, pp.20.
2. K. Meijer et al., "ULCOS: ultra-low CO_2 steelmaking," Ironmaking & Steelmaking, 36 (4) (2009), 249-251.
3. Y. Ohno et al., "Process Characteristics of a Commercial-scale Oxygen Blast Furnace Process with Shaft Gas Injection-up," ISIJ international, 32 (7) (1992), 838-847
4. Z.Y. Zhou et al., "Discrete particle simulation of gas–solid flow in a blast furnace," Computers & Chemical Engineering, 32 (8) (2008), 1760-1772.
5. J.Z. Liu et al., "Injected gas distribution in oxygen blast furnaces with shaft gas injection," Journal of University of Science and Technology Beijing, 36 (6) (2014), 817-823 (in Chinese)
6. S. Natsui et al., "Penetration Effect of Injected Gas at Shaft Gas Injection in Blast Furnace Analyzed by Hybrid Model of DEM-CFD," ISIJ international, 51 (9) (2011), 1410-1417.
7. R.D. Mindlin, "Elastic spheres in contact under varying oblique forces," Journal of Applied Mechanics, 20 (1953), 327-344

8. Ergun, “Fluid flow through packed columns,” Chemical Engineering Progress, 48 (2) (1952), 89-94.
9. C.Y. Wen and Y.H. Yu, “Mechanics of fluidisation. Chemical Engineering Program Symposium Series,” 62 (62) (1966), 100.
10. Z.Y. Zhou et al., “Discrete particle simulation of solid flow in a model blast furnace,” ISIJ international, 45 (12) (2005), 1828-1837.
11. M. Ichida et al., “Influence of ore/coke distribution on descending and melting behavior of burden in blast furnace,” ISIJ international, 31 (5) (1991), 505-514.
12. B. Wright et al., “Gas–solid flow in an ironmaking blast furnace-I: Physical modelling,” Powder Technology, 208 (1) (2011), 86-97.

CFD Modeling and Simulation in Materials Processing 2016
Edited by: Laurentiu Nastac, Lifeng Zhang, Brian G. Thomas, Miaoyong Zhu, Andreas Ludwig, Adrian S. Sabau, Koulis Pericleous, and Hervé Combeau
TMS (The Minerals, Metals & Materials Society), 2016

IMPROVING CURRENT EFFICIENCY THROUGH OPTIMIZING ELECTROLYTE FLOW IN ZINC ELECTROWINNING CELL

Hongdan Wang, Wentang Xia, Wenqiang Yang, Bingzhi Ren

School of Metallurgy and Material Engineering, Chongqing University of Science and Technology, Chongqing 401331, China

Keywords: Zinc electrowinning, Current efficiency, Numerical simulation, Fluid flow

Abstract

In zinc electrowinning process, electrolyte flow in the cell has an important influence on current efficiency. In this article, a 3D mathematical model has been developed and solved by ANSYS FLUENT software to study the flow field and residence time distribution (RTD) of the electrolyte in the zinc electrowinning cell. According to the RTD analytical theory, the influence of different feeding schemes on electrolyte flow pattern has been investigated, and the optimum feeding scheme was obtained. Zinc electrolysis experiments show current efficiency was increased significantly at the optimum feeding scheme.

Introduction

Zinc hydrometallurgy has been the dominant technology of the present extractive metallurgy of zinc metal, and its production accounts for more than 80% of the total quantity [1]. However, there is a shortage of high energy consumption for zinc hydrometallurgy, and about 75% of the total energy consumption occurs in zinc electrowinning [1]. Therefore, the key of saving energy and improving economic efficiency for zinc hydrometallurgy is to reduce power consumption during the zinc electrowinning process. In recent years, numerous measures have been taken to decrease cell voltage and increase current efficiency, such as a reasonable current density, acid zinc ratio, electrolyte temperature, surfactant as well as high purity electrolyte and small distance of electrodes [2-12]. From the kinetic analysis of zinc electrowinning, electrolyte flow is the main driven force of ion motion and also can take away reaction heat in the zinc electrowinning cell. And therefore, to enhance electrolyte flow is of great importance to reduce power consumption during zinc electrowinning process [1].

Li et al. [13] carried out tracer experiments on a zinc electrowinning cell and the residence time distribution of the electrolyte was obtained. The analysis indicated that electrolyte flow was mainly made of mixed flow, and there was "dead zone" in the electrode region. Thus the current recirculation pattern of the electrolyte was not conducive to mass and heat transfer in the cell. Wang [14] investigated the electrolyte flow in an operating zinc electrowinning cell with a combination of physical and mathematical simulation and found there were dead zones in the cell. Su and Li [1, 15] conducted detailed mathematical simulations of single-phase flow of the electrolyte and gas-liquid flow in an operating zinc electrowinning cell, and proposed the interelectrode effective flow rate (IEFR) to evaluate quantitatively the characteristics of the electrolyte flow. In this work, a 3D mathematical model was used to simulate the electrolyte

flow and residence time distribution in a zinc electrowinning cell with five feeding schemes, and the corresponding zinc electrolysis experiments were carried out.

Feeding Schemes of Zinc Electrowinning Cell

The zinc electrowinning cell used in laboratory research is cubic structure. Three sets of anode and cathode could be arranged, and there are five inlets and one outlet. The inlet number 0 and the outlet are located on two opposite faces of the cell, which is the traditional feeding scheme. Four other inlets (number 1 to 4) are in vertical direction with the inlet number 0. The thesis intends to investigate the influence of five different feeding schemes on the electrolyte flow and residence time distribution in the zinc electrowinning cell. The five detailed feeding schemes are shown in Table I, and its physical model is depicted in Figure 1. A set of anode and cathode is merely placed in the zinc cell, and the four new inlets are located between the electrodes.

Table I. Five Feeding Schemes of Zinc Electrowinning Cell

Scheme	Feeding way	Inlet flow rate
I	0#	0#: 2.0L/min
II	0#, 1#	0#: 1.5L/min, 1#: 0.5 L/min
III	0#, 2#	0#: 1.5L/min, 2#: 0.5 L/min
IV	0#, 3#	0#: 1.5L/min, 3#: 0.5 L/min
V	0#, 4#	0#: 1.5L/min, 4#: 0.5 L/min

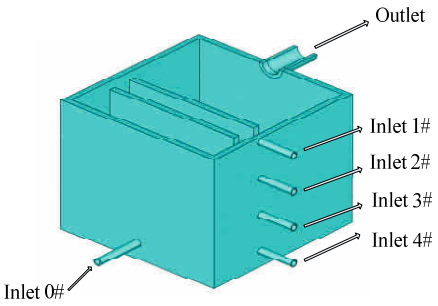

Figure 1. Structure of zinc electrowinning cell.

Mathematical Model

Assumption

This paper mainly deals with the electrolyte flow in the zinc electrowinning cell. In order to simplify the mathematical model, the electrolyte temperature and density, zinc electrolytic deposition, external electric field as well as bubble motion were neglected in the calculation of the electrolyte flow, and the flow field is considered as steady state.

Governing Equations

The electrolyte flow in the zinc electrowinning cell following the mass and momentum conservation laws can be described by

Continuity equation

$$\frac{\partial u_i}{\partial x_i} = 0 \tag{1}$$

where u_i is the i component of the velocity, x_i is the i spatial coordinate.

Momentum equation

$$\frac{\partial}{\partial t}(\rho u_i) + \frac{\partial}{\partial x_j}(\rho u_i u_j) = -\frac{\partial P}{\partial x_i} + \frac{\partial}{\partial x_j}\left[(\mu + \mu_t)\left(\frac{\partial u_i}{\partial x_j} + \frac{\partial u_j}{\partial x_i}\right)\right] + \rho g_i \tag{2}$$

where ρ is the density of the electrolyte, and its value is 1228kg/m^3; p is the pressure; g is the acceleration of gravity; μ_t represents the turbulent viscosity determined by the standard k-ε turbulent model [16]; while μ is the viscosity of the electrolyte , and its value is 0.00397Pa·s.

Mass conservation equation

The RTD analysis means that the fluid flow characteristics in the reactor are investigated according to the RTD curve obtained by stimulus-response technique, which needs to solve the mass conservation equation

$$\frac{\partial}{\partial t}(\rho c) + \frac{\partial}{\partial x_j}(\rho u_j c) = \frac{\partial}{\partial x_j}\left((\mu + \mu_t)\frac{\partial c}{\partial x_j}\right) \tag{3}$$

where c is the concentration of the electrolyte.

Solution Method

The boundary condition of the inlet is set to velocity-inlet. Since the outlet is in the atmosphere, its boundary condition is defined as pressure-outlet and the gauge value is 0 Pa. The liquid surface is set to wall boundary and the specified shear value is 0. The walls of the cell and electrodes are specified as no slip boundary and wall function is used.

A RTD curve can be obtained by stimulus-response technique based on steady-state flow condition in the zinc electrowinning cell. First, the tracer was injected into the electrolyte flowing through the inlet of the zinc cell and its mass fraction was set to 1. After 0.5 second, tracer concentration at inlet became 0. Then in the solution of response, the instantaneous concentration of the tracer as a function of time at outlet was monitored, and then the RTD curve was obtained.

The flow field and residence time distribution of zinc electrolytic cell were simulated by ANSYS FLUENT software. SIMPLE algorithm was adopted and residuals were set to 10^{-4}.

Results and Discussion

Flow Field Analysis

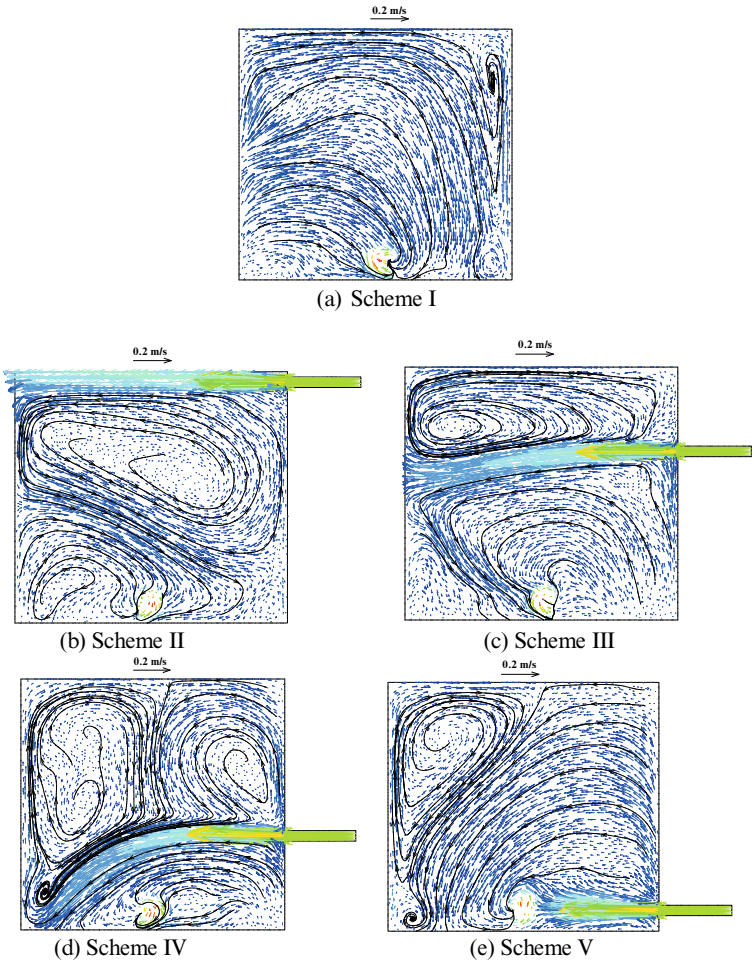

(a) Scheme I

(b) Scheme II

(c) Scheme III

(d) Scheme IV

(e) Scheme V

Figure 2. Velocity distribution between the anode and cathode in zinc electrowinning cell.

In zinc electrowinning, zinc metal is electrodeposited at the cathode and oxygen gas is produced on the anode. The main reaction occurring at the cathode is the conversion of the zinc ions to a metallic state via an electron transfer process. Therefore, the electrolyte flow between the anode and cathode has an important influence on zinc electrolytic deposition reaction. Figure 2 demonstrates the velocity distribution of the electrolyte between the anode and cathode. The flow pattern between the electrodes of five feeding schemes are obviously different. In line with enhancing the electrolyte flow between the anode and cathode, accelerating the electrolyte refresh, reducing the depletion of zinc ion near the cathode, the flow characteristic of feeding scheme III is better than other schemes. Under the mutual effects of the two inlet flows, two recirculating flows are formed between the anode and cathode, which will help renew electrolyte and promote electrolytic deposition.

Residence Time Distribution Analysis

Figure 3 demonstrates the RTD curves calculated in the zinc electrowinning cell with five feeding schemes. From the RTD curves, mean residence time and dead volume fraction can be obtained for every scheme. The flow characteristics in the zinc cell obtained from the RTD curves are given in Table II. It can be known that the longest mean residence time and the smallest dead volume fraction were presented in the feeding scheme III due to better flow field of the electrolyte between the anode and cathode.

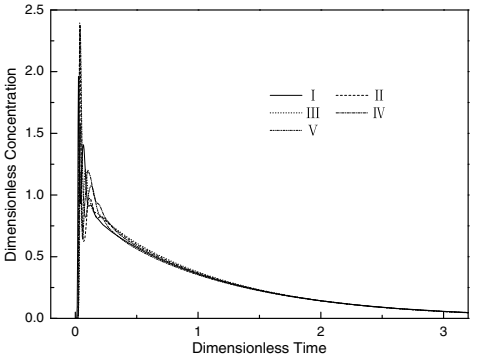

Figure 3. RTD curves in the zinc electrowinning cell with five feeding schemes.

Table II. Fluid Flow Characteristics in the Zinc Electrowinning Cell with Five Feeding Schemes

Feeding scheme	Mean residence time, s	Dead volume fraction, %
I	56.6	41.95
II	57.1	39.76
III	58.8	38.82
IV	57.5	40.17
V	56.1	41.78

Experimental Results of Zinc Electrolysis

Metallic zinc is extracted from the purified zinc sulphate solution and sulphuric acid by electrolysis using aluminium cathodes and lead anodes. According to the simulated feeding schemes, zinc electrolysis experiments were carried out. Table III shows current efficiency during zinc electrowinning process at different feeding schemes. Yet compared to the traditional feeding scheme I, current efficiency of three new feeding schemes have enhanced greatly. In particular for feeding scheme III, current efficiency was increased to 98.90%. Experimental results reveal the strengthening of electrolyte flow between the cathode and anode by changing feeding scheme could help transport zinc ions to the cathodes and discharge heat of reaction, which is very effective for enhancing current efficiency.

Table III. Current Efficiency of Zinc Electrowinning with Five Feeding Schemes

Feeding scheme	Current efficiency (%)
I	89.85
II	96.84
III	98.90
IV	97.98
V	90.10

Conclusions

Flow characteristics of the zinc electrowinning cell with five feeding schemes have been numerically investigated. A number of important conclusions are obtained through the analysis of electrolyte flow and residence time distribution as well as zinc electrolysis experimental results. Since a large part of the electrolyte flows directly into the electrodes by changing feeding scheme, the electrolyte flow between the cathode and anode has been strengthened. This better flow will help transport zinc ions to the cathodes and discharge heat of reaction. Ultimately, current efficiency could be increased. In the next study, the influences of other feeding schemes and flow rate on current efficiency will be investigated in order to guide production effectively.

References

1 Y.B. Su, "Numerical Simulation and Optimization for the Flow Field of the Zinc Electrowinning Cell" (Master dissertation, Central South University, 2012), 6-63.

2 A.C. Scott, R.M. Pitblado, and G.W. Barton, "A Mathematical Model of a Zinc Electrowinning Cell" (Paper presented at the Twentieth International Symposium on the Application of Computers and Mathematics in the Mineral Industries, Johannesburg, October 1987), 51-62.

3 T.F. Parada and E. Asselin, "Reducing Power Consumption in Zinc Electrowinning," *JOM*, 61 (10) (2009), 54-58.

4 M. Mahon, L. Wasik, and A. Alfantazi, "Development and Implementation of a Zinc Electrowinning Process Simulation," *Journal of the Electrochemical Society*, 159 (8) (2012), D486-D492.

5 M. Michael, P. Spencer, and A. Akram, "Application and Optimisation Studies of a Zinc Electrowinning Process Simulation," *Canadian Journal of Chemical Engineering*, 92 (4) (2014), 633-642.

6 D. Majuste et al., "Role of Organic Reagents and Impurity in Zinc Electrowinning," *Hydrometallurgy*, 152(2015), 190-198.

7 Sh. Nakisa, N.P. Ahmadi, and J. Moghaddam, "Electrochemical Study of Pb Anodes for Zinc Electrowinning Industry," *Surface Engineering*, 30 (9) (2014), 650-655.

8 B. Behnajady, A.A. Balesini, and J. Moghaddam, "A New Approach to the Optimisation of Zinc Electrolyte Cold Purification Process by Taguchi's Method," *Canadian Metallurgical Quarterly*, 53 (3) (2014), 333-339.

9 V.M. Alkatsev, M.I. Alkatsev, and V.A. Lin'kov, "Influence of Impurities in Electrolyte (Tin, Germanium, and Antimony) on Current Efficiency within Electrowinning of Zinc," *Russian Journal of Non-ferrous Metals*, 55 (4) (2014), 327-330.

10 L. Li and F.X. Yao, "Practice of Reducing DC Power Consumption in Zinc Electrolysis Production," *Energy Saving of Nonferrous Metallurgy*, (3)2012, 18-20.

11 Y.X. Zhu, "Production Practice on Reducing the Unite Loss of Zinc Electrolytic DC Current," *Hunan Nonferrous Metals*, 23 (3) (2007), 23-25, 80.

12 W. Li, "Study on Energy Waving in Zinc Electrolysis," *Hunan Nonferrous Metals*, 21 (1) (2005), 17-20.

13 X.W. Li and X.M. Li, "Study on Electrolyte Flow in Zinc Electrowinning Cell" (Paper presented at the 6_{th} National Physical Chemistry of Metallurgical Processing Annual Conference, Chongqing, China, 16 December 1986), 70-74.

14 J.W. Wang, "Hydraulic and Numerical Simulation of Electrolyte in Zinc Electrolytic Bath" (Master dissertation, Kunming University of Science and Technology, 2011), 1-66.

15 H.L. Li et al., "Optimization of Operating Conditions and Structure Parameters of Zinc Electrolytic Cell Based on Numerical Simulation for Electrolyte Flow," *Transactions of Nonferrous Metals Society of China*, 24 (5) (2014), 1604-1609.

16 J.J. Wang, Y.P. Bao, and Y. Qu, *Tundish Metallurgy* (Beijing, Bj: Metallurgical Industry Press, 2001), 199-200.

CFD Modeling and Simulation in Materials Processing 2016
Edited by: Laurentiu Nastac, Lifeng Zhang, Brian G. Thomas, Miaoyong Zhu, Andreas Ludwig, Adrian S. Sabau, Koulis Pericleous, and Hervé Combeau
TMS (The Minerals, Metals & Materials Society), 2016

INFLUENCE OF HEAVY REDUCTION (HR) ON THE INTERNAL QUALITY OF THE BEARING STEEL GCr15 BLOOM

Cheng Ji, Chen-hui Wu, Miao-yong Zhu

School of Metallurgy, Northeastern University of China; Shenyang, Liaoning, 110819, China

Keywords: Heavy reduction, Bloom continuous casting, Central segregation and porosity, Bearing steel GCr15

Abstract

Heavy reduction (HR) is an effective method to improve the homogeneity and compactness of slab and bloom with large section size. In the present work, the key technologies of bloom heavy reduction including online detection of strand solidification end, online calculation of minimum reduction amount, enhanced final electromagnetic stirring (F-EMS) and convex roll with curving surface were introduced. The plant results after the HR application showed that the center segregation and porosity of GCr15 steel bloom and rolled bar were reduced effectively, and its internal quality meet the requirement of rolling large size bars and profiles successfully.

Introduction

Heavy reduction (HR) was developed based on the soft reduction (SR) technology, and the compactness of the slab or bloom with large section size could be improved effectively by means of increasing reduction amount. The principle of HR is to impose a large reduction rate/amount on the solidification end of the strand for healing the solidification shrinkage cavity and improving center density without creating cracks.

In the early 1990s, Kawasaki Steel Corp. had proposed the continuous forging process to prevent center porosity for heavy plate production[1], which the slab was reduced greatly with a pair of anvils located before the solidification end. More and more researchers had realized that the heavy reduction in the solidification end could improve porosity significantly. Nippon Steel presented NS Bloom Large Reduction Technology[2], which applied a large reduction amount after complete solidification by a pair of convex-shaped rolls. The reduction energy could be concentrated onto the bloom center, and the center porosity could be reduced efficiently. Sumitomo Metal Industries developed its HR method also, named PCCS (Porosity Control of Casting Slab)[3,4]. In the PCCS technology, center porosities could be effectively decreased by the large roll reduction on the slab just before complete solidification, and the very thick plates have been manufactured through caster-rolling line. In these typical HR methods, the HR position was usually fixed on the strand, and the quality of the slab or bloom could not be improved in any case, because the solidification end is usually changed with the varying of the casting speed and the different casting steel grade. Therefore, POSCO provided a kind of flexible HR method, which was executed by segment in the strand solidification end[5]. The maximum reduction rate of the slab by the segment was 30 mm/min. Zhang et al[6,7] present a new HR approach, named Heavy Reduction Process to Improve Segregation and Porosity (HRPISP), and

they simulated the deformation and dynamic recrystallization (DRX) behavior on the extra-thickness slab HR process by using software THERCAST.
In this paper, the bloom HR technology developed by Northeastern University of China were introduced, and the bearing steel GCr15 was chosen as specific research steel to illustrate the key technologies and their application. The main composition of GCr15 steel is 1.00 Wt Pct C, 0.25 Wt Pct Si, 0.30 Wt Pct Mn, 0.01 Wt Pct P, 0.01 Wt Pct S, and 1.45 Wt Pct Cr. The plant results showed that after the application of HR to the GCr15 bloom, the center segregation and porosity were improved significantly, and the bloom could meet the requirement for rolling larger size GCr15 bars and profiles with the lower rolling reduction ratio.

Key Technologies of Heavy Reduction

Online Detection of Strand Solidification End

Accurate on-line determination of strand solidification end is the basis of heavy reduction. The main methods of solidification end on-line prediction or determination included real-time heat transfer calculation[8], force sensor detection[9], and ultrasonic detection[10]. The ultrasonic detection method was not applied in practice successfully due to the bad contact between the bloom surface and the probe. The real-time calculation method was the most popular method for prediction solidification end, but it is difficult to ensure the accuracy due to the inexact boundary condition and material properties parameters. In the authors' previous work[11], in order to improve the accuracy of simulation results, the material properties were derived by weighted averaging of the phase fractions, and the boundary conditions were obtained by realistic water flux distribution on the slab or bloom surface.
Figure 1 shows the measured tensile strength of the GCr15 bloom by Gleeble 3800. It can be seen that the tensile strength of the GCr15 bloom decreases sharply when the temperature increases from 700ºC to 1000ºC, and the strength is lower than 30MPa when the temperature is higher than 1000ºC. The deformation-resistant ability of the bloom mainly depends on the solidified shell thickness, and the relationship between the stress and the HR amount depends on the shell thickness as well. Figure 2 shows the actual measured reduction amount and pressure of the different withdrawal units during the GCr15 bloom continuous casting process. With the pressure increasing, the reduction amount increased on a quadratic function approximately. Under the same pressure, the reduction amount of second to eighth withdrawal unit became smaller and smaller due to the increasing shell thickness.

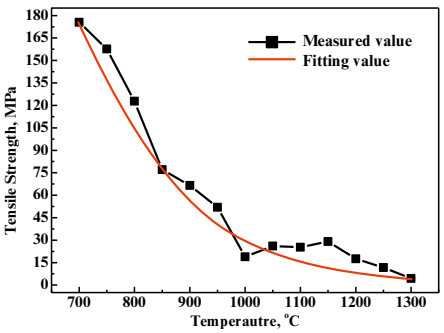

Figure 1. The measured tensile strength of GCr15 bloom

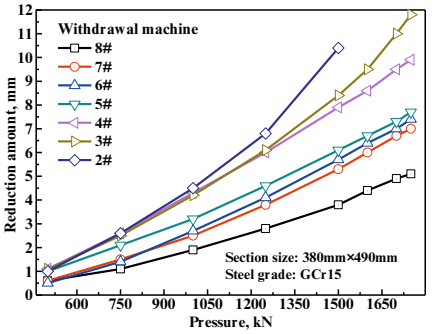

Figure 2. The measured reduction amount and pressure of different withdrawal unit

Figure 3 shows the online detection method of the strand solidification end. The main purpose of left part is to derive the relation ship between the HR amount, HR pressure and the shell thickness based on the measured results as Fig. 2, the nail shooting results and the FEM simulation results[12]. On the right part, combined with the real-time heat transfer simulation results and the online measured HR amount and pressure of each withdrawal unit, the strand solidification end and shell thickness could be detected accurately.

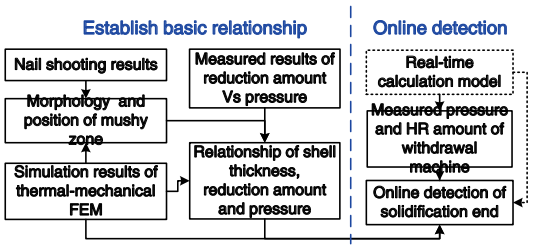

Figure 3. The online detection method of the strand solidification end

Online Calculation of Minimum Reduction Amount

In the bloom continuous casting process, the HR is usually executed by 6-10 withdrawal units which are arranged in the air cooling zone with intervals of 1.0–3.5 m. Therefore the reduction interface is discontinuous, and the reduction amount is generally selected as the primary control parameter. Based on the solidification shrinkage compensation principle, a calculation method for SR amount is derived in the authors' previous work[13]. In order to improve the compactness of bloom, the reduction amount should be higher than the compensation amount of solidification shrinkage in the HR process. Therefore, the minimum reduction amount could be calculated as:

$$R_i = \frac{\Delta A_i}{\eta_i \cdot X_i} = \frac{\left(\int_0^{Y_i} \int_0^{X_i} \rho(x, y, z_i)\,dxdy - \int_0^{Y_{i-1}} \int_0^{X_{i-1}} \rho(x, y, z_{i-1})\,dxdy \right)}{\rho_l \cdot \eta_i \cdot X_i} \quad (1)$$

where, R_i is the minimum reduction amount for i^{th} withdrawal unit, m; ΔA_i is the solidification shrinkage area between the i^{th} and i-1^{th} withdrawal unit, m^2; X_i is the bloom width under i^{th} withdrawal unit, m; η_i is reduction efficiency under i^{th} withdrawal unit; $\rho(x, y, z)$ is steel density function which is related to temperature; ρ_l is steel density at liquidus temperature, kg/m^3; x, y and z are width, thickness, and length of the bloom, respectively.

In Equation (1), the reduction efficiency is defined to characterize the relationship between bloom surface reduction amount and the required reduction amount of the shrinkage volume, and it was derived by thermal-mechanical FEM simulation method[12,14] and stored on the database for online calling. The solidification shrinkage area depends on the mass distribution of the bloom transverse section, which could be calculated according to the strand temperature distribution[13]. Therefore, the minimum reduction amount could be online calculated based on the real-time heat transfer calculation results.

Figure 4 shows the solidification shrinkage area with the different casting speed for the 370 mm × 490 mm GCr15 bloom, and the corresponding derived minimum reduction amount are listed in Table I. The solidification shrinkage area are increased almost linearly with the strand position increasing. With the casting speed increasing, more units participate in the reduction process due to the extended mushy zone, and the total minimum reduction amount decreases due to the increasing of reduction efficiency.

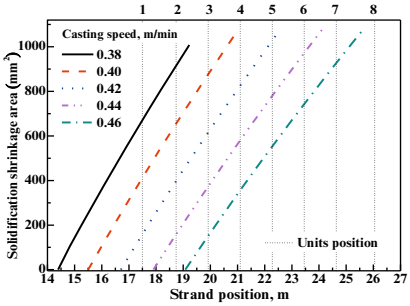

Figure 4. Solidification shrinkage area for 370 mm × 490 mm GCr15 bloom

Table I. Minimum reduction amount for 370 mm × 490 mm GCr15 bloom

Casting speed (m/min)	HR amount							
	2#	3#	4#	5#	6#	7#	8#	Tatol
0.38	8.2	11.1						19.3
0.40	3.7	6.0	8.0					17.8
0.42	2.5	2.6	3.1	5.1	5.9			18.2
0.44		1.7	2.5	3.5	5.2	5.5		17.3
0.46			1.4	1.9	2.5	5.5	5.7	16.0

Enhanced Final Electromagnetic Stirring (F-EMS)

The solute-enriched liquid steel would flow back to the lower solicitation fraction area due to the HR process, and in order to homogenize the solute distribution the final electromagnetic stirring should be installed before the reduction area. However, according to the research by Takahashi et

al.[15], the dendrites begin to form network and block liquid flow when the solid fraction becomes equal to 0.31, and more powerful electromagnetic force is required to drive the liquid flow in this area. Therefore, the Gramme winding was adopted to ensure the uniformity of internal magnetic field, and in order to homogenize solute and temperature effectively the center magnetic intensity should be higher than 100mT with the frequency of 6-10Hz.
Figure 5 shows the effect of F-EMS on the liquid flow and center temperature of the mushy zone for 160mm square 82B steel billet[16]. As the F-EMS applied, the nature convection mechanism is destroyed in mushy zone, and the tangential velocity of molten steel rises and the center temperature decreases evidently.

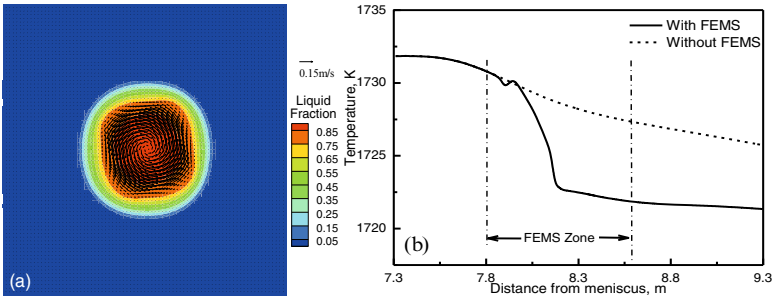

Figure 5. Flow field (a) and temperature field (b) of bloom cross section on the FEMS zone

Convex Roll with Curving Surface

The deformation-resistance of the bloom mainly depends on the completely solidified shell of the bloom both side. The convex roll could avoid the bloom side areas during the HR process, and the reduction efficiency could be improved than that of flat roll significantly. Nippon Steel[2] and POSCO[17] had applied convex roll in the bloom continuous casting process successfully. However, the previous convex roll usually had a directly embossment as shown in Figure 6, and the strain and stress concentrated on the edge of roll-bloom contact area which was prone to cause the surface and subsurface cracks defect. In order to avoid crack defects, a new type of convex roll with curving surface was presented and its profile is shown in Figure 6.
The bloom after HR reduction with convex roll was shown in Figure 7, and it is clearly that the edge of pressed dent on the bloom surface is gentle. After the HR application on the 370 mm × 490 mm GCr15 bloom, the reduction amount with convex roll was about 10 mm when the pressure of the fifth units was 1100kN, and that of the flat roll was no more than 4 mm under the same condition.

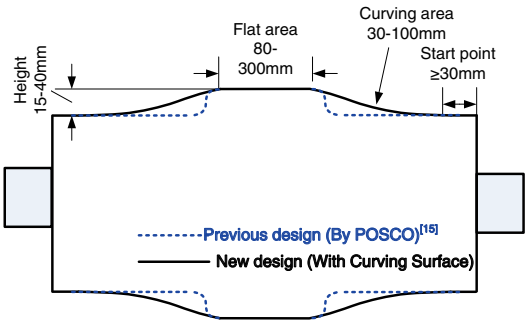

Figure 6. Sketch of convex roll with curving surface

Figure 7. The bloom after HR with convex roll

Application results

In the present work, the HR technology was applied in the Dong-Bei Special Steel bloom continuous casting machine with the bearing steel GCr15. This caster was designed by CONCAST, and its transverse section size was 370 mm × 490 mm at room temperature. This caster has 12 withdrawal units per strand, and the 2nd to 9th units are applied to execute reduction. The macrographs of the blooms and rolled bars (ϕ110mm) transverse section before and after the HR application were compared in Figure 8. It can be seen clearly that the serious center porosity in the transverse bloom section was eliminated evidently after the HR application, and the homogeneity and compactness of rolled bar were improved correspondingly.

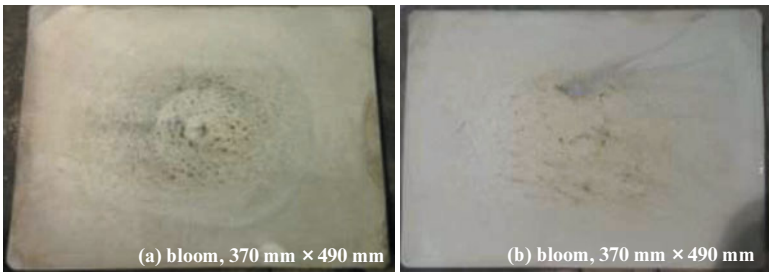

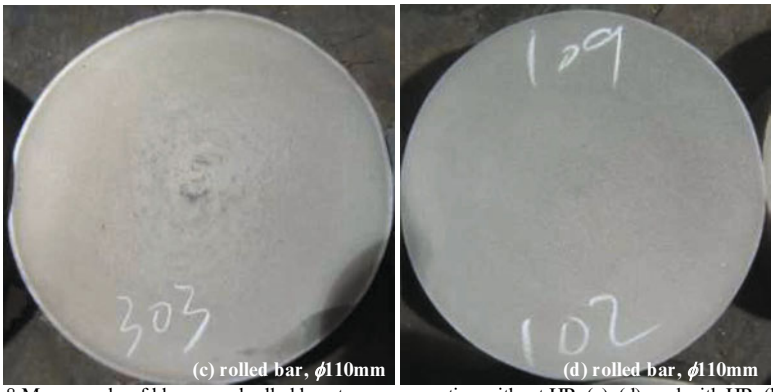

Figure 8 Macrographs of blooms and rolled bars transverse section without HR: (a), (d); and with HR: (b), (d).

According to the practice statistics, the defects rate of bloom center porosity and segregation was decreased from 2.0-2.5 grade to no more than 1.0 grade after the HR application. The compacted and homogenous bloom meet the requirement of rolling large size bars and profiles with lower rolling reduction ratio, and the bloom continuous casting process had replaced the larger ingot process successfully.

Conclusions

HR is an effective method to improve the homogeneity and compactness of slab and bloom with large section size, and its key technologies include online detection of strand solidification end, online calculation of minimum reduction amount, enhanced final electromagnetic stirring (F-EMS) and convex roll with curving surface. The plant results showed that the center segregation and porosity of larger section bloom could be improved significantly after the HR application. The compacted and homogenous bloom could replace the larger ingot to meet the requirement of rolling large size bars and profiles with the lower rolling reduction ratio successfully.

Acknowledgements

The present work is financially supported by the National Natural Science Foundation of China No. 51474058 and Program for Liaoning Excellent Talents in University (LJQ2015036). The special thanks are due to our cooperation companies for industrial trials and application.

References

1. S. Nabeshima et al., “Control of Centerline Segregation in Continuously Cast Blooms by Continuous Forging Process,” *ISIJ International*, 35 (6) (1995), 673-679.
2. M. Takubo et al., “NSENGI's New Developed Bloom Continuous Casting Technology for Improving Internal Quality of Special Bar Quality (NS bloom large reduction),” (Paper presented at *METEC & 2nd ESTAD 2015*, Düsseldorf, Germany, 15 June 2015), 1.
3. 平城正 et al., “高級極厚鋼板用新連続鋳造技術(PCCS 法)の開発,” *Materia Japan*, 48

(1) (2009), 20-22.
4. M. Kawamoto, "Recent Development of Steelmaking Process in Sumitomo Metals," *Journal of Iron and Steel Research, International*, 18 (S2) (2011), 28-35.
5. C.H. Yim et al., "Continuous Cast Slab and Method for Manufacturing the Same," US Patent, US8245760B2, Aug. 21, 2012.
6. X.K. Zhao et al., "The Position Study of Heavy Reduction Process for Improving Centerline Segregation or Porosity with Extra-Thickness Slabs," *Steel Research International*, 85 (4) (2014), 645-658.
7. X.K. Zhao et al., "Dynamic Recrystallization (DRX) Analysis of Heavy Reduction Process with Extra-Thickness Slabs," *Steel Research International*, 85 (5) (2014), 811-823.
8. B. Petrus et al., "Real-time, Model-Based Spray-Cooling Control System for Steel Continuous Casting," *Metallurgical and Materials Transactions B*, 42 (1) (2011), 87-103.
9. Z.F. Wang et al., "Vibration Method to Detect Liquid-Solid Fraction and Final Solidifying End for Continuous Casting Slab," *Steel Research International*, 84 (8) (2013), 724-731.
10. R. L. Parker, J. R. Manning and N. C. Peterson, "Application of Pulse-Echo Ultrasonics to Locate the Solid/Liquid Interface During Solidification and Melting of Steel and Other Metals," *Journal of Applied Physics*, 58 (11) (1985), 4150-4164.
11. C. Ji et al., "Uneven Solidification During Wide-Thick Slab Continuous Casting Process and Its Influence on Soft Reduction Zone," *ISIJ International*, 54 (1) (2014), 103-111.
12. C. Ji, "Thermal-mechanical Model of Uneven Solidification Shell in Wide-Thick Slab Continuous Casting Process with Soft Reduction (SR)," (Presented at the 6th International Conference on Modelling and Simulation of Metallurgical Processes in Steelmaking, Bardolino, Italy, 23 September 2015).
13. C. Ji, S. Luo, and M.Y. Zhu, "Analysis and Application of Soft Reduction Amount for Bloom," *ISIJ International*, 54 (3) (2014), 504-510.
14. S. Luo et al., "Deformation Behavior of Continuous Casting Blooms During Soft Reduction Process," *Journal of University of Science and Technology Beijing*, 32 (7) (2010), 890-894.
15. T. Takahashi, M. Kudoh, and K. Ichikawa, "Fluidity of the Liquid In the Solid-Liquid Coexisting Zone," *Transactions of the Japan Institute of Metals*, 21 (8) (1980), 531-538.
16. D.B. Jiang, M.Y. Zhu, "Flow and Solidification in Billet Continuous Casting Machine with Dual Electromagnetic Stirrings of Mold and the Final Solidification," *Steel Research International*, 86 (9) (2015), 993–1003.
17. C. H. Moon et al., "Effect of the Roll Surface Profile on Centerline Segregation in Soft Reduction Process," *ISIJ International*, 52 (7) (2012), 1266-1272.

CFD Modeling and Simulation in Materials Processing 2016
Edited by: Laurentiu Nastac, Lifeng Zhang, Brian G. Thomas, Miaoyong Zhu, Andreas Ludwig, Adrian S. Sabau, Koulis Pericleous, and Hervé Combeau
TMS (The Minerals, Metals & Materials Society), 2016

NUMERICAL STUDY OF FLOW BEHAVIOR AND OPTIMIZATION OF NOZZLE PORTS IN CONTINUOUS CASTING SLAB MOLD

Shuai Feng, LingXiang Hong, Bo Wang*, Shupei Liu, Zhiliang Yang, Kongfang Feng, Liang Bai, Jieyu Zhang

State Key Laboratory of Advanced Special Steel, School of Materials Science and Engineering, Shanghai University, Shanghai 200072, China

Keywords: Slab mold, Numerical simulation, Flow behavior, VOF model

Abstract

Nozzle plays a key role in determining the flow behavior in the mold of the continuous casting process with and without nozzle gas injection. Different modifications applied to the ports are used to study the flow behavior. The predicted results with k-ε turbulence model show that the backflow phenomenon eliminates owing to a low pressure zone at the ports, the surface velocity decreases, when the curvature is implemented at the internal upper side of the port. This result agrees with the simulation result of other researchers. Meanwhile, increasing the thickness of ports has little influence on the surface level fluctuation. The Reynolds-stress model (RSM) and the Volume of Fluid (VOF) model are used to simulate the air bubbles movement in the mold. The result shows that the air bubbles are closer to the nozzle while using the nozzle with curvature at the internal upper side of the port.

Introduction

The flow pattern in the mold is very important to steel quality in the process of continuous casting. Meniscus shape and its dynamic behavior are a direct consequence of turbulence structure of flow in the slab mold and are related to the design of the submerged entry nozzle (SEN). Different parameters of SEN would lead to different flow structure inside of the mold. Many of the researches have been done by the water modeling and by the numerical simulation to study and improve the design of nozzles to control the steel flow pattern. It is well known that the upper side of port taking curvature would eliminate the lower pressure zone in the SEN.

Nozzle clogging caused by non-metallic inclusions on ceramic walls is a serious problem in the continuous casting, which can be solved by injecting the gas from the top surface of nozzle. The injected gas goes into the liquid steel in the mold and forms gas bubbles. The gas bubbles can reduce the metal flow momentum at the nozzle exit, and decrease the surface velocity by injecting appropriate gas flow rate [1]. The researcher, KLAUS TIMMEL, investigated the distribution and the behavior of bubbles with the X-ray radioscopy in the small-scale model. They had found that the process of bubble formation was determined by a separation of relatively large bubbles from the bottom interface of the gas cavities [2]. A Lagrangian approach was performed to research the transport of bubbles. The results shown that the gas could shift the flow pattern of upper recirculation and lower roll, increase the surface fluctuation and impingement on the narrow surface. This would be more obvious with increasing the flow rate of gas [3].

In the present work, we have studied the ports with curvature and the change of ports thickness to the effects on the flow behavior, steel meniscus and impingement at the narrow surface. For this part, we have used the k-ε turbulence model as the turbulence model. Meanwhile, the bubbles movement is predicted using the Reynolds-stress (RSM) turbulence

* Corresponding author.

E-mail address: bowang@shu.edu.cn (bo wang)

model and the VOF multiphase model for the port with curvature and the port with -15 degrees .

Mathematical Models

The well accepted turbulence model, k-ε turbulence model, is used to simulate the flow behavior in the slab mold without gas injection for different shape of nozzles. The k and ε represents turbulent kinetic energy and turbulent dissipation rate respectively. Some researchers have found that the Reynolds-stress (RSM) turbulence model well predicted the formation of vortices located close to the SEN and near the meniscus than the k-ε turbulence model [4]. Therefore, the Reynolds-stress (RSM) turbulence model is performed to describe the turbulence phenomenon of the liquid and gas phases in the mold. The VOF multiphase model is considered the most suitable one to study the bubbles movement and surface fluctuation in the mold. All governing equations are well addressed in the literatures [1, 5, 7].

Calculation Details

On account of the symmetry of the structure, one quarter of the mold including SEN is chosen for the modeling. The structure of submerged entry nozzle (SEN) is showed in Fig.1, which also marks the modified position. The simulation parameters are listed in TableI . In this work, four different nozzles are studied, as shown in the Table II. A constant steel velocity is imposed at the SEN inlet based on desired casting speed and billet size. The gas was injected through the inlet together with steel phase, the volume fraction of gas is based on its flow rate. At the bottom of the field, a pressure outlet is applied. The flat surface is employed for the top surface. A no-slip boundary condition is put into use for the wall.

Table I. Simulation parameters

Parameter	Value	Parameter	Value
Casting speed,(m/min)	1.2	Viscosity of the liquid steel, (Pa·s)	0.0055
Nozzle immersion, (m)	0.17	Viscosity of the air, ($Pa \cdot s \times 10^{-5}$)	1.7894
Billet size, (m)	0.88×0.22	Density of the liquid steel, (kg/m^3)	7100
Gas flow rate, (L/min)	6.0	Density of the air, (kg/m^3)	1.225
Air zone(m)	0.3	Interfacial tension between steel and air, (N/m)	1.6

Nozzle immersion means the distance from the free surface to the internal upper side of the port in the Table I.

Table II. Simulation cases

Case	Inclination angle	Thickness (m)	Curvature (m)	Number
1	-15°	0.025	0	-15°H25
2	0°	0.025	0.035	R35H25
3	0°	0.030	0.035	R35H30
4	0°	0.040	0.035	R35H40

For the case1, the inclination angle downward 15 degrees, the thickness represents the port thickness.

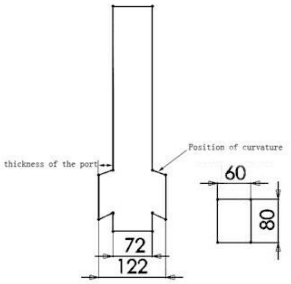

Fig.1 Structure of the SEN and the port

Results and Discussion

Effect of the Curvature at the Internal Upper Nozzle

The k-ε standard turbulence model was used to simulate the effect of SEN ports on flow behavior by applying the curvature at the internal upper port. Fig.2 shows the velocity profile inside the nozzle for case1 and case2. It can be seen from case1 that there exits a backflow phenomenon at the internal upper port owing to a lower pressure, which has great influence on the flow pattern in the mold. However, the backflow can be eliminated when the curvature design of port is used at the internal upper port for case2. These results also have been proved by the previous researcher's work [5]. The turbulent kinetic energy dissipation rates for two cases are shown in Fig.3. The results show that the dissipation rate for case1 is the bigger than case2.

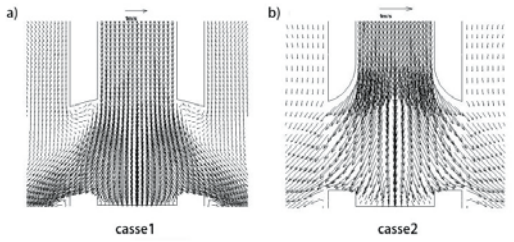

Fig.2 Velocity profile at the ports, a) case1, b) case2

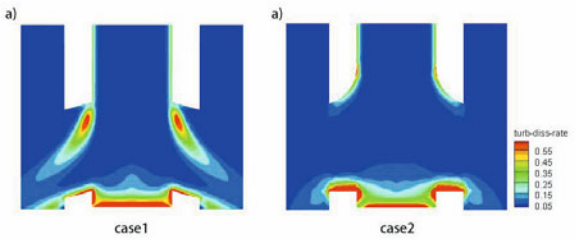

Fig.3 Kinetic energy dissipation rate, a) case1, b) case2

The Modification of curvature in the port can not only efficiently avoid the backflow, but also influence the surface velocity and the velocity magnitude at the impingement point of narrow surface. The Fig.4 presents the results of the flow velocity values along the centerline of 0.001m below free surface. It easily can be seen that the surface fluctuation will substantially decrease when using the curvature applied inside the SEN. It is important to prevent the slag entrapment from the molten steel. Fig.5(a) shows the velocity magnitude along the centerline at the distance of 0.001m from the narrow surface. The results show that the impingement for case2 has smaller effect than case1 on the narrow surface. So, case2 is beneficial to prevent from remelting the solidified shell.

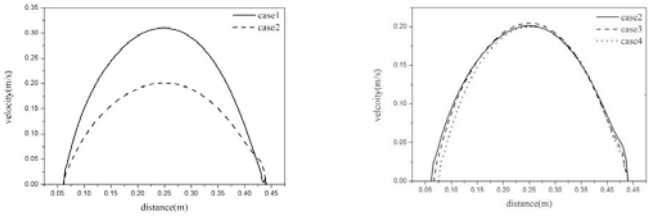

(a) case1 and case2 (b) case2, case3 and case4

Fig.4 Velocity magnitude along the centerline of 0.001m below the top surface

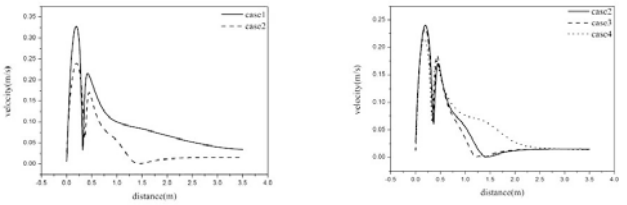

(a) case1 and case2 (b)case2, case3 and case4

Fig.5 Velocity magnitude along the centerline of 0.001m from the narrow surface

The angle of jet is crucial to the flow pattern in the mold of continuous casting slabs. A large jet angle may deliver the molten steel into the more deep zone, which will results in no enough heat to the meniscus, the meniscus would be frozen in the process of continuous casting. But a relative small jet angle would also have some problems, the slag will be exposed at the corner of the domain and caused re-oxidized. The jet angle is determined by the port angle and port area and the wall size [6].

Fig.6 shows the velocity contours at the central symmetrical plane of the mold for case 1 and case 2. The simulation results reveal that the jet angle of case2 is larger than case1. The change of jet velocity profile for the nozzle with -15 degrees is steeper than the SEN with the curvature at the upper internal port from the velocity contours. Besides, it demonstrates that the surface velocity has well agreement with the mentioned above.

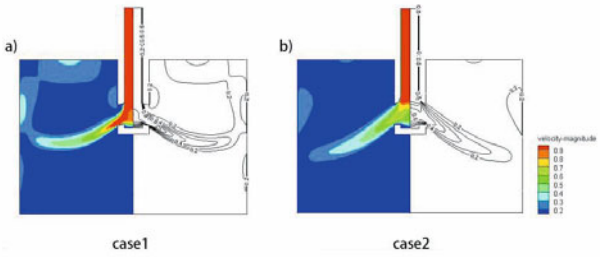

Fig.6 Velocity contours at the wide symmetrical surface, a) case1, b) case2

The effect of port thickness

Port thickness is the part of the SEN design, FADY M. NAJJAR [6] has found that the thicker ports reduce spreading of the jet. In this work, case2, case3 and case4 are illustrated the function of the port thickness. It is observed that the surface velocity has little difference on the three cases, and the trend is the same as the velocity magnitude at 0.001m from narrow surface as shown in Fig.4(b) and Fig.5(b).

Bubble movement

The VOF model and Reynolds-stress (RSM) turbulence model are used to simulate and investigate the movement of bubbles. Fig.7 shows the bubble movement at the 10s, 12s, 14.5s,

16.5s, 18.5s, 20.5s for case1 and case2. The gas is injected into the top surface of SEN with the molten steel, the bubble movement is crucial to the flotation of inclusions and flow pattern. From the circumstance of the bubbles movement at different times, it is seen that some bubbles are tend to close to the deep narrow surface employed by the -15 degrees port, which would be trapped by the solidified shell. Moreover, the result of applying the port with curvature indicates that the less bubbles are delivered to narrow surface, these bubbles are more likely to float with the molten steel.

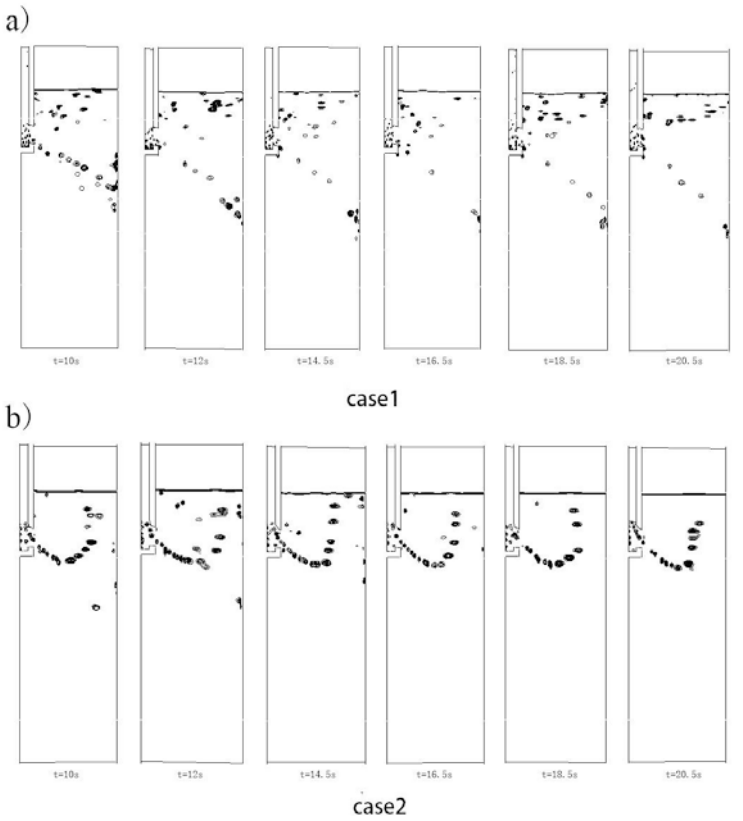

Fig.7 Bubbles movement at different times, a) case1, b) case2

Conclusions

The k-ε standard turbulence model is employed to study the effect of different ports on the flow pattern and velocity at the meniscus. The VOF model and the Reynolds-stress (RSM) turbulence model are developed to investigate the bubbles movement inside of mold. The simulation results indicate that the backflow phenomenon can be eliminated, the surface velocity decreases, the position of impingement point falls down, when applied the curvature at the side of upper internal port. Besides, increasing the thickness of ports has little impact on

the surface level fluctuation, but the velocity at the position of impingement point lessens. When using the curvature modified inside the SEN, air bubbles is dispersed the pool of the mold between SEN and narrow surface and less air bubbles impinged the solidified shell.

Acknowledgement

The author gratefully acknowledges the financial support received from the National Natural Science Foundation of China (No.51474143), Shanghai Economic and Information Commission (No.Hu CXY-2013-1).

Reference

1. Noriko KUBO et al., "Two-phase Flow Numerical Simulation of Molten Steel and Argon Gas in a Continuous Casting Mold," ISIJ International, 42 (2002), 1251-1258.
2. KLAUS TIMMEL et al., "Visualization of Liquid Metal Two-phase Flows in a Physical Model of the Continuous Casting Process of Steel," Metallurgical and Materials Transactions B, 46 (B) (2015), 700-710.
3. Zhong-qiu LIU et al., "Euler-Euler-Lagrangian Modeling for Two-Phase Flow and Particle Transport in Continuous Casting Mold," ISIJ International, 54 (2014), 1314-1323.
4. PÁVEL RAMÍREZ-LÓPEZ et al., "Structure of Turbulent Flow in a Slab Mold," Metallurgical and Materials Transactions B,36 (B) (2005), 787-800.
5. Garcia-hernandez Saul et al., "Numerical Optimization of Nozzle Ports to Improve the Fluidynamics by Controlling Backflow in a Continuous Casting Slab Mold," ISIJ International, 53 (2013), 1794-1802
6. FADY M. NAJJAR, BRIAN G. THOMAS, DONALD E. HERSHEY. "Numerical Study of Steady Turbulent Flow through Bifurcated," Metallurgical and Materials Transactions B, 26 (B) (1994), 749-765.
7. WANG Bo et al., "Mathematical and physical simulation of controlling fluid flow in a slab casting mold," Journal of Iron and Steel Research International, 15 (2008), 532-537.

CFD Modeling and Simulation in Materials Processing 2016
Edited by: Laurentiu Nastac, Lifeng Zhang, Brian G. Thomas, Miaoyong Zhu, Andreas Ludwig, Adrian S. Sabau, Koulis Pericleous, and Hervé Combeau
TMS (The Minerals, Metals & Materials Society), 2016

THE EFFECT OF PULSE WIDTH ON THE CHARACTERISTIC OF DISCHARGE AND FLOW FOR PURE ALUMINUM

Xiang Wang[1,2], Zhishuai Xu[2], Qixin Wang[1,2], Qijie Zhai[2], Ning Pei[1], Yongyong Gong[1,2]*

[1]College of Science,Shanghai University,99 Shangda Road Shanghai China 200444
[2]Shanghai Key Laboratory of Modern Metallurgy&Materials Processing,Shanghai University, 149 Yanchang Road,Shanghai China 200072
*Corresponding author

Keywords: Pulse width,Discharge, Flow velocity

Abstract

In order to study the relationship between flow characteristics and pulse width of the pulse magnetic oscillation (PMO) technique, we used the solenoid coil to process aluminum liquid under variable pulse widths of the PMO technique changed by different capacitors. The electro-magnetic force and flow field of the process of liquid pure aluminum were analysized by ANSYS simulation.

Introduction

In the last 20 years, it has been widely studied and applied in the process of metal solidification by using electromagnetic field[1-4]. The pulsed electromagnetic field has a large instantaneous power, simple manufacturing and operation, low manufacturing costs and better effect of grain refinement, which becomes a new rapidly development technology for metal solidification processing. Pulsed electromagnetic field processing technology includes ECP[5-6], PMF[7-8] and PMO[9-11], etc.

PMO technique are related with many parameters such as peak current, discharge frequency, pulse width, discharge power,etc. The change of pulse width of PMO technique means that the inherent frequency of the oscillation circuit has been changed, which needs to change the capacity of the capacitor or coil structure.Therefore, the change of the pulse width of PMO technique is troublesome, and the related research is not so much. In this paper, the pulse width of PMO technique is changed by altering the capacity of capacitor. Discharge energy and discharge power is calculated by measuring the voltage of the capacitor. Using commercial software ANSYS 15.0,we simulated the treatment process of PMO technique by circuit electromagnetic coupling,electromagnetic field and flow field coupling to reveal the effects of pulse width on the discharge energy,discharge power, electromagnetic force and flow field.

Experimental apparatus and process

The experimental circuit is shown in Figure 1,which includes:3 sets of capacitors connected in parallel installations,whose capacitance value is 3700 F,22200 F,59200 F,respectively;DC charging power supply;SCR trigger switch;Oscilloscope to measure the voltage of capacitor;

copper tube coil;pure aluminum melt.Figure 2 is the sample and device size chart. The graphite is cylindrical crucible.The number of turns of the coil is 5. The processed samples is 99.7% industrial pure aluminum melt. Only one set of capacitor is used at each processing. Discharge frequency is 10Hz.Charge energy is 74J.Pure aluminum is heated to 750℃ by resistance furnace, and poured into the mold at 720℃. The temperature of the mold is 30℃.The voltage waveforms of capacitor were recorded by oscilloscope.

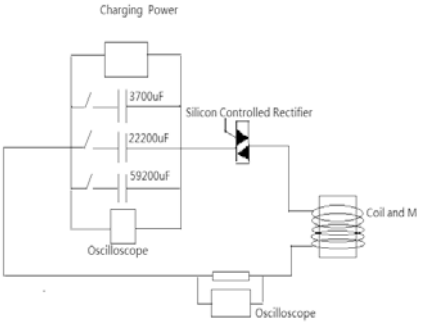

Figure 1. Experimental circuit diagram

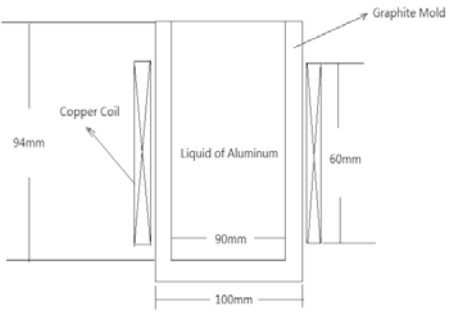

Figure 2. Sample and device size chart

Measurement and analysis

Pulse discharge structure was designed based on RLC circuit, The differential equation of RLC circuit discharge can be expressed as

$$LC\frac{d^2U}{dt^2}+RC\frac{dU}{dt}+U=0 \tag{1}$$

where U is the voltage,C is the capacity,L is the inductance,R is the resistance.U can be expressed as

$$U=U_0e^{-at}\cos(\frac{2\pi}{T}t+\theta) \tag{2}$$

$$a=\frac{R}{2L} \tag{3}$$

$$T=\frac{2\pi}{\sqrt{\frac{1}{LC}-\frac{R^2}{4L^2}}} \tag{4}$$

In a complete discharge cycle, the voltage waveforms is shown in figure 3.

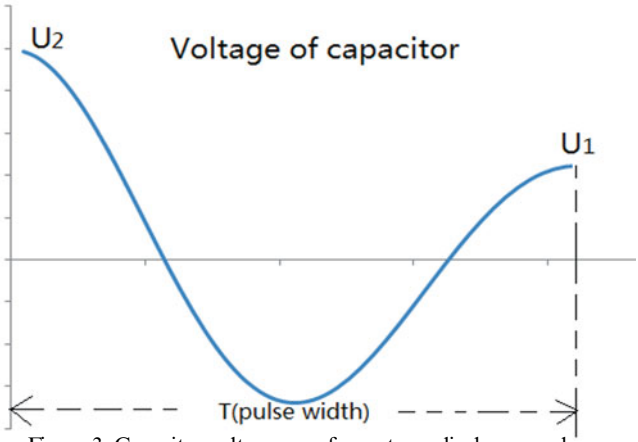

Figure 3. Capacitor voltage waveform at one discharge cycle

The initial voltage of discharge U_1, the end of discharge voltage U_2 and pulse width T can be recorded by oscilloscope. From the measurement data we can obtain:
the discharge energy W_d at one cycle can be expressed as

$$W_d = \frac{1}{2} C_1 U_1^2 - \frac{1}{2} C_2 U_2^2 \tag{5}$$

the discharge power Pw at one discharge cycle can be expressed as

$$P_w = \frac{W_d}{T} \tag{6}$$

The charge energy Wc of 3 sets of capacitors is all set to 74J,the measurment results are shown in table 1.

Table Ⅰ The measurment and calculation result

C/μF	W_c/J	T/ms	U_1/V	U_2/V	W_d/J	P_w/W
3700	74	1.0	200	132.8	41.4	41400
22200	74	2.4	81.6	41.6	54.7	22791
59200	74	4.0	50	22.8	58.6	14650

The value of the pulse width is porvided as 1ms,2.4ms and 4ms,respectively. With the increase of the pulse width, discharge energy W_d becomes larger. but the discharge power Pw becomes small.

Numerical simulation results

In order to investigate the flow of melt due to electromagnetic force under different pulse width,we simulate the process under PMO with ANSYS Multiphysics package. The electromagnetic field is coupled with the electric circuit to calculate the distribution of the electromagnetic force on the melt by using PLANE53 element and CIRCU124 element, and to calculate the waveforms of voltage of capacitor in the circuit. By using FLUID141 element,the flow field is coupled with the electromagnetic field,which leads the electromagnetic force into the fluid to calculate the distribution of velocity on the melt.

As shown in figure 4, the left of the figure is circuit model, the right of the figure is 2D axis symmetric finite element model.Because the pulsed magnetic field is transient,so the transient time analysis is used. The waveforms of vlotage is shown as figur 5.The waveforms of current is shown as figure 6. The electromagnetic force on the melt are calculated with100 steps in the periods time of discharge (T1). There is no electromagnetic force during the interval period (T2, T1<<T2),The flow velocity is calculated with 30 steps in the period (T2).The initial voltages are consistent with the experimental conditions,The initial velocity:Vx=0,Vy=0.The boundary conditions is that:(1) in the junction of melt and mold: Vx=0,Vy=0 (2)melt top surface:Vy=0; (3) Symmetry axis: Vx=0.Physical property parameters of fluid are got from commercial software Procast,as shown in table 4. Zero energy equation model is selected as turbulence model.

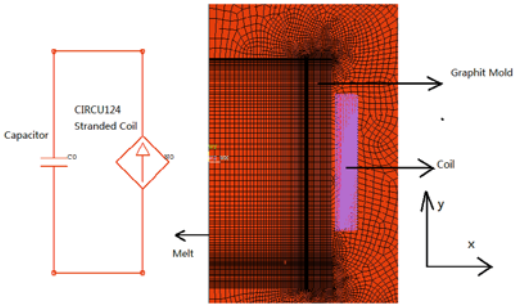

Figure 4. Circuit model and 2D axis symmetric finite element model.

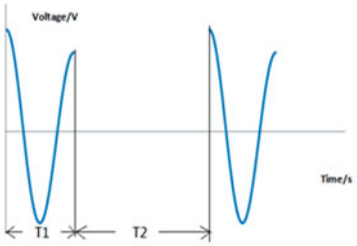

Figure 5. Waveforms of voltage

Figure 6. Waveforms of current

Table Ⅱ shows the simulation results of discharge energy.

Table Ⅱ The simulation results of discharge energy

C/μF	W_c/J	T/ms	U_1/V	U_2/V	W_d/J	P_w/W
3700μF	74	1.02	200	130	42.7	41862
22200μF	74	2.55	81.6	41.1	55.2	21647
59200μF	74	4.2	50	22.4	59.1	14071

TableⅢ Physical property parameters of fluid

	Resistivity/ Ω · m	Relative Permeality	Density/ kg· m^3	Viscosity/ Pa· s
Al	$2.42x10^{-7}$	1	2380	$2.51x10^{-3}$

The results from the ANSYS simulation show that,capacitors with 3700μF,22000μF,59200μF provides the value of pulse width is:1.02ms,2.6ms and 4.2ms, respectively.Figure 7. shows the flow velocity distribution on the complete cross section at the end of the 30 discharge cycles. At this time the flow velocity has been stable, the velocity of every point fluctuates up and down around a certain value. The positions of maximum velocity are close to the mold and central axis.

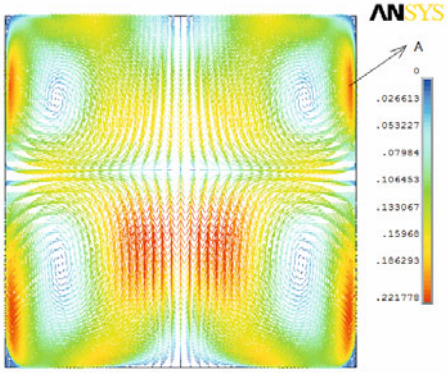

Figure 7. The flow velocity distribution on the complete cross section

Figure 8.shows the shows the time-varying curve of electromagnetic force density at point A (as shown in figure.7) under three different pulse widths of PMO technique. Electromagnetic force density can be expressed as

$$f = J \times B \tag{7}$$

Where J is current density,B is the magnetic flux density. Figure 9. shows the time-varying curve of velocity at point A

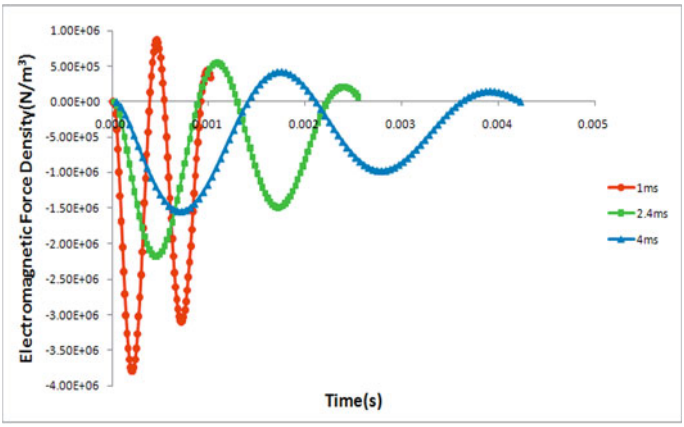

Figure 8. Time-varying curve of electromagnetic pressure force density at point A at one discharge cycle

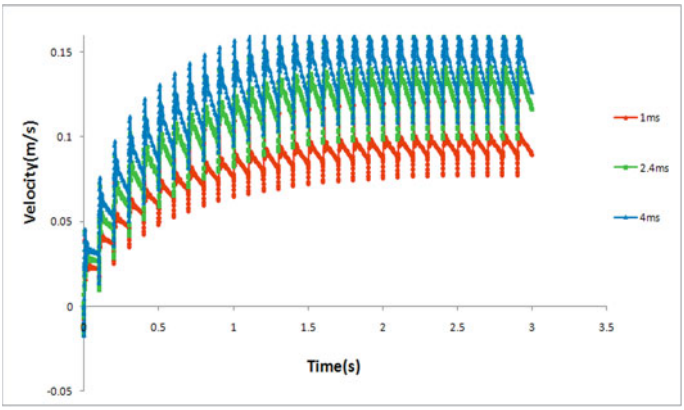

Figure 9. Time-varying curve of the time-varying curve of velocity at point A

Table Ⅲ(the measurement results) and Table Ⅳ(simulation results) show that, from large to small,the sequence of discharge energy is:4ms>2.4ms>1ms; the sequence of discharge power is:1ms>2.4ms>4ms.Figure7. shows that,the velocity reach stable after about 10 discharge cycle. PMO forms 2 general circulation located up and down the melt. Figure 8. shows the sequence of eletromagnetic force at point A:1ms>2.4ms>4ms. Figure 9. shows the sequence of velocity at

point A:4ms>2.4ms>1ms. Pulsed electromagnetic fields have 2 functions for the melt:stir and vibration,the ratio can be expressed as[12]

$$\frac{frot}{firrot} = \frac{\delta}{L} \tag{8}$$

where f_{rot} is stir force,f_{irrot} is magnetice pressure,δ is skin depth,L is characteristic length.So the narrow pulse width means small skin depth, magnetice pressure is large.Vibration is obvous;wide pulse width means the large skin depth,The stir force is large. Flow is more obvious.

Conclusion

Under the same charge energy and discharge frequency, we found:
(1) The large value of pulse width of PMO technique lead large discharge energy and average velocity.Flow is obvious.
(2)The small value of pulse width of PMO technique lead large discharge power and electromagnetic pressure.Vibration is obvious.

Acknowledgement

The authors gratefully acknowledge the financial supports from the National Basic Research Program of China (973 program)(Grant No.2011CB012902) andtheNational Natural Science Foundation of China(Grant Nos.11304194 and 50574056).

References

[1] Ch.VIVES,R. RICOU, " Fluid Flow Phenomena in a Single Phase Coreless Induction Furnace".*METALLURGICAL TRANSACTIONS B*,10(1985),227-235.
[2] J.M.Galpin,Y.Fautrelle, "Liquid-metal flows induced by low-frequency alternating magnetic fields". *Fluid Mech*,239(1992),383-408
[3] DENG An-yuan et al., "Oscillation Characteristics of Molten Metal Free Surface Under Com pound Magnetic Field",*JOURNAL OF IRON AND STEEL REASEARCH,INTERNATIONAL*,18(5) (2011), 5-30,37
[4] Mingjun Li,Takuya Tamura,Kenji Miwa. "Controlling microstructures of AZmagnesium alloys by an electromagnetic vibration technique during solidification: From experimental observation to theoretical understanding".*Acta Materialia*,55(2007),4635–4643
[5] Masayuki NAKADA,Yuh SHIOHARA, Merton C. FLEMINGS. "Modification of solidificati on structures by pulse electric discharging".*ISIJ international*,30(1)(1990),27-33
[6] Xiliang Liao et al., "Refining mechanism of the electric current pulse on the solidification str ucture of pure aluminum". *Acta Materialia*,55(2007):3103-3109
[7] Yu-Lai Gao et al., "Comparative study on structural transformation of low-melting pure Al a nd high-melting stainless steel under external pulsed magnetic field",*Materials Letters*,61(2007), 4011-4014

[8] Xiaoping Ma, Yuansheng Yang , Bin Wang, “Effect of pulsed magnetic field on superalloy m elt”. *International Journal of Heat and Mass Transfer*,52(2009), 5285-5292
[9] Yong-Yong Gong et al., “Structure refinement of pure aluminum by pulse magneto-oscillatio n”,*Materials Science and Engineering A*,497(2008), 147-152.
[10] Dong Liang et al., “Nucleation and grain formation of pure Al under Pulsed Magneto-Oscill ationtreatment”,*Materials Letters*,130(2014),48-50.
[11] Zhishuai Xu et al., “Microstructure modification for semisolid slurry of Al-4.5wt.%Cu alloy by pulse magneto-oscillation treatment”.143th TMS Annual Meeting,San Diego,California,USA, February 16-20,2014,401-407
[12]Furo-cho et al,“Birth and Recent Activities of Electromagnetic Processing of Materials”,ISIJ International,29(12)(1989),981-992

AUTHOR INDEX

CFD Modeling and Simulation in Materials Processing 2016

M

N

O

P

R

S

T

V

W

X

SUBJECT INDEX

CFD Modeling and Simulation in Materials Processing 2016

G

H

I

L

M

N

O

P

R